学 位 論 文

Study of Charm Production from the Measurement of Single Electrons in Au + Au Collisions at $\sqrt{s_{\mathrm{NN}}}$ = 200 GeV

(核子対あたりの重心系衝突エネルギー200 GeV の金＋金原子核衝突における単電子測定によるチャーム生成の研究)

２０１０年１月

広島大学大学院理学研究科
物理科学専攻

蜂谷　崇

目　次

１．主論文

Study of Charm Production from the Measurement of Single Electrons in Au+Au Collisions at $\sqrt{s_{NN}}$ = 200 GeV

(核子対あたりの重心系衝突エネルギー200GeV の金＋金原子核衝突における単電子測定によるチャーム生成の研究)

蜂谷　崇

２．公表論文

(1) Centrality Dependence of Charm Production from a Measurement of Single Electrons in Au+Au Collisions at $\sqrt{s_{NN}}$ =200 GeV

S. S. Adler *et al.*, (別紙、共著者リスト①参照)

Physical Review Letters 94, 082301 (2005).

３．参考論文

(1) Measurement of Single Electrons and Implications for Charm Production in Au+Au Collisions at $\sqrt{s_{NN}}$ = 130 GeV

K. Adcox *et al.*, (別紙、共著者リスト②参照)

Physical Review Letters 88, 192303 (2002).

(2) Measurement of Bottom Versus Charm as a Function of Transverse Momentum with Electron-Hadron Correlations in p + p Collisions at $\sqrt{s}$ = 200 GeV

A. Adare *et al.*, (別紙、共著者リスト③参照)

Physical Review Letters 103, 082002 (2009).

(3) PHENIX inner detectors

M. Allen et al., (別紙，共著者リスト④参照)

Nuclear Instruments and Methods in Physics Research A 499, 549 (2003).

共著者リスト①

S. S. Adler, S. Afanasiev, C. Aidala, N. N. Ajitanand, Y. Akiba, J. Alexander, R. Amirikas, L. Aphecetche, S. H. Aronson, R. Averbeck, T. C. Awes, R. Azmoun, V. Babintsev, A. Baldisseri, K. N. Barish, P. D. Barnes, B. Bassalleck, S. Bathe, S. Batsouli, V. Baublis, A. Bazilevsky, S. Belikov, Y. Berdnikov, S. Bhagavatula, J. G. Boissevain, H. Borel, S. Borenstein, M. L. Brooks, D. S. Brown, N. Bruner, D. Bucher, H. Buesching, V. Bumazhnov, G. Bunce, J. M. Burward-Hoy,4 S. Butsyk, X. Camard, J.-S. Chai, P. Chand, W. C. Chang, S. Chernichenko, C. Y. Chi, J. Chiba, M. Chiu, I. J. Choi, J. Choi, R. K. Choudhury, T. Chujo, V. Cianciolo, Y. Cobigo, B. A. Cole, P. Constantin, D. G. d'Enterria, G. David, H. Delagrange, A. Denisov, A. Deshpande, E. J. Desmond, A. Devismes, O. Dietzsch, O. Drapier, A. Drees, R. du Rietz, A. Durum, D. Dutta, Y. V. Efremenko, K. El Chenawi, A. Enokizono, H. En'yo, S. Esumi, L. Ewell, D. E. Fields, F. Fleuret, S. L. Fokin, B. D. Fox, Z. Fraenkel, J. E. Frantz, A. Franz, A. D. Frawley, S.-Y. Fung, S. Garpman, T. K. Ghosh, A. Glenn, G. Gogiberidze, M. Gonin, J. Gosset, Y. Goto, R. Granier de Cassagnac, N. Grau, S. V. Greene, M. Grosse Perdekamp, W. Guryn, H.-A° . Gustafsson, T. Hachiya, J. S. Haggerty, H. Hamagaki, A. G. Hansen, E. P. Hartouni, M. Harvey, R. Hayano, N. Hayashi, X. He, M. Heffner, T. K. Hemmick, J. M. Heuser, M. Hibino, J. C. Hill, W. Holzmann, K. Homma, B. Hong, A. Hoover, T. Ichihara, V.V. Ikonnikov, K. Imai, D. Isenhower, M. Ishihara, M. Issah, A. Isupov, B.V. Jacak, W.Y. Jang, Y. Jeong, J. Jia, O. Jinnouchi, B. M. Johnson, S. C. Johnson, K. S. Joo, D. Jouan, S. Kametani, N. Kamihara, J. H. Kang, S. S. Kapoor, K. Katou, S. Kelly, B. Khachaturov, A. Khanzadeev, J. Kikuchi, D. H. Kim, D. J. Kim, D.W. Kim, E. Kim, G.-B. Kim, H. J. Kim, E. Kistenev, A. Kiyomichi, K. Kiyoyama, C. Klein-Boesing, H. Kobayashi, L. Kochenda, V. Kochetkov, D. Koehler, T. Kohama, M. Kopytine, D. Kotchetkov, A. Kozlov, P. J. Kroon, C. H. Kuberg, K. Kurita, Y. Kuroki, M. J. Kweon, Y. Kwon, G. S. Kyle, R. Lacey, V. Ladygin, J. G. Lajoie, A. Lebedev, S. Leckey, D. M. Lee, S. Lee, M. J. Leitch, X. H. Li, H. Lim, A. Litvinenko, M. X. Liu, Y. Liu, C. F. Maguire, Y. I. Makdisi, A. Malakhov, V. I. Manko, Y. Mao, G. Martinez, M. D. Marx, H. Masui, F. Matathias, T. Matsumoto, P. L. McGaughey, E. Melnikov, F. Messer, Y. Miake, J. Milan, T. E. Miller, A. Milov, S. Mioduszewski, R. E. Mischke, G. C. Mishra, J. T. Mitchell, A. K. Mohanty, D. P. Morrison, J. M. Moss, F. Mu¨hlbacher, D. Mukhopadhyay, M. Muniruzzaman, J. Murata, S. Nagamiya, J. L. Nagle, T. Nakamura, B. K. Nandi, M. Nara, J. Newby, P. Nilsson, A. S. Nyanin, J. Nystrand, E. O'Brien, C. A. Ogilvie, H. Ohnishi, I. D. Ojha, K. Okada, M. Ono, V. Onuchin, A. Oskarsson, I. Otterlund, K. Oyama, K. Ozawa, D. Pal, A. P. T. Palounek, V. S. Pantuev, V. Papavassiliou, J. Park, A. Parmar, S. F. Pate, T. Peitzmann, J.-C. Peng, V. Peresedov, C. Pinkenburg, R. P. Pisani, F. Plasil, M. L. Purschke, A. K. Purwar, J. Rak, I. Ravinovich, K. F. Read, M. Reuter, K. Reygers, V. Riabov, Y. Riabov, G. Roche, A. Romana, M. Rosati, P. Rosnet, S. S. Ryu, M. E. Sadler, N. Saito, T. Sakaguchi, M. Sakai, S. Sakai, V. Samsonov, L. Sanfratello, R. Santo, H. D. Sato, S. Sato, S. Sawada, Y. Schutz, V. Semenov, R. Seto, M. R. Shaw, T. K. Shea, T.-A. Shibata, K. Shigaki, T. Shiina, C. L. Silva, D. Silvermyr, K. S. Sim, C. P. Singh, V. Singh, M. Sivertz, A. Soldatov, R. A. Soltz, W. E. Sondheim, S. P. Sorensen, I.V. Sourikova, F. Staley, P.W. Stankus, E. Stenlund, M. Stepanov, A. Ster, S. P. Stoll, T. Sugitate, J. P. Sullivan, E. M. Takagui, A. Taketani, M. Tamai, K. H. Tanaka, Y. Tanaka, K. Tanida, M. J. Tannenbaum, P. Tarja´n, J. D. Tepe, T. L. Thomas, J. Tojo, H. Torii, R. S. Towell, I. Tserruya, H. Tsuruoka, S. K. Tuli, H. Tydesjo¨, N. Tyurin, H.W. van Hecke, J. Velkovska, M. Velkovsky, V. Veszpre´mi, L. Villatte, A. A. Vinogradov, M. A. Volkov, E. Vznuzdaev, X. R. Wang, Y. Watanabe, S. N. White, F. K. Wohn, C. L. Woody, W. Xie, Y. Yang, A. Yanovich, S. Yokkaichi, G. R. Young, I. E. Yushmanov, W. A. Zajc, C. Zhang, S. Zhou, S. J. Zhou, and L. Zolin

共著者リスト②

K. Adcox, S. S. Adler, N. N. Ajitanand, Y. Akiba, J. Alexander, L. Aphecetche, Y. Arai, S. H. Aronson, R. Averbeck, T. C. Awes, K. N. Barish, P. D. Barnes, J. Barrette, B. Bassalleck, S. Bathe, V. Baublis, A. Bazilevsky, S. Belikov, F. G. Bellaiche, S. T. Belyaev, M. J. Bennett, Y. Berdnikov, S. Botelho, M. L. Brooks, D. S. Brown, N. Bruner, D. Bucher, H. Buesching, V. Bumazhnov, G. Bunce, J. Burward-Hoy, S. Butsyk, T. A. Carey, P. Chand, J. Chang, W. C. Chang, L. L. Chavez, S. Chernichenko, C.Y. Chi, J. Chiba, M. Chiu, R. K. Choudhury, T. Christ, T. Chujo, M. S. Chung, P. Chung, V. Cianciolo, B. A. Cole, D. G. D'Enterria, G. David, H. Delagrange, A. Denisov, A. Deshpande, E. J. Desmond, O. Dietzsch, B.V. Dinesh, A. Drees, A. Durum, D. Dutta, K. Ebisu, Y.V. Efremenko, K. El Chenawi, H. En'yo, S. Esumi, L. Ewell, T. Ferdousi, D. E. Fields, S. L. Fokin, Z. Fraenkel, A. Franz, A. D. Frawley, S.-Y. Fung, S. Garpman, T.K. Ghosh, A. Glenn, A. L. Godoi, Y. Goto, S.V. Greene, M. Grosse Perdekamp, S. K. Gupta, W. Guryn, H.-A. Gustafsson, T. Hachiya, J. S. Haggerty, H. Hamagaki, A. G. Hansen, H. Hara, E. P. Hartouni, R. Hayano, N. Hayashi, X. He, T. K. Hemmick, J.M. Heuser, M. Hibino, J. C. Hill, D. S. Ho, K. Homma, B. Hong, A. Hoover, T. Ichihara, K. Imai, M. S. Ippolitov, M. Ishihara, B.V. Jacak, W.Y. Jang, J. Jia, B. M. Johnson, S. C. Johnson, K. S. Joo, S. Kametani, J. H. Kang, M. Kann, S. S. Kapoor, S. Kelly, B. Khachaturov, A. Khanzadeev, J. Kikuchi, D. J. Kim, H. J. Kim, S.Y. Kim, Y. G. Kim, W.W. Kinnison, E. Kistenev, A. Kiyomichi, C. Klein-Boesing, S. Klinksiek, L. Kochenda, V. Kochetkov, D. Koehler, T. Kohama, D. Kotchetkov, A. Kozlov, P. J. Kroon, K. Kurita, M. J. Kweon, Y. Kwon, G. S. Kyle, R. Lacey, J. G. Lajoie, J. Lauret, A. Lebedev, D. M. Lee, M. J. Leitch, X. H. Li, Z. Li, D. J. Lim, M. X. Liu, X. Liu, Z. Liu, C. F. Maguire, J. Mahon, Y. I. Makdisi, V. I. Manko, Y. Mao, S. K. Mark, S. Markacs, G. Martinez, M. D. Marx, A. Masaike, F. Matathias, T. Matsumoto, P. L. McGaughey, E. Melnikov, M. Merschmeyer, F. Messer, M. Messer, Y. Miake, T. E. Miller, A. Milov, S. Mioduszewski, R. E. Mischke, G. C. Mishra, J.T. Mitchell, A. K. Mohanty, D. P. Morrison, J. M.Moss, F. Muhlbacher, M. Muniruzzaman, J. Murata, S. Nagamiya, Y. Nagasaka, J. L. Nagle, Y. Nakada, B. K. Nandi, J. Newby, L. Nikkinen, P. Nilsson, S. Nishimura, A. S. Nyanin, J. Nystrand, E. O'Brien, C. A. Ogilvie, H. Ohnishi, I. D. Ojha, M. Ono, V. Onuchin, A. Oskarsson, L. Osterman, I. Otterlund, K. Oyama, L. Paffrath, A. P. T. Palounek, V. S. Pantuev, V. Papavassiliou, S. F. Pate, T. Peitzmann, A. N. Petridis, C. Pinkenburg, R. P. Pisani, P. Pitukhin, F. Plasil, M. Pollack, K. Pope, M. L. Purschke, I. Ravinovich, K. F. Read, K. Reygers, V. Riabov, Y. Riabov, M. Rosati, A. A. Rose, S. S. Ryu, N. Saito, A. Sakaguchi, T. Sakaguchi, H. Sako, T. Sakuma, V. Samsonov, T. C. Sangster, R. Santo, H. D. Sato, S. Sato, S. Sawada, B. R. Schlei, Y. Schutz, V. Semenov, R. Seto, T. K. Shea, I. Shein, T.-A. Shibata, K. Shigaki, T. Shiina, Y. H. Shin, I. G. Sibiriak, D. Silvermyr, K. S. Sim, J. Simon-Gillo, C. P. Singh, V. Singh, M. Sivertz, A. Soldatov, R. A. Soltz, S. Sorensen, P.W. Stankus, N. Starinsky, P. Steinberg, E. Stenlund, A. Ster, S. P. Stoll,M. Sugioka, T. Sugitate, J. P. Sullivan, Y. Sumi, Z. Sun, M. Suzuki, E. M. Takagui, A. Taketani, M. Tamai, K. H. Tanaka, Y. Tanaka, E. Taniguchi, M. J. Tannenbaum, J. Thomas, J. H. Thomas, T. L. Thomas, W. Tian, J. Tojo, H. Torii, R. S. Towell, I. Tserruya, H. Tsuruoka, A. A. Tsvetkov, S. K. Tuli, H. Tydesjo, N. Tyurin, T. Ushiroda, H.W. van Hecke, C. Velissaris, J. Velkovska, M. Velkovsky, A. A. Vinogradov, M. A. Volkov, A. Vorobyov, E. Vznuzdaev, H. Wang, Y. Watanabe, S. N. White,C. Witzig, F. K. Wohn, C. L. Woody, W. Xie, K. Yagi, S. Yokkaichi, G. R. Young, I. E. Yushmanov, W. A. Zajc, Z. Zhang, and S. Zhou

共著者リスト③

A. Adare, S. Afanasiev, C. Aidala, N. N. Ajitanand, Y. Akiba, H. Al-Bataineh, J. Alexander, K. Aoki, L. Aphecetche, R. Armendariz, S. H. Aronson,J. Asai, E. T. Atomssa, R. Averbeck, T. C. Awes, B. Azmoun, V. Babintsev, M. Bai, G. Baksay, L. Baksay, A. Baldisseri, K. N. Barish, P. D. Barnes, B. Bassalleck, A. T. Basye, S. Bathe, S. Batsouli, V. Baublis, C. Baumann, A. Bazilevsky, S. Belikov, R. Bennett, A. Berdnikov, Y. Berdnikov, A. A. Bickley, J. G. Boissevain, H. Borel, K. Boyle, M. L. Brooks, H. Buesching, V. Bumazhnov, G. Bunce, S. Butsyk, C. M. Camacho, S. Campbell, B. S. Chang, W. C. Chang, J.-L. Charvet, S. Chernichenko, J. Chiba, C.Y. Chi, M. Chiu, I. J. Choi, R. K. Choudhury, T. Chujo, P. Chung, A. Churyn, V. Cianciolo, Z. Citron, C. R. Cleven, B. A. Cole, M. P. Comets, P. Constantin, M. Csana´d, T. Cso¨rgo? , T. Dahms, S. Dairaku, K. Das, G. David, M. B. Deaton, K. Dehmelt, H. Delagrange, A. Denisov, D. d'Enterria, A. Deshpande, E. J. Desmond, O. Dietzsch, A. Dion, M. Donadelli, O. Drapier, A. Drees, K. A. Drees, A. K. Dubey, A. Durum, D. Dutta, V. Dzhordzhadze, Y.V. Efremenko, J. Egdemir, F. Ellinghaus, W. S. Emam, T. Engelmore, A. Enokizono, H. En'yo, S. Esumi, K. O. Eyser, B. Fadem, D. E. Fields, M. Finger, Jr., M. Finger, F. Fleuret, S. L. Fokin, Z. Fraenkel, J. E. Frantz, A. Franz, A. D. Frawley, K. Fujiwara, Y. Fukao, T. Fusayasu, S. Gadrat, I. Garishvili, A. Glenn, H. Gong, M. Gonin, J. Gosset, Y. Goto, R. Granier de Cassagnac, N. Grau, S.V. Greene, M. Grosse Perdekamp, T. Gunji, H.-A° . Gustafsson, T. Hachiya, A. Hadj Henni, C. Haegemann, J. S. Haggerty, H. Hamagaki, R. Han, H. Harada, E. P. Hartouni, K. Haruna, E. Haslum, R. Hayano, M. Heffner, T. K. Hemmick, T. Hester, X. He, H. Hiejima, J. C. Hill, R. Hobbs, M. Hohlmann, W. Holzmann, K. Homma, B. Hong, T. Horaguchi, D. Hornback, S. Huang, T. Ichihara, R. Ichimiya, Y. Ikeda, K. Imai, J. Imrek, M. Inaba, Y. Inoue, D. Isenhower, L. Isenhower, M. Ishihara, T. Isobe, M. Issah, A. Isupov, D. Ivanischev, B.V. Jacak, J. Jia, J. Jin, O. Jinnouchi, B. M. Johnson, K. S.Joo, D. Jouan, F. Kajihara, S. Kametani, N. Kamihara, J. Kamin, M. Kaneta, J. H. Kang, H. Kanou, J. Kapustinsky, D. Kawall, A.V. Kazantsev, T. Kempel, A. Khanzadeev, K. M. Kijima, J. Kikuchi, B. I. Kim, D. H. Kim, D. J. Kim, E. Kim, S. H. Kim, E. Kinney, K. Kiriluk, A. Kiss, E. Kistenev, A. Kiyomichi, J. Klay, C. Klein-Boesing, L. Kochenda, V. Kochetkov, B. Komkov, M. Konno, J. Koster, D. Kotchetkov, A. Kozlov, A. Kra´l, A. Kravitz, J. Kubart, G. J. Kunde, N. Kurihara, K. Kurita, M. Kurosawa, M. J. Kweon, Y. Kwon, G. S. Kyle, R. Lacey, Y.-S. Lai, Y. S. Lai, J. G. Lajoie, D. Layton, A. Lebedev, D. M. Lee, K. B. Lee, M. K. Lee, T. Lee, M. J. Leitch, M. A. L. Leite, B. Lenzi, P. Liebing, T. Lis?ka, A. Litvinenko, H. Liu, M. X. Liu, X. Li, B. Love, D. Lynch, C. F. Maguire, Y. I. Makdisi, A. Malakhov, M. D. Malik, V. I. Manko, E. Mannel, Y. Mao, L. Mas?ek, H. Masui, F. Matathias, M. McCumber, P. L. McGaughey, N. Means, B. Meredith, Y. Miake, P. Mikes?, K. Miki, T. E. Miller, A. Milov, S. Mioduszewski, M. Mishra, J. T. Mitchell, M. Mitrovski, A. K. Mohanty, Y. Morino, A. Morreale, D. P. Morrison, T.V. Moukhanova, D. Mukhopadhyay, J. Murata, S. Nagamiya, Y. Nagata, J. L. Nagle, M. Naglis, M. I. Nagy, I. Nakagawa, Y. Nakamiya, T. Nakamura, K. Nakano, J. Newby, M. Nguyen, T. Niita, B. E.Norman, R. Nouicer, A. S. Nyanin, E. O'Brien, S. X. Oda, C. A. Ogilvie, H. Ohnishi, H. Okada, K. Okada, M. Oka, O. O. Omiwade, Y. Onuki, A. Oskarsson, M. Ouchida, K. Ozawa, R. Pak, D. Pal, A. P. T. Palounek, V. Pantuev, V. Papavassiliou2 J. Park, W. J. Park, S. F. Pate, H. Pei, J.-C. Peng, H. Pereira, V. Peresedov, D.Yu. Peressounko, C. Pinkenburg, M. L. Purschke, A. K. Purwar, H. Qu, J. Rak, A. Rakotozafindrabe, I. Ravinovich, K. F. Read, S. Rembeczki, M. Reuter, K. Reygers, V. Riabov, Y. Riabov, D. Roach, G. Roche, S. D. Rolnick, A. Romana, M. Rosati, S. S. E. Rosendahl, P. Rosnet, P. Rukoyatkin, P. Ruz?ic?ka, V. L. Rykov, B. Sahlmueller, N. Saito, T. Sakaguchi, S. Sakai, K. Sakashita, H. Sakata, V. Samsonov, S. Sato, T. Sato, S. Sawada, K. Sedgwick, J. Seele, R. Seidl, A.Yu. Semenov, V. Semenov, R. Seto, D. Sharma, I. Shein, A. Shevel,3 T.-A. Shibata, K. Shigaki, M. Shimomura, K. Shoji,

P. Shukla, A. Sickles, C. L. Silva, D. Silvermyr, C. Silvestre, K. S. Sim, B. K. Singh, C. P. Singh, V. Singh, S. Skutnik, M. Slunec?ka, A. Soldatov, R. A. Soltz, W. E. Sondheim, S. P. Sorensen, I.V. Sourikova, F. Staley, P.W. Stankus, E. Stenlund, M. Stepanov, A. Ster, S. P. Stoll, T. Sugitate, C. Suire, A. Sukhanov, J. Sziklai, T. Tabaru, S. Takagi, E. M. Takagui, A. Taketani, R. Tanabe, Y. Tanaka, K. Tanida, M. J. Tannenbaum, A. Taranenko, P. Tarja´n, H. Themann, T. L. Thomas, M. Togawa, A. Toia, J. Tojo, L. Toma´s?ek, Y. Tomita, H. Torii, R. S. Towell, V-N. Tram, I. Tserruya, Y. Tsuchimoto, C. Vale, H. Valle, H.W. van Hecke, A. Veicht, J. Velkovska, R. Vertesi, A. A. Vinogradov, M. Virius, V. Vrba, E. Vznuzdaev, M. Wagner, D. Walker, X. R. Wang, Y. Watanabe, F. Wei, J. Wessels, S. N. White, D. Winter, C. L. Woody, M. Wysocki, W. Xie, Y. L. Yamaguchi, K. Yamaura, R. Yang, A. Yanovich, Z. Yasin, J. Ying, S. Yokkaichi, G. R. Young, I. Younus, I. E. Yushmanov, W. A. Zajc, O. Zaudtke, C. Zhang, S. Zhou, J. Zima´nyi, and L. Zolin

共著者リスト④

M. Allen, M.J. Bennett, M. Bobrek, J.B. Boissevain, S. Boose, E. Bosze, C. Britton, J. Chang, C.Y. Chi, M. Chiu, R. Conway, R. Cunningham, A. Denisov, A. Deshpande, M.S. Emery, A. Enokizono, N. Ericson, B. Fox, S.-Y. Fung, P. Giannotti, T. Hachiya, A.G. Hansen, K. Homma, B.V. Jacak, D. Jaffe, J.H. Kang, J. Kapustinsky, S.Y. Kim, Y.G. Kim, T. Kohama, P.J. Kroon, W. Lenz, N. Longbotham, M. Musrock, T. Nakamura, H. Ohnishi, S.S. Ryu, A. Sakaguchi, R. Seto, T. Shiina, M. Simpson, J. Simon-Gillo, W.E. Sondheim, T. Sugitate, J.P. Sullivan, H.W. van Hecke, J.W. Walker, S.N. White, P. Willis, N. Xu

主論文

Study of Charm Production from the Measurement of Single Electrons in Au + Au Collisions at $\sqrt{s_{\mathrm{NN}}} = 200$ GeV

Takashi Hachiya

Department of Physical Science, Graduate School of Science
Hiroshima University
Kagamiyama 1-3-1, Higashi-Hiroshima, 739-8526, Japan

January 2010

Abstract

Quark Gluon Plasma (QGP) is a new state of matter in which constituents of nucleon (quarks and gluons) are deconfined. High energy heavy ion collision is a unique tool to create and study QGP. Two important findings, jet suppression and strong elliptic flow, have been reported from the experiments at RHIC. They are considered to be evidence of QGP formation in high energy heavy ion collisions.

Heavy quarks (charms and bottoms) are clean probes to study characteristics of QGP created in heavy ion collisions. Because of their large masses, heavy quarks are only produced in the initial stage of heavy ion collisions. Therefore, heavy quark production is sensitive to the initial gluon density. Moreover, the measurement of heavy quarks provide an important baseline of quarkonium suppression which is a proposed signature of QGP formation in heavy ion collisions.

The PHENIX experiment has measured transverse momentum spectra ($0.4 < p_{\rm T} < 4.0$ GeV/c) of single electrons from the semi-leptonic decays of heavy flavors as a function of centrality in Au + Au collisions at $\sqrt{s_{\rm NN}} = 200$ GeV. Signal electrons from heavy flavor decays are statistically extracted from large amount of photonic electron background which comes from Dalitz decays of light neutral mesons and photon conversions. A thin (1.7% of radiation length) photon converter has been installed to the PHENIX detector acceptance during a part of the data taking period. The converter increases only photonic background electrons by a fixed factor. Thus, by comparing the data sets with and without the converter, the photonic component and the signal component are accurately separated. After subtracting a small background of K_{e3} and vector mesons decays, the remaining contribution of electrons is the semi-leptonic decays of heavy flavors, mainly charms at low $p_{\rm T}$.

The centrality dependence of the total charm production has been studied. For all centralities, we found that the total charm production in Au + Au collisions is scaled by the number of nucleon-nucleon collisions. This indicates that most of charm quarks are produced in the initial stage of space time evolution in high energy heavy ion collisions. For minimum bias Au + Au collisions, the total charm cross section per binary collision is $\sigma_{c\bar{c}} = 622 \pm 57({\rm stat}) \pm 160({\rm sys})$ μb. The measured total charm cross section is consistent with a next-to-leading-order perturbative quantum chromodynamics calculation within the theoretical and the experimental uncertainties.

Contents

List of Figures

List of Tables

Chapter 1

Introduction

One of the most important issues in natural science is to search for and study the fundamental constituents of matter. In the last half of the 20th century, it is realized that quarks and gluons are the constituents of nucleon (the proton and the neutron). This theory is experimentally confirmed by deep inelastic scattering of electron and proton [1].

Quantum Chromodynamics (QCD) describes the strong interaction of quarks and gluons with color charge exchange and is a component of the standard model of particle physics [27]. A feature of QCD is the momentum transfer (Q) dependence of the strong coupling constant $\alpha_s(Q)$ which is expressed as Eq. 1.1 [27]:

$$\alpha_s(Q) \approx \frac{12\pi}{(33 - 2n_f)\ln(Q^2/\Lambda^2_{QCD})}. \tag{1.1}$$

Here, n_f is the number of active quark flavors with quark mass less than Q and Λ_{QCD} is the scale parameter of the strong interaction ($\Lambda_{QCD} \approx 200$ MeV). Figure 1.1 shows the running $\alpha_s(Q)$ as a function of the momentum transfer measured in several experiments. The curve in Fig. 1.1 indicates the QCD prediction.

At a large momentum transfer ($Q > \Lambda_{QCD}$) and equivalently at a short distance, $\alpha_s(Q)$ decreases logarithmically, and quarks and gluons behave almost freely. This is called as "asymptotic freedom". The feature of asymptotic freedom allows us to describe the strong interaction at large Q^2 in term of perturbation theory. In contrast, $\alpha_s(Q)$ becomes large at small momentum transfer ($Q \approx \Lambda_{QCD}$), at long distance. Thus, the perturbative approach is not applicable. In this region, quarks strongly attract each other and form color neutral state such as mesons (quark-antiquark pairs) and baryons (bound state of three quarks). This phenomenon is called as "color confinement". Because of this "confinement" feature of QCD, a single colored-quark has never been observed.

1.1 Quark Gluon Plasma

According to asymptotic freedom of QCD, under extreme conditions such as high temperature and/or high density, the matter does not consist of normal hadrons, but of many-body system of deconfined quarks and gluons. This state of matter is called as "Quark Gluon Plasma" (QGP) [2, 3]. Based on a simple dimensional calculation, a phase transition from

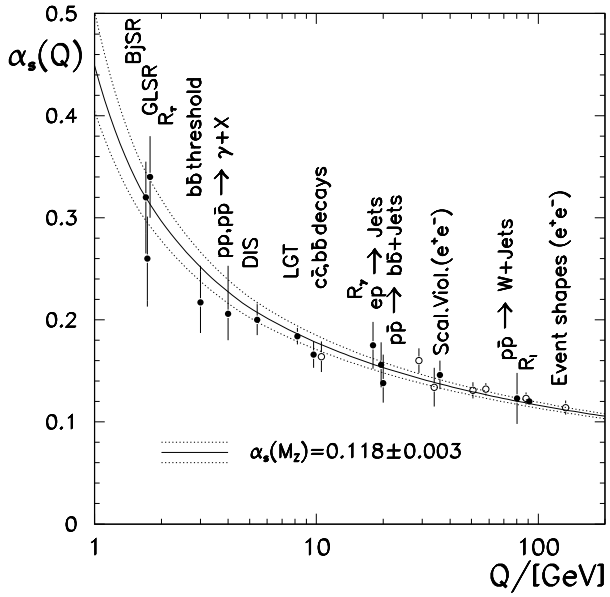

Figure 1.1: Running coupling constant α_s of strong interaction as a function of the momentum transfer, Q. These values are measured in several experiments and are compared to the QCD prediction.

hadronic matter to QGP would occur the critical temperature $T_c \sim 180$ MeV, where the strong coupling constant is order of unity. Thus, the perturbative description is suspicious. Lattice QCD is a powerful tool to study the phase transition in such a strong coupling regime. Lattice QCD predicts a phase transition to QGP [4]. Figure 1.2 shows the lattice QCD prediction of the energy density/T^4 as a function of temperature. The energy density rapidly increases around the critical temperature (T_c) and approach the arrows shown at right side of the figure. The arrows represent the energy density ε_{SB} of "Stefan Boltzmann" limit in the QGP phase. The predicted critical temperature is $T_c \approx 180$ MeV and the corresponding critical energy density is $\varepsilon_c \approx 1$ GeV/fm^3 which is roughly 10 times larger than that of the normal nuclear matter ($\varepsilon = 0.14$ GeV/fm^3).

If QGP is assumed as an ideal gas of massless quarks and gluons ("Stefan-Boltzmann" limit), the energy density ε_{SB} is expressed as follows:

$$\varepsilon_{SB} = \left\{ \frac{7}{8} d_q + d_g \right\} \frac{\pi^2}{30} T^4 \tag{1.2}$$

$$= \left\{ \frac{7}{8} \cdot 2_f \cdot 2_s \cdot 2_q \cdot 3_c + 2_s \cdot 8_c \right\} \frac{\pi^2}{30} T^4 \tag{1.3}$$

$$= 37 \cdot \frac{\pi^2}{30} T^4 \tag{1.4}$$

where d_q and d_g stand for the degree of freedom of quarks and gluons in QGP and 7/8 is a factor from which quark is fermion. The d_q consists of flavor (2), spin (2), quark/antiquark (2) and color (3) and the d_g is spin(2) and color(8) degree of freedom, respectively. On the other hand, for lower temperature, if hadronic matter were a ideal gas of massless

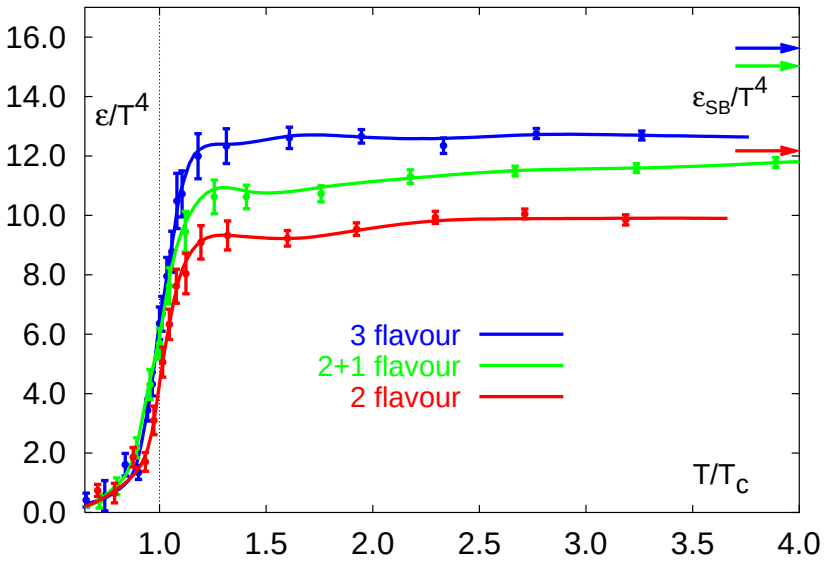

Figure 1.2: The energy density / T^4 from the recent lattice QCD calculation as a function of T/T_c [4]. The significant increase appears around $T \approx T_c$.

pions, the degree of freedom of pion gas (d_π) is 3 and its energy density in the hadron gas is $3\,\frac{\pi^2}{30}\,T^4$. The energy density in QGP is roughly ten times larger than that in hadron matter. This is due to the explicit appearance of the color degree of freedom in QGP.

Strikingly speaking, the phase transition from hadronic matter to QGP at high temperature and zero net baryon density is now considered to be a rapid cross over. Figure 1.3 shows a theoretical phase diagram of nuclear matter as a function of baryo-chemical potential μ and temperature T [5]. In this figure, there are two kinds of phase transitions. One is a transition to the QGP phase at high temperature and low density. The other is a transition to a color superconductivity phase (2SC) of matter at low temperature and high density. Such a condition of high temperature and low baryon density is considered to have existed in the early Universe in the first 10^{-5} second after the Big Bang [2]. Since it is difficult to study directly about the early Universe, high energy heavy ion collision is an only possible tool to reproduce QGP in the laboratory. Therefore, the high energy heavy ion collision provides a great opportunity to realize the QGP state.

Relativistic Heavy Ion Collider (RHIC) at Brookhaven National Laboratory (BNL) began to collide the Au nucleus in $\sqrt{s_{\rm NN}} = 130$ GeV in year 2000, then archived its full energy of $\sqrt{s_{\rm NN}} = 200$ GeV in year 2001. A large set of experimental observations strongly implies the formation of QGP [6]. Two most important observations are "suppression of particle production at high transverse momentum ($p_{\rm T}$)" and "strong elliptic flow". We briefly review these observations.

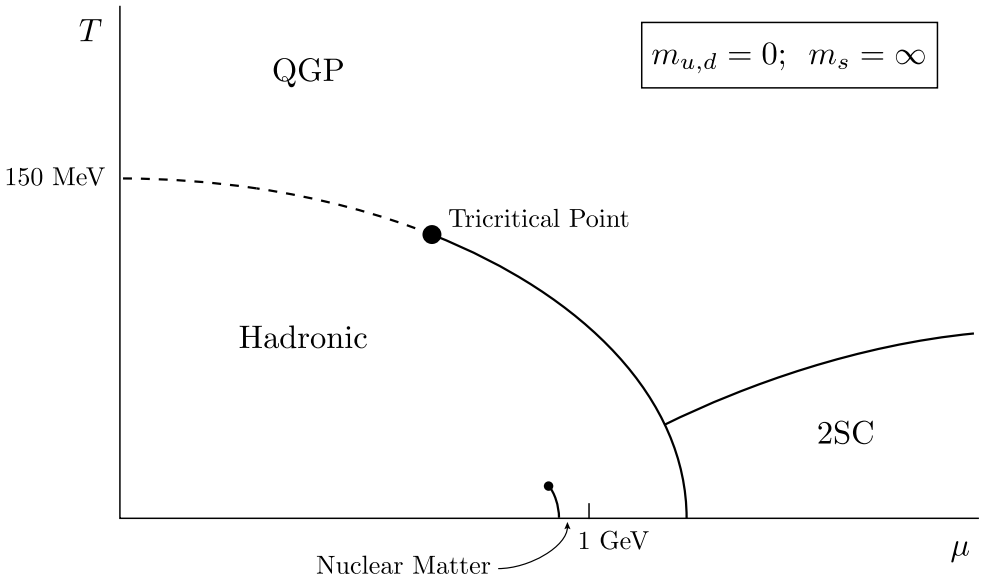

Figure 1.3: Theoretical phase diagram of nuclear matter [5]. The curves represent the phase boundaries between these phases.

High p_{T} Suppression

High p_{T} particles are produced in point-like hard-scatterings of high energy partons, and then fragmented into hadron jet. In nucleus-nucleus collisions ($A+A$), the scattered high p_{T} partons pass through the dense matter created in the collision. Therefore, these partons may suffer an energy loss in the matter due to the parton-matter interactions, e.g. gluon bremsstrahlung radiations [7, 8]. By contrast, if partons propagate through the matter without any energy losses, the production of high p_{T} particles should scale linearly with the number of point-like parton scatterings.

In order to study the high p_{T} particle production, "nuclear modification factor (R_{AA})" is defined as follows:

$$R_{AA} = \frac{dN_{AA}/dp_{\mathrm{T}}}{\langle T_{AA}\rangle\, d\sigma_{pp}/dp_{\mathrm{T}}}, \tag{1.5}$$

where dN_{AA}/dp_{T} and $d\sigma_{pp}/dp_{\mathrm{T}}$ are the invariant cross section as a function of p_{T} for $A+A$ and $p+p$ collisions, respectively. $\langle T_{AA}\rangle$ is the nuclear overlap function which is equivalent to the $N+N$ integrated luminosity in a $A+A$ collision event. $\langle T_{AA}\rangle$ depends on the impact parameter of the collision event. $\langle T_{AA}\rangle$ as a function of impact parameter (b) can be calculated from geometrical overlap of the colliding nuclei. If $R_{AA} = 1$, this indicates that the particle production in $A+A$ collisions is described by the simple superimposition of the particle production in $p+p$ collisions (binary scaling).

PHENIX experiment reported the R_{AA} of neutral pions in central and peripheral Au + Au [9] and minimum bias d + Au collisions [10] at $\sqrt{s_{\mathrm{NN}}} = 200$ GeV shown in Fig. 1.4. The central Au + Au collisions demonstrates the strong suppression of the factor 0.3 for π^0 production compared to the peripheral Au + Au collisions which is consistent to

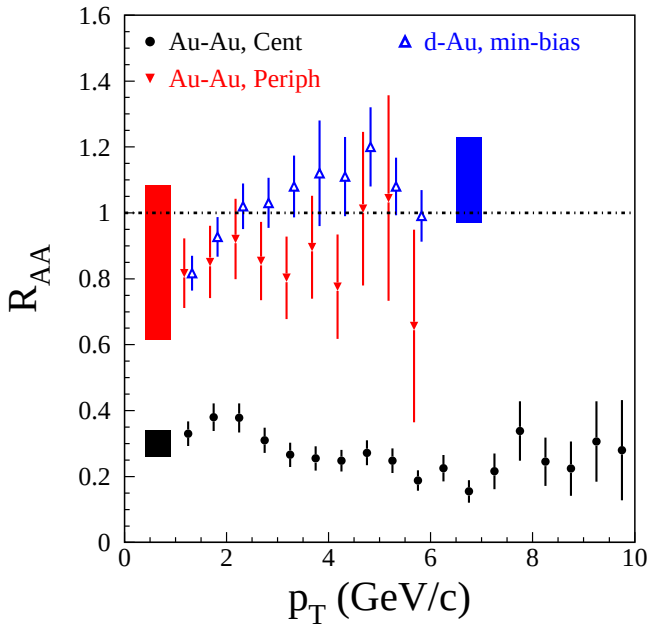

Figure 1.4: π^0 $R_{AA}(p_{\rm T})$ for central and peripheral Au + Au collisions [9] and $\pi^0 R_{d{\rm Au}}(p_{\rm T})$ for minimum bias d + Au collisions [10]. The boxes on the left and the right side of the figure show the systematic errors for the Au + Au and the d + Au points, respectively.

unity ($R_{AA} = 1$). In contrast to Au + Au collisions, $R_{d{\rm Au}}$ (R_{AA} in d + Au) presents only the contribution of the initial-state normal nuclear effect such as Cronin effect [66] and gluon shadowing [70], since the small size of deuteron is not enough to produce hot-dense matter. In Fig. 1.4, $R_{d{\rm Au}}$ is larger than unity for $p_{\rm T} > 2$ GeV/c and it increases slightly with increasing $p_{\rm T}$. This behavior of $R_{d{\rm Au}}$ is consistent with the expectation based on Cronin effect. By comparison with R_{AA} and $R_{d{\rm Au}}$, it is obvious that the central Au + Au collisions produce extremely dense matter.

Elliptic Flow

"Elliptic flow" is an azimuthal anisotropy of particle production. The strength of elliptic flow is sensitive to the early stage of space-time evolution of the colliding system. In non-central collisions, the overlap region of two colliding nuclei has an almond shape at $t = 0$. This initial spatial anisotropy is transferred to the momentum anisotropy of produced particles. In the case of that the mean free path (L) of partons in the system is much smaller than the system size ($L \ll R$), the scatterings of the partons generate the pressure gradient. The pressure gradient in short axis of the almond is steeper than that in long axis. Then, the elliptic flow is developed. The collective expansion of the system reduces the initial spatial anisotropy and the pressure gradient becomes small with time. This indicates that the earlier thermalization of the system is required for the stronger elliptic flow since the initial almond shape disappears gradually by the collective

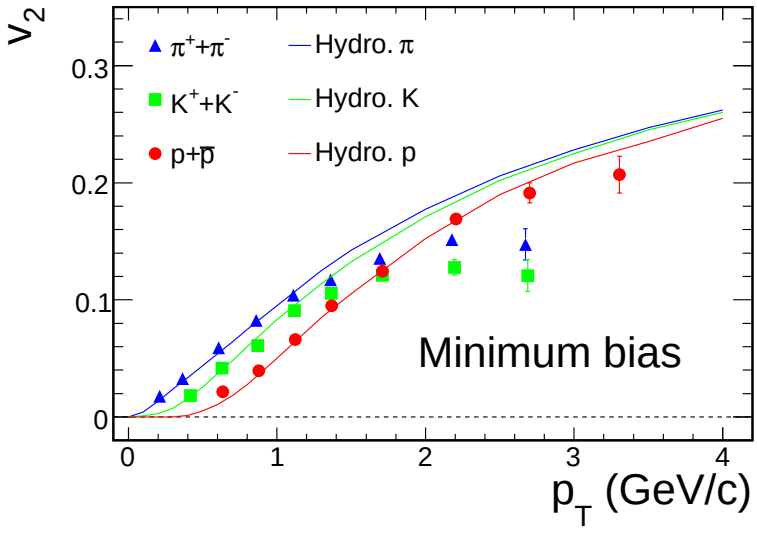

Figure 1.5: Azimuthal anisotropy (v_2) of π, K and protons as a function of p_{T} in minimum bias Au + Au collisions at $\sqrt{s_{\mathrm{NN}}} = 200$ GeV [13]. These are compared to the hydrodynamical calculation [15].

expansion. Therefore, the strength of the elliptic flow provides an information about the thermalization time of which the system reaches the thermal equilibration [11].

Experimentally, the azimuthal distribution of particle emissions is studied in term of Fourier expansion expressed in Eq. 1.6:

$$E\frac{d^3N}{d^3p} = \frac{d^2N}{2\pi p_{\mathrm{T}} dp_{\mathrm{T}} dy}\left(1 + 2\sum_{n=1}^{\infty} v_n(p_{\mathrm{T}})\cos\left[n(\phi - \Psi_r)\right]\right), \tag{1.6}$$

where ϕ is the azimuthal angle of the produced particle, Ψ_r is the azimuthal angle of the reaction plane and $v_n(p_T)$ is the magnitude of the n th order harmonics. The reaction plane is defined as the plane span by the direction of the impact parameter and the direction of the beam axis. The second order harmonic v_2 of Fourier expansion represents the strength of the elliptic flow.

STAR experiment first reported the strong elliptic flow in relatively peripheral Au + Au collisions at $\sqrt{s_{\mathrm{NN}}} = 130$ GeV [12]. The detailed measurements of v_2 were continued by the RHIC experiments in Au + Au collisions at $\sqrt{s_{\mathrm{NN}}} = 200$ GeV. Figure 1.5 shows the elliptic flow strength (v_2) of π, K and proton as a function of p_{T} measured by PHENIX [13]. The curves in Fig. 1.5 represent a hydrodynamical calculation including a first order phase transition with a freeze-out temperature of 120 MeV [15]. The measured v_2 has a clear particle-mass dependence. This mass effect is a consequence of radial expansion in which the heavier particles flow out to higher p_{T}. The v_2 of π, K and p are well reproduced by the model calculation at lower p_{T} ($p_{\mathrm{T}} < 1.5$ GeV/c). The strong v_2 implies that the system reaches the thermal equilibration quickly at $\tau \simeq 0.6$ fm/c [2].

By contrast, the model calculation fails to reproduce the data at high p_{T}, since hydrodynamical picture is not applicable in higher p_{T} region. The quark coalescence model

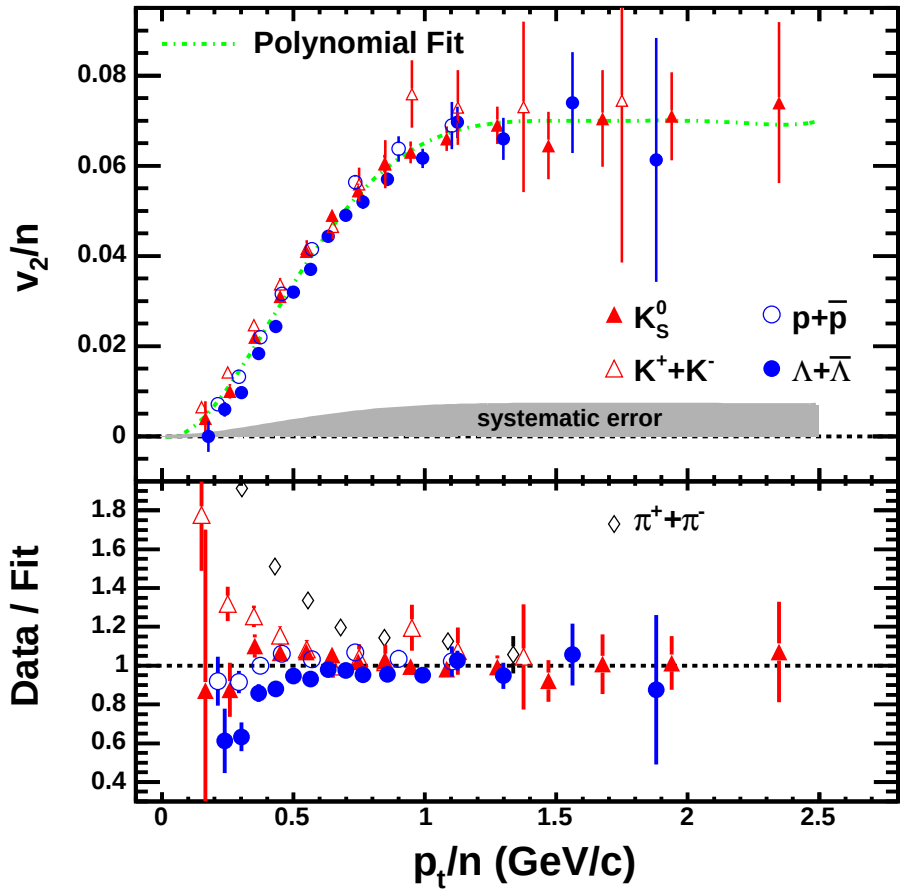

Figure 1.6: Scaled azimuthal anisotropy (v_2/n) as a function of p_{T}/n [14]. The n indicates the number of constituent quarks in a hadron.

[16] is a possible scenario that can explain the scaling property of constituent-quark number. Figure 1.6 shows the quark number scaling [14]. Therefore, the result suggests QGP formation since the strong elliptic flow is developed in the quark-level reaction.

1.2 Thesis Motivation

The property of the dense matter and its space-time evolution needs to be studied in more detail, although it has been observed by previous measurements that the dense matter is created in high energy heavy ion collisions. Heavy quarks (charms and bottoms) are clean probes to observe initial stage of the dense matter. Heavy quarks are only produced in point-like hard-scatterings in nucleon-nucleon and nucleus-nucleus collisions, since their masses (M_Q) are larger than the typical energy scale of QCD (Λ_{QCD}). At the energy scale of $Q^2 \sim M_Q^2$, the strong coupling constant is $\alpha_s \sim 0.3$ (see Fig. 1.1) which is small enough to apply perturbative QCD calculation to the production of heavy quarks. In high energy nucleon-nucleon collisions, the heavy quarks are primarily produced via gluon

fusions (e.g. $gg \rightarrow c\bar{c}$). Therefore, the total yield of heavy quarks is sensitive to the initial gluon density [17, 18]. Once heavy quarks are produced, they traverse the dense matter and suffer an possible energy loss via parton-matter interactions, e.g. bremsstrahlung radiation of gluons. But it is expected that the energy loss of heavy quarks is smaller than that of lighter quarks since their heavy mass reduces the available phase space for gluon radiation ("dead cone effect")[19]. In addition, the cold nuclear effects such as "Cronin effect" [66] and "nuclear shadowing"[70] could also modify the yield and p_{T} distribution of heavy quarks. Therefore, these effects need to be studied through the systematic measurements of heavy quarks in $p+p$, $p+A$ and $A+A$.

In this thisis, we measured the centrality dependence of the total charm production via a measurement of single electrons from their semi-leptonic decays. The PHENIX experiment has an unique ability to measure electrons with wide p_{T} range. During RHIC year 2002 to 2004 (Run 2 to Run 4), the PHENIX detector collected the data in $p+p$, $d+\mathrm{Au}$ and $\mathrm{Au}+\mathrm{Au}$ collisions at $\sqrt{s_{\mathrm{NN}}} = 200$ GeV. Using these data, the initial gluon density via the total charm production is studied in this thesis.

This thesis is organized as follows. Chapter 2 introduces the theoretical and the experimental background of high energy heavy ion collisions and heavy flavor productions. Chapter 3 explains the RHIC accelerator complex and the PHENIX detector. Chapter 4 describes the analysis method. Especially, the separation between the signal and the background is explained in detail. In chapter 5, the result of electron measurement is shown and the interpretation is discussed. Chapter 6 is finally the conclusion of this thesis.

Chapter 2

Theoretical and Experimental Overview

Heavy quarks (charms and bottoms) provide clean informations of property of dense matter created in high energy heavy ion collisions. Since heavy quarks are mainly produced in initial hard scattering, the total produced yield of heavy quarks is sensitive to initial gluon density. As same as light quark, heavy quarks suffer energy losses when they propagate through the dense matter, although their larger masses are expected to induce smaller energy losses. At the beginning of this chapter, the theoretical and the experimental approaches of heavy quark production are overviewed.

In latter part, the standard picture of high energy heavy ion collisions is introduced. This describes space-time evolution of the dense matter created in the collisions. The modification of heavy quark production in heavy ion collisions is reviewed.

2.1 Heavy Quark Measurement

There are two types of methods for heavy quark measurement, "direct" and "indirect" method. In direct methods, heavy flavor mesons (D and B mesons) are reconstructed by catching all decay products from their hadronic decays (e.g. $D \rightarrow K\pi$). Because of the limited acceptance of the PHENIX detector and the large amount of background hadrons in heavy ion collisions, it is difficult to measure heavy quark production in PHENIX by the direct methods. On the other hand, the measurement of single electrons from semi-leptonic decays of heavy flavor hadrons is one of the most powerful methods in indirect methods. These electrons are called as "heavy flavor electrons" in this thesis. Figure 2.1 shows a schematic view of heavy flavor measurement by the direct and the indirect method.

The overall history from the heavy quark production to the electron measurement are expressed as Eq.2.1:

$$p+p\ (A+A) \overset{pQCD}{\longrightarrow} c(b) \overset{fragmentation}{\longrightarrow} D(B) \overset{weak\,decays}{\longrightarrow} e. \tag{2.1}$$

Here, "$pQCD$" denotes the heavy quark production which is calculable by perturbative QCD, "$fragmentation$" is the fragmentation (hadronization) process of heavy quarks, and "$weakdecays$" is the semi-leptonic decays into electrons (e).

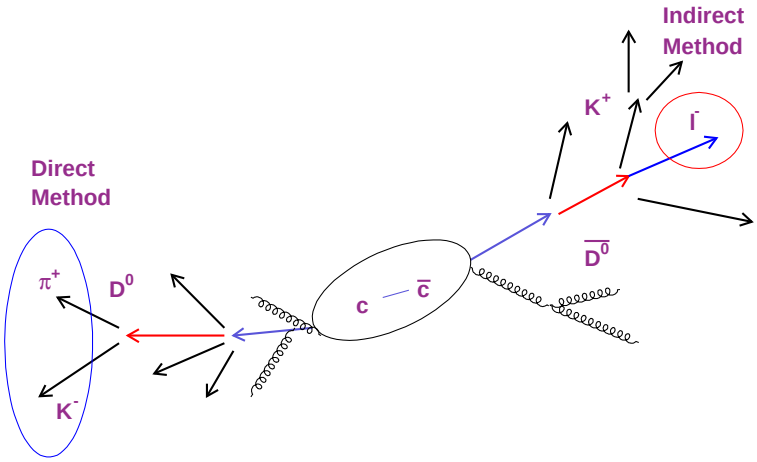

Figure 2.1: Schematic view of heavy flavor measurement.

In 1970's, the indirect method was carried out in $p+p$ collisions at CERN Intersecting Storage Ring (ISR) ($\sqrt{s} = 30 - 63$ GeV). Heavy flavor electrons were first measured in e/π ratio ($e/\pi \sim 10^{-4}$ for $p_{\rm T} > 1.3$ GeV/c) [21, 22, 23, 24]. The measured large yield was interpreted as evidence of charm production [25].

The difficulty of indirect method are large amount of background from internal (Dalitz) and external conversions of photons from the hadron decays (e.g. $\pi^0 \rightarrow \gamma + \gamma$) which is called as "photonic electrons". In order to reduce background of photonic electrons from photon conversions, the PHENIX detector is designed to minimize an amount of material around the beam pipe. In addition, the external converter is used to determine photonic electrons experimentally. These are explained in section 4

Each steps from the production to the measurement expressed in Eq. 2.1 are described in following sections.

2.2 Heavy Quark Production

2.2.1 Heavy Quark in pQCD

The hard-scatterings of partons containing in the colliding protons can produce the heavy quark pairs. The general perturbative expression of the partonic cross section for the heavy quark production can be written by the following equation (Eq. 2.2) [20]:

$$\sigma_{ij}(\hat{s}, m_Q^2, \mu_R^2) = \frac{\alpha_s^2(\mu_R^2)}{m_Q^2} \sum_{k=0}^{\infty} (4\pi\alpha_s(\mu_R^2))^k \sum_{l=0}^{k} f_{ij}^{(k,l)}(\eta) \ln^l \left(\frac{\mu_R^2}{m_Q^2}\right). \quad (2.2)$$

Here, $\hat{s} = x_1 x_2 s$ is the partonic energy squared in the center of mass. The index i and j are the parton types (q,$\bar{q}$,g) which interact in the particular Feynman diagrams. The dimensionless scaling function $f_{ij}^{(k,l)}$ represents the amplitude of a given partonic scattering diagrams. The dimensionless parameter $\eta = \hat{s}/4m_Q^2 - 1$ expresses the production threshold

of the heavy quark. It means that total partonic energy $\hat{s}$ must be at least larger than $2m_Q$ to create a heavy quark pair. μ_R is the renormalization scale and $\mu_R = m_Q$ is usually used for the heavy quark production. The index k indicates the order of subprocess diagrams. The $k = 0$ and $k = 1$ correspond to Leading Order (LO) and Next to Leading Order diagram (NLO) which the cross section of LO and NLO is a function of α_s^2 and α_s^3, respectively. When $k = 1$ and $l = 1$, the logarithmic term $\ln(\mu_R^2/m_Q^2)$ appears. The LO processes are "gluon fusion ($gg \to Q\bar{Q}$)" and "$q - \bar{q}$ annihilation ($q\bar{q} \to Q\bar{Q}$)" shown in Fig. 2.2 (a) and (b). The gluon fusion process dominates the $q\bar{q}$ annihilation in high energy collisions, since there are much large number of gluons in proton at small-x. The some NLO processes are shown in Fig. 2.2 (c), (d) and (e). In general, the NLO processes are smaller contribution than the LO processes. However, the logarithmic term are developed in the NLO process for $l = 1$, so that this logarithmic term ($\ln\left(\mu_R^2/m_Q^2\right)$) can make the NLO process to be even larger contribution than the LO process.

Using the partonic cross section described above, the total cross section of heavy quark production in $p + p$ collisions is formulated as following function (Eq. 2.3) [20]:

$$\sigma_{pp}(s, m_Q^2) = \sum_{i,j=q,\bar{q},g} \int_{\frac{4m_Q^2}{s}}^{1} d\tau \int_{\tau}^{1} \frac{dx_1}{x_1} f_i^p(x_1, \mu_F^2) f_j^p\left(\frac{\tau}{x_1}, \mu_F^2\right) \sigma_{ij}(\tau s, m_Q^2, \mu_R^2). \quad (2.3)$$

Here, $f_i^p(x_1, \mu_F^2)$ is Parton Distribution Function (PDF) in a proton. PDF is a probability density of partons in proton described in term of Bjorken variable (x) and momentum transfer scale (μ_F^2), where x is the momentum fraction of proton carried by a parton and μ_F^2 is called as factorization scale. The PDFs are experimentally determined by deep inelastic lepton-nucleon scatterings (DIS) and hard scatterings in $p + p$ collisions with a wide range of x and μ_F^2. The DGLAP equation [27] can describe the PDF evolution with respect to the momentum scale. The shape of PDF are derived from the comparison of the theoretical calculation to the experimental measurement. Several theorist groups published their own calculations of PDFs [29, 30, 31]. Fig. 2.3 shows the PDF published by the CTEQ group [29].

There are 3 parameters for the perturbative calculation of the total cross section in Eq. 2.3, m_R, μ_R and μ_F. The variation of these parameters can make the uncertainty of the calculation. Thus, the uncertainty is usually determined using these conditions : $1/2m_Q < \mu_R, \mu_F < 2m_Q$, $1.2 < m_c < 1.8$ GeV and $4.5 < m_b < 5.0$ GeV.

In a recent work, Fixed-Order plus Next-to-Leading-Log calculation (FONLL) is performed to evaluate the heavy quark production [32, 33]. The FONLL is based on purterbative QCD including the NLO fixed-order calculation (FO) and the resummation of the logarithm of p_{T}/m_Q ($\alpha_s^n(\log^k(p_{\mathrm{T}}/m_Q))$) with next-to-leading logarithmic accuracy (NLL). The logarithmic term due to multiple gluon radiations can contribute the heavy quark production at higher p_{T} ($p_{\mathrm{T}} > m_Q$). In order to compare with the experimental data directly, the FONLL framework introduces additionally the non-purterbative information in self-consistent way. The non-purtertative information related to the hadronization of heavy quark into hadrons is determined by the experimental data in $e^+ + e^-$ collisions at LEP [34].

Figure 2.4 shows the p_{T} spectrum of B hadrons measured in CDF compared with the FONLL calculation in $p + \bar{p}$ collisions at $\sqrt{s} = 1960$ GeV [37, 38, 34, 35]. Figure 2.5

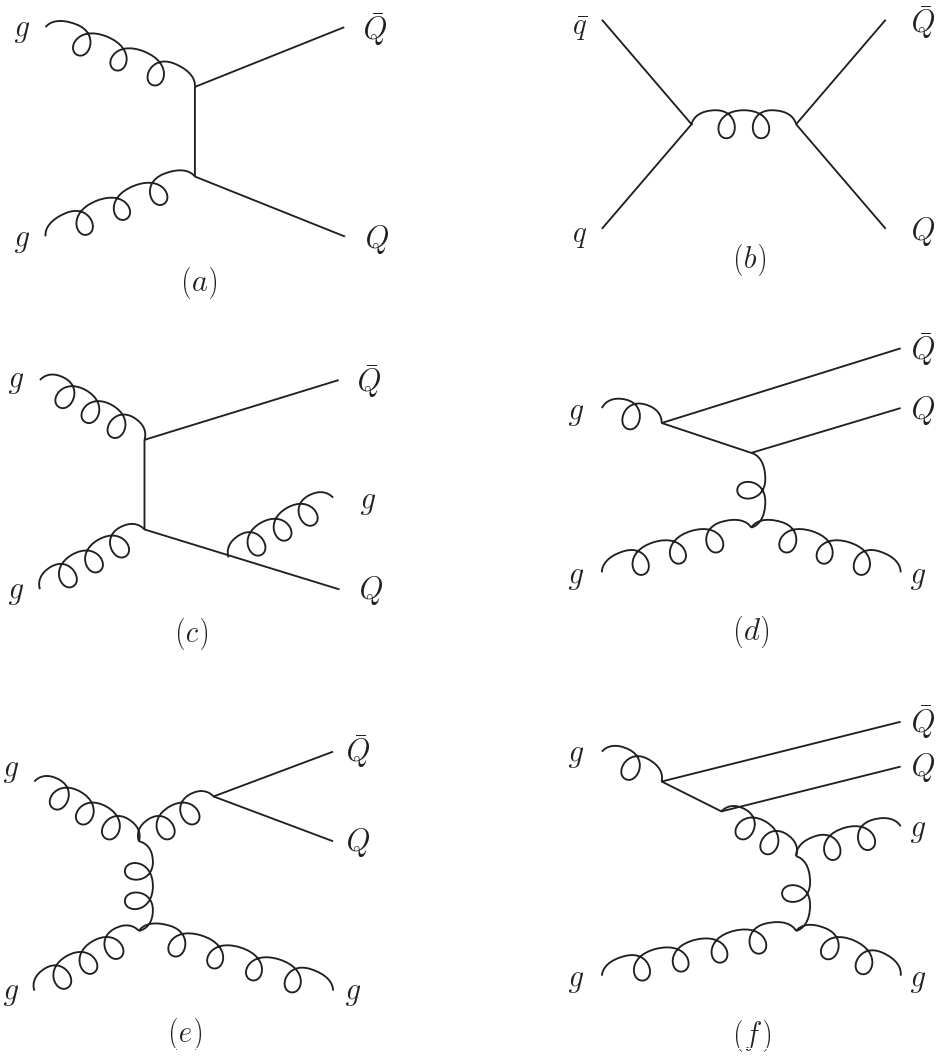

Figure 2.2: The LO and some NLO diagrams of heavy quark production. (a) gluon fusion. (b) $q\bar{q}$ annihilation. (c) pair creation with gluon emission. (d) flavor excitation. (e) gluon splitting (f) gluon splitting but of flavor excitation character [26].

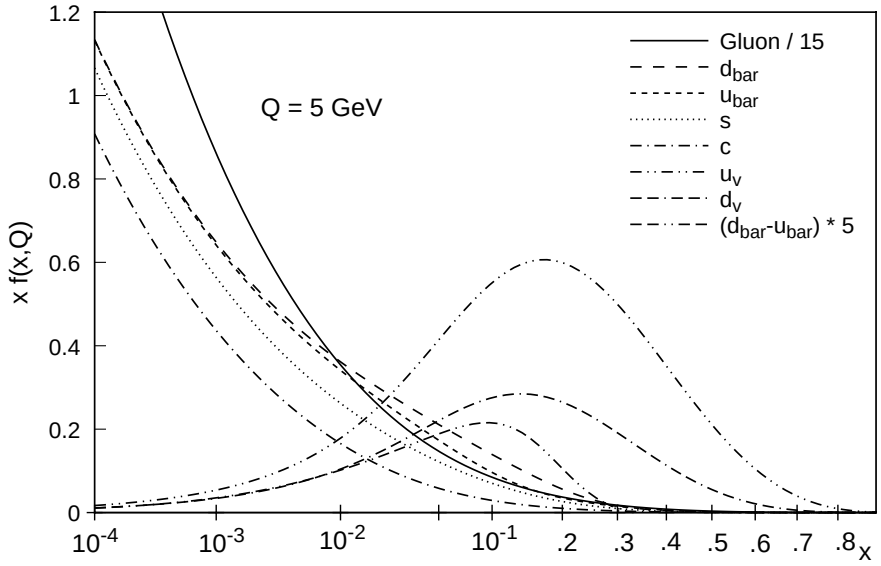

Figure 2.3: Parton Distribution Function as a function of x at $Q = 5$ GeV calculated by the CTEQ group [29].

(a) shows the differential invariant cross section of electrons from semi-leptonic decays of heavy flavors compared with the FONLL calculations in $p + p$ collisions at $\sqrt{s} = 200$ GeV, and Fig. 2.5 (b) is the ratio of the data and the calculation. The FONLL calculations for both collision energies are in good agreement with the experimental data. The FONLL predicts the total cross section in $p + p$ collisions at $\sqrt{s} = 200$ GeV for charm ($\sigma_{c\bar{c}}^{\mathrm{FONLL}} = 256^{+400}_{-146}$ μb) and bottom ($\sigma_{b\bar{b}}^{\mathrm{FONLL}} = 1.87^{+0.99}_{-0.67}$ μb) quarks, respectively.

2.2.2 Fragmentation Functions

Quarks produced in the hard scattering are not directly measured. The nature of asymptotic freedom in QCD prohibits the isolation of colored-quark. Therefore, quarks (q) combine each other so that the colorless state of a hadron is formed. The bound state of q (colored-q) and $\bar{q}$ (anti-colored) is called meson, and the state of three quarks with three different colors is baryon, respectively. The process that quarks are bound to form colorless hadron is generally called as "Fragmentation" or "Hadronization".

After quark and anti-quark pair is initially produced, the quark pair separates in opposite direction. When the distance between the pair exceeds about 1 fm, the potential energy due to the color confinement (string) become so large that one or more $q - \bar{q}$ pairs are created. Eventually all the initial quark energy is converted into two jets of hadrons.

The fragmentation of a quark into hadrons are described by the fragmentation function $D_q^h(z)$, which is the probability that a parton (q) is fragmented into a particular hadron (h) with z. Here, $z \equiv E_h/E_q$ is a fraction of the initial quark (q) energy carried by the hadron. The $D_q^h(z)$ satisfies the momentum and probability conservation (Eq 2.4).

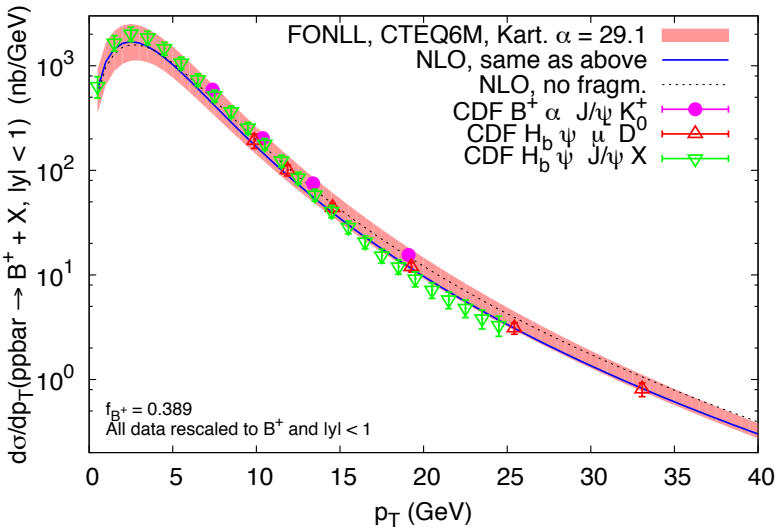

Figure 2.4: p_{T} spectra of B hadrons measured at CDF compared with the FONLL predictions [35, 36].

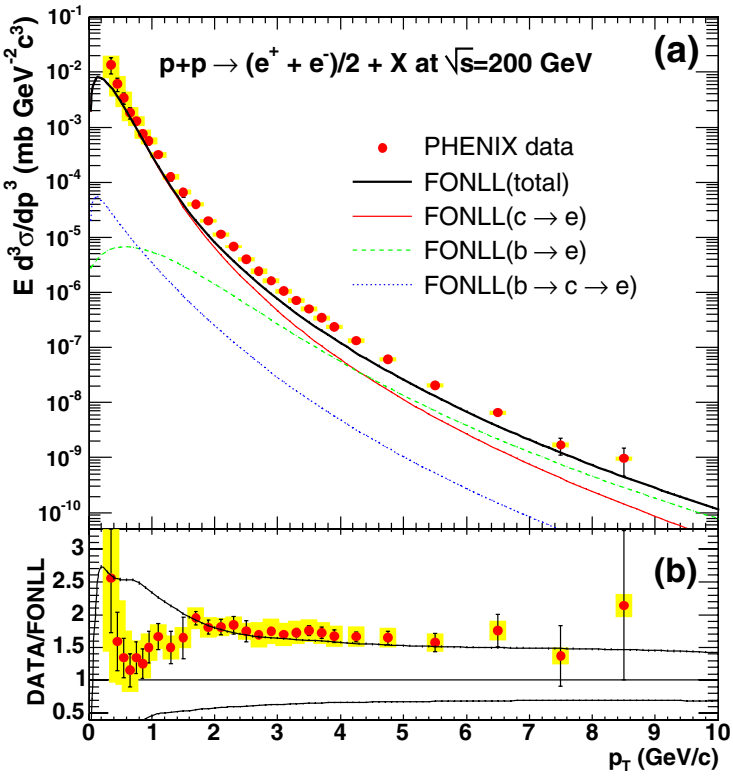

Figure 2.5: (a) Differential invariant cross section of electrons from heavy-flavor decays compared with the FONLL calculation. (b) Ratio of the data and the FONLL calculation. [39].

$$\sum \int z D_q^h(z,\mu^2)\, dz = 1 \tag{2.4}$$

Based on "factorization theorem", the differential cross section of the heavy flavor hadrons can be written as follows:

$$\frac{d\sigma^H}{dp_{\rm T}} = \int d\hat{p}_{\rm T}\, dz\, \frac{d\sigma^Q}{d\hat{p}_{\rm T}} D_Q^H(z)\, \delta(p_{\rm T} - z\hat{p}_{\rm T}), \tag{2.5}$$

where $p_{\rm T}$ and $\hat{p}_{\rm T}$ are the transverse momenta of heavy flavor hadrons and heavy quarks. The $d\sigma^Q\,/\,d\hat{p}_{\rm T}$ is the differential cross section of heavy quarks, and the D_Q^H is the fragmentation function of heavy flavors.

A heavy flavor meson retains a large fraction of the momentum of the primordial heavy quark [40]. The heavy quark has large mass so that the energy of the heavy flavor meson is less affected by the fragmentation with the light quark. Therefore, the fragmentation function of heavy quarks is much harder than that of light quarks.

The heavy quark fragmentation function $D_Q^h(z,\mu^2)$ needs to be described by phenomenological (non-perturbative) models including the perturbative calculation of the DGLAP evolution equation. The most popular parameterizations of $D_Q^h(z,\mu^2)$ are listed as follows:

$$\text{Peterson } \textit{et al.}\ [41] \ :\ D(z) \propto \frac{1}{z}\left(1 - \frac{1}{z} - \frac{\epsilon}{1-z}\right)^{-2}, \tag{2.6}$$

$$\text{Kartvelishvili } \textit{et al.}\ [42] \ :\ D(z) \propto z^{\alpha}\,(1-z)\,, \tag{2.7}$$

$$\text{Collins\&Spiller } [43] \ :\ D(z) \propto \left(\frac{1-z}{z} + \frac{(2-z)\epsilon_C}{1-z}\right) \times \left(1+z^2\right)\left(1 - \frac{1}{z} - \frac{\epsilon_C}{1-z}\right)^{-2}, \tag{2.8}$$

$$\text{Colangelo\&Nason } [44] \ :\ D(z) \propto (1-z)^{\alpha}\, z^{\beta}, \tag{2.9}$$

$$\text{Bowler } [45] \ :\ D(z) \propto \frac{(1-z)^a}{z^{-(1+bm_T^2)}} \exp\left(-\frac{bm_T^2}{z}\right), \tag{2.10}$$

$$\text{Braaten } \textit{et al.}\ [46] \ :\ \text{(see Eq. (31), (32) in [46])}. \tag{2.11}$$

where ϵ, ϵ_C, a, bm_T^2, α and β are non-perturbative parameters depending on the heavy flavor hadron. In general, the non-perturbative parameters in these formulae do not have an absolute meaning. These parameters are determined by the experimental results in the $e^+ + e^-$ collisions, since the fragmentation function is independent of the type of the initial hard scattering processes.

In PYTHIA [28] (a widely used pQCD event generator) with the default setting of the parameters, the Bowler fragmentation function (2.10) is used. The default parameters in PYTHIA are $a = 0.3$ and $b = 0.58$ GeV^{-2}. The peterson fragmentation function (Eq. 2.6) is most popular for heavy flavor hadrons. The ϵ parameter in the Eq. 2.6 was obtained for charms and bottoms in [47], for example, the $\epsilon_c \approx 0.05$ and the $\epsilon_b \approx 0.006$ in the case of using the leading-logarithmic approximation in the perturbative calculation. The most

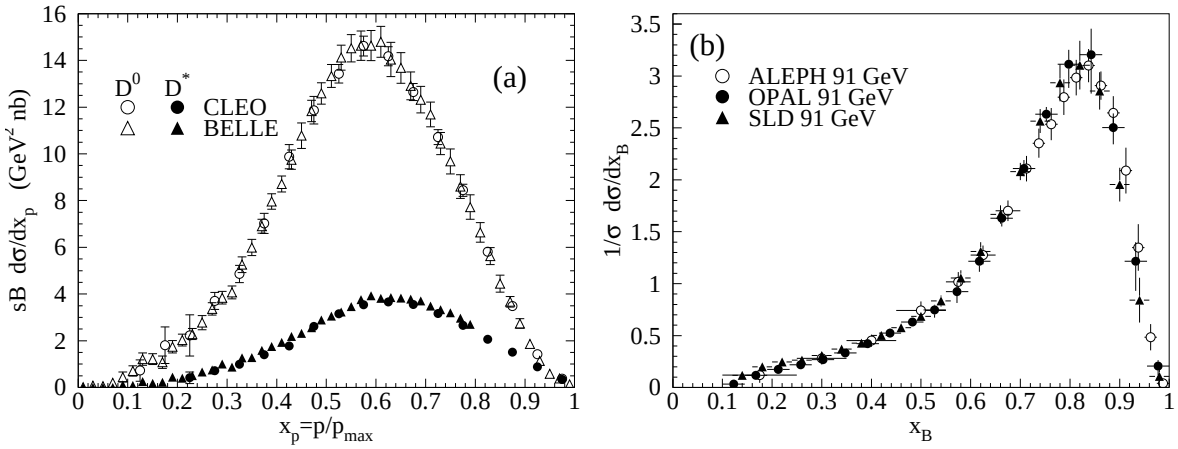

Figure 2.6: (a) Inclusive cross section measurement for the production of D^0 and D^{*+} in $e^+ + e^-$ collisions in the CLEO and BELLE as a function of $x_p = p/p_{max}$ which is approximately z [49, 50]. (b) Fragmentation function of b quarks into B hadrons as a function of $x_B = z$ measured in ALEPH, OPAL and SLD [51, 52, 53].

accurate approach to derive the fragmentation function is to use the Mellin transform of the D_Q^H and determine the moment of the Mellin transform from the experimental result [48].

Experimental studies of the heavy quark fragmentation function have been performed. Figure 2.6 (a) shows the inclusive cross-section of D^0 and D^* times branching ratios as a function of x_p measured in $e^+ + e^-$ collisions at the CLEO and the BELLE experiment [49, 50]. The variable x_p approximates the z. Figure 2.6 (b) shows the fragmentation function of the b quarks into B hadrons measured in the ALEPH and the CLEO at LEP and the SLD at SLAC [51, 52, 53].

2.2.3 Semi-Leptonic Decays

We measure electrons from the semi-leptonic decays of hadrons containing charm (c) and bottom (b) quarks. The semi-leptonic decays shown in Figure 2.7 are simply explained in the standard technique, "spectator model". In the spectator model, the light antiquark ($\bar{q}$) which accompany the heavy quark Q in the hadron is assumed to play no role in the decay [54, 55]. Therefore, the decay of Q can be treated in same way as the leptonic decay of a free muon.

The semi-leptonic decay width in the model can be written as follows:

$$\Gamma_{sl}^{(Q)} = \frac{m_Q}{2^8\pi^3}\int dx\,dy\,\theta(x+y-x_m)\theta(x_m-x-y+xy)\times\overline{\sum}|M^{(Q)}|^2 \qquad (2.12)$$

where x and y are the rescaled energies of the charged and neutral leptons, $x = 2E_e/m_Q$, $y = 2E_\nu/m_Q$, in the heavy quark rest frame. $x_m = 1-(m_q/m_Q)^2$ is the kinematic limit of energy transfer. The m_q/m_Q is equal to m_s/m_c for c decay and m_c/m_b for b decay.

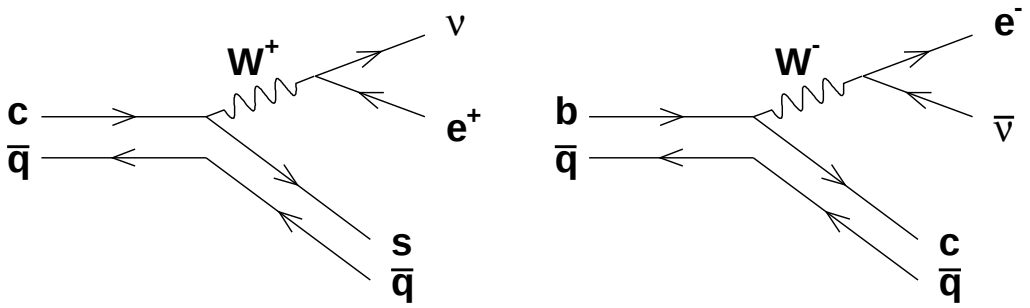

Figure 2.7: Semi-leptonic decay diagram of the D and B meson in "spectator model".

The matrix elements for c and b decay are :

$$\overline{\sum}|M^c|^2 = 64\,G_F^2\,|V_{cs}|^2\,c\cdot e^+\;s\cdot\nu, \tag{2.13}$$

$$\overline{\sum}|M^b|^2 = 64\,G_F^2\,|V_{cb}|^2\,b\cdot\overline{\nu}\;c\cdot e^-, \tag{2.14}$$

where b, c, s, ν, $\overline{\nu}$, ν, e^+ and e^- are the four-momenta of the decay particles. V_{cs} and V_{cb} are elements of Cabibbo-Kobayashi-Maskawa (CKM) matrix. $G_F = 1.16632 \times 10^{-5}(\mathrm{GeV}^{-2})$ is Fermi constant, the coupling constant of weak interaction.

The differential decay width for charms and bottoms can be calculated from Eq. 2.12 as follow:

$$\frac{d\Gamma_{sl}^{(c)}}{dx} = |V_{cs}|^2\,\Gamma_0(m_c)\left[\frac{12x^2(x_m-x)^2}{(1-x)}\right], \tag{2.15}$$

$$\frac{d\Gamma_{sl}^{(b)}}{dx} = |V_{cb}|^2\,\Gamma_0(m_b)\left[\frac{2x^2(x_m-x)^2}{(1-x)^3}\right](6-6x+xx_m+2x^2-3x_m), \tag{2.16}$$

where Γ_0 is the rescaled muon decay width

$$\Gamma_0(m_Q) = \frac{G_F^2 m_Q^5}{192\pi^3}.$$

The resulting electron spectra for charm and bottom decays are shown in Fig. 2.8. In this figure, both the electron spectra from CKM favored ($b \to c$ and $c \to s$) and CKM disfavored ($b \to u$ and $c \to d$) decay mode are included. The CKM disfavored spectra are harder than the CKM favored spectra. But the contribution from CKM disfavored mode is small and negligible (e.g. $|V_{ub}|/|V_{cb}| = 0.08 \pm 0.02$).

If $M_c = 1.4$ GeV, the theoretical estimate of the decay width is $\Gamma_{sl}(D) = 1.1 \times 10^{-10}$ MeV. On the other hand, using the measured branching ratios (e.g. 17.2% for D^+) and the lifetimes (e.g. 1051×10^{-15}(s)) of D mesons [27], the experimental decay width is calculated as $\Gamma_{sl}(D^+) = (1.07 \pm 0.13) \times 10^{-10}$ MeV. These two values are consistent each other. Therefore, the theoretical model can describe nicely the semi-leptonic decays of heavy flavors.

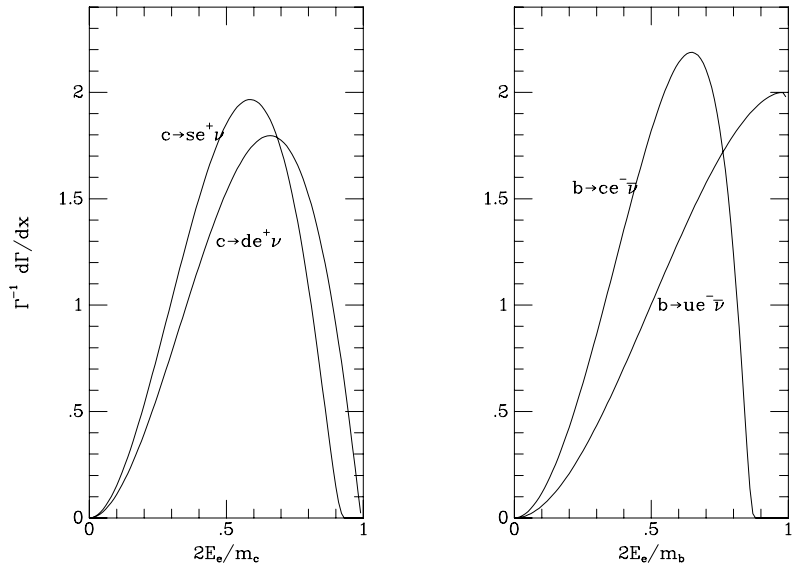

Figure 2.8: The normalized decay width spectra for charms (left panel) and bottoms (right panel) as a function of the relative momentum of electrons ($2E_e/m_e$). Both CKM favored and disfavored spectra are plotted.

2.3 High Energy Heavy Ion Collisions

High-energy heavy-ion collision is a possible way to realize a high temperature and a high energy density condition in the laboratory, where quark-gluon plasma (QGP) is expected to form. In heavy ion collisions, two Lorentz-contracted nuclei pass through each other and a lot of nucleon-nucleon collisions take place in the overlap region of the colliding nuclei. Their deposited energies generate the high energy density object spread in the space, like a fire ball which produces many secondary hadrons at a later time.

The experimental investigations had started at Bevalac (1975 - 1985) of the Lawrence Berkeley National Laboratory (LBL), and continued at Alternating Gradient Synchrotron (AGS) (1987 - 1995) of the Brookhaven National Laboratory (BNL), Super Proton Synchrotron (SPS) (1987 - present) of the European Organization for Nuclear Research (CERN) and Relativistic Heavy Ion Collider (RHIC) of the BNL. However the fixed target experiments at Bevalac, AGS and SPS could not observe the clear evidence of QGP formation. The first collider experiment at RHIC finally confirmed the existence of QGP.

2.3.1 Space Time Evolution

The phenomenon of the high-energy heavy-ion collision is very complicated since the matter produced in the collision undergoes several phase from the initial hard scattering to the final hadron emission. J. D. Bjorken illustrated space-time evolution of high energy heavy ion collision based on hydrodynamic [56]. In the Bjorken's picture assuming "central plateau" (high energy limit), the space-time evolution can be separated into four individual phases characterized by a proper time $\tau = \sqrt{t^2 + z^2}$. Figure 2.9 shows a light-

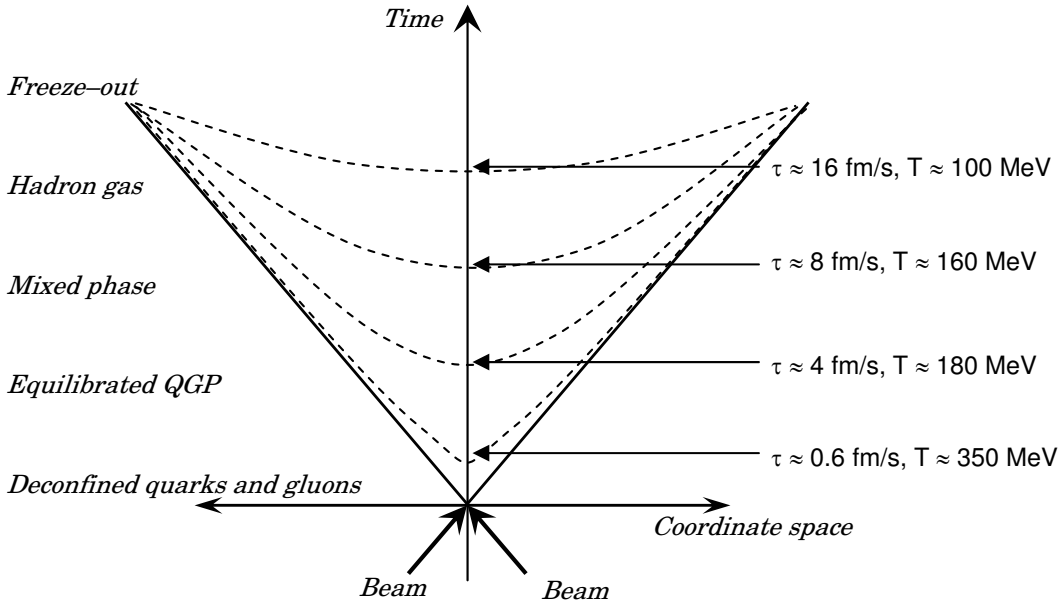

Figure 2.9: A light-cone diagram of space-time evolution in high energy heavy ion collisions. The values of time and temperature for various phases are taken from [57]. The mixed phase exists if the phase transition is first order.

cone diagram of the space-time evolution in heavy ion collision. The proper times for each phases are defined as a hyper-surface in Fig. 2.9. The value of the proper times τ in Fig. 2.9 are described in [57].

We consider that the two Lorentz contracted "disks" along the longitudinal (z) axis collides head-on at $z = 0$ and time $t = 0$ in the center of mass frame. The thickness of the disk represents $R/\gamma \approx 1$ fm where γ is the Lorentz factor. After the collision, the disk carrying a large amount of baryon number recedes from the overlap region. In the overlap region, the hard scatterings between partons, quarks and gluons, occur which can be described by perturbative QCD following parton cascade, and a huge amount of energy is deposited in the matter. This initial phase is named as pre-equilibrium phase.

The multiple scatterings of partons continue and these partons spread their momenta for shorter time, so that the matter would reach the local thermal equilibrium, and the QGP phase is formed. The time to form the QGP phase is called as "thermalization time" τ_0 which is expected to be 0.6 fm/s [57]. Once the local equilibration is archived, the QGP matter would expand hydrodynamically until the matter cools down to the critical temperature T_c of the QGP phase transition ($T_c \approx 180$MeV).

At T_c, the QGP matter begins to hadronize so that quarks and gluons are confined into color singlet hadrons. If the phase transition between the QGP to the hadron phase is the first order phase transition, a mixture of QGP and hadronic matter would appear during the transition (mixed phase). In the mixed phase, the volume fraction of hadronic matter in the QGP phase increases gradually with expansion. The temperature in the system stays at T_c because hadronic matter releases latent heat of the transition. Even

though the phase transition from hadronic matter to QGP is now considered to be a rapid cross over at zero baryon density.

After the system completes to hadronize at $\tau \approx 8$ fm, the produced hadrons interact with each other in the hadronic matter. This is called as "hadron gas phase". The hadronic matter keeps the collective expansion until the system temperature drops to freeze-out temperature ($T_F \approx 100$MeV) where the system size is still larger than the mean free path of the interacting hadrons. Finally the hadrons freely move away from the hadronic matter under T_F and those are detected in our measurement at approximately infinite distance.

2.3.2 Energy Density

The formation of QGP requires a sufficiently large energy density. The density is expected to be on the order of 1 GeV/fm^3 which is about 10 times larger than that in normal nucleus (≈ 0.14 MeV/fm^3). It is interesting how much energy density can be reached at the formation time (τ_0) of QGP in high energy heavy ion collisions.

In Bjorken's picture, the expansion of the system is one dimensional along with z and is cylindrically symmetry until the time reaches τ_0. The volume of the system at τ_0 is written as $\Delta V = \pi R^2 dz$ where R is a radius of the colliding nucleus. Energy (E) in the volume is written as follow:

$$E = \langle m_{\mathrm{T}} \rangle \frac{dN}{dy} \delta y = \frac{dE_{\mathrm{T}}}{dy} \delta y, \tag{2.17}$$

where $\langle m_{\mathrm{T}} \rangle = \sqrt{p_{\mathrm{T}}^2 + m^2}$ is a transverse energy of the produced hadrons (transverse mass), dN/dy is the rapidity density of particle multiplicity and y is rapidity defined as follows:

$$y = \frac{1}{2} \ln \left(\frac{t+z}{t-z} \right). \tag{2.18}$$

The transverse energy of the produced hadrons can contribute to the energy density of the initial system.

Using both the volume ΔV and the energy (E), the energy density (ε_{Bj}) of the system at τ_0 can be expressed as:

$$\varepsilon_{Bj} = \frac{E}{\Delta V}, \tag{2.19}$$

$$= \frac{\langle m_{\mathrm{T}} \rangle}{\pi R^2} \frac{dN(\tau_0)}{dz} = \frac{\langle m_{\mathrm{T}} \rangle}{\pi R^2 \, \tau_0} \frac{dN(\tau_0)}{dy}, \tag{2.20}$$

$$= \frac{1}{\pi R^2 \, \tau_0} \frac{dE_{\mathrm{T}}(\tau_0)}{dy}, \tag{2.21}$$

where E_{T} is the total energy and $dz = \tau dy$ at central rapidity ($y = 0$). We equated $\langle m_{\mathrm{T}} \rangle \frac{dN}{dy} = \frac{dE_{\mathrm{T}}}{dy}$. This energy density ε_{Bj} is generally referred as "Bjorken energy density" [56].

Although τ_0 is not well known, the energy density ε_{Bj} was evaluated for the AGS, SPS and RHIC experiments using the measured value of dE_{T}/dy and the normally used

value of $\tau_0 = 1$ fm/c. These ε_{Bj} are summarized in Tab. 2.1. The energy density ε_{Bj} in RHIC low energy ($\sqrt{s_{\rm NN}} = 19.6$ GeV) is compared to the recalculated ε_{Bj} in SPS energy ($\sqrt{s_{\rm NN}} = 17.2$ GeV), and found to be consistent [62]. There is a factor of 2.6 increase of the ε_{Bj} between RHIC low energy and highest energy ($\sqrt{s_{\rm NN}} = 200$ GeV).

Table 2.1: The summary of Bjorken energy density ε_{Bj} for several collision systems and energies.

Accelerator	Colliding Nucleus	$\sqrt{s_{\rm NN}}$ (GeV)	ε_{Bj} (GeV/fm^3)	
AGS	Au + Au	5	1.5	[58]
SPS	Pb + Pb	17	2.9	[59, 60]
RHIC	Au + Au	19.6	2.2	[62]
	Au + Au	130	4.7	[61, 62]
	Au + Au	200	5.4	[62]

2.3.3 Collision Geometry

The geometrical aspect of high energy heavy ion collisions has an important role in collision dynamics. Two colliding nuclei only interact in the region of the geometrical overlap as shown in Fig 2.10. The region is characterized by impact parameter b which is the distance between the centers of the colliding nuclei. The nucleons in the colliding nuclei are separated into 2 groups, "participant" and "spectator" illustrated in Fig. 2.10. The participant is the nucleons in the overlap region where nucleon-nucleon collisions take place. On the other hand, the spectator passes away into longitudinal direction with little interaction. This geometrical treatment of the collision is known as "Participant-Spectator model".

In experiment, high energy heavy ion collision is characterized by "centrality" to study the matter produced in the collision systematically, since impact parameter can not directly measured. Centrality represents a percentile of total cross section of inelastic nucleus nucleus collision.

The Glauber model [63] is used to associate b with centrality and to evaluate the geometric parameters such as b, the number of participants ($N_{\rm part}$), the number of nucleon-nucleon collisions ($N_{\rm coll}$) and the nuclear overlap function ($T_{AB}(b)$). In the Glauber model, the nucleus-nucleus collisions are treated as multiple nucleon interactions. Nucleon of colliding nucleus is assumed to travel in a straight line and not to deflect after the collision.

The nuclear thickness function of nucleus A is defined as follow [2, 64]:

$$T_A(\mathbf{s}) = \int dz \rho_A(z, \mathbf{s}), \tag{2.22}$$

where ρ_A is the mass number density normalized by its mass number and $T_A(\mathbf{s})$ is the number of nucleons per unit area along with z axis at the point from the center of the nucleus represented by a 2D vector $\mathbf{s}$. The vector $\mathbf{s}$ is in the transverse plane with respect

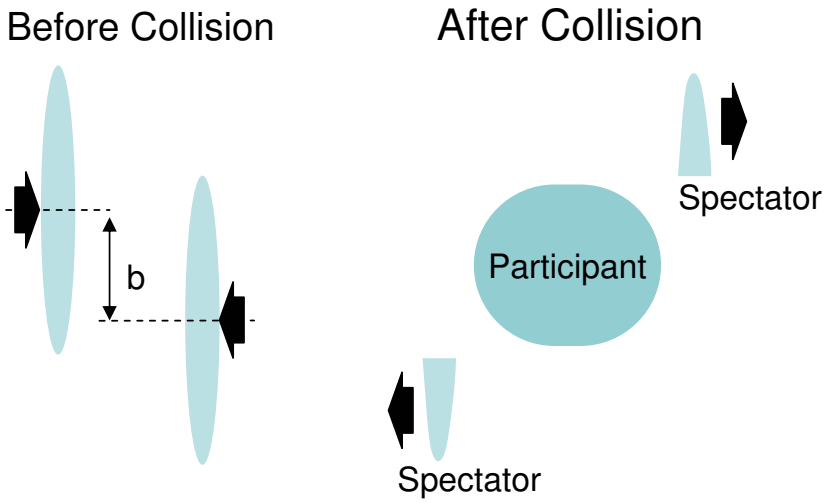

Figure 2.10: Participant-spectator model of high energy heavy ion collision. Two colliding nuclei approach with impact parameter b before the collision. After the collision, the spectator nucleons pass away into the longitudinal direction.

to z. Using $T_A(\mathbf{s})$ and b, the nuclear overlap function of nucleus A and B is defined as follow:

$$T_{AB}(\mathbf{b}) = \int d^2s\, T_A(\mathbf{s})\; T_B(\mathbf{s}-\mathbf{b}), \tag{2.23}$$

where $d^2s = 2\pi s ds$ is the 2 dimensional area element. Eq. 2.23 means that the nucleon in nucleus A has a chance of a collision with the nucleon in nucleus B at the same 2 dimensional position. Therefore, $N_{\rm coll}$ is defined as follows:

$$N_{\rm coll}(b) = \int d^2s\; \sigma_{NN}^{in}\, T_A(\mathbf{b})\, T_B(\mathbf{s}-\mathbf{b}) = \sigma_{NN}^{in} \cdot T_{AB}(\mathbf{b}), \tag{2.24}$$

where σ_{NN}^{in} is the inelastic cross section of the nucleon-nucleon interaction.

In order to evaluate these geometrical parameters described above, Monte Carlo calculations of the Glauber model are performed. The Woods-Saxon parameterization is used for a realistic nuclear mass density $\rho_A(r)$ as follows:

$$\rho_A(r) = \frac{\rho_0}{1+\exp\left(\frac{r-R_A}{a}\right)}, \tag{2.25}$$

where R_A is the radius of the nucleus and a is the diffusion parameter. When the distance between the nucleons becomes less than $\sqrt{\sigma_{NN}^{in}/\pi}$ in the calculation, we consider a collision between these two nucleons take places. The result of the Glauber model calculation is summarized in section 4.2.3.

2.4 Heavy Quarks in Nucleus-Nucleus Collisions

2.4.1 Initial Production

The production of heavy quarks in $p+p$ collisions can be calculated in pQCD formalism, since their large masses requires hard-scatterings with large momentum transfer, as discussed in the previous section. Heavy quarks are produced via initial hard-scatterings in Nucleus-Nucleus ($A+A$) collisions. Therefore, it is expected that the yield of heavy quarks is proportional to the number of nucleon-nucleon hard-scatterings. This can be expressed in terms of the nuclear overlap function, T_{AA}:

$$N_{AA}^{\mathrm{HQ}} = T_{AA} \cdot \sigma_{pp}^{\mathrm{HQ}}, \tag{2.26}$$

where N_{AA}^{HQ} is the invariant yield of heavy quarks in $A+A$ collisions and $\sigma_{pp}^{\mathrm{HQ}}$ is the invariant cross section in $p+p$ collisions. Here, we neglect the initial and final state effects in $A+A$ collisions. These initial and final state effects can modify the heavy quark production and are discussed in the next sections.

2.4.2 Pre-equilibrium Production

In addition to the initial production, it is predicted [18] that there are the pre-equilibrium production and the thermal production.

In the pre-equilibrium stage of the space-time evolution, secondary parton scatterings in the dense matter could lead to heavy quark production. The yield of heavy quarks produced in the pre-equilibrium stage could be approximately proportional to the thermalization time of the dense matter. If the pre-equilibrium production is separated from the initial production, we can measure the thermalization time.

In the thermal stage, the heavy quark production is treated in the same way as the thermal production of light quarks (u, d, s). The heavy quark in the thermal stage is produced through gluon fusion $gg \rightarrow Q\bar{Q}$ and quark-antiquark annihilation $q\hat{q} \rightarrow Q\bar{Q}$. However their large mass suppress the thermal production of heavy quarks relative to that of light quarks. If a reasonable temperature is assumed ($T \sim 200-400$ MeV), the thermal production is far below the initial production.

Figure 2.11 shows calculated p_{T} distributions of charm quarks produced in the initial, pre-equilibrium and thermal stage in central Au + Au collisions at $\sqrt{s_{\mathrm{NN}}} = 200$ GeV [65]. The pre-equilibrium production is about 10% compared with the initial production. On the other hand, the thermal production is negligibly small.

2.4.3 Cold Nuclear Effects

There are some known effects in normal nuclear matter which can affect the yield and p_{T} spectra of produced particles. They are generally called as "cold nuclear matter effect" or "initial state effect". In order to study the property of the matter created in the high energy heavy ion collisions, it is necessary to take these nuclear effects into account. The cold nuclear effects, "Cronin effect" and "nuclear shadowing effect", are described in this section.

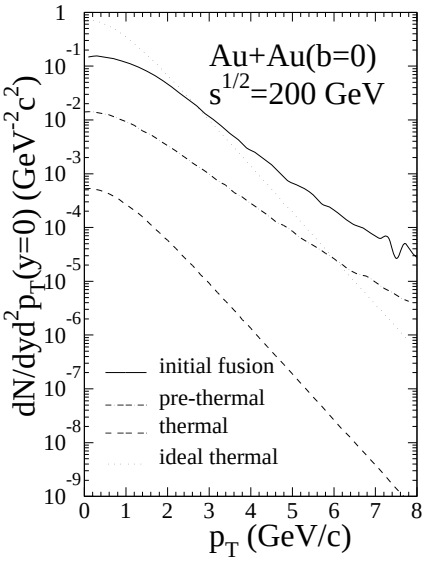

Figure 2.11: A theoretical calculation of charm quark production as a function of p_{T} in central Au + Au collisions at $\sqrt{s_{\mathrm{NN}}} = 200$ GeV. The initial (solid), pre-equilibrium (dot-dashed) and thermal production (dashed) are plotted, respectively [65].

Cronin Effect

Cronin effect [66] is an enhancement of the particle production in proton + nucleus ($p + A$) collisions compared to the number of nucleon-nucleon collisions scaling (N_{coll}). The enhancement is explained that the incident parton undergoes the multiple scatterings in the target nucleus before hard-collision, so that its momentum become broad [67]. Therefore, the Cronin enhancement depends on the nuclear thickness or the number of collision. The cross section in $p + A$ collisions is expressed as follows:

$$E\,\frac{d^3\sigma}{d^3p}(p_{\mathrm{T}}, A) \;=\; E\,\frac{d^3\sigma}{d^3p}(p_{\mathrm{T}}, p = 1) \times A^{\alpha(p_{\mathrm{T}})}, \tag{2.27}$$

where $\alpha(p_{\mathrm{T}})$ represents a parameter of the modification compared to N_{coll} scaling. If the $\alpha(p_{\mathrm{T}}) = 1$, the cross section in $(p + A)$ is consistent with N_{coll} scaling. From the identified charged hadron measurement in PHENIX experiment, the $\alpha(p_{\mathrm{T}}) > 1$ is observed for $p_{\mathrm{T}} > 1.5$ GeV/c in d + Au collisions at $\sqrt{s_{\mathrm{NN}}} = 200$ GeV [68].

Nuclear Shadowing Effect

The fact that the structure function F_2 per nucleon in nucleus is significantly different from that of a free nucleon is a well known nuclear effect. This was discovered in the measurement of a deep inelastic muon scattering by the European Muon Collaboration (EMC) in 1982 [70]. The modification of the nuclear structure function is illustrated by the ratio of F_2^A and F_2^D as a function of Bjorken x shown in Fig 2.12 [71]. The ratio can be subdivided by four regions with respect to x. For $x < 0.05$, "shadowing" where the ratio

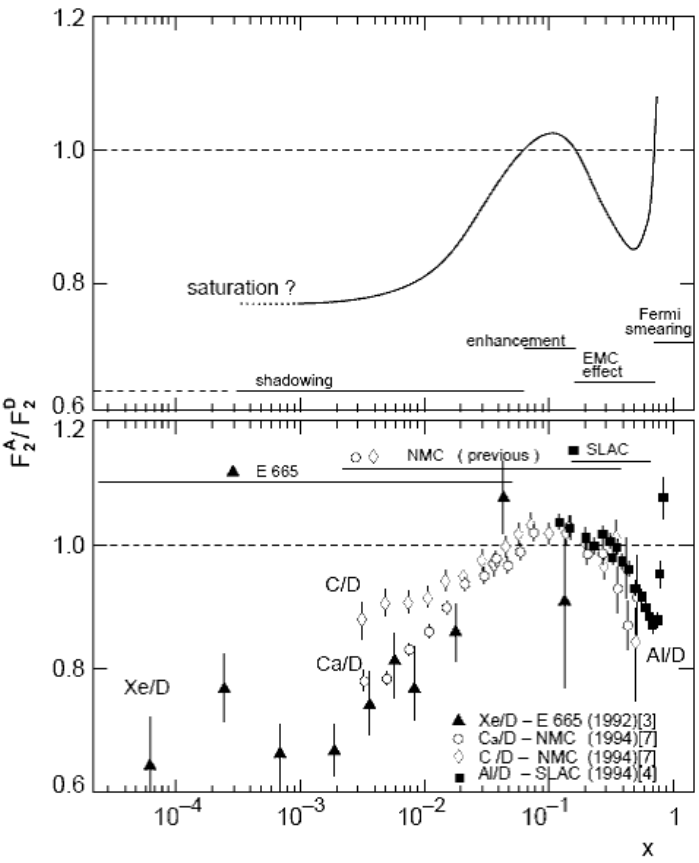

Figure 2.12: Modification of nuclear structure function per nucleon. (top) a phenomenological curve. (bottom) a set of experimental results [71].

is smaller than unity. For $0.05 < x < 0.15$, "anti-shadowing" where the ratio is slightly larger than unity. For $0.15 < x < 0.6$, the EMC effect where the ratio is a fall increasing x. For $0.6 < x$, the ratio rises by Fermi motion.

This modification of the structure function affects the particle production in the collision. The relevant x region in the RHIC energy can be estimated using Eq. 2.28 and p_{T} of the produced parton in the mid-rapidity.

$$x = \frac{2\,p_{\mathrm{T}}}{\sqrt{s}} \tag{2.28}$$

For the parton with $1 < p_{\mathrm{T}} < 10$, the x region corresponds to $0.01 < x < 0.1$ where the shadowing effect can appear.

The EKS98 model [73] parameterizes the nuclear modification of parton distribution in nucleus. A cross section of heavy quarks in $p + A$ and $A + A$ collisions is calculated using the EKS98 model [72]. Figure 2.13 shows the ratio of the cross-sections for charm (left) and bottom (right) at mid-rapidity in $p + A$ and $A + A$ collisions. At the RHIC energy, as shown in Figure 2.13, the charm production is not much modified since the nuclear

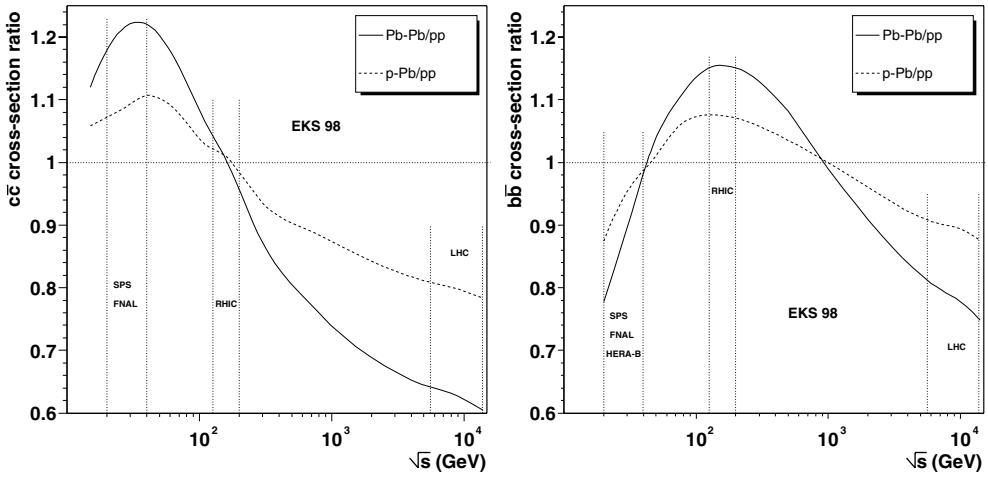

Figure 2.13: The ratio of the cross section for the $c\bar{c}$ (left) and the $b\bar{b}$ (right) in $p+A$ and $A+A$ collisions. The nuclear effect of the PDF's are calculated using the EKS98 nuclear weight functions [72].

shadowing at the x region relevant for charm production in the EKS98 model is small. By contrast, the bottom production is slightly enhanced by the anti-shadowing effect.

2.4.4 Final State Effects in QGP

Medium Modification

When an energetic parton passes through the dense matter created in heavy ion collisions, the parton suffers the energy loss due to parton-matter interaction, e.g. gluon radiation. We can see a similar process in electromagnetics. A high-energy charged particle traversing charged matter lose its energy by "bremsstrahlung" which is photon radiation due to interaction of the particle with the matter. The bremsstrahlung is described using the electromagnetic potential from the moving charged particle, so called $Li\acute{e}nard-Wiechert$ potential.

It is predicted that the radiative energy loss of heavy quarks is smaller than that of light quarks, since its larger mass reduces the available phase space for gluon radiation (dead cone effect [19]). A similar mass dependence of energy loss can be seen in electromagnetics. The energy loss of muons by bremsstrahlung is much smaller than that of electrons.

There are two theoretical calculations to treat the energy loss process quantitatively for light and heavy quarks. One is the BDMPS model [75] in which the radiated gluons suffer the final state interaction (non-abelian effects) in the colored-dense matter. The total energy loss in the BDMPS model is described in terms of transport coefficient $\hat{q}$ and is proportional to L^2 as follows:

$$\delta E \propto \hat{q}L^2 \qquad \left(\hat{q} \equiv \frac{\langle q_{\mathrm{T}}^2 \rangle}{\lambda}\right), \tag{2.29}$$

where $\hat{q}$ means the average squared transverse momentum (q_{T}) transfered from the matter to the parton per mean free path (λ). The L is the path length of the parton in the matter.

The other is the GLV (DGLV) model [76, 77, 78] in which the radiative energy loss is characterized by the gluon density (dN_g/dy) in the dense matter. The energy loss in the GLV model can be analytically calculated for the limit of the thin matter. The fractional energy loss of a fast parton with energy E is expressed as follow [79]:

$$\frac{dE}{E} \propto \frac{1}{A_\perp}\frac{dN_g}{dy} L \log\frac{E}{\mu}, \tag{2.30}$$

where $A_\perp$ is the transverse size of the dense matter and μ is the Debye screening scale. The nuclear modification of PDF and the longitudinal Bjorken expansion of the matter is also taken into account in the GLV model for the realistic calculation.

Figure 2.14 shows the nuclear modification factor R_{AA} of π^0 in top 5% central Au + Au collisions at $\sqrt{s_{\mathrm{NN}}}$ = 200 GeV [83]. The measured $\pi^0 R_{AA}$ is compared to the BDMPS (left) and the GLV calculation (right) with various values of the model parameters, respectively. These models can describe the measured $\pi^0 R_{AA}$ with $\hat{q} = 13.2^{+2.1}_{-3.2}$ GeV^2/fm for the BDMPS and $dN_g/dy = 1400^{+270}_{-150}$ for the GLV models.

On the other hand, these models can not describe the measured R_{AA} of electrons from heavy flavor decays as shown in Fig. 2.15 [84]. The measured electron R_{AA} is smaller than these model predictions for high p_{T} where $\hat{q} = 14$ GeV in the BDMPS and $dN_g/dy = 1000$ in the GLV are used. The data shows the opposite trend compared to the prediction of the less energy loss for heavy quarks. This indicates that the radiative energy loss due to gluon bremsstrahlung is not adequate to describe fully the measured suppression of heavy flavors, and the additional energy loss mechanism is required.

In recent theoretical studies [80, 81, 82], it is proposed that the contribution from the collisional energy loss due to the elastic scattering becomes important for heavy quark, although the collisional process is negligibly small for light quark. Figure 2.16 shows the theoretical calculation of the collisional and radiative energy loss as a function of momentum for charm (left) and bottom (right) quarks. The collisional energy loss for both charm and bottom quarks makes a larger contribution than the radiative loss for low p_{T} and becomes gradually smaller for high p_{T}. The combined approach of the collisional and radiative energy loss can describe the substantial part of the heavy quark energy loss shown as the green band in Fig. 2.15. But there is a still small difference between the data and the model.

2.4.5 Aim of This Study

The motivation of this thesis is to study the initial gluon density of the dense matter created in heavy ion collision. Because their large mass, heavy quarks are only produced in point-like hard-scatterings in $A + A$ collisions. Such hard scatterings take place in the early time of space-time evolution before the possible QGP formation. Thus, the heavy quark production is sensitive to the initial condition of the collision, especially the initial gluon density.

The first aim of this study is to investigate whether the total production of heavy quarks in Au + Au collisions is scaled by N_{coll}, especially charms at low p_{T}. If the N_{coll}

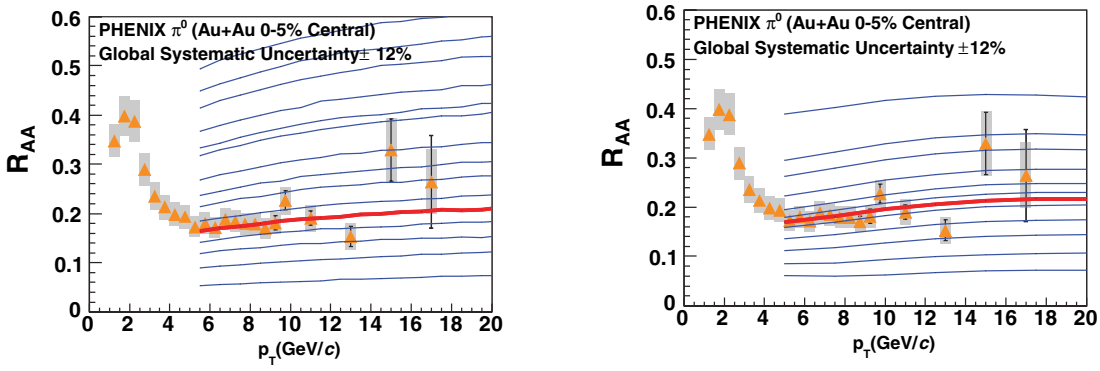

Figure 2.14: Both the left and right panel show $\pi^0 R_{AA}$ for top 5% central Au + Au collisions at $\sqrt{s_{\rm NN}} = 200$ GeV [83]. $\pi^0 R_{AA}$ are compared with the BDMPS (left) and the GLV (right) model with various parameters. The red curves indicate the best fit curve of the models.

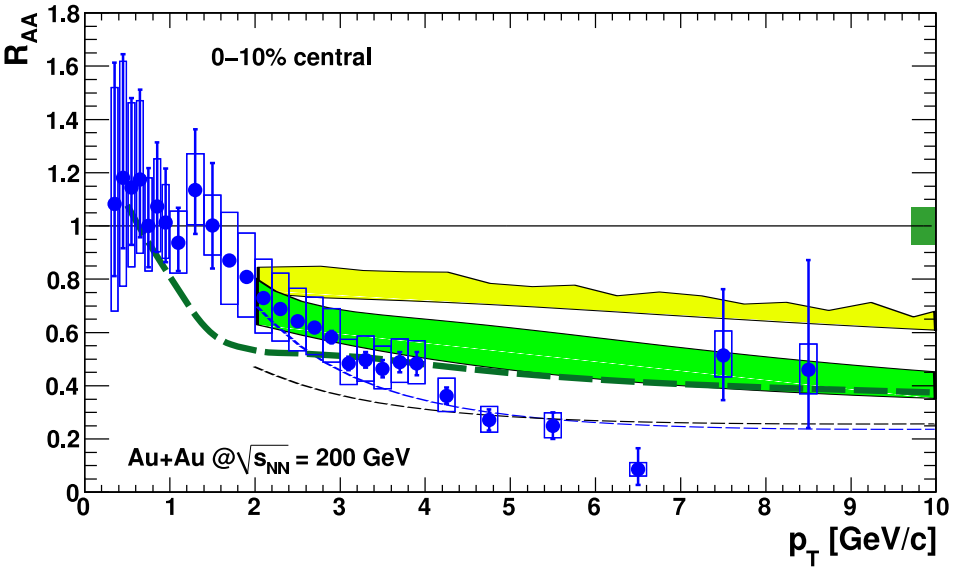

Figure 2.15: R_{AA} of electrons from heavy flavor decays for top 10% central Au + Au collisions at $\sqrt{s_{\rm NN}} = 200$ GeV [84]. The electron R_{AA} is compared with the models. The green dot curve is the BDMPS, and the yellow band is the GLV models. The green band shows the combined collisional and the radiative energy loss model.

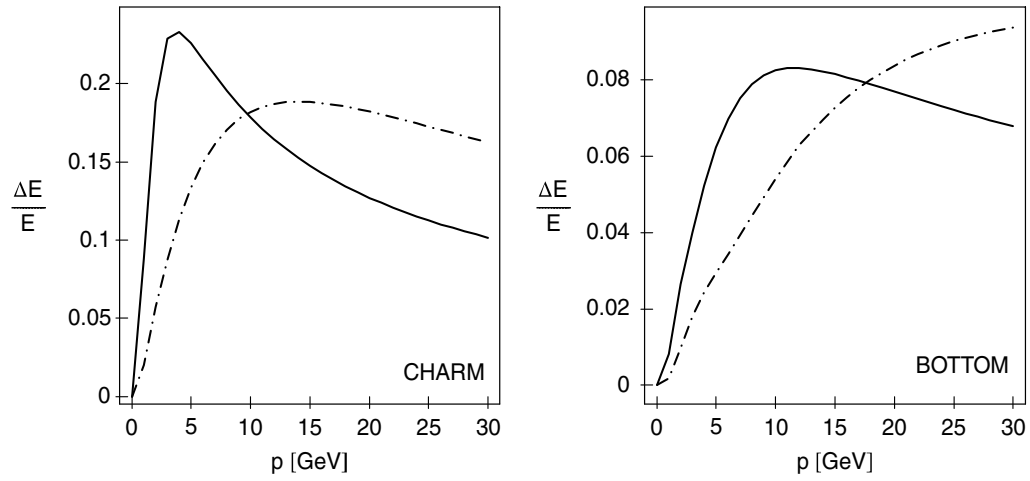

Figure 2.16: The fractional energy loss of the collisional and radiative process as a function of momentum for charm (left) and bottom (right) quarks [82]. The solid and dot-dashed curves correspond to the collisional and radiative process, respectively.

scaling of the total charm production can be observed, it will strongly suggest that the high p_{T} suppression of charm quarks is caused by the final state effects in QGP, such as energy losses of partons. The cold nuclear effects can modify both the total yield and the spectral shape of produced charms. Therefore, the measurement of the total charm production provides an important baseline for the high p_{T} suppression.

In addition, this study can put quantitative constraints on the gluon shadowing effect, even though the modification of the charm production due to the shadowing effect is expected to be small. According to the EKS98 model for the shadowing of nuclear PDF, the gluon density of Pb with $Q^2 = 5.39$ GeV^2 is roughly 5% smaller than that of proton at $x \sim 0.02$. This means that, if the EKS parameterization is correct, charm production due to gluon fusions in heavy ion collisions will be 10% smaller than that with N_{coll} scaling in $p + p$. If the other processes are included, the modification of the charm production due to the shadowing will be reduced.

Once the cold nuclear effects can be understood, we can study additional productions of charms in the pre-equilibrium and thermal stage of space-time evolution in heavy ion collisions. The additional productions are expected to provide some informations related to the thermalization time and the temperature of the dense matter. Therefore, the systematic measurement of the charm productions in $p + p$, $d+$Au and Au + Au collisions is necessary to study these effects due to the initial production, the additional production, the cold nuclear effects and the final state effects.

As a first step of this important study, we measured the centrality dependence of the total charm productions from single electron measurement in Au + Au collisions at $\sqrt{s_{\mathrm{NN}}} = 200$ GeV. These result are compared with $p + p$ and $d +$ Au data. The measurements and the results are described in the next sections.

Chapter 3

Experimental Setup

3.1 Relativistic Heavy Ion Collider

The Relativistic Heavy-Ion Collider (RHIC) at Brookhaven National Laboratory (BNL) was constructed to study the characteristics of a new phase of sub-atomic matter created in heavy ion collisions. A collision energy at RHIC is one order of magnitude higher than the AGS at BNL and the SPS at CERN [85]. RHIC can accelerate a variety of nuclear beams from protons (p) to light ions to gold ions (Au) with its maximum energy up to 250 GeV for p and 100 GeV per nucleon for Au. Figure 3.1 shows a schematic view of the accelerator complex. Protons and Au ions are initially produced and accelerated by the Linac and the Tandem Van de Graaff pre-accelerator, respectively. The produced beam is sent to the Booster Synchrotron followed by the Alternating Gradient Synchrotron (AGS). AGS then accelerates the beam upto 28 GeV for p and 10.8 GeV for Au per nucleon, and injected into the RHIC rings. The beams are finally accelerated up to its maximum energy.

RHIC has two individual accelerator rings with 3.83 km circumference. The two rings intersect at six intersection points. There were initially four experiments, PHENIX, STAR, BRAHMS and PHOBOS placed at the intersection points of RHIC, and they are designed to study the various aspects of dense matter created in heavy ion collisions and the spin structure of nucleon using polarized p beams. RHIC had started the operation from year 2000 and it is continuing its operation. All four experiments has started taking data at the start of RHIC. BRAHMS and PHOBOS had stopped data taking in year 2006. PHENIX and STAR is continuing the operation . During that period, RHIC had collided various nuclear species with various energies. These are summarized in Tab. 3.1.

3.2 PHENIX Detector Overview

The Pioneering High Energy Nuclear Interaction eXperiment (PHENIX) is designed to measure several fundamental probes of high-energy nuclear interactions [86]. In order to measure photons, leptons and hadrons simultaneously, and to separate leptons from much larger number of hadrons, the PHENIX detector has a good particle identification capability in broad p_{T} range with good momentum and energy resolution.

The PHENIX detector is organized by three parts of detector systems: the global

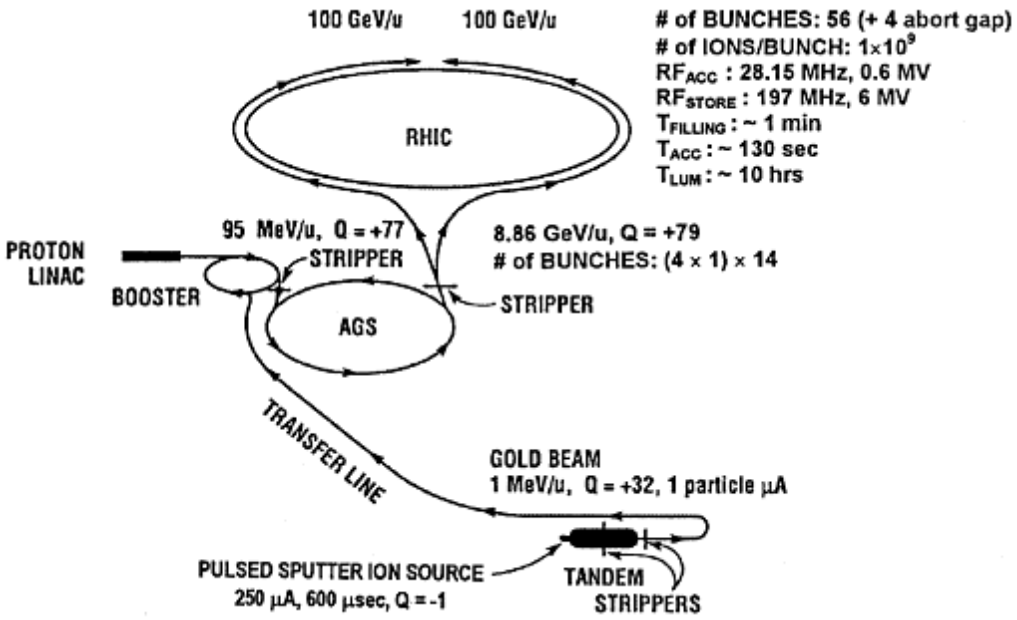

Figure 3.1: The RHIC accelerator complex.

Table 3.1: Summary of RHIC operation. The integrated luminosity is recorded in PHENIX.

Run	Species	$\sqrt{s_{\rm NN}}$	$\int Ldt$		year
1	Au + Au	130	1	μb^{-1}	2000
2	Au + Au	200	24	μb^{-1}	2001/02
	$p+p$	200	0.15	pb^{-1}	
3	d + Au	200	2.74	nb^{-1}	2002/03
	$p+p$	200	0.35	pb^{-1}	
4	Au + Au	200	241	μb^{-1}	2003/04
	Au + Au	62.4	9	μb^{-1}	
5	Cu + Cu	200	3	nb^{-1}	2005
	Cu + Cu	62.4	0.19	nb^{-1}	
	Cu + Cu	22.4	2.7	μb^{-1}	
	$p+p$	200	3.8	pb^{-1}	
6	$p+p$	200	10.7	pb^{-1}	2006
	$p+p$	62.4	0.1	pb^{-1}	
7	Au + Au	200	813	μb^{-1}	2007
8	d + Au	200	80	nb^{-1}	2007/08
	$p+p$	200	5.2	pb^{-1}	
9	$p+p$	500	14	nb^{-1}	2008/09
	$p+p$	200	16	pb^{-1}	

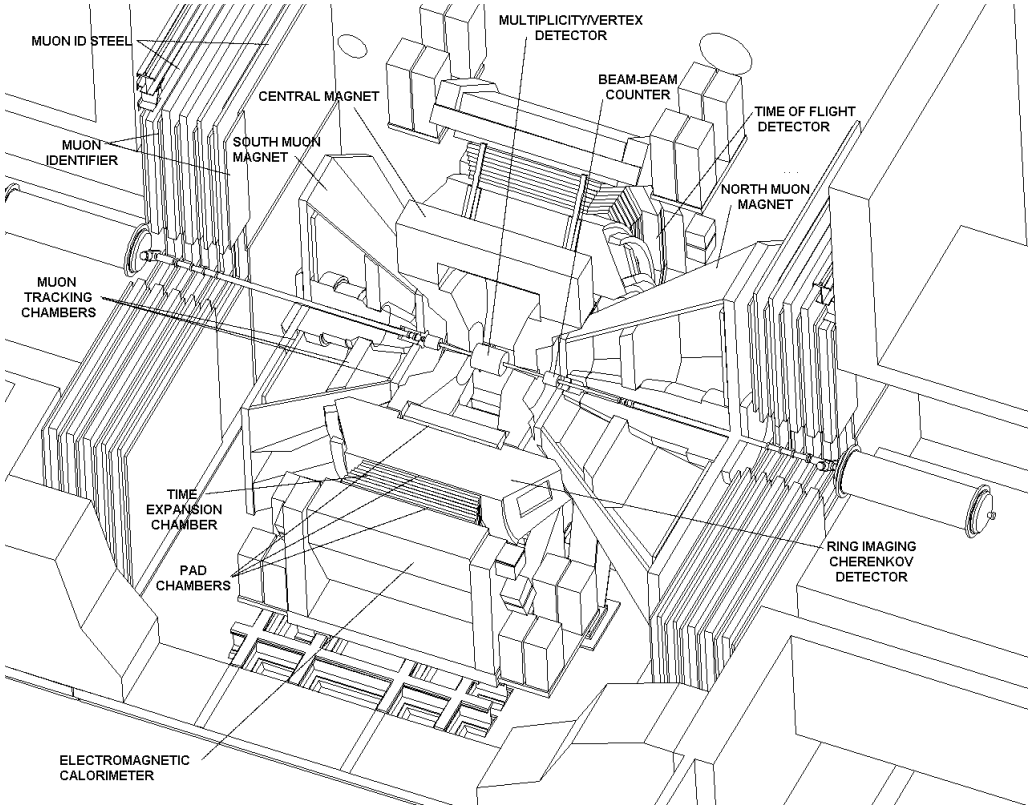

Figure 3.2: The cutaway drawing of the PHENIX detector.

detectors, the central arm spectrometers and the muon arm spectrometers. Figure 3.2 shows a bird's eye view of the PHENIX detector.

The global detector consists of a pair of the beam-beam counters (BBC) and a pair of the zero-degree calorimeters (ZDC). They produce a minimum bias trigger and give an event characterization of the heavy ion collisions.

The central arm spectrometer measures electrons, photons and charged hadrons at central rapidity region. The magnetic field for the central arm spectrometer is supplied by the central magnet which provides an axial field parallel to the beam axis. The central arm spectrometer is constructed by two almost symmetrical spectrometer arms, named as the West arm and the East arm. The West arm and the East arm covers the central rapidity region (pseude-rapidity, $|\eta| \leq 0.35$) and a quarter of full azimuthal angle ($\Delta\phi = \pi/2$). The central arms consist of several detector subsystems for charged particle tracking, particle identification and calorimetry. Drift chambers (DC) and a layer of pad chambers (PC) are placed at the most-inner of the central arm and measure charged particle trajectories with good momentum resolution. The time projection chamber (TEC) in the East arm provides additional particle tracking and identification. The time-of-flight counters (TOF) in the East arm identifies charged hadrons up to 2.4 GeV/c for π/K and 4 GeV/c for p. The ring imaging Ĉerenkov detectors (RICH) have a good capability of electron separation from large number of produced hadrons. The electro-magnetic calorimeter (EMCal) is placed at the most outside of the central arm and measures total energy of photons and electrons.

Figure 3.3 (top) shows the schematic view of the central arm spectrometer from the beam axis.

The muon arm spectrometers are instrumented to measure muons and consist of a pair of the spectrometer arm, named as the North arm and the South arm. They cover the forward and the backward pseudo rapidity ($1.15 \leq |\eta| \leq 2.25$ for the South arm and $1.15 \leq |\eta| \leq 2.44$ for the North arm) and the full azimuthal angle ($\Delta\phi = 2\pi$). Each of the muon spectrometer arms consists of a muon tracker (MuTr) followed by a muon identifier (MuID). Figure 3.3 (bottom) shows a side view of the PHENIX detector. When the PHENIX detector is seen from the East arm side, the South and North muon arm spectrometers are placed in the left and right side of the central magnet, respectively.

In order to measure both soft and hard/rare probes such as $J/\psi \rightarrow e^+e^-$ process and high $p_{\rm T}$ particle production, the PHENIX detector has the first (LVL1) and the second (LVL2) level trigger and a very fast data acquisition system (DAQ).

We give the detailed description of these detector subsystems and DAQ systems in the next section.

3.3 Global Detector

3.3.1 Beam Beam Counter

The beam beam counter (BBC) is a pair of identical Ĉerenkov detector arrays [87]. The BBC is placed ± 144 cm far from the center of the PHENIX detector along with the beam axis. The BBC covers $3.1 < |\eta| < 3.9$ and full azimuthal angle ($\Delta\phi = 2\pi$). A BBC array (Figure 3.4 (a)) is composed of 64 Ĉerenkov detector elements. One element (Figure 3.4 (b)) consists of a hexagonal-cylinder shaped quartz Ĉerenkov radiator and a 15 stage mesh-dynode type photomultiplier tube (Hamamatsu R6178). The BBC is required to work in a strong magnetic field (3 kG).

The BBC plays several important roles in the measurement of the collisions. The BBC provides the minimum bias trigger for level-1 trigger. The BBC is used to determine the collision vertex along with the beam axis (z vertex) and the centrality for event characterization. In addition, the BBC measures the collision timing for the time-of-flight measurement.

The BBC measures the arrival time of charged particles emitted from the collisions. The arrival times (T_S and T_N for the south and the north side of the BBC) are determined to calculate a truncated average of hit timings in individual BBC elements with $\sigma = 40 \pm 0.5$ ps of timing resolution. The vertex position (z) and the start timing (t_0) of a collision are determined using T_S and T_N:

$$z = \frac{c}{2} \times (T_S - T_N) \tag{3.1}$$

$$t_0 = \frac{1}{2} \times (T_S + T_N - \frac{L}{c}) \tag{3.2}$$

Here, $L(= 144$ cm) is a known distance from the center of PHENIX to the BBC location along with beam axis and c is the speed of light. The z information is used for both offline analysis, and level-1 trigger (LVL1). The combination of z position and more than

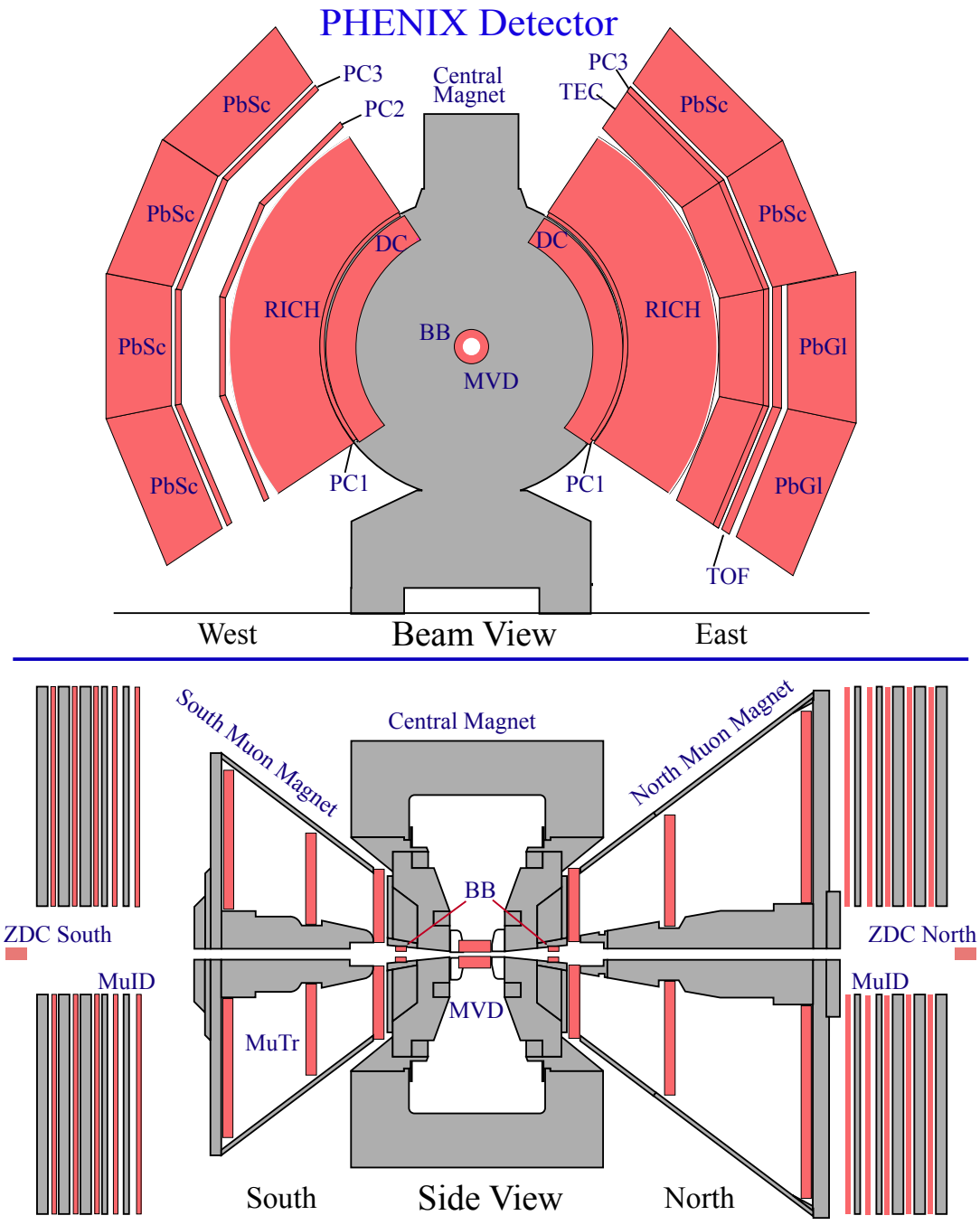

Figure 3.3: The composition of PHENIX detector in Run 2 operation: (top) the beam view of the central arm. (bottom) the side view of the PHENIX detector.

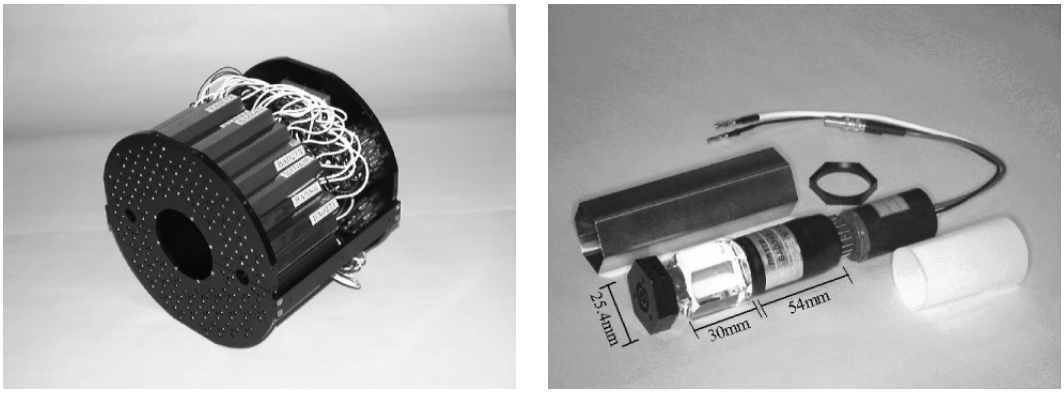

(a) (b)

Figure 3.4: (a) A BBC array comprising 64 BBC elements. (b) A BBC element.

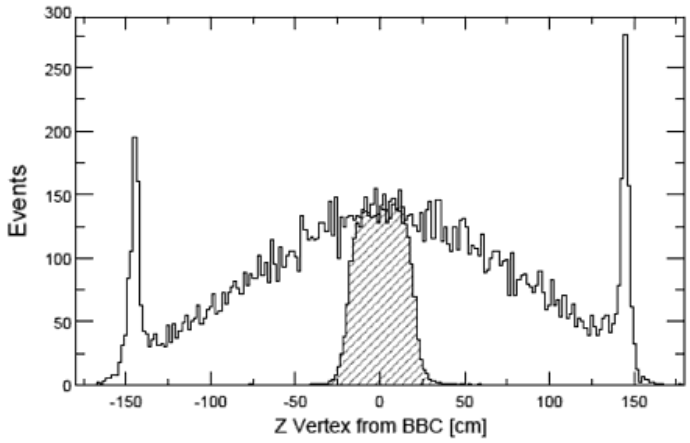

Figure 3.5: The z vertex distribution. The shaded area corresponds to the events triggered by LVL1.

2 hit PMT's is required to produce LVL1. Figure 3.5 shows z vertex distribution. The shaded area in Fig. 3.5 corresponds to the event selected by LVL1 condition. The position resolution of z vertex is $\sigma_z = 0.7$ mm, and this corresponds to 23 ps of t_0 resolution [88]. In Fig. 3.5, The peak around $z = \pm 144$ cm corresponds collisions outside of the BBCs, e.g. beam-gas collisions.

Each of BBC element is calibrated using a MIP peak. The pulse height information measured in all BBC elements is summed up to measure total charged particle multiplicity in BBC acceptance. This multiplicity information combined with the ZDC is used for determination of collision centrality as described in section 4.2.2.

3.3.2 Zero Degree Calorimeter

The zero degree calorimeter (ZDC) [89, 90] is a pair of hadron calorimeters which are placed at 18 m up and downstream of the center of the PHENIX along with the beam

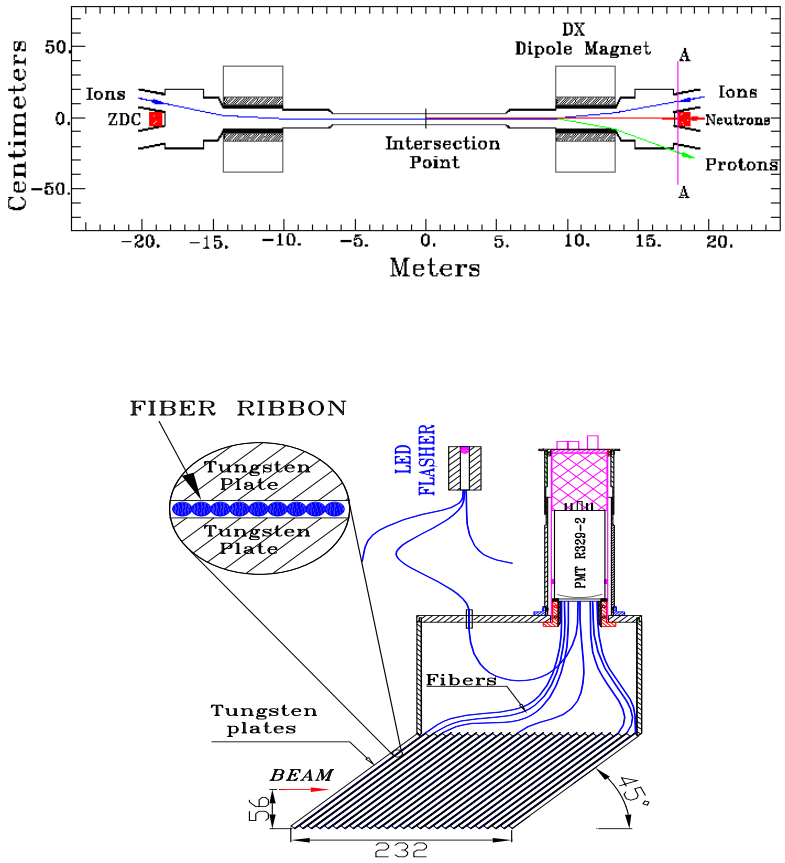

Figure 3.6: (top) The location of the ZDC. (bottom) A side view of a ZDC module.

axis and covers $|\theta| < 2$ mrad with respect to the beam axis shown in top of Fig. 3.6. The ZDC consists of three identical modules. One module is a sandwich type sampling calorimeter with a photomultiplier tube read-out (Hamamatsu R329-2) consisting of 5 mm thick tungsten absorber layers interleaved with optical fiber (0.5 mmϕ) read-out layers. The total thickness of a ZDC module is 2 interaction length (Λ_I). A ZDC module samples Čerenkov lights emitted from secondary charged particles in the fiber layers. Figure 3.6 (bottom) shows a side view of one ZDC module.

The ZDC measures spectator neutrons emitted from heavy ion collisions at RHIC. Since the ZDC is located behind the beam bending magnets (DX) shown in Figure 3.6 (top), all charged particles are swept out by the DX magnets. The energy resolution at single neutron peak is approximately 21% [91], where the single neutron peak is measured in low multiplicity events. A coincidence hit of both the ZDC gives a minimum bias selection of the collisions. The neutron multiplicity calculated from the total energy in the ZDC is correlated with the event geometry. Therefore, the ZDC multiplicity combined to the BBC are used to determine collision centralities. The ZDC also measures neutrons from mutual Coulomb dissociations in heavy-ion collisions. This is used for luminosity monitoring. The cross section of the Coulomb dissociation in Au + Au collisions at $\sqrt{s_{\rm NN}} = 130$ GeV is measured to be $\sigma_{\rm MCD} = 3.67 \pm 0.26$ barns [91].

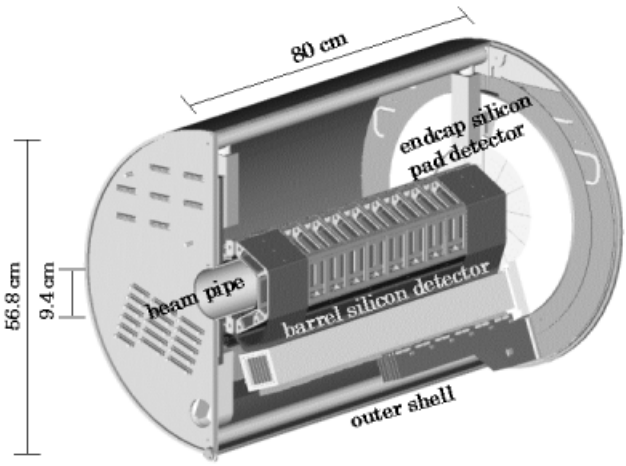

Figure 3.7: The schematic view of the MVD

3.3.3 Multiplicity Vertex Detector

Multiplicity Vertex Detector (MVD) [87] is a array of silicon (Si) detectors comprising a barrel strip detector and a pair of end-cap pad detectors. The barrel detector consists of two layers of Si strip elements (300 μm thick and 200 μm pitch). The inner and outer layer cover 2π in azimuth and ± 32 cm in z-position. The bottom part of the outer layer is only installed to reduce the amount of material in the central arm acceptance, since most of the background electrons is from photon conversions.

MVD is placed at the center of the PHENIX detector with $|z| < \pm 35$ cm along with the beam pipe. The radius of the MVD outer shell is about 30 cm. Figure 3.7 shows a schematic view of the MVD.

The purpose of the MVD is to measure charged particle multiplicity and to determine a position of collision vertex. The MVD information is not used in this analysis. But the composition of the MVD needs to be described in detail for electron analysis. The amount of material in the MVD is approximately 1.1% radiation length (X_0), and it is a major source of background electrons from photon conversions. During the "converter run", a photon converter described in section 3.6 was installed wrapping around the MVD outer shell. The detailed list of the MVD material is summarized in Tab. 3.2. The MVD was installed for the first three years of the PHENIX operation. After these periods, the MVD was removed. Therefore, background electrons from photon conversions are significantly reduced in Run 4 analysis compared to Run 2 analysis.

Table 3.2: Summary of the MVD composition and their radiation lengths

Description	Material	Thickness (mm)	Rad. Length (mm)	Thickness X_0 (g/cm^2)
Beam Pipe	Be	1.016	353	0.29 %
MVD				
Inner Shell	Al	0.01	89	0.01 %
	adhesive	0.0508	254	0.02 %
	Roha cell	3	5000	0.06 %
	adhesive	0.0508		0.02 %
	Al	0.01		0.01 %
Inner Cell	Si	0.3	94	0.32 %
Rohacell Cage	Rohacell	24.4		0.11 %
Outer Si	Si	0.3		0.32 %
Kapton Cable	Kapton	0.05	250	0.02 %
	Cu	0.005	14	0.02 %
	Cu	0.005		0.02 %
Outer Shell	Al	0.01		0.01 %
	adhesive	0.0508		0.02 %
	Rohacell	6		0.11 %
	adhesive	0.0508		0.02 %
	Al	0.01		0.01 %
Air before DCH	Air	1980	304200	0.65 %
Ar	Ar	252.5	109708.2	0.23 %

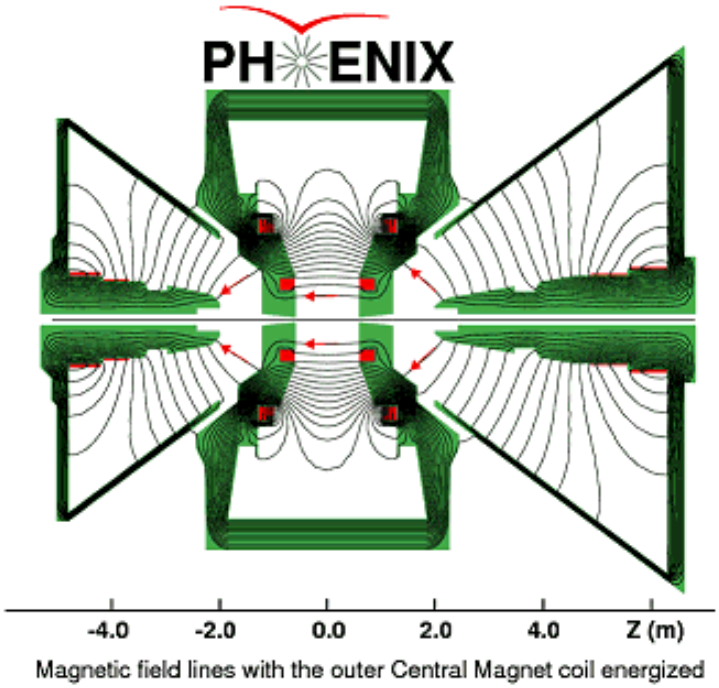

Figure 3.8: A cutaway view of the PHENIX magnets. The line shows the contour of the magnetic field.

3.4 Central Arm Spectrometer

3.4.1 Central Magnet

The central magnet [92] is energized by two pairs of concentric coils and provides a axially symmetric magnetic field parallel to the beam pipe. The field strength at $R = 0$ cm is 0.5 T in Run 2 (0.9 T in Run 4) and gradually decrease with approximately Gaussian profile. Then, the field reaches almost zero for region $R > 250$ cm. Therefore, electrons can pass through the RICH with a straight line, because there is no magnetic field in the RICH. Figure 3.8 shows a cutaway view of the PHENIX magnet systems with the field lines of the central and the muon magnet.

3.4.2 Drift Chambers

The Drift Chambers (DC) are placed at the front of both the East and the West arms with a radius of 2.0 to 2.4 m far from the beam axis [93]. Each DC has a cylindrical shape with $|z| < 90$ cm and $\pi/2$ azimuthal angle (ϕ) coverage shown in Fig. 3.9 (top).

The DC is supported by a titanium frame and filled with 20 equal sectors covering 4.5 degrees in azimuth. There are 6 types of wire modules stacked radially in each sector. They are called $X1$, $U1$, $V1$, $X2$, $U2$ and $V2$. Each module contains 4 sense planes and 4 cathode planes forming wire cells with a $2 - 2.5$ cm drift space in the ϕ direction. The $X1$ and $X2$ wire cells run in parallel to the beam axis to measure particle trajectories in

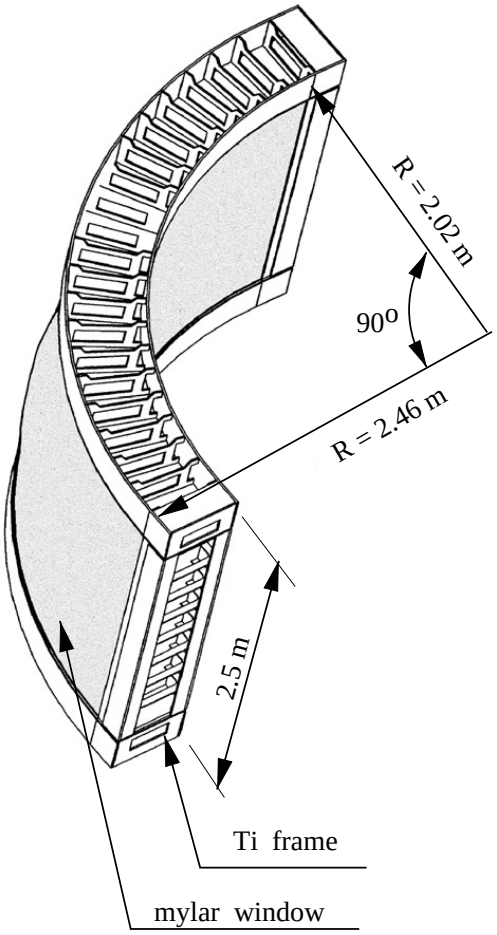

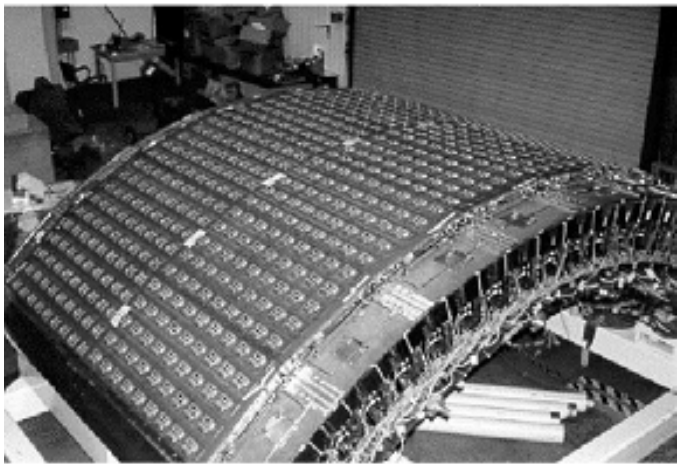

Figure 3.9: (top) A schematic view of the DC with 20 DC sectors. (bottom) A picture of the DC covered by the PC.

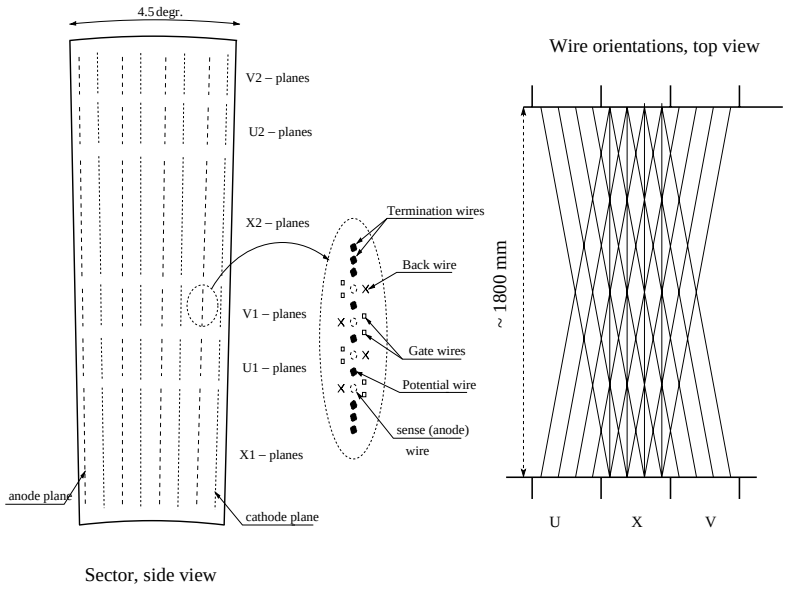

Figure 3.10: (left)The layout of X and U,V stereo wires in a sector. (right) The schematic diagram of X, U and V orientation.

$r-\phi$. These wire cells are followed by two set of small angle U, V wire planes. The $U1$, $V1$, $U2$ and $V2$ wires have stereo angles of approximately 6° relative to the X wires and measure the z coordinate of the tracks. The X, U and V cells contain 12, 4 and 4 sense wires, respectively. As a result, there are 40 sense wires in each cell. Figure 3.10 shows the layout of sense planes and sense wire cells in a sector. The U and V stereo wires start in a sector on one side and end in a neighboring sector on the other side of the DC.

The DC measures the charged particle trajectories in the $r-\phi$ plane to determine their momentum with good resolution. It is required that the DC recognizes the track for the highest multiplicity. To satisfy the requirement, the DC is designed to have single wire resolution better than 150 μm in $r-\phi$, single wire track separation better than 1.5 mm, single wire efficiency better than 99%, and spatial resolution in z axis better than 2 mm. Moreover, to reduce the single wire occupancy, the wires are electrically isolated into two halves at the middle of the DC ($z=0$) using kapton of 100 μm thickness. Therefore, the DC system has 6400 sense wire (40/2 wires/cell * 80 cells/side * 2 sides/arm * 2 arms = 6400 wires). This corresponds to 12800 readout channels The DC operates with a mixture of 50% Ar, 50% ethane gas and small fraction of alcohol. Figure 3.9 (b) shows a picture of the DC covered by PC.

3.4.3 Pad Chambers

The Pad Chambers (PC) consist of three individual layers of multi-wire proportional chambers [93]. The first inner layer of the PC (PC1) are placed between the DC and the RICH in both the East and the West arms. The second layer (PC2) is located behind the RICH in the West arm only. The third layer (PC3) is mounted in front of the EMCal.

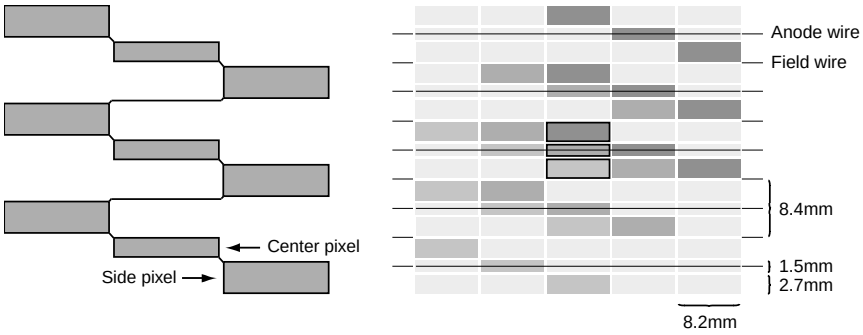

Figure 3.11: (left) The pad and pixel geometry. (right) A cell defined by three pixels.

The installed radii of these three PC layers correspond to 248, 419 and 490 cm from the beam pipe, respectively. A layout of three PC layers in both the East and the West arms can be seen in Fig. 3.3. Each PC contains a single wire plane inside a gas volume bounded by two cathode planes. One cathode is finely segmented into an array of pixels to read out the induced charge through specially designed electronics. The PC operates with a gas mixture of 50% argon and 50% ethane.

The PCs are the only non-projective detectors in the central arm tracking system and provide three-dimensional space-point of charged particles with high efficiency. The PC1 is also used to determine z-coordinate of the track measured by the DC. The PC2 and PC3 are needed to recognize particle trajectories, because many background tracks are produced by particle decays and particle-detector interactions outside the DC.

A special pad design was invented to archive a high pixel granularity and small readout channels. Figure 3.11 (left) shows the pixel configuration of a pad. The nine by nine interleaved pixels are grouped together to form single readout channel. Each cell recognizes a valid hit and contains three pixels which are connected to different but neighboring pads shown in Fig. 3.11 (right). So, the hit information can be broken down to the cell level by identifying the triplets of the pads. The cell size is 8.4 mm for the PC1 and PC2 , and is twice for the PC3, since the PC3 is twice far from the beam pipe compared to the PC1. The spacial resolutions of the PC1 and PC 3 in z direction is ± 1.7 mm and ± 3.6 mm, respectively.

3.4.4 Ring Imaging Čerenkov Detector

The Ring Imaging Čerenkov detector (RICH) [94, 95] is a gas Čerenkov detector and is a primary device for identifying electrons among the very large number of charged pions. The RICH is placed behind the PC1 in both the East and the West arms. Figure 3.3 shows the RICH location.

The RICH consists of a $40\,\mathrm{m}^3$ gas vessel with an entrance and exit windows of the aluminized Kapton, two intersecting spherical mirrors and two arrays of 16×80 photo multiplier tubes (PMT). A PMT array is placed behind the central magnet so that particles from the collision do not directly hit the PMT array. Each PMT (Hamamatsu H3171S) is housed in a magnetic shield. A Winston cone is attached at the entrance of the shield

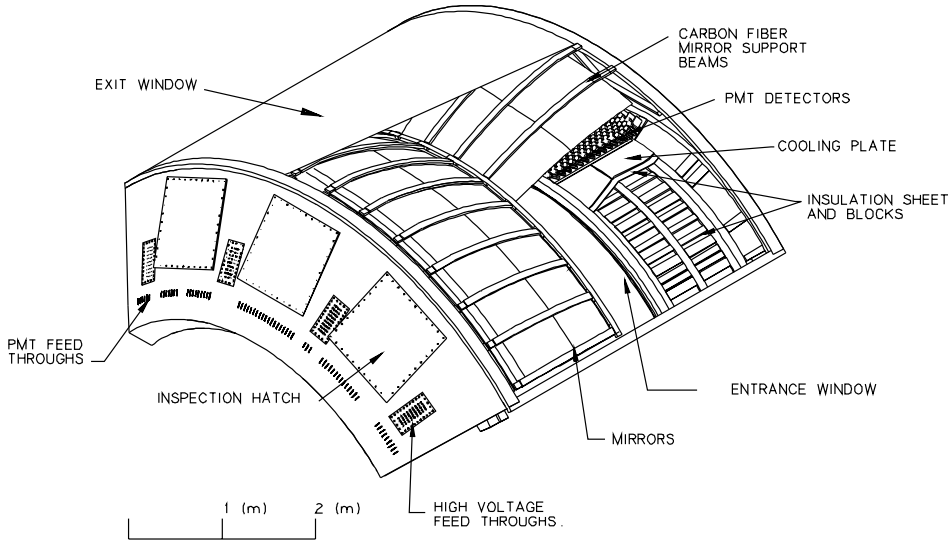

Figure 3.12: A cutaway view of the RICH gas vessel with the spherical mirrors.

with 50 mm diameter to collect Čerenkov photon efficiently. Figure 3.12 shows a cutaway view of the RICH.

An electron passing through the RICH emits Čerenkov lights. The spherical mirror reflects the Čerenkov photons and focuses on the PMT array forming a ring-shaped pattern. The diameter of the Čerenkov ring which corresponds the emission angle of the Čerenkov photon is defined by a type of a gas radiator. The vessel is filled with CO_2 gas at 1 atm as Čerenkov radiator. This corresponds to Čerenkov threshold of 4.9 GeV/c for pion. Figure 3.13 shows the top view of the RICH. The Čerenkov photons emitted by an electron are reflected to the PMT arrays, although a charged hadron passes away without Čerenkov light emissions.

3.4.5 Time Of Flight Counters

The Time-Of-Flight counters (TOF) [94] play an important role for particle identification of charged hadrons. The TOF is designed to provide π/K separation at momenta up to 2.4 GeV/c and K/p up to 4.0 GeV/c within 4 σ.

The TOF is placed at 5.1 m far from the beam pipe in the East arm and covers the range of $70 - 110^\circ$ in poler angle (θ) and 30° in azimuth (ϕ). The location of the TOF is shown in Fig. 3.3. The TOF consists of 10 panels which is composed of 96 plastic scintillator slats with read-out PMT (Hamamatsu R3478S) attached at both ends of the slat. Thus, 960 slats of the scintillators and 1920 channels of PMTs are totally installed. A slat is 1.5×1.5 cm^2 in width and depth and is aligned to $r - \phi$ direction. Figure 3.14 shows the schematic view of one panel in which 96 slats are arranged.

The TOF measures an arrival time (stop time) by taking an average time at both end of PMTs. This time-of-flight of a charged particles is determined by using the arrival time and the start time provided by the BBC. The particle identification is performed using

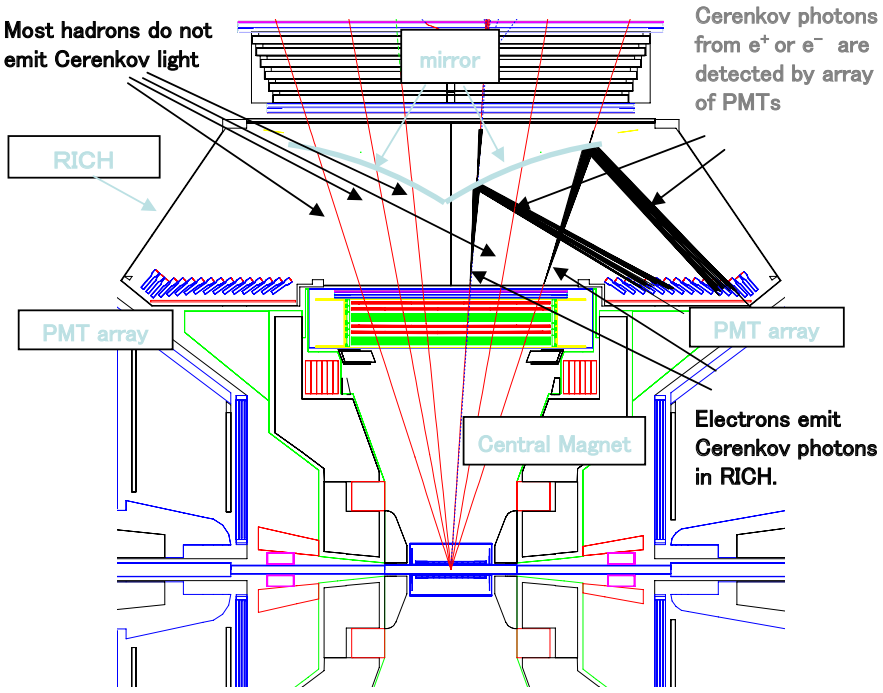

Figure 3.13: The top view of the RICH. An electron emits Čerenkov photons.

the squared mass of the measured particle expressed as:

$$m^2 = \frac{p^2}{c^2}\left[\left(\frac{t_{\mathrm{TOF}}}{L/c}\right)^2 - 1\right], \tag{3.3}$$

where p is the momentum, t_{TOF} is the time of flight, L is the flight path length and c is the speed of light. The time resolution for the time-of-flight measurement is archived to be $\sigma \simeq 120$ ps [105].

3.4.6 Electromagnetic Calorimeter

The electromagnetic calorimeter (EMCal) [96] is used to measure the spatial position and energy of electrons and photons produced in heavy ion collisions. The EMCal is located at the most outside of the central arm. The EMCal consists of two different detector systems. One is a Pb-Scintillator calorimeter (PbSc) which provides 4 and 2 sectors for the West and East arms, and the other is Pb-Glass calorimeter (PbGl) which occupies 2 lower sectors of the East arm. The location of the PbSc and the PbGl calorimeters are shown in Fig. 3.3.

The PbSc is a shashlik type sampling calorimeter made of alternating tiles of Pb and scintillator and consists 15552 individual towers. Each PbSc tower contains 66 sampling cells ($55 \times 55 \times 375$ mm^3) and has a thickness of 18 radiation length (X_0) and about 30 mm of Molière radius. These cells are optically connected 36 longitudinally penetrating

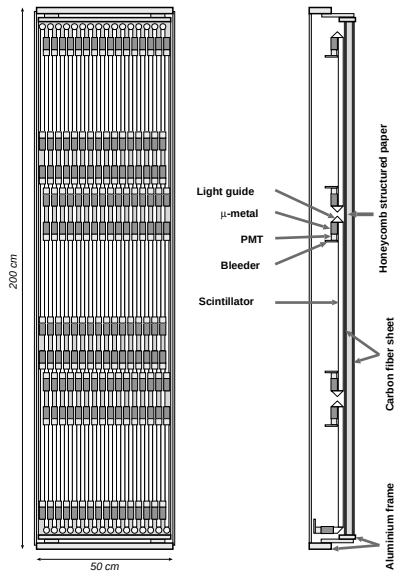

Figure 3.14: Schematic view of the single TOF panel which is composed of the 96 scintillator slats.

wavelength shifting fibers for light collection. Light is readout by 30 mm PMT (FEU115M) at the back of the towers. A single basic structure is called as a module which consists from 4 towers. Figure 3.15 shows a PbSc module.

On the other hand, the PbGl is Čerenkov calorimeter which consists 9216 lead glass modules with PMT readout (FEU84). Each PbGl module is $40 \times 40 \times 400$ mm^3 and has 14.4 X_0 and 36 mm of Molière radius. The PbGl has been used previously in CERN WA98 experiment [97]. Figure 3.16 shows an unit array of the PbGl modules.

The EMCal has a important role in particle identification using the informations of measured energy, time and shower shape of electromagnetic cascade. The energy resolutions of the PbSc and the PbGl are obtained using electron and positron beam at a test experiment for the PbSc and the PbGl respectively:

$$\left.\frac{\sigma_E}{E}\right|^{\mathrm{PbSc}} = \frac{8.1\%}{\sqrt{E(\mathrm{GeV})}} \oplus 2.1\%,$$

$$\left.\frac{\sigma_E}{E}\right|^{\mathrm{PbGl}} = \frac{5.9\%}{\sqrt{E(\mathrm{GeV})}} \oplus 0.8\%.$$

The position resolutions are also obtained:

$$\sigma_x^{\mathrm{PbSc}}(E,\theta) = \left(1.55(\mathrm{mm}) \oplus \frac{5.7(\mathrm{mm})}{\sqrt{E(\mathrm{GeV})}}\right) \oplus \Delta \times \sin(\theta),$$

$$\sigma_x^{\mathrm{PbGl}}(E) = 0.2(\mathrm{mm}) \oplus \frac{8.4(\mathrm{mm})}{\sqrt{E(\mathrm{GeV})}},$$

where σ_x^{PbSc} depends on both energy and impact angle (θ) of incident particle and Δ is given by radiation length.

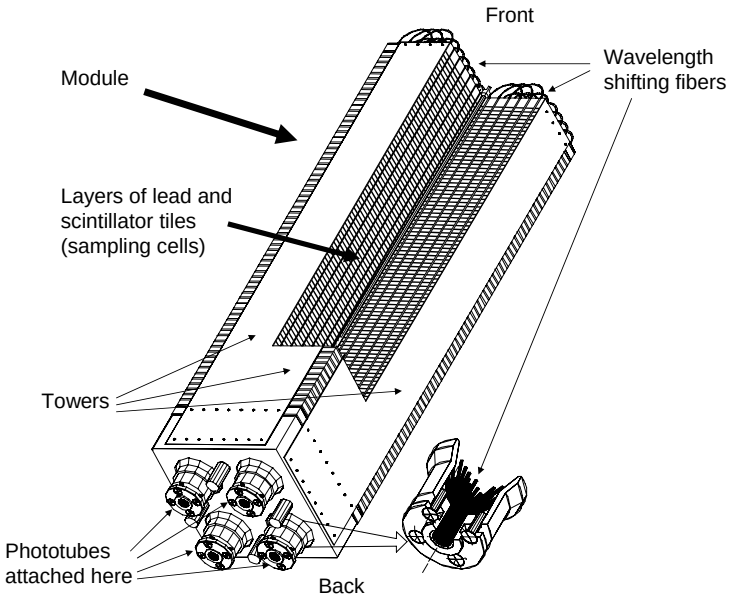

Figure 3.15: The PbSc module consisting 4 towers.

Timing information is used for both particle identification and pattern recognition to find overlapped clusters. In particular, the timing information is a good tool to separate neutral baryons from photons. The time resolutions of the PbSc are obtained as 120 and 400 ps for electrons and charged pions, respectively. On the other hand, time measurement is difficult for the PbGl, since the arrival time of hadrons are faster than the Čerenkov light of electro-magnetic shower produced near the front of the module.

3.5 Data Acquisition System

The PHENIX detector is designed to measure a wide range of observables such as soft hadron production and rare probes such as photons, single leptons and lepton pairs on a variety of colliding systems from $p+p$ to Au + Au. The number of tracks passed through the detector varies from only a few tracks in $p+p$ to several hundred tracks in central Au + Au collisions. The expected interaction rate also varies from a few kHz from central Au + Au to approximately 500 kHz for $p+p$ collisions. To handle a variety of event size and rate seamlessly, the PHENIX Data Acquisition system (DAQ) [98] consists of the detector front ends equipped with the pipelined and dead-timeless features and higher level trigger systems. Figure 3.17 shows a general schematic diagram of the PHENIX DAQ.

The RHIC delivers the 9.4 MHz fundamental clock which corresponds to 106 ns of time interval between beam crossings. All of PHENIX Front End Electronics modules are synchronized to the RHIC clock. Signals produced in the various subsystems are processed by Front End Modules (FEMs) that converts the detector analog signals into digital data. The FEM for each subsystem is placed in the PHENIX Intersection Region (IR). A FEM

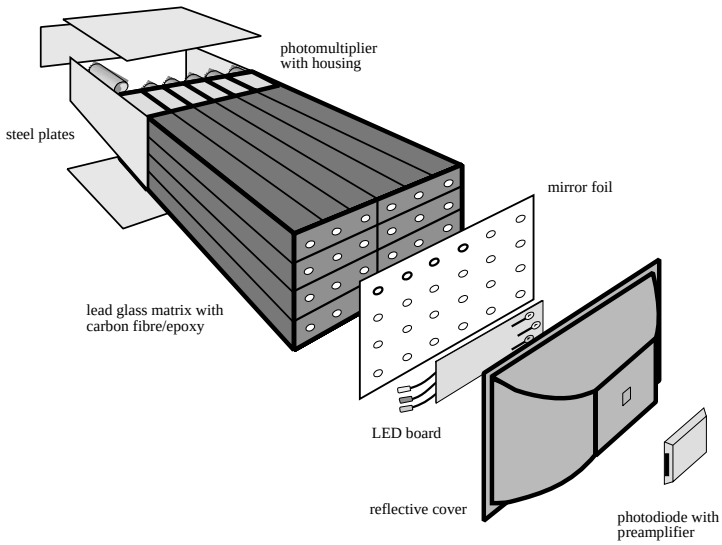

Figure 3.16: An unit array of the PbGl modules.

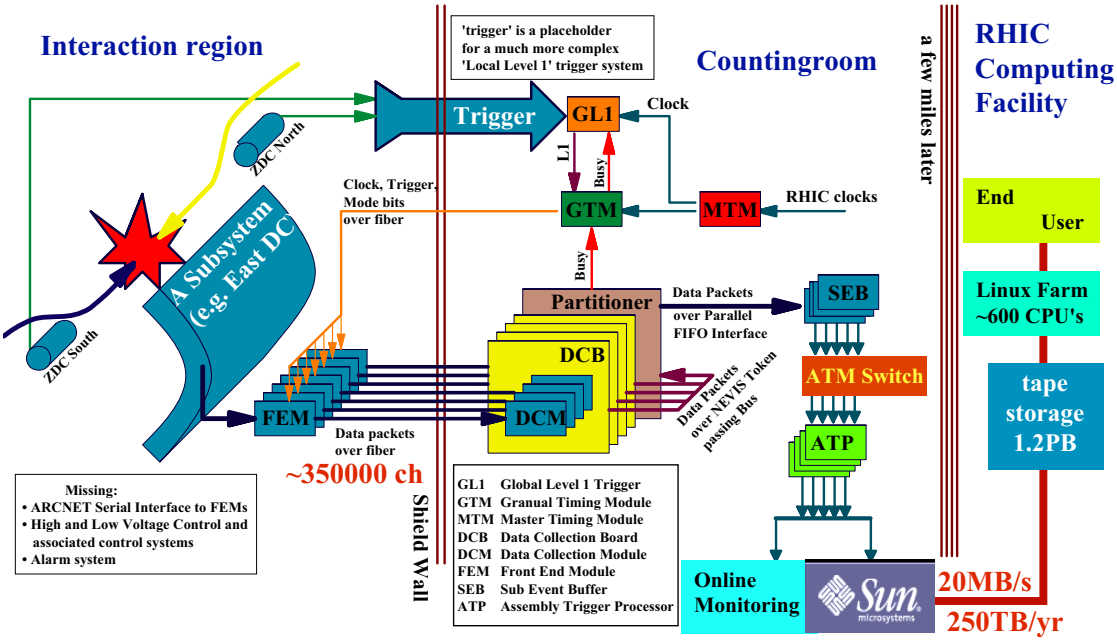

Figure 3.17: Schematic diagram of the PHENIX DAQ.

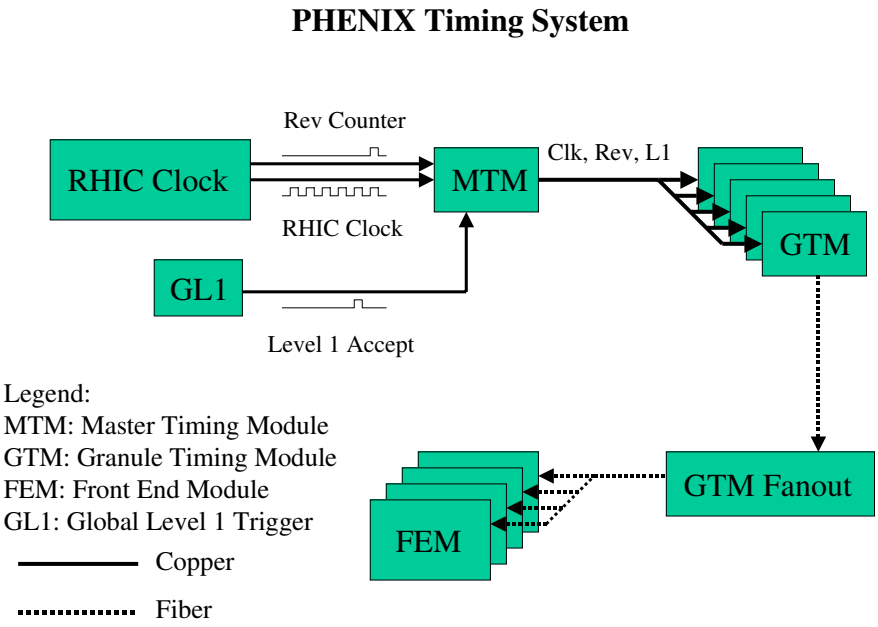

Figure 3.18: Block diagram of the PHENIX timing system.

module can buffer the data of up to 40 beam crossings to wait for the LVL1 decisions and to wait for digitization and readout of triggered event. We have two types of data collection methods in the FEM. The first type is that the signal is digitized in real time in every clock period. The BBC, ZDC, DC and PC use the method. The second type is that the signal is stored in analog form in Analog Memory Units (AMU) and is only digitized after the event is accepted by the LVL1 trigger. The RICH, EMCal and MVD adopted the second method.

All the FEM's are synchronized by the master clock produced in the PHENIX timing system. Figure 3.18 shows a block diagram of the timing system. The RHIC clock is received by the Master Timing Module (module). The MTM distributes the master clock by fanning out the RHIC clock, where the internal phase locked loop is used to minimize the clock jitter. The master clock is transmitted to the FEM via the Granual Timing Module (GTM). Thus, all the FEM's are processed in a single clock. The GTM is prepared for a unit of detector elements. In addtion, the GTM send the control commands (mode bits) and trigger decisions.

The purpose of the Level-1 trigger (LVL1) is to select interesting events and provide event rejection for the limited DAQ rate. The Global Level-1 (GL1) system generates the LVL1 decision based on logical combinations of the Local Level-1 (LL1) decisions. The LL1 is generated by individual trigger detector such as the BBC and the ZDC independently. The GL1 can treat totally 128 bits of the LL1 inputs to make the LVL1 decision.

Once the LVL1 decision is generated, the decision signal is sent to the FEM via the GTM, then the data buffered in the FEM are transfered to the Data Collection Module (DCM) located at the PHENIX Counting House. The FEM, GTM and DCM are connected via a fiber optic cable to eliminate a large number of noise, cross-talk and grounding

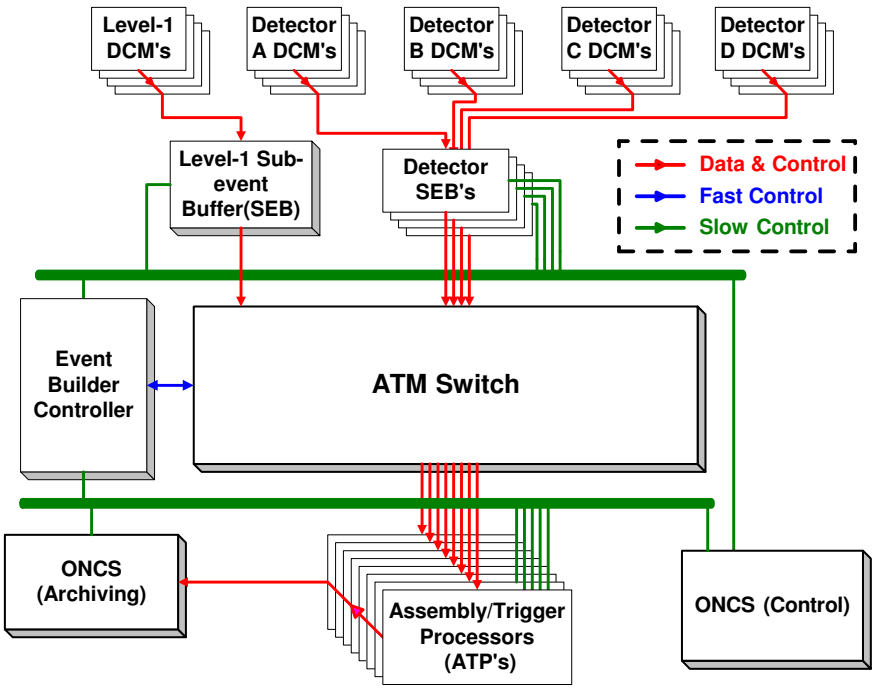

Figure 3.19: Block diagram of the EVB architecture.

problems. At the maximum LVL1 trigger rate, the whole FEM's send over 100 Gbytes of data per second. The DCM is designed to receive this large amount of data. After receiving the data, the DCM performs the zero suppression, error checking and data formatting to generate data packets. The zero suppression is to compress the data by comparing the preset threshold. In addition, the DCM provides a busy signal which are returned to the GL1 to hold off further triggers.

Many parallel streams of the data packets from the DCMs are sent to the event builder (EVB). The EVB performs the final stage of event assembly. Figure 3.19 shows a block diagram of the EVB architecture. In the EVB, the streams of the data packets from the DCMs are first received and buffered in a set of the Sub Event Buffers (SEB). These data are transfered on request to a set of Assembly/Trigger Processors (ATP) via Asynchronous Transfer Mode switch (ATM). The final events assembled in the ATPs are transmitted to the PHENIX Online Control System (ONCS) for logging and monitoring processes. The format of the final event is called "PHENIX Raw Data Format (PRDF)". The raw data are sent to High Performance Storage System (HPSS) at RHIC Computing Facility (RCF) and converted to physical quantities for analysis.

Typical data logging rates for Au + Au collisions increased from 100 Hz in Run 2 and 1 kHz Run 4, then finally reached 5 kHz in Run 7.

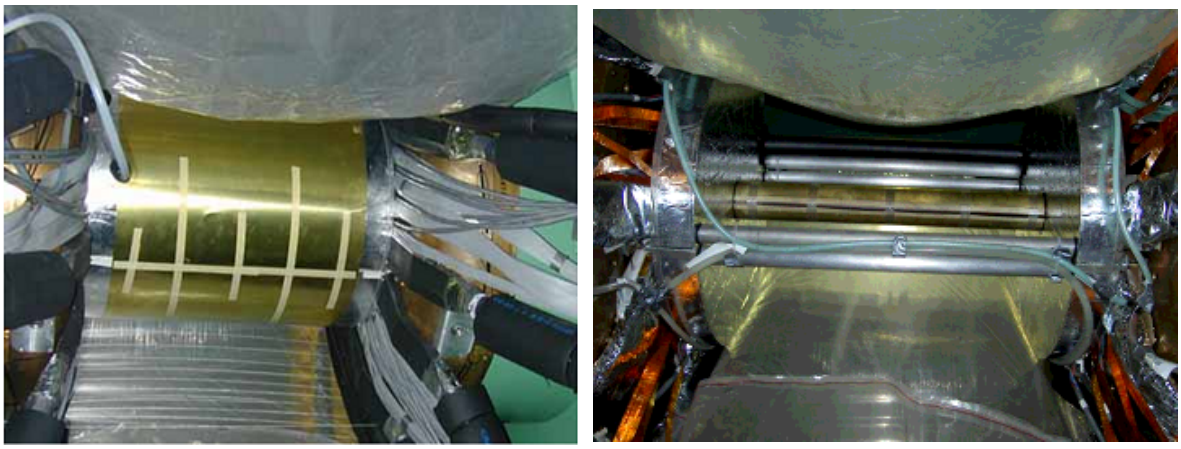

Figure 3.20: (left) Photon converter installed to wrap around the MVD outer shell in Run 2. (right) Converter placed around the beam pipe in Run 4 because the MVD was removed.

3.6 Photon Converter

A photon converter is a key component to separate signal and background electrons in the converter method described in section 4.10.1. The converter is a thin brass sheet of 1.7% radiation length (X_0). In a part of Run 2, the converter was installed wrapping around the MVD outer shell. On the other hand, the converter was placed directly around the beam pipe in Run 4 since the MVD was removed. Figure 3.20 shows the picture of the converter in Run 2 (left) and Run 4 (right), respectively. The basic parameters of the converter is summarized in Tab. 3.3. The radiation length of the converter was precisely determined since the size and weight of the converter was measured.

Table 3.3: The basic parameters of the photon converter

Parameters	
Length	190.5 (cm)
Width	60.96 (cm)
Thickness	0.0254 (cm)
Weight	2500.405 (g)
Area density	0.215313 (g/cm^2)
Mass density	8.476889 (g/cm^3)
X_0	1.68%

Component (X_0 (g/cm^2))	Composition
Cu (12.86)	70%(68.5%-71.5%)
Zn (12.43)	30%
Fe (13.84)	< 0.05%
Pb (6.37)	0.07%

Chapter 4

Analysis

4.1 Outline

In this chapter, the analysis of heavy flavor electron measurement in Au + Au collisions at $\sqrt{s_{\rm NN}}$ = 200 GeV is described. The data used in this analysis is recorded by the PHENIX detector with a minimum bias trigger (MB) during the Run 2 period of the RHIC operation. The definition of the MB trigger and the event characterization are described in section 4.2. The reconstruction of charged particle tracks and the electron identification are described in section 4.3 and 4.4.3

Inclusive electrons consists of three components: (1) signal electrons from semi-leptonic decays of open heavy flavors (namely heavy flavor electrons), (2) "photonic" background electrons from Dalitz decays of light neutral mesons and photon conversions in the detector materials, (3) background electrons from K_{e3} decays and two electron decays of vector mesons. In addition, electrons from quarkonium decays and Drell-Yan are also background included in the component (3). Here, both the component (1) and (3) are called as "non-photonic" electrons. To separate and extract non-photonic and photonic electrons, "Converter method" is used. The converter method is described in section 4.10.1.

The invariant yield is obtained using the extracted signal of heavy flavor electrons. The invariant yield is a Lorentz invariant form of the yield expressed as:

$$E\frac{d^3N}{dp^3} = \frac{d^2N}{2\pi p_{\rm T} dy dp_{\rm T}}, \tag{4.1}$$

where N is the raw yield of heavy flavor electrons per event. To obtain the invariant yield, the correction factors are applied which are the geometrical acceptance, the track reconstruction and the electron identification efficiency. These correction factors are estimated using a GEANT [99] based Monte Carlo simulation of the PHENIX detector described in section 4.9. The systematic uncertainties for signal extraction and correction factors are described in section 4.12.

4.2 Event Selection

In this section, the definition of the minimum bias trigger, the determination of the event characterization are described.

4.2.1 Minimum Bias Trigger

In this analysis, the minimum bias (MB) trigger is defined by a coincidence of both the BBC and the ZDC signals. Because the BBC can measure charged particles at pseudo-rapidity 3.1 to 3.9, the BBC is sensitive to both inelastic Au + Au collisions and backgrounds from beam-gas and/or upstream interactions. On the other hand, the ZDC is sensitive to the inclusive Au + Au interactions which include not only inelastic collisions, but also mutual Coulomb dissociations. In the case of the mutual Coulomb dissociations, there is almost no signal in the BBC. Therefore, in order to select only the inelastic Au + Au collisions and reduce the backgrounds from bean-gas interactions, the coincidence of both the BBC and the ZDC is required as the MB trigger. The detailed definition of the MB trigger is a coincidence of more than 2 hits PMT in both side of the BBC and a coincidence of hits in both side of the ZDC. In addition, the position of collision vertex is selected for the MB trigger to optimize the acceptance of the central arm. The requirements of the vertex positions are $|z| < 75$ cm in online and $|z| < 20$ cm in offline analysis, respectively.

Efficiency of the MB trigger is studied. The MB trigger efficiency is expressed as

$$\varepsilon_{\mathrm{MB}} = \varepsilon_{\mathrm{BBC}} \times \varepsilon_{\mathrm{ZDC}}, \tag{4.2}$$

where $\varepsilon_{\mathrm{BBC}}$ and $\varepsilon_{\mathrm{ZDC}}$ correspond to the trigger efficiencies by the BBC and the ZDC, respectively. The BBC efficiency ($\varepsilon_{\mathrm{BBC}}$) is estimated using a Monte Carlo simulation based on the GEANT [99] with HIJING 1.35 event generator [100] as input. The BBC response in the simulation is tuned so that the charge and time distributions in all 128 PMT and the LVL1 logic of the BBC are reproduced. The systematic uncertainty of the efficiency is estimated by changing the model parameters in HIJING and the threshold of the hit PMT. The BBC efficiency is obtained as [101]:

$$\varepsilon_{\mathrm{BBC}} = 93.1 \pm 0.4(\mathrm{stat}) \pm 1.6(\mathrm{sys})\%. \tag{4.3}$$

The ZDC efficiency $\varepsilon_{\mathrm{ZDC}}$ is estimated using the relative fraction of the ZDC triggered events in the BBC triggered events. The ratio is obtained as 97.5%. The BBC triggered events include 60% of the background due to high luminosity and 40% of the ZDC inefficiency. Therefore, the ZDC efficiency $\varepsilon_{\mathrm{ZDC}}$ is obtained as [102]:

$$\varepsilon_{\mathrm{ZDC}} = 99.0^{+1.0}_{-1.5}\%. \tag{4.4}$$

Finally, the MB trigger efficiency is obtained as:

$$\varepsilon_{\mathrm{MB}} = \varepsilon_{\mathrm{BBC}} \times \varepsilon_{\mathrm{ZDC}} = 92.2^{+2.5}_{-3.0}\% \tag{4.5}$$

4.2.2 Centrality Determination

The nucleus collisions are classified by "centrality". The centrality is an experimental variable to relate to the geometrical information of the nucleus collisions, e.g. impact parameter (b) and number of participants (N_{part}).

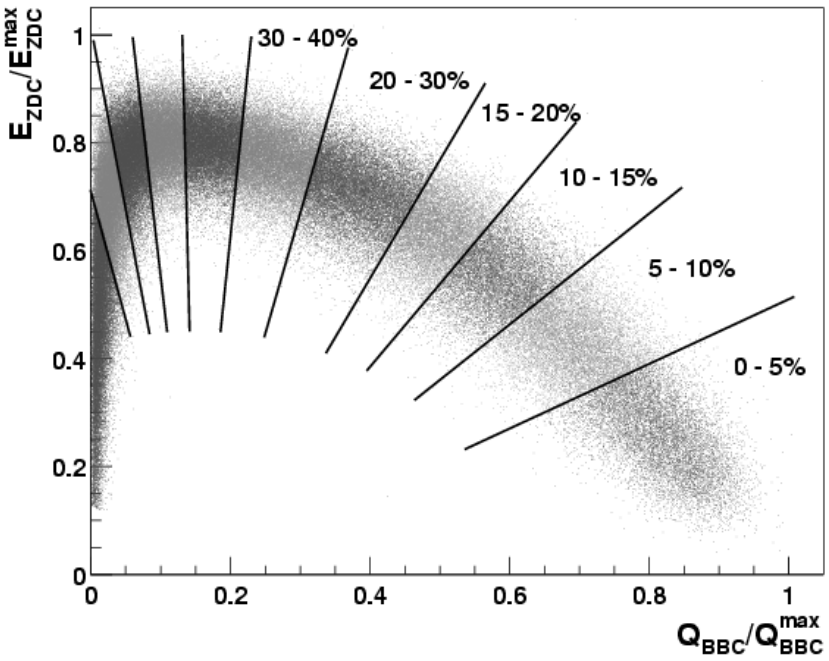

Figure 4.1: The centrality determined by the correlation between the ZDC total energy and the BBC multiplicity [105].

For the centrality determination, a correlation between the BBC multiplicity ($Q_{\rm BBC}$) and the ZDC total energy ($E_{\rm ZDC}$) is used. The BBC measures the charged particle multiplicity in the rapidity range $3.1 < \eta < 3.9$ which increases proportionally with respect to $N_{\rm part}$. On the other hand, the ZDC measures the total energy which corresponds to the number of spectator neutrons. The spectator is a part of nucleus not to participate in the collision, and thus decreases with respect to $N_{\rm part}$. Therefore, anti-correlation is seen for the signals between the BBC and the ZDC as shown in Fig. 4.1. Similar anti-correlation was measured in the NA49 experiment [103].

The relation between the centrality and the impact parameter is determined using a Monte Carlo simulation of the Glauber model including the detector response [104]. The boundary of the centrality is defined in the "clock method " and is expressed in terms of an angle $\phi_{\rm cent}$ as:

$$\phi_{\rm cent} = \tan^{-1}\left(\frac{(Q_{\rm BBC} - Q_0)/Q_{\rm BBC}^{\rm max}}{E_{\rm ZDC}/E_{\rm ZDC}^{\rm max}}\right), \tag{4.6}$$

where $Q_{\rm BBC}^{\rm max}$ and $E_{\rm ZDC}^{\rm max}$ correspond to the maximum values of the BBC multiplicity and the ZDC energy, respectively. The origin of the clock is $(0, 0.2 \cdot Q_{\rm BBC}^{\rm max})$ which is determined by the simulation. The lines shown in Fig. 4.1 indicate the centrality boundaries from central to peripheral collisions. The range of the centrality is from 0 to 92% due to the MB trigger efficiency.

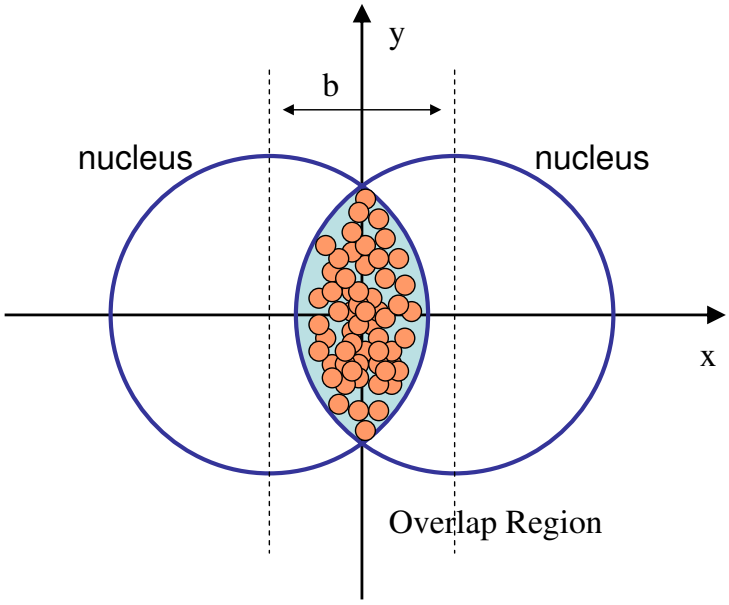

Figure 4.2: Schematic view of the colliding nuclei.

4.2.3 Glauber Calculation

The number of participants ($N_{\rm part}$) and the number of nucleon-nucleon collisions ($N_{\rm coll}$) described in section 2.3.3 are useful to compare the observable (e.g. the production cross section of charged particles) in $p+p$ and nucleus+nucleus ($A+A$) collisions. The $N_{\rm part}$ is the number of nucleons included in the overlap region of colliding nuclei in $A+A$ collisions shown in Fig. 4.2. Thus, the $N_{\rm part}$ can be interpreted as the size of the the overlap region and is related to the total volume of the dense matter formed in the collision. $N_{\rm coll}$ is the number of inelastic nucleon collisions which is used to study the medium modification of high $p_{\rm T}$ particles.

To estimate an average number of the impact parameter (b), $N_{\rm part}$ and $N_{\rm coll}$ for the corresponding centrality classes, a Monte-Carlo simulation of the Glauber model is performed [63]. The Glauber model is a simple geometrical picture of a nucleus-nucleus collision. In the Glauber model, nucleon is assumed to travel in a straight line.

When the distance (d) between the nucleons becomes less than $d < \sqrt{\sigma^{in}_{NN}/\pi}$ in the calculation, a collision is considered to take place. Here, σ^{in}_{NN} represents to the inelastic cross section of the nucleon-nucleon collisions. The nucleon collided with other nucleons is called as "wounded nucleon". In the Glauber model, the wounded nucleon is considered to be identical to the normal nucleon, although one might think that the wounded nucleon is different with the normal nucleon. For the realistic calculation of Au + Au collisions at $\sqrt{s_{\rm NN}} = 200$ GeV, the Woods-Saxon parameterization $\rho_A(r)$ in Eq. 2.25 are used with $R_A = 6.38$ fm, $a = 0.54$ fm and the inelastic cross section is $\sigma^{in}_{NN} = 42$ mb. The systematic uncertainties of the Glauber calculations are estimated by changing the parameters and the simulation conditions. The definition of the centrality class is also slightly changed to study the systematic uncertainty. Figure 4.3 and 4.4 show the systematic uncertainties

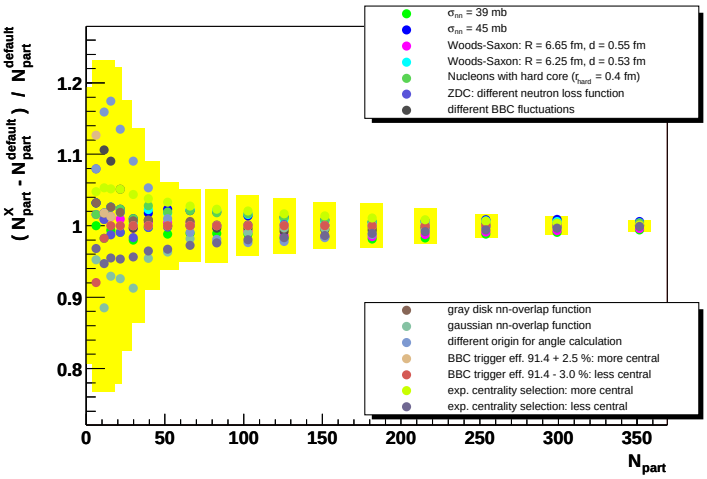

Figure 4.3: Systematic uncertainty of the $N_{\rm part}$.

as a function of $N_{\rm part}$ and $N_{\rm coll}$, respectively. The result of the Glauber calculation is summarized in Tab. 4.1 [106].

4.3 Charged Particle Tracking

Charged particles emitted from nucleus-nucleus collisions pass through the magnetic field and bend along with a plane perpendicular to beam pipe until these particles arrive at the DC. Once these particles reach the DC, these particles go away in straight lines, since there is almost no magnetic field at the outside of the DC.

The DC reconstructs charged particle trajectories using the Combinatorial Hough Transform method (CHT) which is a general algorithm for finding straight line tracks. In the Hough transform, any pairs of the DC hits are mapped into a feature space defined by ϕ and α. The ϕ is the polar angle at the intersection of the track with a reference circle near the mid-point of the DC, and α is the inclination angle of the track at that point relative to the straight line. Figure 4.5 (left) shows a schematic view of these variables. In this coordinate, the DC hit pairs from an actual track make a clear peak in the feature plane, although the random pairs from different tracks result in a flat background. If a track has n hits in the DC, the peak height is $n(n-1)/2$. Figure 4.6 shows an example of hits in a part of the DC in the feature plane (left) and the corresponding hit distribution in the Hough transform feature space (right) [107].

Once a track is found in $\phi - \alpha$ plane, the z-coordinate of the track is determined using the Hough transform with the associated PC1 cluster and the stereo U and V wire informations of the DC. The variable zed is the z-coordinate of the intersection point with the reference radius and the θ is the polar angle between the track and the beam axis (z-axis) in the $r - z$ plane shown in Fig. 4.5 (right). Finally, the reconstructed track is traced back to the event vertex measured by the BBC.

The momentum (p) of a charged particle is determined using its polar angle (θ) and

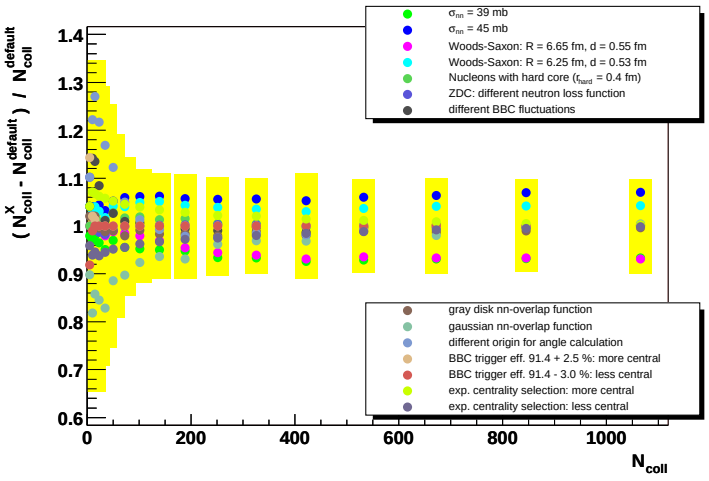

Figure 4.4: Systematic uncertainty of the $N_{\rm coll}$.

Table 4.1: Summary of centrality, b, $N_{\rm part}$, $N_{\rm coll}$ and T_{AA}

Centrality (%)	b (fm)	$< N_{\rm part} >$	$< N_{\rm coll} >$	$< T_{AA} >$ (mb^{-1})
0 - 10	3.2 ± 0.2	325.2 ± 3.3	955.4 ± 93.6	22.75 ± 1.56
10 - 20	5.7 ± 0.3	234.6 ± 4.7	602.6 ± 59.3	14.35 ± 1.00
20 - 30	7.4 ± 0.3	166.6 ± 5.4	373.8 ± 39.6	8.90 ± 0.72
30 - 40	8.7 ± 0.4	114.2 ± 4.4	219.8 ± 22.6	5.23 ± 0.44
40 - 50	9.9 ± 0.4	74.4 ± 3.8	120.3 ± 13.7	2.86 ± 0.28
50 - 60	11.0 ± 0.4	45.5 ± 3.3	61.0 ± 9.9	1.45 ± 0.23
60 - 70	11.9 ± 0.5	25.7 ± 3.8	28.5 ± 7.6	0.68 ± 0.18
70 - 80	13.5 ± 0.5	13.4 ± 3.0	12.4 ± 4.2	0.30 ± 0.10
80 - 92	14.1 ± 0.6	6.3 ± 1.2	4.9 ± 1.2	0.12 ± 0.03
0 - 20	4.4 ± 0.2	279.9 ± 4.0	779.0 ± 75.2	18.55 ± 1.27
20 - 40	8.1 ± 0.4	140.4 ± 4.9	296.8 ± 31.1	7.07 ± 0.58
40 - 60	10.5 ± 0.4	60.0 ± 3.6	90.7 ± 11.8	2.16 ± 0.26
60 - 92	13.0 ± 0.5	14.5 ± 2.5	14.5 ± 4.0	0.35 ± 0.10
minimum bias	9.5 ± 0.4	109.1 ± 4.1	257.8 ± 25.4	6.14 ± 0.45

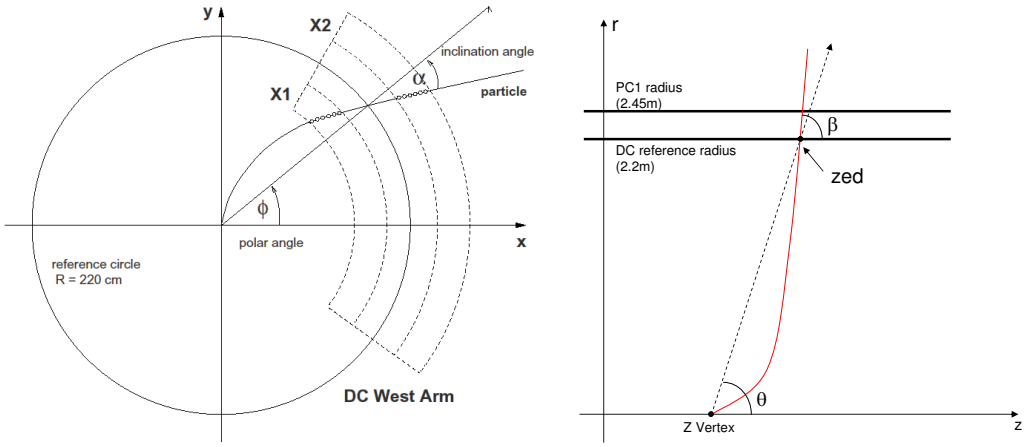

Figure 4.5: (left) The schematic view of a reconstructed track by the DC in the $x - y$ plane. (right) The schematic view of a reconstructed track by the DC in the $r - z$ plane.

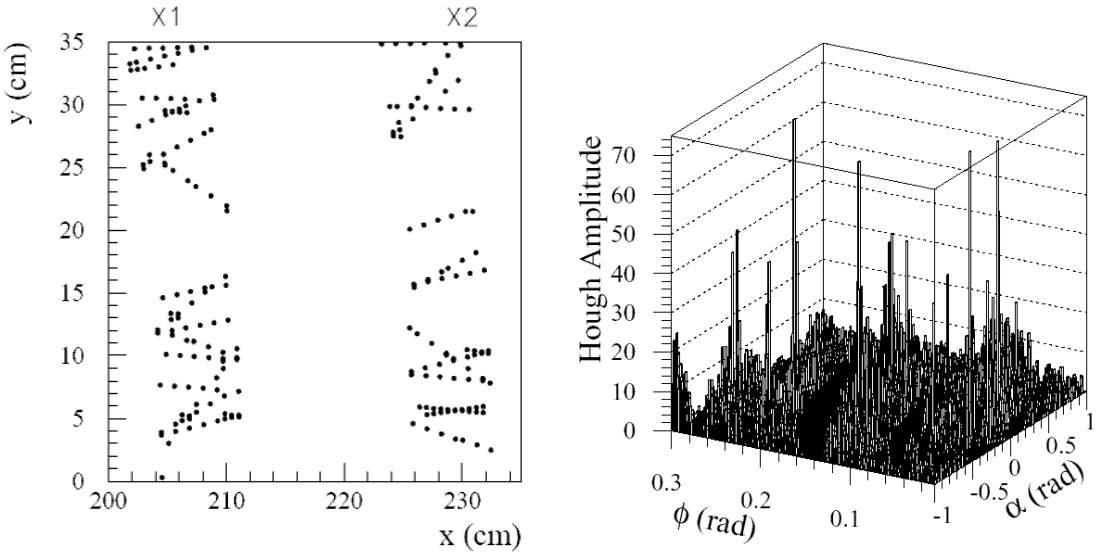

Figure 4.6: (left) The DC hits in the $x-y$ plane. (right) The corresponding hit distribution in the feature space [107].

the inclination angle (α). Especially, the transverse momentum (p_{T}) is approximately expressed as:

$$\alpha \approx \frac{K}{p_{\mathrm{T}}}, \tag{4.7}$$

where $K = 87$ (mrad GeV/c) is the effective field integral between the collision vertex and the DC. Because of the non-uniform shape of the focusing magnetic field, an analytical calculation is not possible for momentum determination. Therefore, the four-dimensional field-integral grid ($f(p, r, \theta_0, z)$) is constructed for momentum reconstruction and for the entire radial extent of the central arms in order to trace the entire trajectory of the track from the event vertex [107]. The parameters in the field grid are: the total momentum of the particle (p), the radius (r), the polar angle of the particle at the vertex (θ_0) and the z coordinate of the vertex (z).

The momentum scale is verified by comparing the known proton mass with the measured value. The mass value of proton is measured using the time of flight information by the TOF. The accuracy of the momentum scale is better than 0.7%. The momentum resolution is directly related to the α resolution:

$$\frac{\delta p}{p} = \frac{\delta \alpha}{\alpha} = \frac{1}{K}\sqrt{\left(\frac{\sigma_{\mathrm{ms}}}{\beta}\right)^2 + (\sigma_\alpha p)^2}, \tag{4.8}$$

where $\delta\alpha$ is the measured angular spread and β is velocity. The momentum resolution is composed from the contribution of the multiple scattering (σ_{ms}) and the contribution of the intrinsic pointing resolution of the DC (σ_α). These values are estimated to be $\sigma_{ms} = 0.61$ (mrad GeV/c) and $\sigma_\alpha = 0.86$ (mrad) using the high energy hadron track in the zero field data [108, 109]. The momentum resolution is finally determined to be $\delta p/p \simeq 0.7\% \oplus 1.0\% \times p$ (GeV/c) [110].

The quality of the reconstructed tracks is defined using the hit informations of the X and the stereo U and V wires and the associated PC1 cluster. The "quality" is a 6 bit variable to describe the track quality. The definition of quality is described in Tab. 4.2.

Table 4.2: Bit definition of the track quality.

bit	decimal	description
0 (LSB)	1	X1 hits used
1	2	X2 hits used
2	4	UV hits used
3	8	UV unique (no hit sharing)
4	16	PC1 cluster used
5 (MSB)	32	PC1 unique (no cluster sharing)

4.3.1 Matching to the Outer Detector

The reconstructed tracks are extended as straight lines and projected into the outer detectors such as the RICH, TOF and EMCal. The inter-detector association of the track is performed by searching for the closest hit in these detector. The closest hit from the track projection point is identified as "associated hit".

The distance in both the ϕ and z direction between the projection point and the associated hit is approximately Gaussian with a width (σ_{match}) expressed as:

$$\sigma_{\mathrm{match}} = \sqrt{\left(\sigma_{\mathrm{det}}^{\mathrm{match}}\right)^2 + \left(\frac{\sigma_{\mathrm{ms}}^{\mathrm{match}}}{p\beta}\right)^2}, \tag{4.9}$$

where $\sigma_{\mathrm{det}}^{\mathrm{match}}$ is the finite detector resolution and $\sigma_{\mathrm{ms}}^{\mathrm{match}}$ is the contribution of the multiple scattering. The mean value of the distribution is tuned to be zero for the detector alignment. The residual distribution between the projection point and the associated hit is referred as the matching distribution. The matching distributions of ϕ and z are independent each other. In this analysis, the widths of the matching distributions of ϕ and z are normalized by their standard deviations, and then these are used for the track selection. This selection of the tracks is called as "matching cut".

4.4 Electron Identification

For electron identification, some variables are measured and calculated from the RICH and the EMCal. In this section, the definition of these variables are described.

4.4.1 Electron ID with RICH

The electron identification (ID) is performed by mainly the RICH described in section 3.4.4. Čerenkov lights emitted by an electron is reflected by the spherical mirror in the RICH and is focused as a ring shape on the PMT arrays of the RICH shown in Fig. 4.7. The hit PMT is defined so that a PMT detects more than 0.1 photo-electrons (N_{pe}).

To determine association of the RICH signal with the reconstructed track, the track is reflected by the spherical mirror and the reflected line is projected onto the PMT arrays of the RICH. If the track is an electron, the reflected line should be projected to the center of a ring formed by hit PMTs. Then, we count the number of hit PMTs (n0) within a association radius (r_{asso}) from the projection point. The association radius (r_{asso}) is ideally 5.9 ± 2.5 cm and depends on both flight path length of the Čerenkov light, refraction index of the radiator (CO_2) and velocity of the electron. Therefore, the range of the association radius is set from 3.4 to 8.4 cm. Using the association with the RICH, four variables for the electron ID are defined as follows:

- n0 − Number of hit PMT within r_{asso}.
- npe0 − Number of photo-electrons in all hit PMTs within r_{asso}. Using number of photo-electrons in single hit PMT i (N_{pe}^{i}), npe0 is expressed as:

$$\mathsf{npe0} \equiv \sum N_{pe}^{i} \tag{4.10}$$

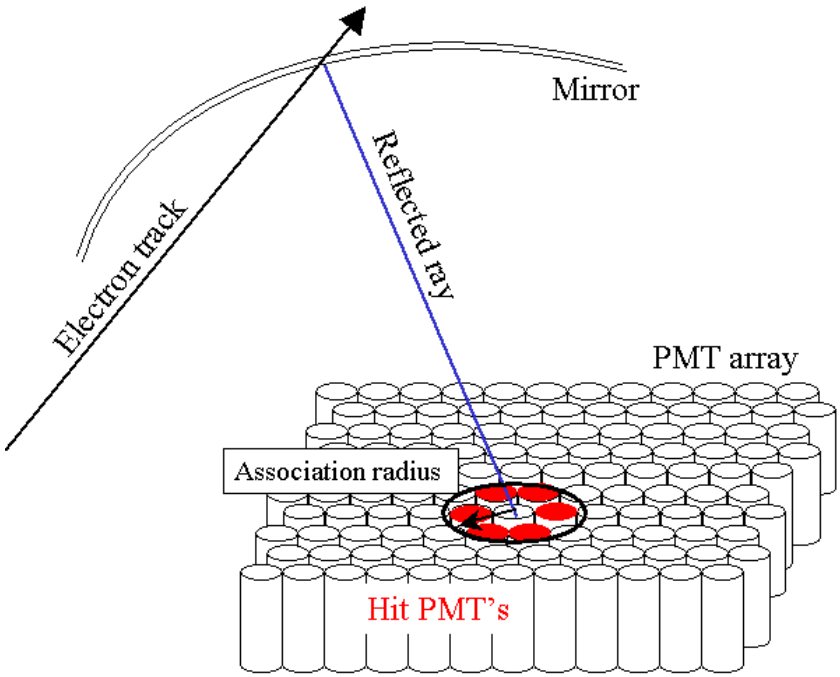

Figure 4.7: The schematic view of the reflected line by the RICH mirrors and hit PMTs in the PMT array with the tight association radius.

- disp – Displacement between a measured ring center (r_m) and a position of track projection. The measured ring center is the weighted average of the hit PMT position (r_i) expressed as:

$$r_m \equiv \frac{\sum r_i \times N_{pe}^i}{\text{npe0}}, \tag{4.11}$$

- chi2/npe0 – χ^2-like variable of the ring shape between the expected and the measured ring. Using the projection point (r_0) and r_i, chi2/npe0 is expressed as:

$$\text{chi2/npe0} \equiv \frac{\sum_{r_{\text{asso}}} (r_i - r_0)^2 \times N_{pe}^i}{\text{npe0}}, \tag{4.12}$$

The variable n0 and npe0 represents the quality of association between the track and the RICH hit. The variable disp and chi2/npe0 indicate the quality of the ring shape reconstructed in the RICH.

4.4.2 Electron ID with EMCal

The EMCal is another main detector for the electron ID which provides the complementary information to the RICH. Four variables measured in the EMCal are used for the electron ID. These four variables are defined as follows:

- emcsdphi_e − Distance in ϕ direction between the track projection position (pemcphi) and the hit position (emcphi) in the EMCal. The hit position is the center of the energy cluster at the surface of the EMCal. The distance is normalized by its standard deviation ($\sigma_{\mathsf{emcdphi}}(p)$). The emcsdphi_e is expressed as :

$$\mathsf{emcsdphi\_e} \equiv \frac{\mathsf{emcphi} - \mathsf{pemcphi}}{\sigma_{\mathsf{emcdphi}}(p)}. \tag{4.13}$$

- emcsdz_e − Distance in z direction between the track projection position (pemcz) and the hit position (emcz) in the EMCal. The distance is normalized by its standard deviation ($\sigma_{\mathsf{emcdz}}(p)$). The emcsdz_e is expressed as :

$$\mathsf{emcsdz\_e} \equiv \frac{\mathsf{emcz} - \mathsf{pemcz}}{\sigma_{\mathsf{emcdz}}(p)} \tag{4.14}$$

- dep − Energy(E) - momentum (p) matching, where E is the energy measured by the EMCal and p is the momentum of the track. Since an electron deposits full energy in the EMCal and the mass of electron is small compared to its momentum, the energy to momentum ratio (E/p) must be about unity. On the other hand, E/p is less than unity for hadron since hadron deposits only a fraction of its full energy. Using its standard deviation ($\sigma_{E/p}(p)$), the dep is expressed as:

$$\mathsf{dep} \equiv \frac{E/p - 1}{\sigma_{E/p}(p)}, \tag{4.15}$$

- emcdt − Time information (t_{EMC}) measured in the EMCal. Using its standard deviation ($\sigma_{t_{\mathrm{EMC}}}(p)$), the emcdt is expressed as:

$$\mathsf{emcdt} \equiv \frac{t_{\mathrm{EMC}}}{\sigma_{t_{\mathrm{EMC}}}(p)}. \tag{4.16}$$

4.4.3 Summary of Electron ID Conditions

The cut values required for the event selection, the track selection and the electron ID are summarized in Tab. 4.3. These required cuts are determined to increase both the statistics and purity of electrons as much as possible.

There are some comments on these cuts. (1) A large fraction of the DC in the West arm is unstable during Run 2. Therefore, the East arm is only used in this analysis. (2) The loose quality value in the DC is required to increase statistics. In electron analysis, the coincidence of hits in the three detectors (the DC, RICH and EMCal) are required to identify electrons. Therefore, possible contaminations from the ghost tracks might be reduced.

Applying these cuts for the electron ID, clean electron samples can be extracted. Figure 4.8 (left) shows the E/p ratio of electron sample for $0.5-0.6$ GeV/c in p_{T}. Here, all of these cuts except the dep cut are required for the electron ID. The red and the blue histograms correspond to the E/p ratio associated with the RICH hit (Real) and background (BG)

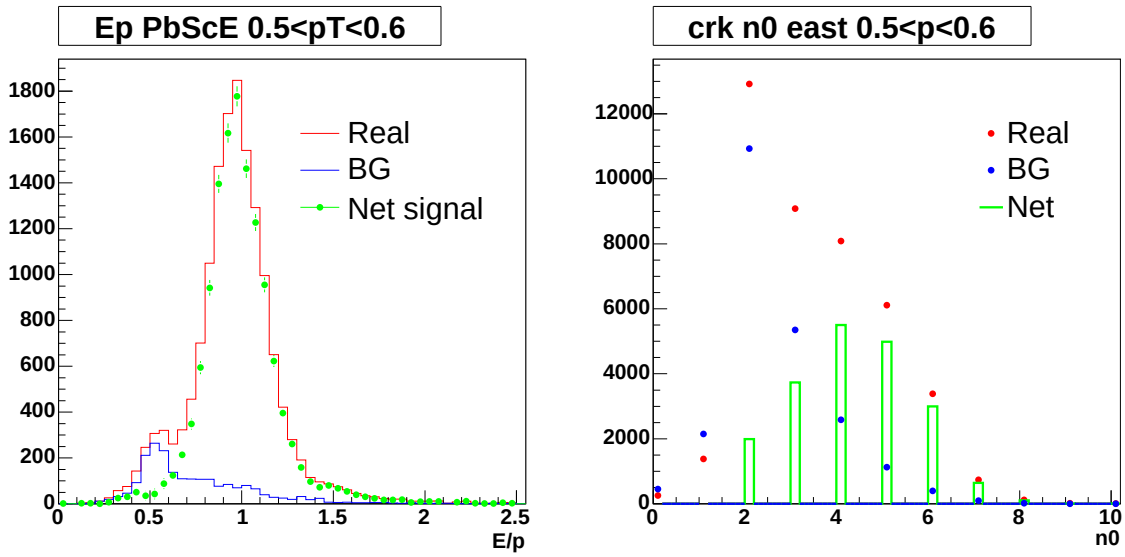

Figure 4.8: (left) Energy to momentum (E/p) ratio (right) n0 distribution in RICH. In both panels, electron signals are clearly seen.

estimated by the "flip and slide" method described in section 4.5. The net signal (green) shows the peak around one. As the other example, the n0 distribution is shown in Fig. 4.8 (right). The red, blue and green histograms show the associated, background and net signal, respectively. These examples indicate that these cuts can work well for the electron extraction from huge hadron backgrounds. After the electron ID cuts are applied, the hadron backgrounds due to the random association still remain as roughly 10% which is described in section 4.5.

Table 4.3: Summary of the required cut values for the electron ID.

Variables	Required cuts
Trigger selection	MB trigger
Collision vertex	$\lvert Z_{\rm BBC}\rvert < 20$ cm
Spectrometer	The East arm
Track quality	Not required
Matching of track	$\sqrt{\mathsf{emcsdphi\_e}^2 + \mathsf{emcsdz\_e}^2} < 2.0$
RICH hit	$\mathsf{n0} \geq 3$
Ring shape	$\mathsf{chi2/npe0} < 10.0$
Matching of ring center	$\mathsf{disp} < 5.0$
Energy momentum matching	$-2.0 < \mathsf{dep} < 3.0$
EMCal time	$\mathsf{emcdt} < 2.0$ or $\mathsf{ttof} < 0.3$

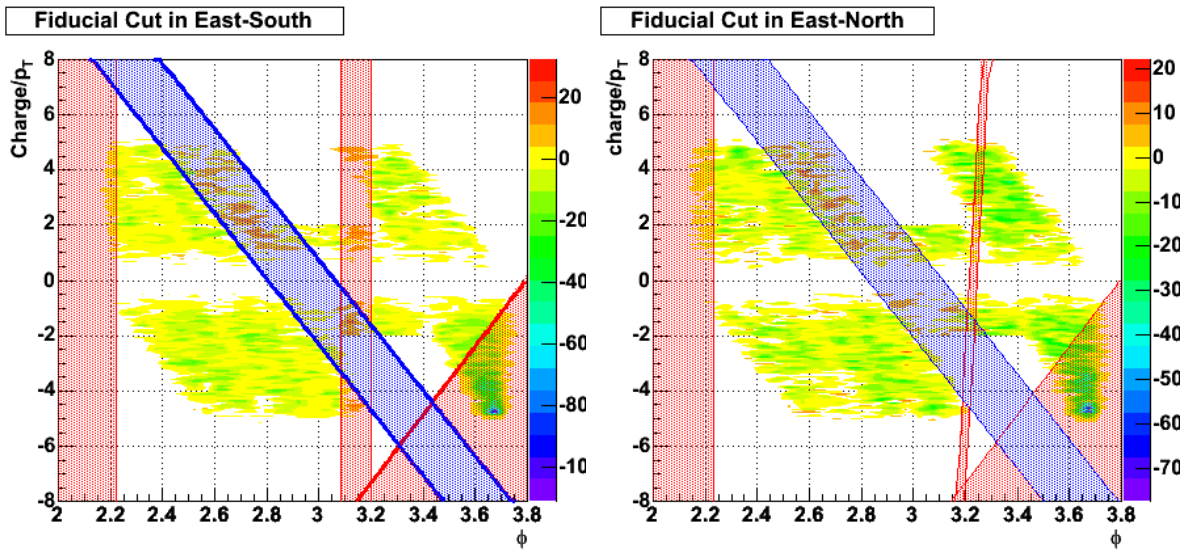

Figure 4.9: Fiducial volume for the East-South (left) and the East-North (right). The red and the blue lines show the boundaries of the fiducial cut E and F, respectively. The shaded areas are removed out in the analysis.

4.4.4 Fiducial Cut

The selection of the fiducial volume is introduced to control the stability of the detector acceptance. There are two definitions of the fiducial volumes which is denoted as "E" and "F". The E fiducial cut is for removing the difference of the detector acceptance between the data with and without the photon converter. These two data sets are compared to extract non-photonic electrons described in section 4.10.1. The F fiducial cut is for removing the discrepancy of the acceptance between the real data and the simulation.

These fiducial volumes are defined in the plane of "charge/p_{T} vs ϕ" at the DC. The ϕ is an azimuthal angle of the reconstructed track at the DC. Since the south and north side of the DC are independent detectors, the fiducial volumes are defined for each side of the East-South and the East-North, respectively. The definitions of the fiducial cuts E and F for the East-South and the East-North are summarized in Tab. 4.4. Figure 4.9 shows the fiducial volume in the plane of "charge/p_{T} vs ϕ" for the East-South (left) and the East-North (right), respectively. The shaded areas shown in Fig. 4.9 are removed out by these fiducial cuts. An additional fiducial cut for a sector one of the PbGl EMCal are applied so that the tracks with p_{T} less than 0.5 GeV/c are removed. Because the ϕ distribution in the real data is different with that in the simulation.

In order to verify whether the fiducial cut works, the ϕ distribution of electrons between the data with that without the converter is compared. Figure 4.10, 4.11, 4.12 and 4.13 show the phi distributions of e^+ and e^- for the East-South and the East-North, respectively. In these figure, the blue and the red histograms correspond to the data with and without the converter. From the comparisons, the acceptance between the data with and without the converter are in good agreement.

Table 4.4: Summary of the fiducial cuts E and F for the East-South and the East-North.

Fiducial cut for the East South	
E	charge/p_{T} > -46.804 + 12.338 $\times\phi$
E	$2.22 < \phi < 3.085$
E	$3.20 < \phi$
F	charge/p_{T} > 36.175 -11.81 $\times\phi$
F	charge/p_{T} < 33.26 - 11.86 $\times\phi$

Fiducial cut for the East North	
E	charge/$p_{\mathrm{T}} > -46.804 + 12.338 \times \phi$
E	charge/$p_{\mathrm{T}} < -551.5 + 170.0 \times \phi$
E	charge/$p_{\mathrm{T}} > -546.5 + 170.0 \times \phi$
E	$\phi > 2.23$
F	charge/$p_{\mathrm{T}} > 36.9 - 11.85 \times \phi$
F	charge/$p_{\mathrm{T}} < 33.357 - 11.809 \times \phi$

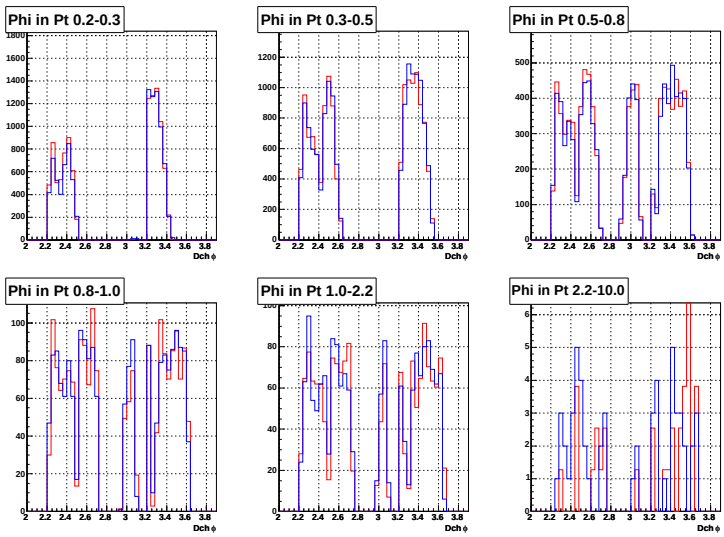

Figure 4.10: ϕ distributions of e^+ in the East-South. The red and the blue histograms correspond to the data with and without the converter.

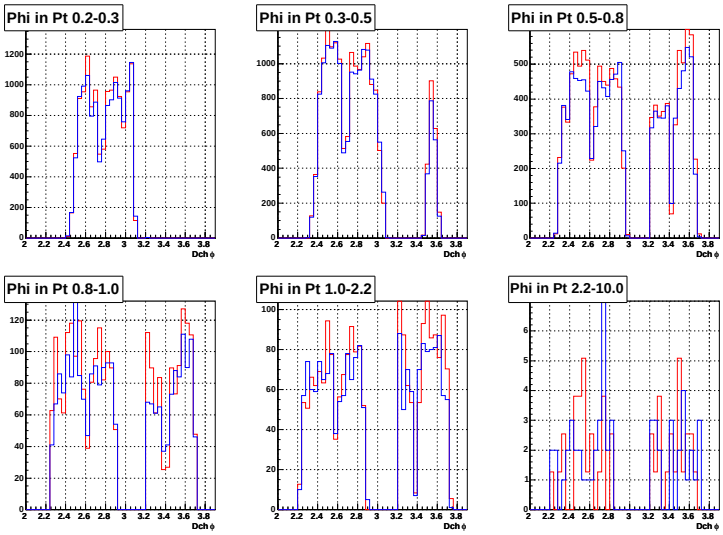

Figure 4.11: ϕ distributions of e^- in the East-South. The red and the blue histograms correspond to the data with and without the converter.

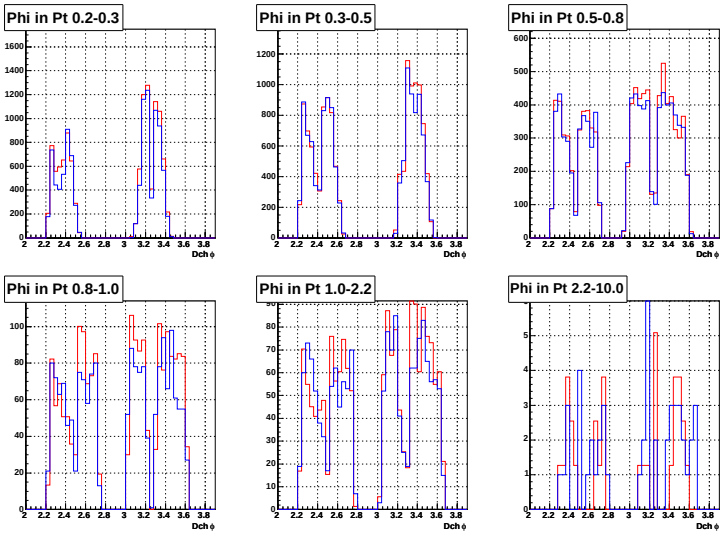

Figure 4.12: ϕ distributions of e^+ in the East-North. The red and the blue histograms correspond to the data with and without the converter.

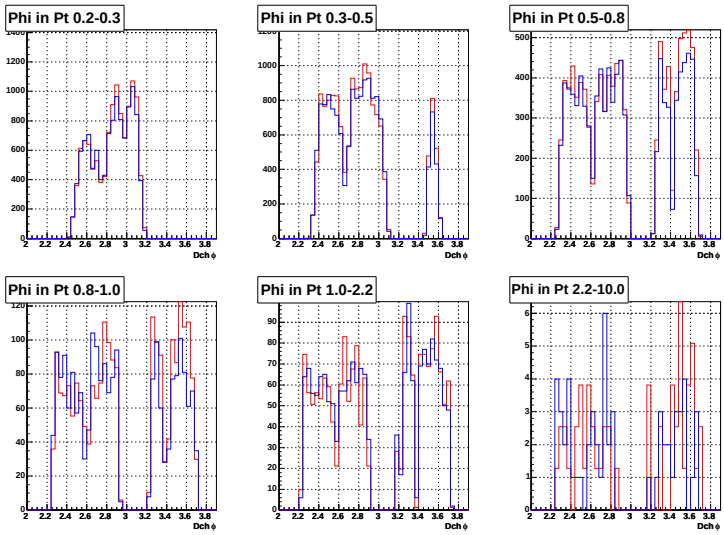

Figure 4.13: ϕ distributions of e^- in the East-North. The red and the blue histograms correspond to the data with and without the converter.

4.5 Hadron Background

A small fraction of the backgrounds from the hadron contamination remains in the electron samples after the electron ID cuts is applied. The origin of the mis-identified electron samples is mainly due to accidental association of the reconstructed track with the hit in the RICH. These backgrounds are estimated by an event mixing method. The event mixing is performed in software by flipping the z coordinate of the track in a same event, and then searching for the association of the flipped track with the RICH hit. For example, if a track has 45 cm of z-coordinate, the z-value of the flipped track is -45 cm. However, a flipped track near $z = 0$ is almost same with its original track. To treat such a track, the z component of a track within $|z| < 35$ cm is slided toward the opposite side of the z coordinate. If a track has 20 cm in z, the z value of the slided track is -15cm ($= 20 - 35$ cm). Since these flipped and slided tracks provide only random association with the RICH hit, the random hadron backgrounds are statistically estimated. This event mixing method is called as "flip and slide method". Figure 4.14 shows the schematic diagram of the flip and slide method. The backgrounds estimated by the method are statistically subtracted from the reconstructed electrons to obtain the net signals.

Figure 4.15 shows E/p ratios for four p_{T} ranges. The red and the blue points show the total and background (BG) electron candidates. The green histograms represent the net signals obtained by the subtraction of the background from the total electron candidates. From the figure, by comparing the total and background electron candidates, the backgrounds from random hadron association are estimated to be about 10%.

After the subtraction of the random backgrounds, the other background components still remain which are shown as a lower tail of the E/p distributions in Fig. 4.15. These backgrounds are electrons from K_{e3} decays and photon conversions that occur far from the collision vertex. These background electrons reconstructs with higher momentum

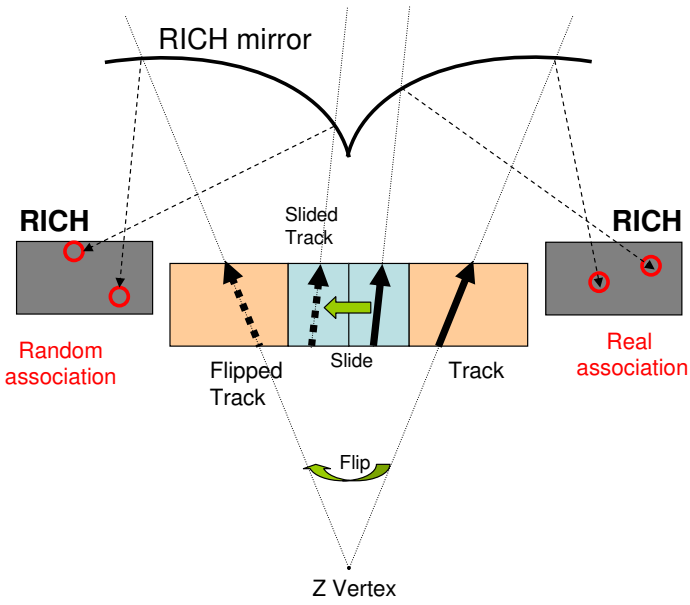

Figure 4.14: Schematic view of the flip and slide method.

compared with its actual momentum due to the tracking algorithm. Therefore, the E/p ratio of the background electrons has lower value. These background components are studied using a GEANT simulation [99] of the PHENIX detector described in section 4.10.6.

4.6 Run Selection

The dead and/or the hot area of the detector is possibly changed during the Run 2 operation period. The run-by-run detector condition is studied to verify whether the data used in this analysis is taken with the stable condition. Figure 4.16 shows the run dependence of the inclusive electron yield for six p_{T} classes, which correspond to 0.2-0.3, 0.3-0.5, 0.5-0.8, 0.8-1.0, 1.0-2.2 and $p_{\mathrm{T}} < 2.2$ GeV/c, respectively. In these figures, the red and the blue points correspond to the positron and the electron yield, respectively.

The photon converter has been installed during a part of the run period. The run periods with and without the converter are called as the converter run and the non-converter run respectively. In Fig. 4.16, the electron yield in the converter run is constantly higher than that in the non-converter run. On the other hand, the electron yield in the non-converter run is less stable than that in the converter run. Thus, a good run period in the non-converter run is used in this analysis.

The actual run lists for the converter run and the non-converter run are summarized in Tab. 4.5. The data statistics for the converter run and the non-converter run are shown in Tab. 4.6. The minimum bias events are subdivided for five centrality classes, 0-10%, 10-20%, 20-40%, 40-60% and 60-92%, respectively.

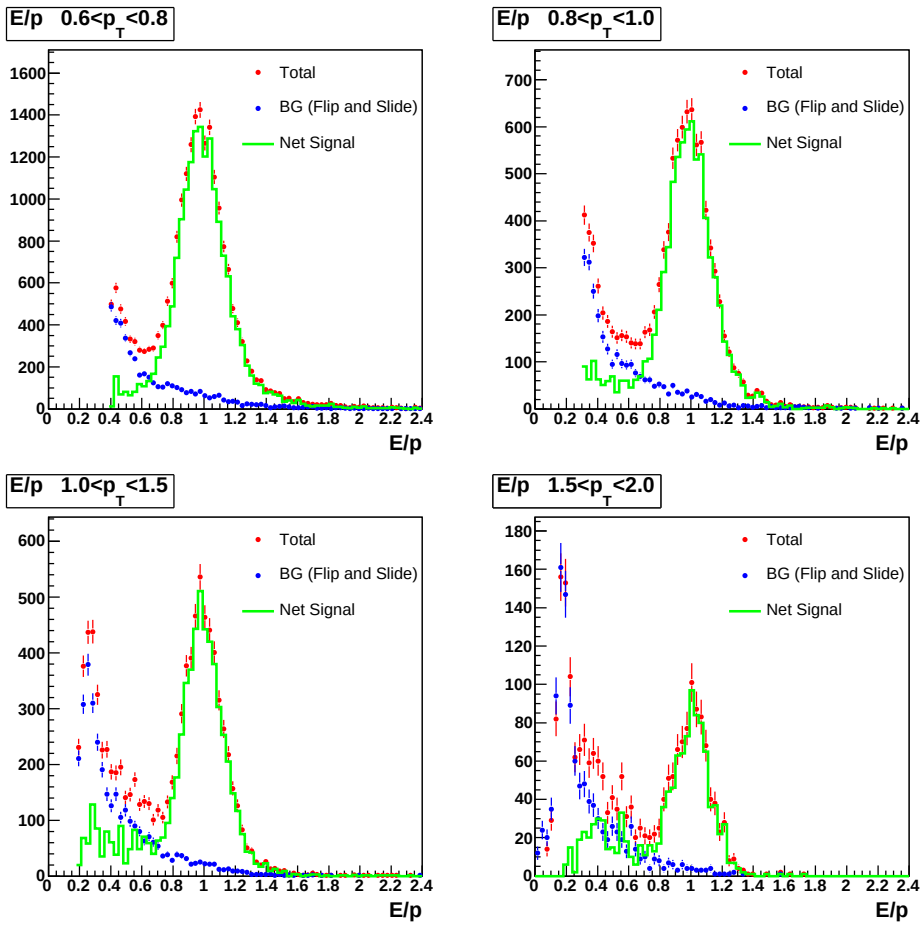

Figure 4.15: E/p distributions for four p_{T} ranges. The net signal in each panel is extracted by subtracting the backgrounds (BG) from the total electron candidates (Total).

Table 4.5: Summary of the run lists for the converter run and the non-converter run.

the converter run								
28623	28625	28627	28632	28718	28749	28750	28751	28761
28765	28768	28775	28777	28781	28791	28794	28795	28798
28902	28903	28956	28958	28961	28962	28966	28968	28971
28972	28973	29014	29015	29016	29017	29036		

the non-converter run								
29116	29146	29171	29178	29179	29183	29184	29185	29186
29212	29213	29255	29267	29268	29368	29372	29380	29386
29392	29393	29401	29404	29445	29446	29454	29459	29461
29510	29512	29514	29515	29529	29534	29537	29561	29562
29563								

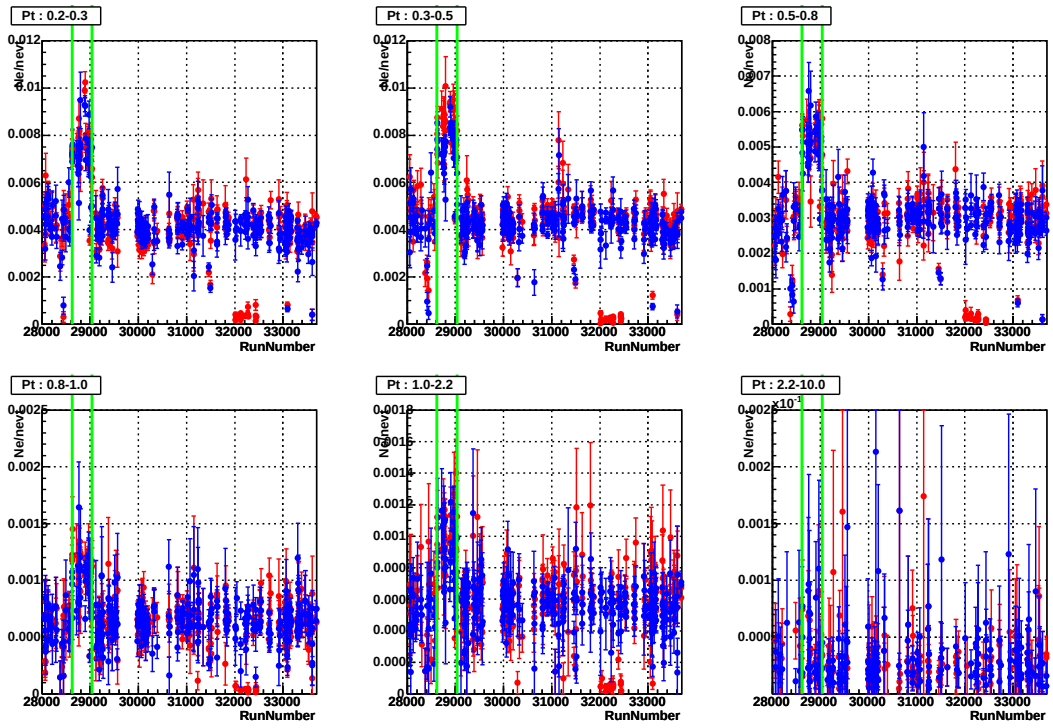

Figure 4.16: The run dependence of the raw electron yield for East-South. The red and the blue points correspond to the positron and the electron yield, respectively.

Table 4.6: Summary of event samples for the converter run and the non-converter run.

Centrality	non-converter run	converter run
Minimum bias	2,544,577	2,253,413
0-10 %	247,060	220,410
10-20 %	280,233	248,604
20-40 %	553,849	490,245
40-60 %	562,982	497,595
60-92 %	900,453	796,559

4.7 Raw Yield of Inclusive Electrons

Applying the electron ID cut described in section 4.4.3, the raw yields of inclusive electrons are obtained for both the converter run and the non-converter run. The backgrounds from the hadron contaminations estimated by the flip and slide method are subtracted statistically. Figure 4.17 shows the raw yield of inclusive electrons as a function of p_{T} in minimum bias Au + Au collisions. The blue and the red histograms correspond to the yield in the converter run and the non-converter run, respectively. They are normalized by their number of analyzed events independently. Since additional photon conversions take place in the converter run, the blue histogram is always higher than the red one. The spectra become closer at high p_{T}. This indicates that a fraction of photonic electrons becomes smaller at higher p_{T}. Figure 4.18 shows the raw yield of inclusive electrons for 0-10%, 10-20%, 20-40%, 40-60% and 60-92% centrality classes, respectively. From the comparison of the electron spectra with and without the converter, we can separate the photonic electron and the non-photonic electron components. The details of the analysis is described in section 4.10.5.

4.8 Detector Response in Simulation

The geometrical acceptance and the electron ID efficiencies are estimated using the Monte Carlo simulations of the PHENIX detector based on the GEANT simulator [99]. This detector simulator is called as "PISA". In order to calculate the acceptance and the electron ID efficiency, the detector responses in the simulation should be the same with those in the data. For the electron analysis, the background is mainly electrons from photon conversions. Thus, the material budget in the simulation is crucial to estimate the background. In this section, the detector responses and the material budget in the simulation are described.

4.8.1 Comparison between Real Data and Simulation

To study the detector responses in the PISA simulation, all the electron ID variables are compared with that in the real data. If the variable in the simulation is different from that in the real data, the simulation is tuned to reproduce the real data accurately. These comparisons are performed using the electron samples. To select the electron samples, all the electron ID cuts except the compared variable are required (to be the same as the real data). Table 4.7 shows the summary of the required cuts for the comparison of each variable. In Tab. 4.7, the symbol "○" and "×" mean whether the cut is required or not required, respectively. For example, when we compare the RICH variable n0 between the simulation and the real data, the electron sample is selected by emcsdphi_e, emcsdz_e, dep and emcdt. It should be noted that a tighter cut in emcsdz_e is required for the comparison of emcsdphi_e, since the two dimensional matching cut variables are independent each other.

Figure 4.19 shows the comparisons of the variables between the real data and the simulation. The plots from the top-left to the bottom-right in Fig. 4.19 correspond to the emcsdphi_e, emcsdz_e, n0 and dep, respectively. These distributions are normalized by

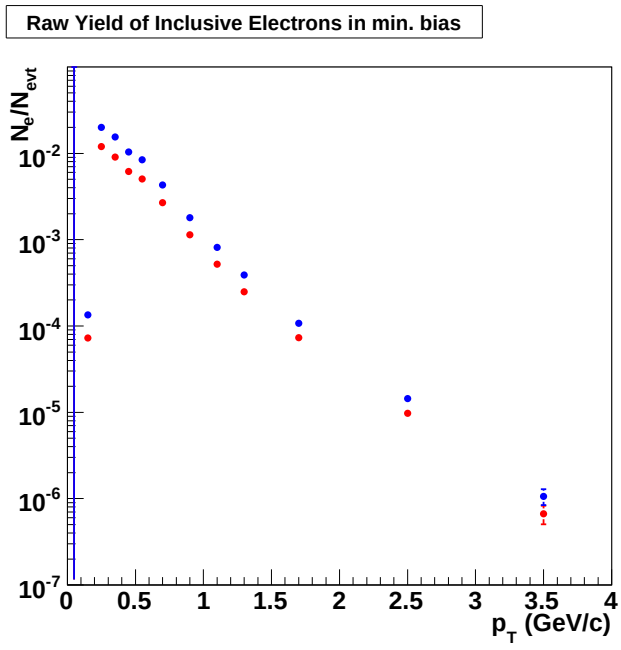

Figure 4.17: The raw yield of inclusive electrons as a function of p_{T} in minimum bias $\mathrm{Au}+\mathrm{Au}$ collisions. The blue and the red points represent the electron yields in the converter run and the non-converter run, respectively.

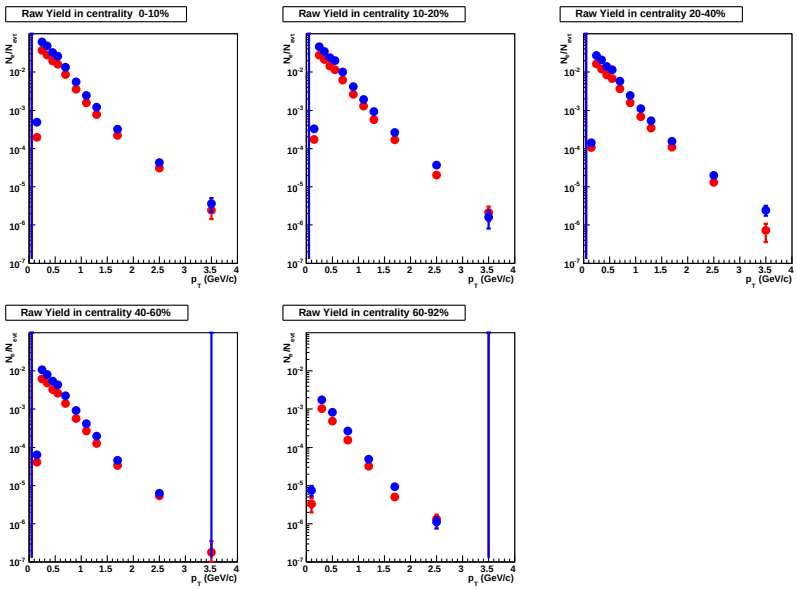

Figure 4.18: The raw yield of inclusive electrons as a function of p_{T}. The blue and the red points represent the electron yields in the converter run and the non-converter run. These six panels correspond to the six centrality classes, 0-10%, 10-20%, 20-40%, 40-60% and 60-92%, respectively.

the number of the entries. These comparisons indicate that the detector responses in the simulation are in good agreement with the read data. The detailed comparisons of the individual electron ID variables are described in Appendix A.1.

Table 4.7: Summary of the required cuts for the comparison between the real data and the simulation. The symbol "○" and "×" mean whether the cut is required or not required, respectively. The variables, sdphi and sdz, are shortened forms of emcsdphi_e and emcsdz_e, respectively.

Applied Cut	Compared Variables					
	sdphi(z)	n0	chi2/npe0	disp	dep	emcdt
$\sqrt{\text{sdphi}^2 + \text{sdz}^2} < 2$	× (sdz < 1)	○	○	○	○	○
n0 ≥ 3	○	×	○	○	○	○
chi2/npe0 < 10	○	×	×	×	○	○
disp < 5	○	×	×	×	○	○
$-2 <$ dep	○	○	○	○	×	×
emcdt < 2	○	○	○	○	○	×

4.8.2 Material Budget in Simulation

Photon conversions are the main source of photonic electron backgrounds. Most of photon conversions occur in the beam pipe and the MVD. If photon conversions in the beam pipe and the MVD are accurately modeled in the PISA simulation, photonic electron backgrounds can be correctly subtracted using the converter method described in section 4.10.1. Therefore, it is important to verify whether the material budget of the PHENIX detector in the simulation is the same as the real one.

The material budget of the PHENIX detector are studied using the yield of electron-positron (e^+e^-) pairs from photon conversions. Figure 4.20 shows the invariant mass distribution of e^+e^- pairs. The red and the black points correspond to the real and the combinatorial background pairs, respectively. The combinatorial backgrounds are estimated by an event mixing method. There are 3 peaks at 5, 15 and 75 MeV/c^2 in Fig. 4.20 which are artificially produced by the tracking algorithm. Since the track reconstruction algorithm assumes that all tracks originate from the collision vertex, the electrons produced by photon conversions at the point far from the vertex are reconstructed with incorrect momenta. Figure 4.21 shows the schematic view of the mis-reconstruction of the conversion pair. As a result, the reconstructed mass of pair is shifted from its original value, even though its original value is very close to zero. This shift is approximately proportional to the magnetic field integral. This indicates that these artificial peaks can be used to identify the positions where the photon conversions occur. The first peak around 5 MeV/c^2 is mainly from π^0 Dalitz decays, the second peak around 15 MeV/c^2 is from photon conversions at the beam pipe and the MVD except the outer shell and the third peak around 75 MeV/c^2 are from the conversions at the MVD outer shell, respectively.

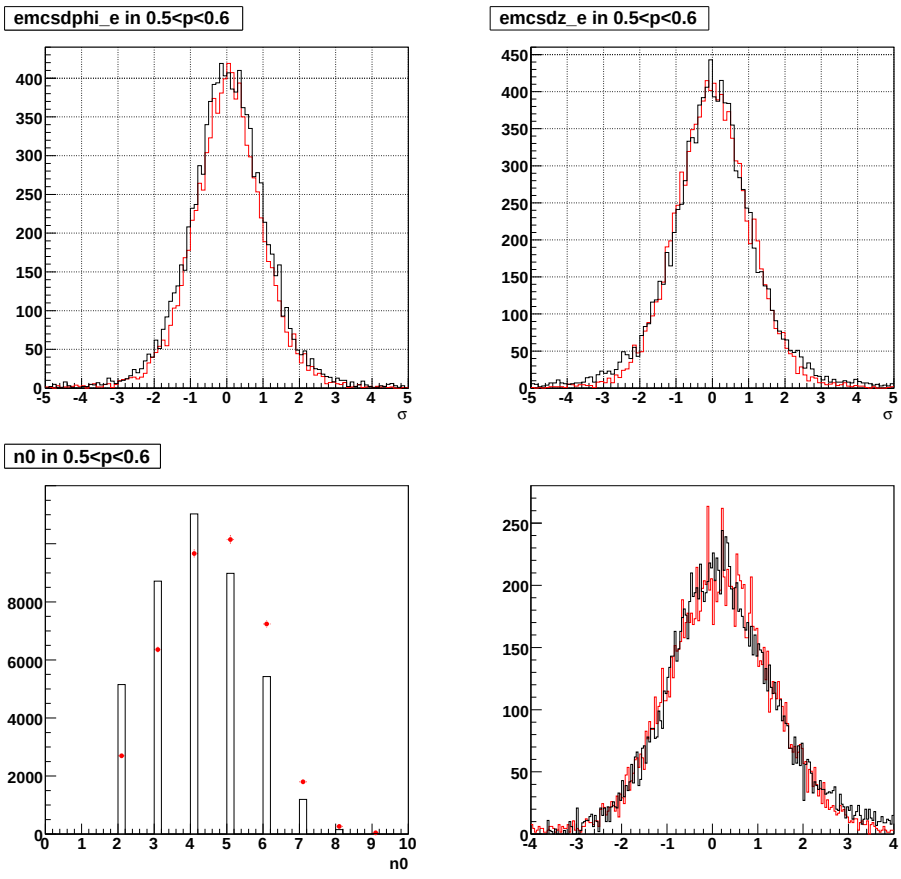

Figure 4.19: Comparisons of the detector response between the real data and the simulations. The detector response of emcsdphi_e (top-left), emcsdz_e (top-right), n0 (bottom-left) and dep (bottom-right) are shown, respectively. The black and red lines correspond to the real data and the simulation.

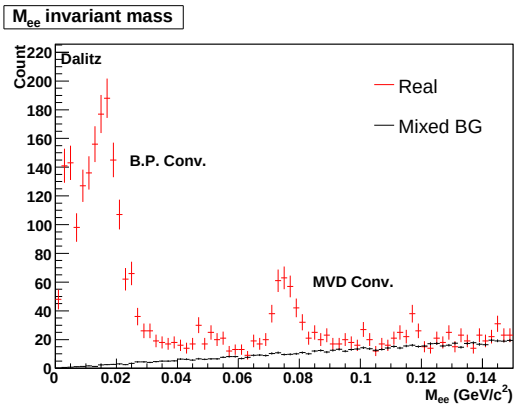

Figure 4.20: Invariant mass distribution of e^+e^- pairs. The red and black points correspond to the real and the combinatorial background pairs estimated by an event mixing method.

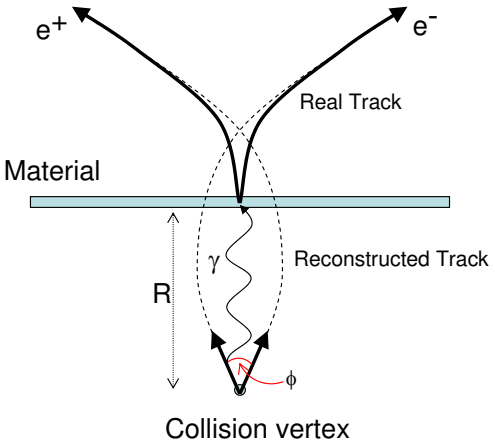

Figure 4.21: Schematic view of track reconstruction. The electrons produced at $R > 0$ are reconstructed with incorrect momenta. This results in the fake invariant mass of the reconstructed conversion pairs.

Figure 4.22 show the invariant mass distribution of e^+e^- pairs in the real data (left) and the simulation (right). The combinatorial backgrounds have been already subtracted. The red and blue histograms correspond to the pair yield in the non-converter run and the converter run, respectively. In both the real data and the simulation, the peak at 75 MeV/c^2 in the converter run is much higher than that in the non-converter run, since the converter increases photon conversions around the MVD outer shell. Here, π^0 simulations are used for the pair analysis. The conditions of π^0 simulations are described in section 4.10.2.

In order to compare the material budget between the real data and the simulation quantitatively, we define the following variables:

- $N_{\rm BP}$: the pair yield for $M_{e^+e^-} < 40$ MeV/c^2 where the Dalitz decays (0.8% X_0 equivalent) and the conversions at the beam pipe (0.29% X_0) and the MVD (0.9% X_0) except the outer shell are included,

- $N_{\rm MVD}$: the pair yield for $60 < M_{e^+e^-} < 100$ MeV/c^2 where the conversions at the MVD outer shell (0.17% X_0) and the converter (1.7% X_0) are included,

- $R_{\rm material}$: the ratio of $N_{\rm MVD}$ to $N_{\rm BP}$.

$$R_{\rm material} = \frac{N_{\rm MVD}}{N_{\rm BP}}. \tag{4.17}$$

where X_0 is the radiation length.

The converter gives a good reference to study the amount of the material. Since the converter in the simulation is implemented using the measured thickness and the

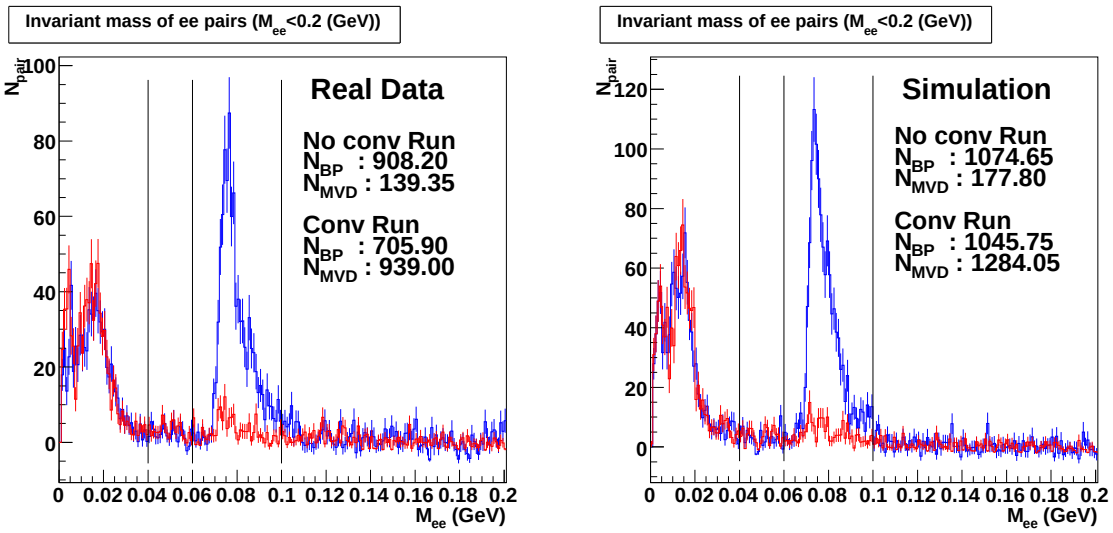

Figure 4.22: Invariant mass distribution of e^+e^- pairs in the real data (left) and the simulation (right). The red and blue histogram correspond to the non-converter and the converter run, respectively.

measured weight, $N_{\rm MVD}$ in the simulation should be the same with that in the real data in the converter run. Therefore, $R_{\rm material}$ shows the accurate information of $N_{\rm BP}$ compared with $N_{\rm MVD}$. This means that the material amount of both the beam pipe and the MVD except the outer shell can be studied by comparing $R_{\rm material}$ between the real data and the simulation.

Before the $R_{\rm material}$ calculation, the $p_{\rm T}$ distribution of the pairs between real data and simulation are compared since the invariant mass distribution is sensitive to the $p_{\rm T}$ spectrum of the pairs, Figure 4.23 shows the $p_{\rm T}$ distributions of the pairs in $0-40$ (left) and $60-100$ MeV/c^2 (right) in the converter run. The red histogram corresponds to the real data, and the black, the green, the blue, the magenta and the light blue histograms correspond to π^0 simulation with $p_{\rm T}$ threshold of 0.0, 0.6, 1.0, 1.5 and 2.5 GeV/c. In both figures, the shape of the $p_{\rm T}$ distribution in the real data is well reproduced by the simulation above each $p_{\rm T}$ threshold. From the comparison of $p_{\rm T}$ distribution, we decide to use two sets of the simulation data with the $p_{\rm T}$ threshold of 0.0 and 0.6 GeV/c. For $R_{\rm material}$ calculation, we select the pairs with $p_{\rm T} > 0.7$ GeV/c.

In addition, in order to increase the statistics of $N_{\rm BP}$ in the simulation, $N_{\rm BP}$ in the non-converter run of the simulation is combined with that in the converter run of the simulation. But, it is not so simple to combine these $N_{\rm BP}$. In the converter run, electrons emitted inside the converter suffers the radiative energy loss in the converter. This blocking effect modifies the invariant mass distribution within $M_{e^+e^-} < 40$ MeV/c^2 in the converter run. On the other hand, this blocking effect does not appear in the non-converter run. For this reason, the mass within $M_{e^+e^-} < 40$ MeV/c^2 in the converter run is slightly smaller than that in the non-converter run. This effect is shown in both Fig. 4.22 (left) and (right). Therefore, the blocking effect for the pair yield needs to be taken into account when the $N_{\rm BP}$ for the converter and non converter run are combined.

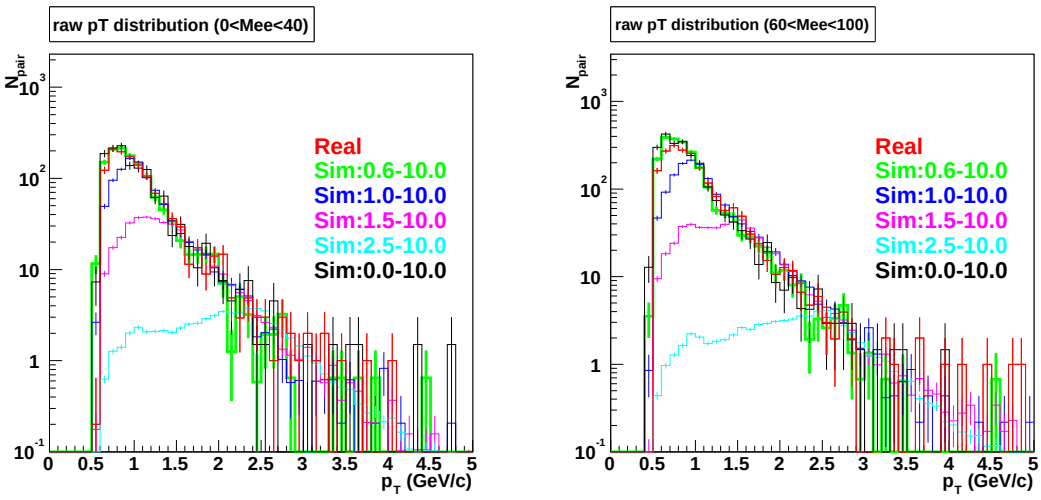

Figure 4.23: Raw p_{T} distribution of e^+e^- pairs from $M_{e^+e^-} < 40$ MeV (left) and $60 < M_{e^+e^-} < 100$ MeV (right). Red histogram shows real data, and the others are a set of simulation data

The efficiency of the blocking effect $\varepsilon^{\mathrm{pair}}_{\mathrm{block}}$ for the pair yield is estimate by the simulation as follows:

$$\varepsilon^{\mathrm{pair}}_{\mathrm{block}} = \frac{N^{\mathrm{noconv}}_{\mathrm{BP}}}{N^{\mathrm{conv}}_{\mathrm{BP}}}, \tag{4.18}$$

where $N^{\mathrm{noconv}}_{\mathrm{BP}}$ and $N^{\mathrm{conv}}_{\mathrm{BP}}$ are correspond to N_{BP} in the non-converter run and the converter run, respectively. The blocking effect of the pair is obtained to be $\varepsilon^{\mathrm{pair}}_{\mathrm{block}} = 1.068$. By using this $\varepsilon^{\mathrm{pair}}_{\mathrm{block}}$, N_{BP} is combined as.

$$N_{\mathrm{BP}} = \frac{1}{2} \cdot (N^{\mathrm{conv}}_{\mathrm{BP}} + 1/\varepsilon^{\mathrm{pair}}_{\mathrm{block}} \cdot N^{\mathrm{noconv}}_{\mathrm{BP}}). \tag{4.19}$$

Table 4.8 shows N_{BP} and N_{MVD} in the real data and the simulation. After the N_{BP} and N_{MVD} are normalized by number of events, R_{material} is calculated and compared between the real data and the simulation. The results are summarized in Tab. 4.9. As a result, the material budget in the simulation is found to be consistent with that in the real data within statistical uncertainty ($99.8\% \pm 4.2\%$). This value is obtained from the double ratio of $R^{\mathrm{real}}_{\mathrm{material}}$ to $R^{\mathrm{sim}}_{\mathrm{material}}$.

The another double ratio is calculated using the pairs with $p_{\mathrm{T}} > 0.9$ GeV/c. That double ratio with $p_{\mathrm{T}} > 0.9$ GeV/c is found to be $101.0\% \pm 5.33\%$. The difference of these two values is 1.2% (101.0%/99.8%). We assigned 4.4% ($= \sqrt{(4.2\%)^2 + (1.2\%)^2}$) for systematic uncertainty of the material budget.

Table 4.8: Summary of $N_{\rm BP}$ and $N_{\rm MVD}$ in the non-converter run and the converter run.

Real data			
dataset	$N_{\rm evt}$	$N_{\rm MVD}$	$N_{\rm BP}$
noconv.	2544590	226 $\pm$ 18.87	1320.75 $\pm$ 36.89
conv.	2253420	1532.4 $\pm$ 42.50	1110.3 $\pm$ 34.66
π^0 simulation			
	$N_{\rm evt}$	$N_{\rm MVD}$	$N_{\rm BP}$
noconv. ($p_{\rm T} \geq 0.0$)	667129	151.7 $\pm$ 13.51	801 $\pm$ 28.47
noconv. ($p_{\rm T} \geq 0.6$)	666825	308.6 $\pm$ 19.77	1808.8 $\pm$ 42.80
conv. ($p_{\rm T} \geq 0.0$)	667328	1057.3 $\pm$ 34.27	740.25 $\pm$ 27.83
conv. ($p_{\rm T} \geq 0.6$)	666714	2349.65 $\pm$ 51.22	1703.4 $\pm$ 42.25

Table 4.9: Summary of the material amounts in real data and simulation.

dataset	$N_{\rm MVD}$	$N_{\rm BP}$	$R_{\rm material}$
sum of real data	1532.4 $\pm$ 42.45	1101.8 $\pm$ 22.94	1.391 $\pm$ 0.0482
sum of sim. with $p_{\rm T} > 0.0$	1057.3 $\pm$ 34.27	745.46 $\pm$ 19.25	1.418 $\pm$ 0.0588
sum of sim. with $p_{\rm T} > 0.6$	2349.65 $\pm$ 51.22	1698.14 $\pm$ 29.07	1.384 $\pm$ 0.0384
combined the 2 sim. set			1.394 $\pm$ 0.0321
Double ratio ($R^{\rm real}_{\rm material}/R^{\rm sim}_{\rm material}$)			0.998 $\pm$ 0.042

4.9 Correction

4.9.1 Acceptance Correction

The measured electron yield is smeared by the detection efficiency of the PHENIX detector. In order to obtain the true invariant yield, the acceptance and the detector efficiency needs to be corrected. The acceptance correction factor ($\varepsilon_{\rm acc}$) is composed from the geometrical acceptance($\varepsilon_{\rm geom}$), the track reconstruction efficiency ($\varepsilon_{\rm track}$) and the electron ID efficiency ($\varepsilon_{\rm eID}$) expressed as:

$$\varepsilon_{\rm acc} = \varepsilon_{\rm geom} \times \varepsilon_{\rm track} \times \varepsilon_{\rm eID}. \tag{4.20}$$

These efficiencies are determined simultaneously using the PISA simulation with single electron and position inputs. In the PISA simulation, the 1 M single electron and positron events are generated with flat $p_{\rm T}$ slope up to 10 GeV/c, $|y| < 0.6$, 2π in azimuth and $|z| < 30$ cm. The correction factor ($\varepsilon_{\rm acc}$) is determined as follows:

$$\varepsilon_{\rm acc} = \frac{\text{Measured electrons with eID cut}}{\text{Input electrons}} \times 1.2, \tag{4.21}$$

where a factor 1.2 is a normalization factor of the input electrons to unit rapidity (0.6/0.5).

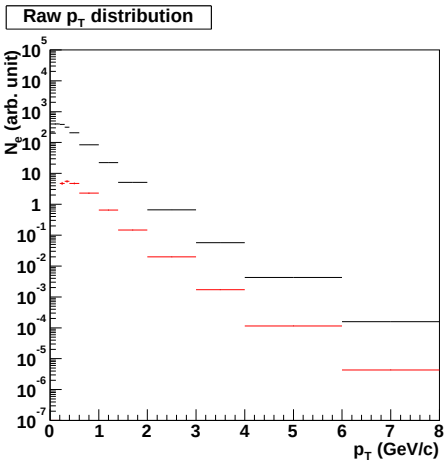

Figure 4.24: p_{T} distribution of electrons. The black and the red histograms correspond to the input and the reconstructed electrons, respectively.

Table 4.10: The parameters for the electron spectrum

p0 (GeV/c)	2.329
p1	-14.30

In order to determine the p_{T} dependence of $\varepsilon_{\mathrm{acc}}$, the p_{T} slope of the input and measured electrons is modified using a p_{T} weight of electron spectrum which is previously measured in Au + Au collisions at $\sqrt{s_{\mathrm{NN}}} = 200$ GeV [111]. The p_{T} spectrum of electrons is parameterized as follows:

$$E\frac{dN_e^3}{dp^3} \propto f(p_{\mathrm{T}}) = \left(1 + \frac{p_{\mathrm{T}}}{p0}\right)^{p1}, \tag{4.22}$$

where $p0$ and $p1$ are parameters summarized in Tab. 4.10. Figure 4.24 shows the raw p_{T} distributions of input and reconstructed electrons in the simulation. These p_{T} shapes are already modified by the p_{T} weight.

The efficiencies $\varepsilon_{\mathrm{acc}}$, $\varepsilon_{\mathrm{geom}}$, $\varepsilon_{\mathrm{track}}$ and $\varepsilon_{\mathrm{eID}}$ are determined by the PISA simulation. Figure 4.25 shows the p_{T} dependence of the efficiencies for e^+ and e^- at the East-South and the East-North, respectively. The black and the red histograms (from top 2 histograms in each panel) show the pure geometrical acceptance before and after applying the fiducial cut. Those are calculated assuming what the detectors efficiency is 100%. The green and black (thick) histograms show the efficiencies of $\varepsilon_{\mathrm{geom}} \times \varepsilon_{\mathrm{track}}$, $\varepsilon_{\mathrm{geom}} \times \varepsilon_{\mathrm{track}} \times \varepsilon_{\mathrm{eID}}$. These efficiencies are determined using only 5 σ matching cut at the EMCal and all the electron ID cuts, respectively.

The obtained electron ID efficiency ($\varepsilon_{\mathrm{eID}}$) is checked and confirmed by the real data. The electron ID efficiency in the real data is determined by using e^+e^- pairs from photon conversions [112]. These conversion pairs are selected by requiring the invariant mass

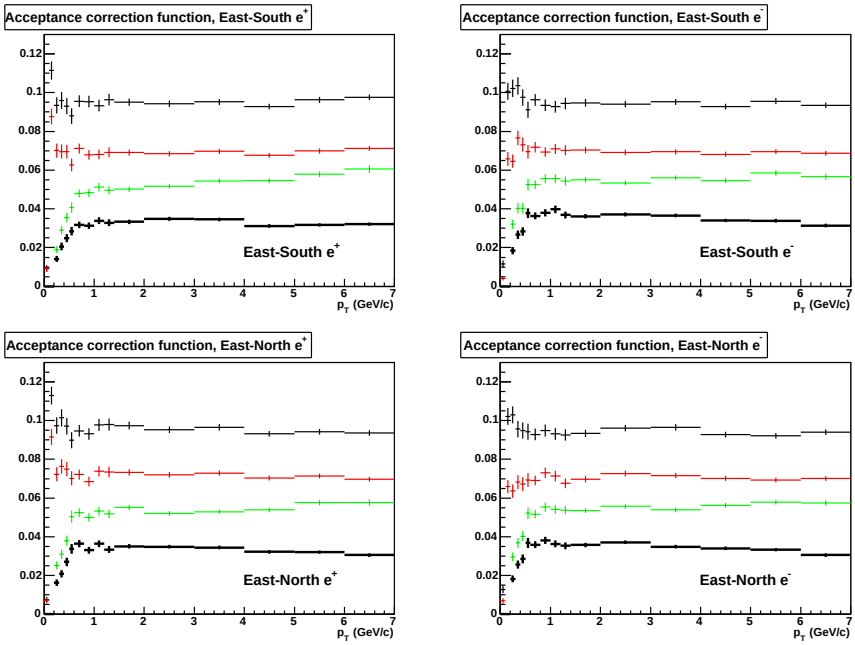

Figure 4.25: The acceptances for e^+/e^- at the East-South/East-North, respectively. In each panel, the black and the red histograms (from top 2 histograms) show the pure geometrical acceptance with and without the fiducial cut. The green and the thick-black histograms show the acceptance determined by only 5 σ matching cut and all the electron ID cuts.

within $60 < M_{e^+e^-} < 90$ MeV/c^2 in the converter run. The combinatorial background is estimated by an event mixing method and subtracted to get the net yield of the conversion pairs. In order to determine the electron ID efficiency, the yields of the conversion pairs are compared with and without the standard electron ID cut. In the first case, the pair yield is calculated by selecting a track with the standard electron ID cut and the second track in the pair without any eID cuts. In the second case, the pair yield is calculated by selecting both two track with the standard electron ID cut. Then, the ratio of these two yields provide the electron ID efficiency. The efficiencies for several electron ID cuts are summarized in Tab. 4.11.

In order to confirm the electron ID efficiency, we calculate an alternative correction function by combining the pure geometrical acceptance in the simulation and the electron ID efficiency by the real data. Then, the alternative function is compared with that by only the simulation. Figure 4.26 shows the $p_{\rm T}$ dependence of the acceptance correction functions. The black and the green histograms correspond to the acceptance functions by the simulation and the combined method, respectively. These acceptance functions are in good agreement each other up to 5 GeV/c. We decided to use an simple average of these two acceptance functions as the acceptance correction factor. The red histogram in Fig. 4.26 shows the average of the acceptance.

Finally, we determine the geometrical acceptance ($\varepsilon_{\rm geom}$), the tracking efficiency ($\varepsilon_{\rm track}$) and the eID efficiency ($\varepsilon_{\rm eID}$) separately. These are calculated as follows.

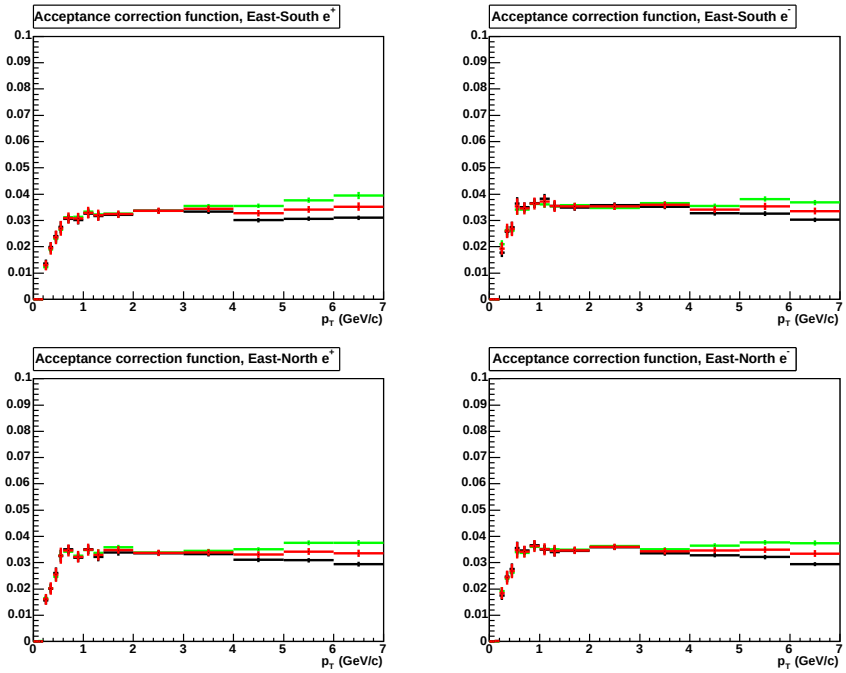

Figure 4.26: The acceptance functions for e^+/e^- at the East-South/East-North, respectively. In each plot, the green histogram is calculated from the simulation, and the black is calculated from the real data. The red histogram is the average of the green and the black one.

For the geometrical acceptance ($\varepsilon_{\rm geom}$),

$$\varepsilon_{\rm geom} = \frac{N_e}{\rm input}, \tag{4.23}$$

where N_e is the number of reconstructed tracks with the fiducial cut and "input" is the number of input electrons in the simulation. Here, the $\varepsilon_{\rm geom}$ is normalized to dN/dy. In this calculation, no track and electron ID cut is required.

For the tracking efficiency ($\varepsilon_{\rm track}$),

$$\varepsilon_{\rm track} = \frac{N_e \text{with } |\mathsf{dr}| < 5}{N_e}, \tag{4.24}$$

where dr represents the matching cut ($\sqrt{\mathsf{emcsdphi\_e}^2 + \mathsf{emcsdz\_e}^2}$). A numerator is selected by 5 σ of the matching cut.

For the electron ID efficiency ($\varepsilon_{\rm eID}$),

$$\varepsilon_{\rm eID} = \frac{N_e \text{with eID cut}}{N_e \text{with } |\mathsf{dr}| < 5}, \tag{4.25}$$

where all of the standard electron ID cuts are required in the numerator. These obtained values are summarized in Tab. 4.12. The systematic uncertainty of these values are described in section 4.12.

Table 4.11: Electron ID efficiencies determined by the conversion pair analysis

Variables	Efficiency
$\sqrt{\mathsf{emcsdphi\_e}^2 + \mathsf{emcsdz\_e}^2} < 2.0$	0.956
$\mathsf{n0} >= 3$	0.860
$\mathsf{chi2/npe0} < 10$	0.933
$\mathsf{disp} < 5$	0.966
$-2 < \mathsf{dep}$	0.958
$\mathsf{emcdt} < 2$	0.961

Table 4.12: Summary of the efficiencies determined in the PISA simulation.

Name	Efficiency (%)
$\varepsilon_{\mathrm{geom}}$	14.1
$\varepsilon_{\mathrm{track}}$	75.3
$\varepsilon_{\mathrm{eID}}$	64.7

4.9.2 Multiplicity Dependent Efficiency Loss

The detector performance depends on the detector occupancy since multi-particle signals is merged into the single hit in the high multiplicity environment such as central Au + Au collisions. In addition to the track reconstruction and the electron ID efficiencies, the multiplicity dependent efficiency loss ($\varepsilon_{\mathrm{mult}}$) due to the detector occupancy need to be taken into account. The $\varepsilon_{\mathrm{mult}}$ is determined by embedding a simulated single electron track into a real event and measuring the probability that the embedded electron track is correctly reconstructed [113].

The efficiency loss is independent of p_{T}. The efficiency losses are determined for minimum bias and five centrality classes as shown in Tab. 4.13. The systematic uncertainty on the $\varepsilon_{\mathrm{mult}}$ is assigned as 7%.

Table 4.13: Summary of the multiplicity dependent efficiency loss

Centrality	$\varepsilon_{\mathrm{mult}}$
minimum bias	0.781
0-10%	0.738
10-20%	0.760
20-40%	0.817
40-60%	0.887
60-92%	0.953

4.10 Heavy Flavor Electrons

Inclusive electrons contain three components as follows:

1. "Photonic electrons" : Background electrons from Dalitz decays of light neutral mesons (π^0, η, η', ρ, ω and ϕ) and photon conversions in the detector material.
2. "Non-Photonic electrons"
   (a) "Heavy Flavor" : Signal electrons from semi-leptonic decays of hadrons containing charm and bottom quarks,
   (b) "The Other Background": Background electrons from K_{e3} decays ($K \to \pi e \nu$) and di-electron decays of ρ, ω and ϕ. The small contributions from J/ψ and Drell-Yan process are also included.

Heavy flavor electrons is the signal in this analysis and needs to be extracted from inclusive electrons. In order to separate the non-photonic and the photonic electron components, the converter method is used. After the separation, the third component (the other background) still remains. The third component is subtracted step by step. The converter method is described in section 4.10.1. The subtraction of the other background is described in section 4.10.6 and 4.10.6.

4.10.1 Converter Method

The converter method is used to separate non-photonic and photonic electrons with high precision. To extract non-photonic electrons, the inclusive electron yield in the converter run is directly compared with that in the non-converter run. The photon converter is a thin brass sheet of 1.7% radiation length which is described in section 3.6. The photon converter increases only the yield of photonic electrons by a fixed factor R_γ determined by its radiation length. Therefore, the comparison of these two datasets provides a clear separation of these components. The yield of inclusive electrons with ($N_e^{\mathrm{Conv-in}}$) and without the converter ($N_e^{\mathrm{Conv-out}}$) is expressed as:

$$N_e^{\mathrm{Conv-out}} = N_e^{\gamma} + N_e^{\mathrm{non-}\gamma}, \tag{4.26}$$

$$N_e^{\mathrm{Conv-in}} = R_\gamma N_e^{\gamma} + (1-\epsilon) N_e^{\mathrm{non-}\gamma}, \tag{4.27}$$

where N_e^{γ} ($N_e^{\mathrm{non-}\gamma}$) is the yield of photonic and non-photonic electrons, and ϵ represents small loss of electrons due to the converter. This small loss is denoted as "blocking effect". Next, the ratio of the electron yield (R_{CN}) with and without the converter is defined as follows:

$$R_{\mathrm{CN}} = \frac{N_e^{\mathrm{Conv-in}}}{N_e^{\mathrm{Conv-out}}} = \frac{R_\gamma + (1-\epsilon) R_{\mathrm{NP}}}{1 + R_{\mathrm{NP}}}, \tag{4.28}$$

where R_{NP} is the ratio of non-photonic to photonic electrons ($N_e^{\mathrm{non-}\gamma}/N_e^{\gamma}$). If there were no contribution from non-photonic electrons, then $R_{\mathrm{CN}} = R_\gamma$. Eq. 4.28 can be transformed for R_{NP}:

$$R_{\mathrm{NP}} = \frac{R_\gamma - R_{\mathrm{CN}}}{R_{\mathrm{CN}} - 1 + \epsilon} = \frac{N_e^{\mathrm{non-}\gamma}}{N_e^{\gamma}}. \tag{4.29}$$

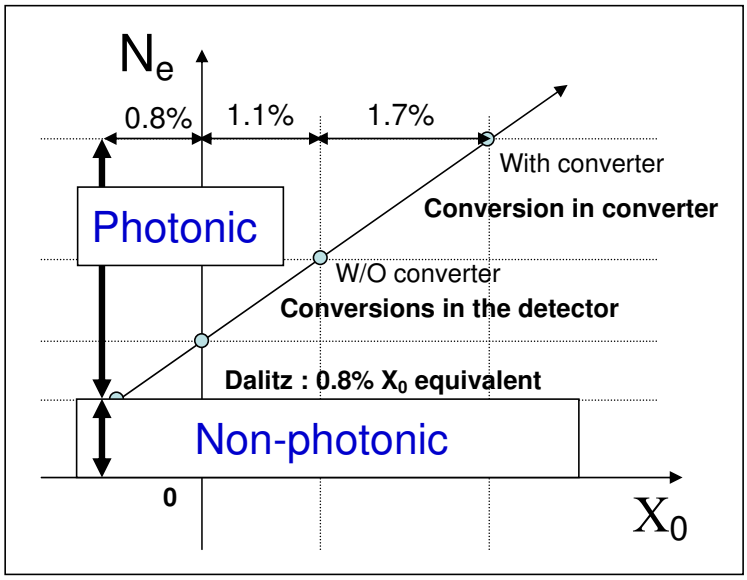

Figure 4.27: Relation between the inclusive electron yield and the thickness of the detector material.

$R_{\rm NP}$ expresses a significance of non-photonic electrons relative to photonic electrons.

Finally, photonic and non-photonic electrons are determined as:

$$N_e^{\gamma} = \frac{N_e^{\rm Conv-in} - (1-\epsilon)N_e^{\rm Conv-out}}{R_\gamma - 1 + \epsilon}, \tag{4.30}$$

$$N_e^{\rm non-\gamma} = \frac{R_\gamma N_e^{\rm Conv-out} - N_e^{\rm Conv-in}}{R_\gamma - 1 + \epsilon}. \tag{4.31}$$

These equations indicate that R_γ is the key parameter to extract non-photonic electrons. Figure 4.27 shows the relation between the inclusive electron yield and the thickness of the detector material in radiation length. In this figure, the non-photonic electron yield is same in both with and without the converter. However, the photonic electron yield is increased. The photonic electron yield per photon is approximately given by $Y \propto \delta + \frac{7}{9}t$, where δ is the branching ratio of Delitz decay per photon relative to 2 γ (for π^0, η and η') and 1 γ (for ρ, ω and ϕ) decay, and t is the thickness of the conversion material in radiation length. The factor $\frac{7}{9}$ is the approximate probability of photon conversions in one unit of radiation length. For π^0, the parameter δ is 0.6% which is half of the branching ratio of π^0 Dalitz decays (1.198/2). By applying $\delta \simeq 0.8$ and $t \approx 1.1\%$ ($t \approx 2.8\%$) without (with) the converter, $R_\gamma \approx 1.9$ is roughly estimated. Since there are some $p_{\rm T}$ dependence for δ, the complete formula of R_γ is determined using the PISA simulation.

4.10.2 Simulation Study

The simulation study is one of the most important parts in the converter method since R_γ is determined by the PISA simulation.

The photonic source of electrons is a mixture of light neutral mesons (π^0, η, η', ρ, ω and ϕ) with different $p_{\rm T}$ slopes. For these photonic sources, π^0 is the main source and η is the second main source. The contributions of π^0 and η relative to the all photonic sources are roughly 80% and 20%, respectively. The other sources contribute only small fractions. Therefore, R_γ for π^0 and η are first determined separately by the simulations, then they are combined with a weight of their relative yield. Here, the $p_{\rm T}$ dependences of these particle yields are modeled by the cocktail calculation of the simple event generator [114] which is described in section 4.10.2. In the following, we denote that $R_\gamma^{\pi^0}$ and R_γ^{η} is R_γ for π^0 and η. In next sections, we describe the simulation study step by step.

Input for Simulation

The most important source of photonic electrons is π^0. For the input of the PISA simulation, the $p_{\rm T}$ slope of π^0 is obtained by fitting simultaneously the $p_{\rm T}$ spectra of π^+, π^- [105] and π^0 [115] in minimum bias Au + Au collisions measured by PHENIX. The two fitting functions corresponding the lower and higher $p_{\rm T}$ ranges are expressed as:

$$
\begin{aligned}
f(p_{\rm T}) &= \frac{1}{2\pi p_{\rm T}}\frac{d^2N}{dydp_{\rm T}}, && (4.32)\\
&= p0\cdot(1+p_{\rm T}/p1)^{p2} \quad (0.5 < p_{\rm T} < 5.0\ {\rm GeV}/c), && (4.33)\\
&= p0\cdot(1+p_{\rm T}/p1)^{p2} + p3\cdot p_T^{-8.0} \quad (1.5 < p_{\rm T} < 12.0\ {\rm GeV}/c), && (4.34)
\end{aligned}
$$

where $p0-p3$ are parameters summarized in Tab. 4.14.

Table 4.14: Parameters for the fit functions of π^0.

$p_{\rm T}$ range	$p0$	$p1$	$p2$	$p3$
$0.5-5.0$ GeV/c	416.54	2.32603	-13.8865	-
$1.5-12.0$ GeV/c	0.41898	356909	-763859	23.2689

Figure 4.28 shows the $p_{\rm T}$ spectra of charged and neutral pions with the fit functions. The charged pion means an average of π^+ and π^-. Figure 4.29 shows the ratio of the pion spectra to the fit functions.

Cocktail Calculation

The other light mesons contributing to photonic electrons are η, η', ρ, ω and ϕ. The shapes of the $p_{\rm T}$ distributions for these mesons are determined by a $m_{\rm T}$ scaling of π^0 spectrum. In the $m_{\rm T}$ scaling, a spectral shape of a hadron is assumed to be reproduced by replacing the input π^0 $p_{\rm T}$ ($p_{\rm T}^{\pi^0}$) with a hadron $p_{\rm T}$ of $p_{\rm T}^h = \sqrt{(p_{\rm T}^{\pi^0})^2 + m_h^2 - m_{\pi^0}^2}$. Here, m_h, m_{π^0} are

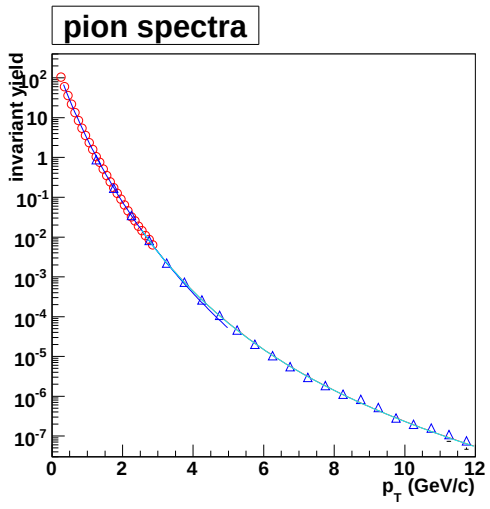

Figure 4.28: The p_{T} spectra of pions with the fit functions. The red and the blue points correspond to charged and neutral pion, respectively

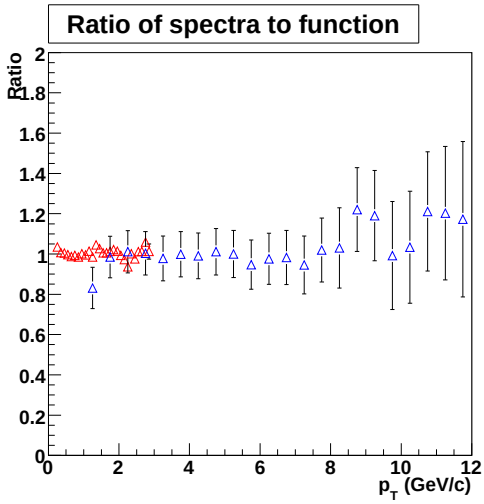

Figure 4.29: The ratio of the pion spectra to the fit functions.

mass of its hadron and π^0, respectively. In addition, the absolute normalizations of the m_{T} scaled spectra are given by the ratio of the meson to pion yield at high p_{T} ($p_{\mathrm{T}} \sim 5$ GeV/c). The meson to pion ratios used in the analysis are summarized in Tab. 4.15. Here, the η/π^0 ratio is a world average of measurement [116], and the ϕ/π^0 ratio is consistent with the PHENIX measurement [119]. Using the p_{T} spectra of these mesons, the p_{T} distributions of electrons from Dalitz decays and others are determined using the simple hadron decay generator [114]. The branching ratios of Dalitz decays for these mesons are summarized in Tab. 4.16.

Simulation Dataset

Using the p_{T} spectra determined by the m_{T} scaling, extensive PISA simulations are performed. The several sets of the simulation data for π^0 and η are generated to determine R_γ. All simulations are performed at the RIKEN-CCJ.

The simulation datasets are summarized in the following list. All the particles in the simulations are generated with a flat distribution in $|y| < 0.6$, 2π in azimuth and $|z| < 30$ cm.

- Five sets of π^0 with different p_{T} thresholds. The five p_{T} thresholds correspond to 0, 0.6, 1.0, 1.5 and 2.5 (GeV/c), respectively. The p_{T} slope is determined by fitting the measured pion spectra. All the datasets are produced with and without the converter.

- Five sets of η with different p_{T} thresholds. The five p_{T} thresholds correspond to 0, 0.6, 1.0, 1.5 and 2.5 (GeV/c), respectively. The p_{T} slope is determined by the m_{T} scaling. All the datasets are produced with and without the converter.

Table 4.15: Mesons to pion ratios

η/π^0	0.45 ± 0.1	[116, 117]
η'/π^0	0.25 ± 0.13	[118]
ρ/π^0	1.0 ± 0.5	[118]
ω/π^0	1.0 ± 0.5	[118]
ϕ/π^0	0.4 ± 0.2	[118]

Table 4.16: Branching ratios of the mesons decaying to electrons and photons

$\pi^0 \to 2\gamma$	98.798 ± 0.032 (%)
$\pi^0 \to \gamma e^+e^-$	1.198 ± 0.032 (%)
$\eta \to 2\gamma$	39.43 ± 0.26 (%)
$\eta \to \gamma e^+e^-$	0.6 ± 0.08 (%)
$\eta' \to \gamma e^+e^-$	$< 9 \times 10^{-4}$
$\rho \to e^+e^-$	$(4.54 \pm 0.1) \times 10^{-5}$
$\omega \to \pi^0 e^+e^-$	$(5.9 \pm 1.9) \times 10^{-4}$
$\omega \to e^+e^-$	$(6.95 \pm 0.15) \times 10^{-5}$
$\phi \to \eta e^+e^-$	$(1.15 \pm 0.1) \times 10^{-4}$
$\phi \to e^+e^-$	$(2.96 \pm 0.04) \times 10^{-4}$

The p_{T} thresholds are introduced to increase statistics for high p_{T} effectively. All of the simulation data are generated with and without the converter for the R_γ determination. The π^0 simulation is used not only for the electron analysis, but also for the electron pair analysis.

4.10.3 Determination of R_γ

Determination of $R_\gamma^{\pi^0}$

We determine $R_\gamma^{\pi^0}$ from the π^0 simulation data. $R_\gamma^{\pi^0}$ is the ratio of the photonic electron yields from π^0 with and without the converter. Since π^0 is the most dominant source of photons and photonic electrons, $R_\gamma^{\pi^0}$ is very close to R_γ. A small correction due to η contribution need to be taken into account. The η contribution is described in the next sections.

Figure 4.30 shows $R_\gamma^{\pi^0}$ as a function of p_{T}. Here, all five datasets of π^0 simulations are combined to increase the statistics. As a result, $R_\gamma^{\pi^0}$ is approximately constant at 1.83 at high p_{T}, but there is a small p_{T} dependence at low p_{T}.

Determination of R_γ^{η}

The η is the second dominant source of photonic electrons. Since the mass of η is larger than π^0, the available phase space of Dalitz decays for η is slightly larger than that of π^0.

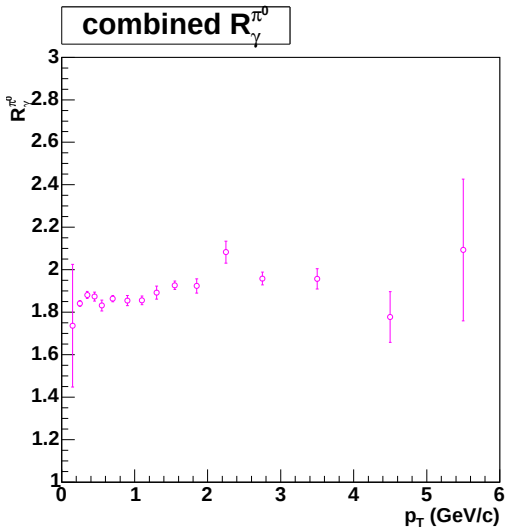

Figure 4.30: $R_\gamma^{\pi^0}$ as a function of p_{T}.

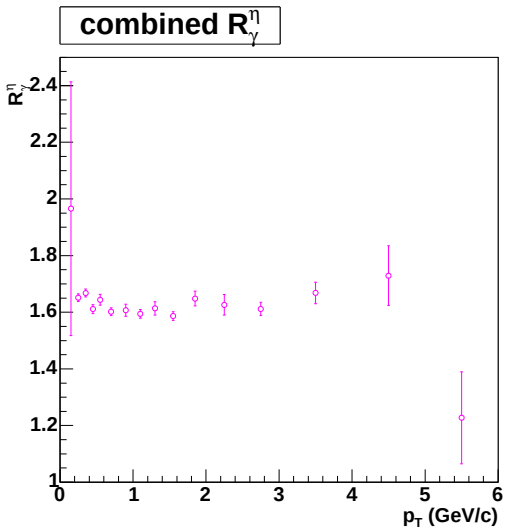

Figure 4.31: R_γ^{η} as a function of p_{T}.

Therefore, the Dalitz branching ratio relative to two photon decay of η is slightly larger than that of π^0. The relative branching ratio (Dalitz decay / two photons) is 1.2% for π^0 and 1.5% for η. This difference makes R_γ^η smaller than $R_\gamma^{\pi^0}$. Figure 4.31 shows R_γ^η as a function of p_{T}. All five datasets of η simulations are combined as same as the $R_\gamma^{pi^0}$ calculation. The R_γ^η is approximately constant at 1.6.

Total R_γ: Combine All Contributions

To obtain the total R_γ, $R_\gamma^{\pi^0}$ and R_γ^η are combined based on their relative yield in Au + Au collisions at RHIC. The combined R_γ ($R_\gamma^{\pi^0+\eta}$) is expressed as follows:

$$R_\gamma^{\pi^0+\eta} = \frac{R_\gamma^{\pi^0}\cdot N_e^{\pi^0} + R_\gamma^\eta \cdot N_e^\eta}{N_e^{\pi^0}+N_e^\eta} = \frac{R_\gamma^{\pi^0} + R_\gamma^\eta \cdot \epsilon^{\eta/\pi^0}}{1+\epsilon^{\eta/\pi^0}}, \tag{4.35}$$

where $N_e^{\pi^0}$ and N_e^η are the electron yields from π^0 and η decays, respectively. ϵ^{η/π^0} is the ratio of the electron yields from Dalitz decays between π^0 and η.

In addition to π^0 and η, the contributions from the other hadrons (η', ω and ϕ) need to be taken into account for the total R_γ determination. We treat that these contributions to R_γ is small and and have similar shapes to R_γ^η, because the branching ratios of Dalitz decays relative to photon decays for η', ω and ϕ are similar to η. Therefore, we replace ϵ^{η/π^0} with ϵ^{h/π^0} in order to include these hadron contributions in the R_γ calculation. Thus, the equation 4.35 is modified as follows:

$$R_\gamma^{\pi^0+\eta} \rightarrow R_\gamma = \frac{R_\gamma^{\pi^0} + R_\gamma^\eta \cdot \epsilon^{h/\pi^0}}{1+\epsilon^{h/\pi^0}}, \tag{4.36}$$

where ϵ^{h/π^0} is the ratio of the electron yields from Dalitz decays of all hadrons (h) except π^0 to π^0, Here, the numerator (h) includes the contributions of η, η', ω and ϕ.

The ratio ϵ^{h/π^0} is obtained using the cocktail calculation of photonic electrons described in section 4.10.2. Figure 4.32 shows the ratio of the electron yields from Dalitz decays of η, η', ω, ϕ relative to π^0, respectively. From these ratios, the ratio ϵ^{h/π^0} is obtained as shown in Fig. 4.33. The red, the green and the blue histograms correspond to the center value (e.g. $\eta/\pi^0 = 0.45$), the lower (e.g. $\eta/\pi^0 = 0.35$) and the upper limit (e.c. $\eta/\pi^0 = 0.55$) of the systematic uncertainty, respectively.

The ϵ^{h/π^0} is parameterized as follows:

$$\epsilon^{h/\pi^0} = f(p_{\rm T}) = p_0 + p_1/\sqrt{p_{\rm T}}, \tag{4.37}$$

where the p_0 and p_1 are the parameters as summarized in Tab. 4.17.

Table 4.17: The parameters of the fit function in Eq. 4.37

p_0	0.313909
p_1	-0.098408

Finally, we obtained the total R_γ. Figure 4.34 shows the R_γ as a function of $p_{\rm T}$. The red and the blue points are $R_\gamma^{\pi^0}$ and R_γ^{η}, respectively. The green represents the total R_γ.

4.10.4 Blocking Effect

In the converter run, electrons emitted inside the converter suffer a small energy loss, mainly due to bremsstrahlung, when electrons passes through the converter. This energy loss causes the reduction of the electron yields. We call this effect as "blocking effect". Here, we consider the blocking effect for the single electron yield, even though the blocking effect affects both the single electron and e^+e^- pair yields. The blocking effect for the pairs is already described in section 4.8.2.

The blocking effect should affect equally both photonic and non-photonic electrons. Since R_γ is simply calculated as the ratio of the electron yields with and without the converter, R_γ automatically includes the blocking effect for photonic electrons. Thus, the blocking effect only appears for non-photonic electrons in Eq. 4.31. The factor ϵ in Eq. 4.31 represents a partial loss of the non-photonic electron yield due to the blocking effect.

The blocking effect is studied by the PISA simulation of π^0 Dalitz decays. Since electrons from Dalitz decays originate at a collision vertex, these electrons undergo the same blocking effect with non-photonic electrons in both the simulation and the real data. Therefore, we can study the blocking effect by the simulation. In the simulation study, the electron yields from π^0 Dalitz decays are compared with and without the converter. Figure 4.35 shows the ratio of electrons from Dalitz decays with and without the converter. The ratio represents $(1-\epsilon)$. As the result, the loss ϵ due to the blocking effect is $\epsilon = (1-0.979) = 0.021(2.1\%)$. We assigned 25% of the systematic uncertainty for the blocking effect.

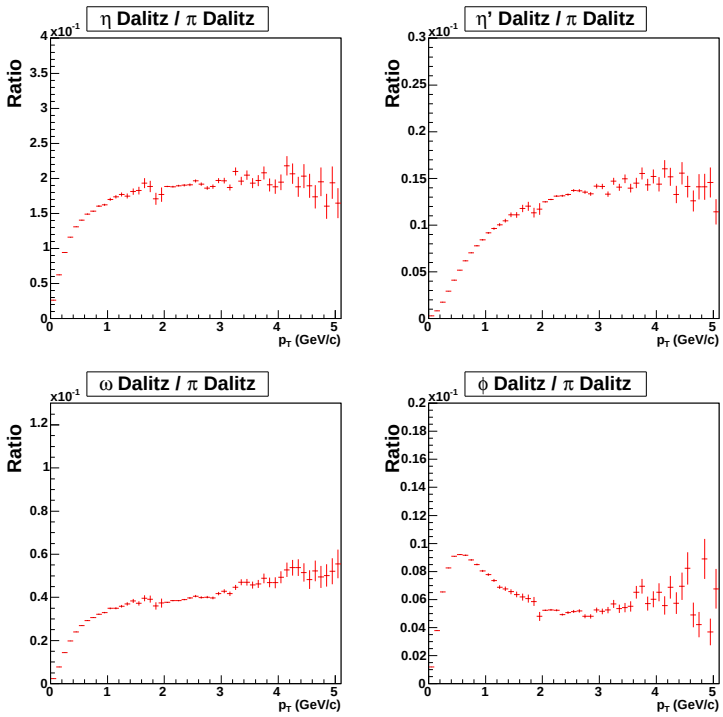

Figure 4.32: The ratio of the electron yields from Dalitz decays of the other hadrons relative to π^0.

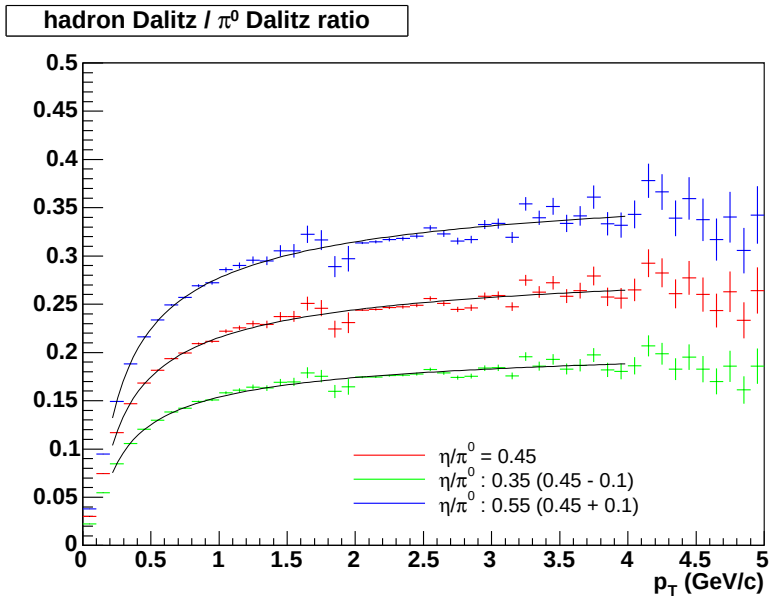

Figure 4.33: the ratio of the electron yield from Dalitz decays of all other hadrons ($h = \eta+\eta'+\omega+\phi$) to π^0. The red, the green and the blue histograms correspond to $\eta/\pi^0 = 0.45$, $0.35(0.45-0.1)$ and $0.55(0.45+0.1)$, respectively.

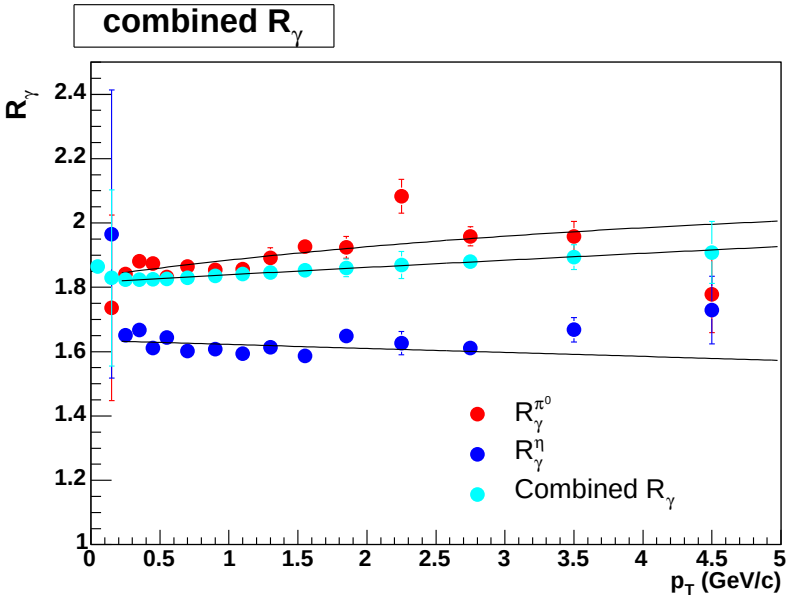

Figure 4.34: The total R_γ from all hadrons decaying to electrons.

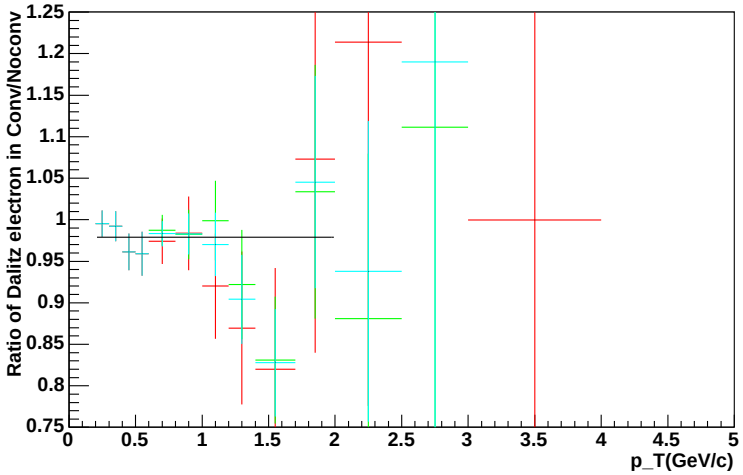

Figure 4.35: The ratio of electrons from Dalitz decays with and without the converter. The ratio is determined by the PISA simulation of π^0 Dalitz decays.

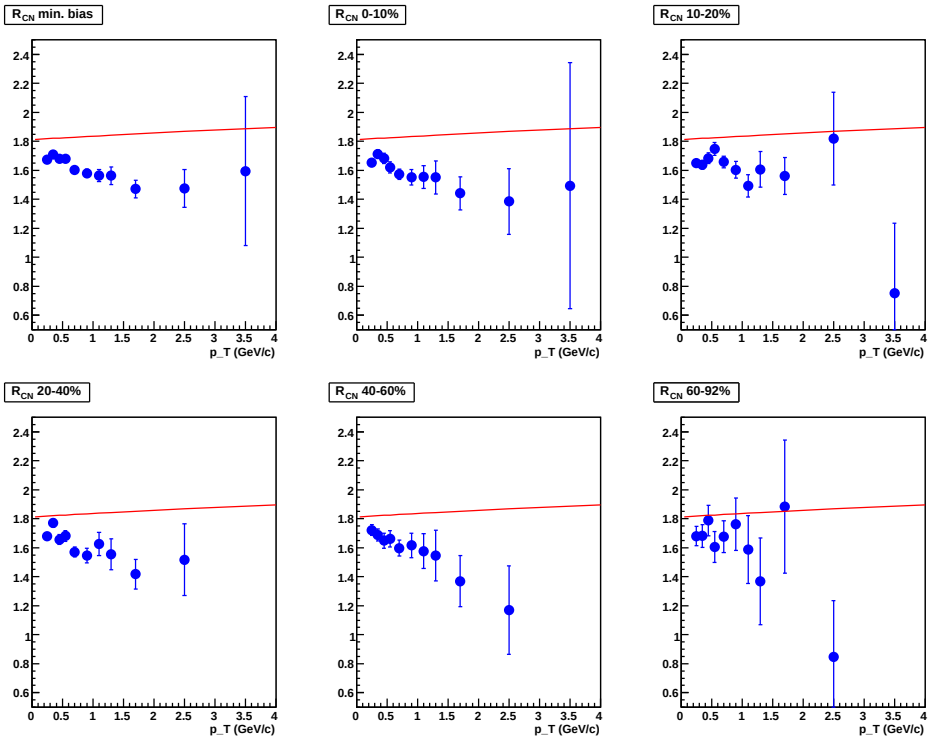

Figure 4.36: $R_{\rm CN}$ in real data and R_γ in simulation for minimum bias and five centrality classes.

4.10.5 Extraction of Non-photonic Electrons

The ratio of inclusive electrons ($R_{\rm CN}$) with and without the converter in real data is expressed in Eq. 4.28. $R_{\rm CN}$ is compared with R_γ. If there were no contribution from non-photonic electrons, then $R_{\rm CN} = R_\gamma$. Figure 4.36 shows the $R_{\rm CN}$ and the R_γ as a function of $p_{\rm T}$. The blue points and the red curves are the $R_{\rm CN}$ and R_γ. From the top-left to the bottom-right, the panels correspond to minimum bias and five centrality classes (0-10%, 10-20%, 20-40%, 40-60% and 60-92%), respectively. The difference between $R_{\rm CN}$ and R_γ is seen clearly, and the $R_{\rm CN}$ gradually decreases for high $p_{\rm T}$ compared to R_γ. This difference indicates that the existence of non-photonic electrons.

In order to show directly the significance of non-photonic electrons, the ratio $R_{\rm NP}$ is calculated from $R_{\rm CN}$ and R_γ as expressed in Eq. 4.29. Figure 4.37 shows the "$1 + R_{\rm NP}$" distribution for minimum bias and five centrality classes. It denotes that "$1 + R_{\rm NP}$" is the ratio of the inclusive electron yield relative to the photonic electron yield. The signal of non-photonic electrons can appear above unity in Fig. 4.37. From the figure, the contribution of non-photonic electrons increases with $p_{\rm T}$. The fraction of non-photonic electrons are 40% relative to photonic electrons for $p_{\rm T} > 1.0$ GeV/c.

The raw yield of non-photonic electrons can be statistically extracted using Eq. 4.31. Figure 4.38 shows the raw $p_{\rm T}$ distributions in minimum bias Au + Au collisions. The red, the light blue and the magenta spectra correspond to the $p_{\rm T}$ distribution of inclusive, non-photonic and photonic electrons, respectively.

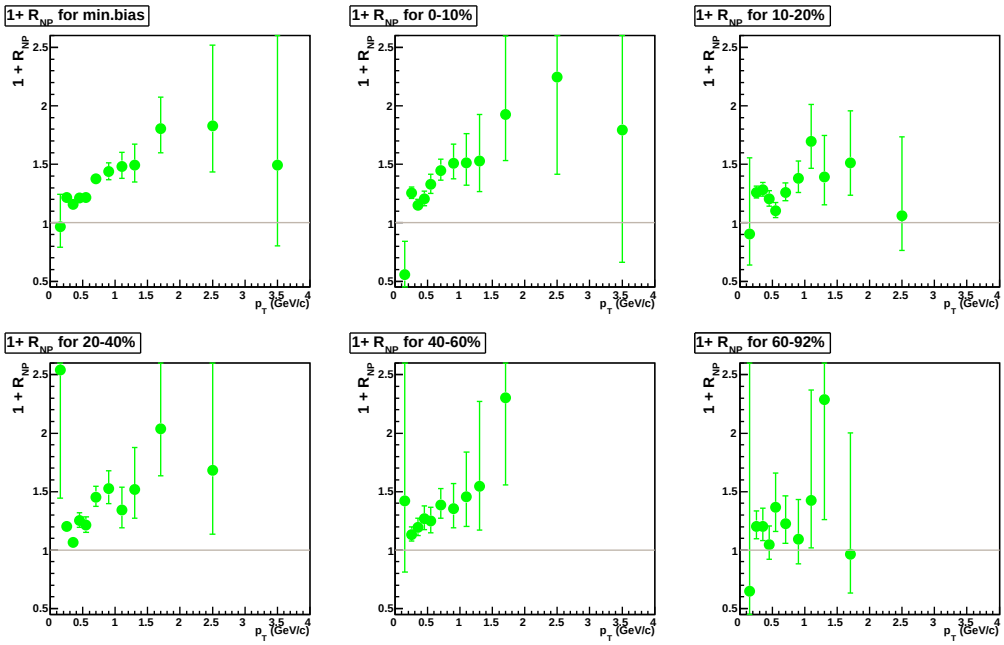

Figure 4.37: The $1 + R_{\mathrm{NP}}$ distributions as a function of p_{T} for minimum bias and five centrality classes. The points above 1.0 show a fraction of non-photonic electrons relative to photonic electrons.

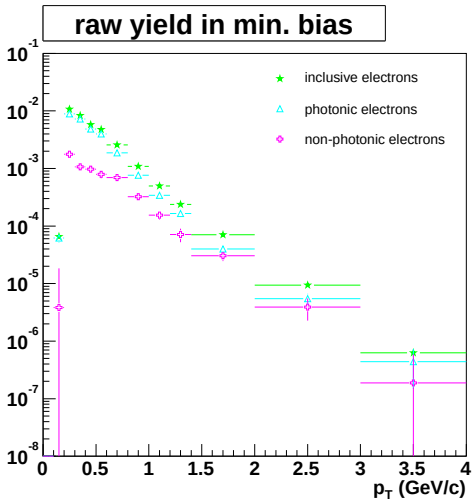

Figure 4.38: Raw p_{T} spectrum of inclusive electrons (green) in minimum bias Au + Au collisions are decomposed into non-photonic (magenta) and photonic electrons (light blue).

4.10.6 Background from K_{e3} decays and vector meson decays

After non-photonic electrons are extracted by the converter method, small backgrounds still remain. These backgrounds are electrons from K_{e3} decays and two electron decays of light vector mesons. Electrons from J/ψ decays and Drell-Yan process are also background, but they are negligibly small especially for low p_{T}. In this section, the backgrounds from K_{e3} decays and light vector meson decays are described.

K_{e3} Decay Background

The background electrons from K_{e3} decays ($K \rightarrow \pi e \nu$) are determined by the PISA simulations. The input p_{T} distribution for the simulation is obtained by fitting the p_{T} spectrum of kaon in minimum bias Au + Au collisions measured by PHENIX [105]. Here, the K^+ and K^- spectra are averaged for the fitting. The fit function is expressed as follows:

$$\frac{1}{2\pi p_{\mathrm{T}}} \frac{dN}{dy dp_{\mathrm{T}}} = f(p_{\mathrm{T}}) = p_0 \cdot e^{-p_{\mathrm{T}}/p_1}, \tag{4.38}$$

where p_0 and p_1 are the parameters. Figure 4.39 show the kaon spectrum with the fit function. The fit parameters are summarized in Tab. 4.18.

Table 4.18: The parameter obtained by fitting the kaon spectrum.

Parameter	Value
p_0	23.1648
p_1 (GeV/c)	0.317162

10M events are generated for each of K^+, K^- K^0_S and K^0_L, respectively. Figure 4.40 shows the raw p_{T} distributions of electrons from K_{e3} decays. From the left to the right, the panels correspond to electrons from K^+, K^-, K^0_L and K^0_S decays, respectively.

The absolute normalization of electrons from K_{e3} decays in the simulation is determined using dN/dy of kaons in minimum bias collisions measured in PHENIX. These dN/dy are summarized in Tab. 4.19. The average dN/dy of K^+ and K^- are used for K^0_L and K^0_S.

Table 4.19: dN/dy of K^+, K^- and $\langle K \rangle$ in minimum bias Au + Au collisions [105].

	K^+	K^-	$\langle K \rangle$
dN/dy	13.6 ± 1.5	12.7 ± 1.2	13.1 ± 1.0

In order to obtain the electron spectra from K_{e3} decays for the five centrality classes, the electron spectrum in simulation is modified using the p_{T} weight which is the ratio of the kaon yield measured in minimum bias to that in each centrality. Figure 4.41 shows the ratio of the kaon yield for minimum bias and the five centrality classes. For the

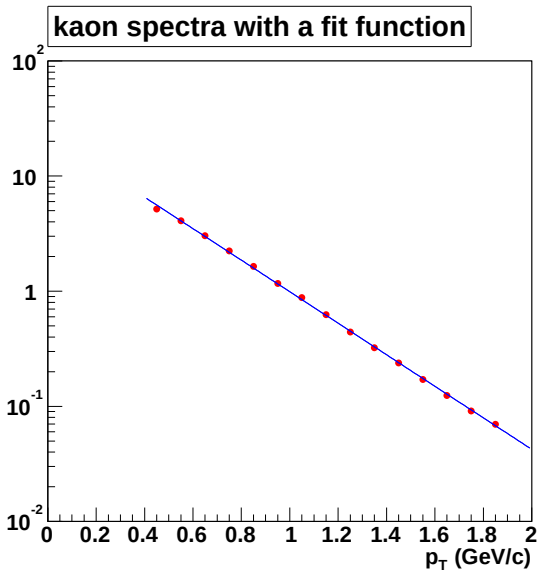

Figure 4.39: The averaged p_{T} spectrum of K^+ and K^- with the fitting function.

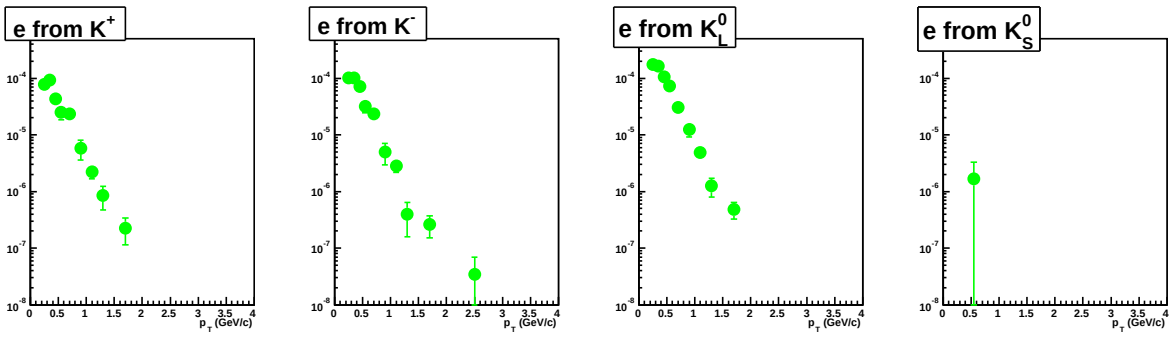

Figure 4.40: Raw p_{T} distributions of electrons from K^+, K^-, K^0_L and K^0_S decays, respectively

centrality dependence of electrons from K_{e3} decays, the multiplicity dependent efficiency loss described in section 4.9.2 is also taken into account.

Since the simulation accurately reproduces the detector response, the electron spectra from K_{e3} decays in the simulation can be directly compared with the real data. Figure 4.42 shows the ratio between electrons from K_{e3} decays and photonic electrons. From the top-left to the bottom-right, the panels correspond to the minimum bias and the five centrality classes, respectively. The contribution of electrons from K_{e3} decays relative to photonic electrons is 5% at low p_{T} and smaller at high p_{T}.

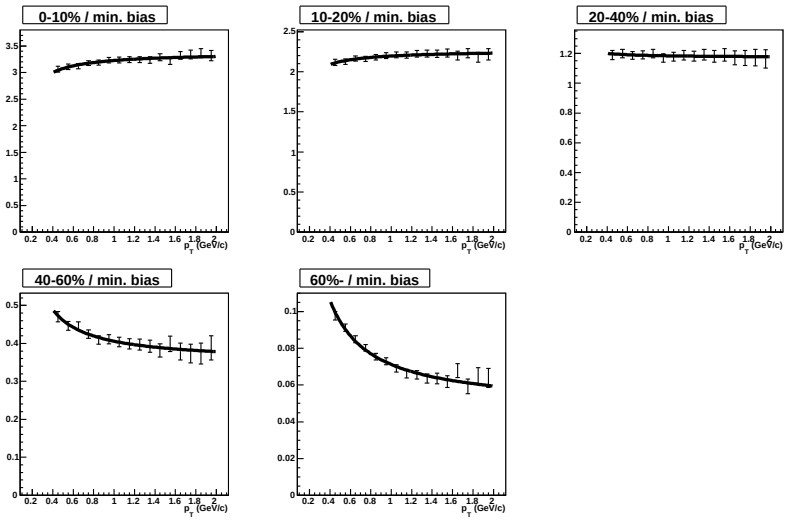

Figure 4.41: The ratio of kaon spectra in minimum bias to that in five centralities

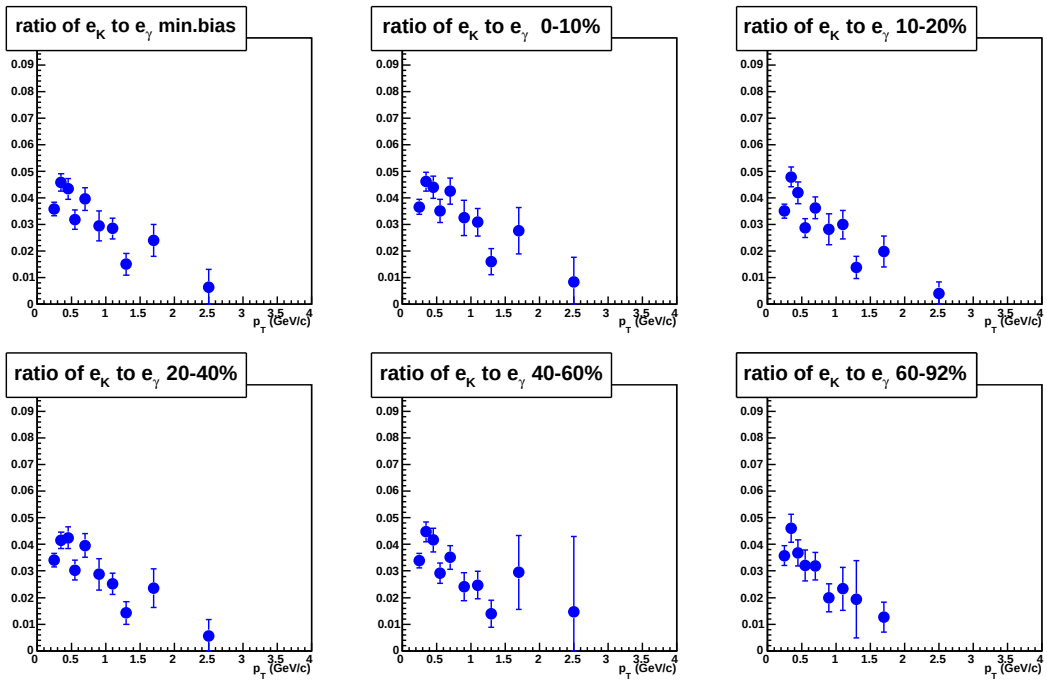

Figure 4.42: The ratio of electrons from K_{e3} decays to photonic electrons

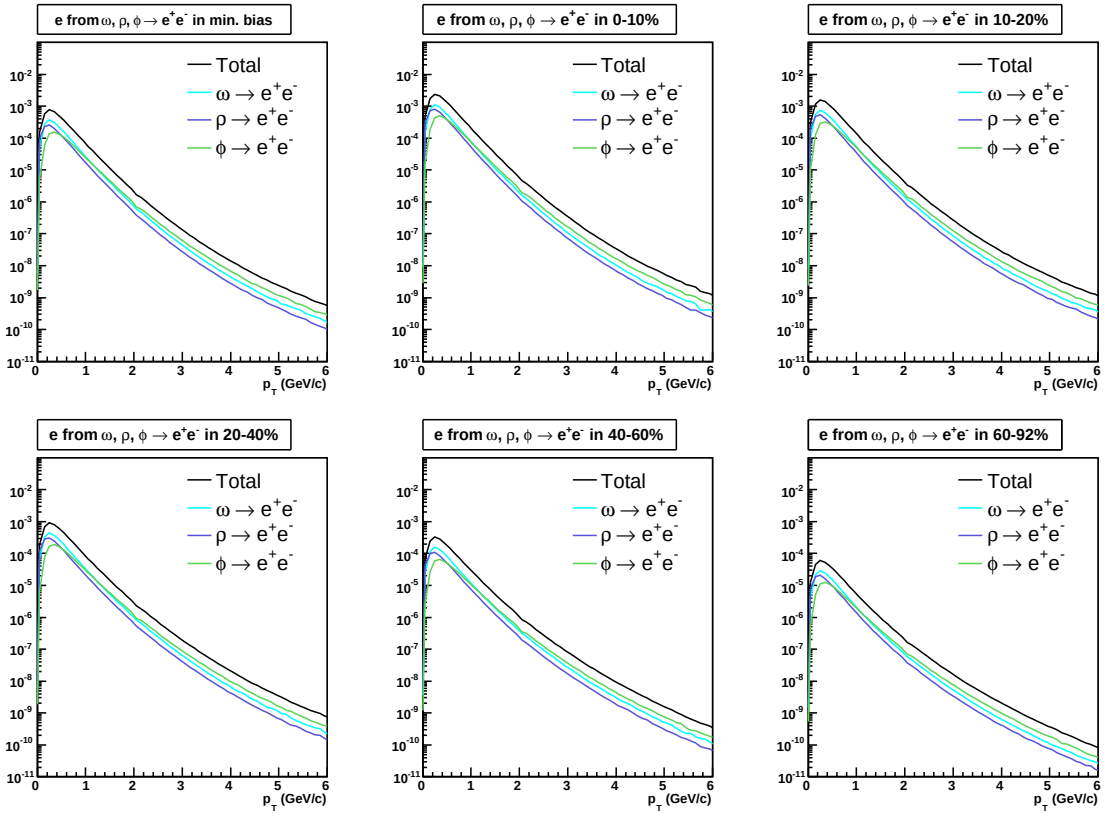

Figure 4.43: p_{T} spectra of ω, ρ and $\phi \rightarrow e^{+}e^{-}$ for each centrality

Background from two electron decays of light vector mesons

The background electrons from two electron decays of light vector mesons (ρ, ω and $\phi \rightarrow e^{+}e^{-}$) are determined by the cocktail calculation described in section 4.10.2 and appendix B. Figure 4.43 shows the p_{T} spectra of electrons from the decays of these light vector mesons. From the top-left to the bottom-right, the panels correspond to minimum bias and the five centrality classes.

It should be noted that the m_{T} scaling is slightly modified, since the m_{T} scaling of pion does not well reproduce the spectral shape of kaon and proton. The modified formula of m_{T} scaling is expressed as follows:

$$p_{\mathrm{T}}^{h} = \sqrt{(p_{\mathrm{T}}^{\pi^0})^2 + m \cdot (M_h^2) - M_{\pi^0}^2}, \tag{4.39}$$

where m is a factor to change the weight of the mass. In case of that $m > 1$ is set, the p_{T} slope becomes more harder than the original m_{T} scaling. Figure 4.44 shows the p_{T} spectra of kaon (left) and proton (right) with two m_{T} scaled functions. The red and the blue curves correspond to the functions with $m = 1.0$ and $m = 1.7$, respectively. The blue curve reproduces better than the red curve. Therefore, we used $m = 1.7$ for the modified m_{T} scaling.

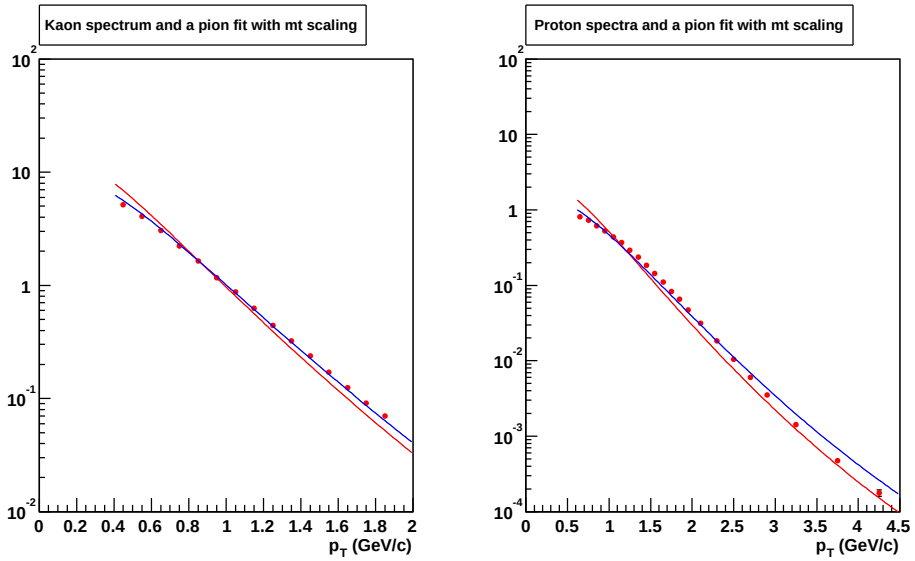

Figure 4.44: p_{T} spectra of kaon (left) and proton (right) compared with 2 m_{T} scaling functions. The red and blue correspond to m_{T} scaling with $m = 1.0$ and $m = 1.7$, respectively.

4.11 Bin Width Effect

After the background subtractions and the acceptance corrections are performed, the invariant differential yield of heavy flavor electrons is obtained. There still remains a bin width effect due to the finite bin width of the obtained p_{T} spectrum. In this analysis, we have so far assumed that the mean p_{T} ($\langle p_{\mathrm{T}} \rangle$) in a bin is equal to the center of its bin in the electron histogram. But this is not really correct if the electron spectrum has a steeply falling shape. In this case, the $\langle p_{\mathrm{T}} \rangle$ is shifted to lower p_{T} than its bin center. This bin width effect is larger for the wider bin width. Thus, we correct the bin width effect.

This correction is performed base on the PYTHIA heavy flavor spectrum described in next section. We first fit the PYTHIA spectrum by an empirical function as follows:

$$f(p_{\mathrm{T}}) = \left(\frac{a}{1 + b \cdot p_{\mathrm{T}} + e^{c+d \cdot p_{\mathrm{T}}} \cdot p_{\mathrm{T}}^3} \right)^e , \tag{4.40}$$

where a, b, c, d and e are the fit parameters. Using this function, we calculate the $\langle p_{\mathrm{T}} \rangle$ for each p_{T} bin. The data point in each p_{T} bin is moved to its $\langle p_{\mathrm{T}} \rangle$ value.

4.12 Systematic Uncertainties

The systematic uncertainties are studied. The sources of the systematic uncertainties in this analysis are mainly classified as follows:

1. Uncertainty of inclusive electrons : geometrical acceptance and electron identification.

2. Uncertainty of background subtraction : background from decays of K_{e3} and vector mesons.

3. Uncertainty of the converter method.

These three uncertainties, 1, 2 and 3 are independent each other. Thus, these uncertainties are estimated separately.

4.12.1 Systematic Uncertainty of Inclusive Electrons

The systematic uncertainty of inclusive electrons are composed of the errors of the geometrical acceptance and the electron ID efficiency due to the applied cuts.

First, the uncertainty of the geometrical acceptance is considered. In this analysis, the dead and the hot area of the detectors are removed by applying the fiducial cut and the acceptance in the simulation is tuned as described in section 4.8.1. To estimate the uncertainty of the geometrical acceptance, the position dependence of the electron yield are compared in the real data and simulation. Figure 4.45 and 4.46 show the e^+ and e^- yield as a function of the DC phi value. The red and the green correspond to the real data and the simulation, respectively. From the comparison, we assign 10 % uncertainty for the geometrical acceptance.

Second, the statistical fluctuation of the acceptance correction function is assigned as a systematic uncertainty. The acceptance correction function is described in section 4.9.1. This uncertainty is calculated as the ratio of the statistical error to the content value in each p_{T} bin of the correction function. Figure 4.47 shows the ratio of the error and the content as a function of p_{T}. From the figure, we assigned conservatively that the systematic uncertainty is 3.0% at $p_{\mathrm{T}} = 0.3$ GeV/c and 2.5% for higher p_{T}.

Third, the systematic uncertainties of the electron ID efficiency for each cut variable are estimated using inclusive electrons. We measured the fluctuation of the inclusive electron yields by changing the electron ID cuts tighter and looser. Then, the fluctuation of the electron yield is assigned as the systematic uncertainty for each electron ID cut. The tighter and looser cuts for the electron ID used in this study are summarized in Tab. 4.20. The obtained systematic uncertainties for each cut variables are also summarized in Tab. 4.20. The systematic uncertainty of $\varepsilon_{\mathrm{mult}}$ is described in section 4.9.2. Figure 4.48 shows the p_{T} dependence of the systematic uncertainties for the electron ID variables. Finally, these uncertainties are added in quadrature to obtain the total systematic uncertainty of the electron ID. The total systematic uncertainty of the electron ID is 11.8%.

4.12.2 Systematic Uncertainty of Electrons from K_{e3} and Vector Meson Decays

The systematic uncertainty of electrons from decays of K_{e3} and light vector mesons are considered separately. The uncertainty from K_{e3} decays includes two components. One is the systematic uncertainty of the kaon measurement (11.2%), and the other is the uncertainty of the electron ID (11.8%). These two components are added in quadrature to obtain the total uncertainty of K_{e3} decays. To evaluate the uncertainty relative to non-photonic electrons, these values are multiplied by the ratio of the electron yields from

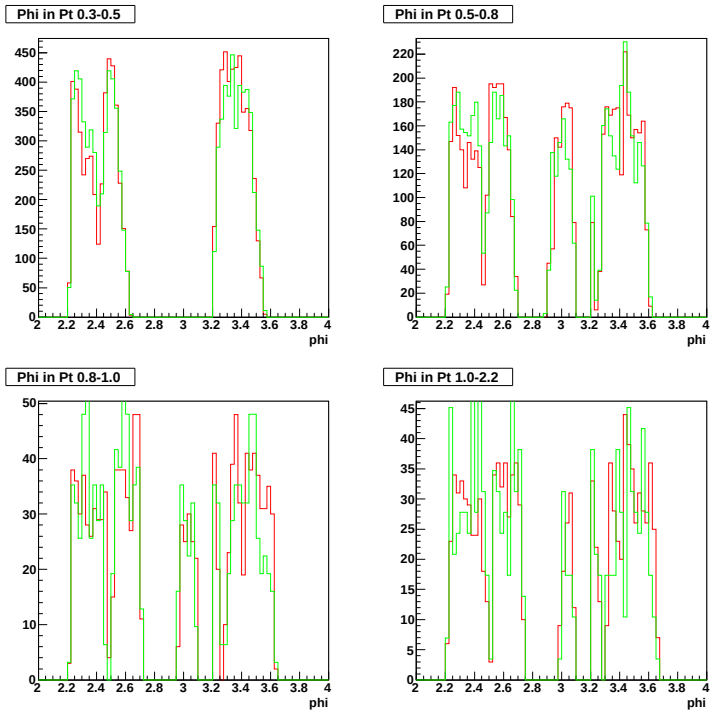

Figure 4.45: Comparison of the e^+ yield as a function of the DC phi.

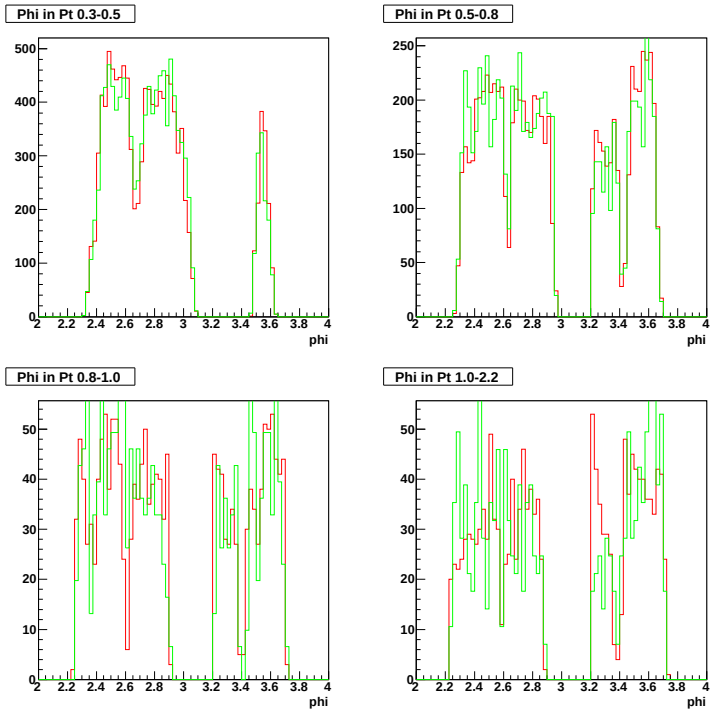

Figure 4.46: Comparison of the e^- yield as a function of the DC phi.

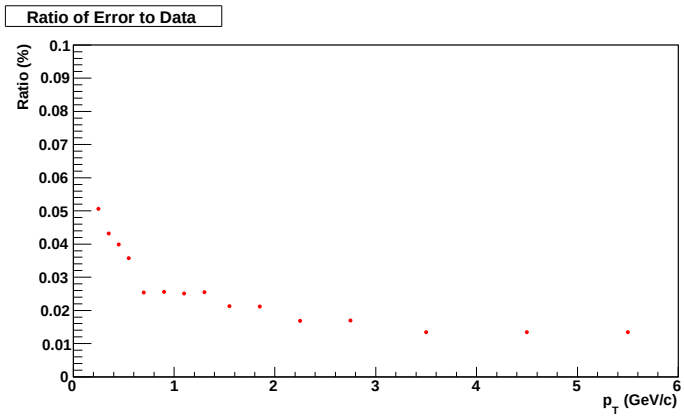

Figure 4.47: Ratio between the statistical error and the value of the geometrical acceptance in the simulation.

Table 4.20: The Summary of the systematic uncertainties for the electron ID cut variables and the others.

Variables	Cut			Systematic	Comments
	tighter	std.	looser	uncertainty	
$\sqrt{\text{emcsdphi\_e}^2 + \text{emcsdz\_e}^2}$	1.5	2.0	2.5	3.0%	
n0	4.0	3.0	2.0	3.0%	
chi2/npe0	7.0	10.0	15.0	5.0%	
disp	3.0	5.0	7.0	3.0%	
dep	-1.5	-2.0	-2.5	2.0%	
emcdt	1.0	2.0	3.0	2.0%	
MC statistics				2.5%	
Acceptance				5.0%	10% at low p_{T}
$\varepsilon_{\mathrm{mult}}$				7.0%	
Total				11.8 %	

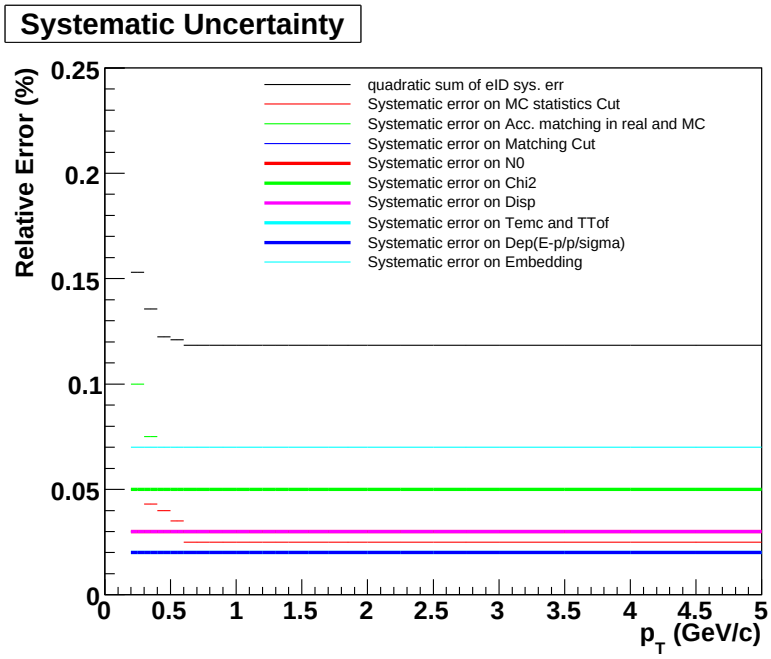

Figure 4.48: Systematic uncertainty of the acceptance and the electron ID variables

K_{e3} decays to non-photonic electrons. Figure 4.49 (left) shows the uncertainty of electrons relative to non-photonic electrons as a function of p_{T}. From the figure, the uncertainty of this component contributes only at lower p_{T}.

Next, the uncertainty from two electron decays of light vector mesons (ρ, ω and ϕ) is also estimated. The uncertainty also includes two components. One is the meson to the pion ratios which are assigned 50% uncertainty for all mesons at high p_{T}. The second is the systematic uncertainty of the charged and the neutral pion measurement. These two components are added in quadrature. Figure 4.49 (right) shows the p_{T} dependence of the uncertainty of electrons from light vector meson decays. The uncertainty increases slightly at high p_{T}.

4.12.3 Uncertainty of The Converter Method

The uncertainty of the converter method consists of four components as listed below:

A Material budgets in the real data and the simulation (4.4%).

B η/π^0 ratio (0.45 ± 0.1).

C Acceptance with and without the converter (2.5%).

D Blocking effect (25% of 0.021).

In the component A, the uncertainty of the material budget is estimated as 4.4% in e^+e^- pair analysis. Since the material budget affects directly R_γ, this 4.4% uncertainty can

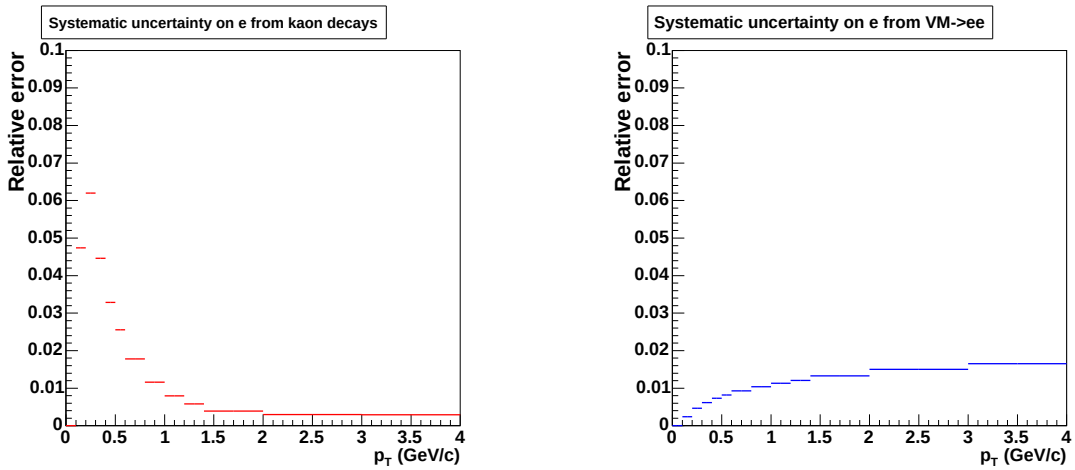

Figure 4.49: Systematic uncertainty of electrons from K_{e3} decays (left) and two electron decays of light vector mesons (right).

propagate to the uncertainty of R_γ. In the section 4.8.2, the uncertainty of the material budget is estimated using $R_{\rm material} = N_{\rm MVD}/N_{\rm BP}$. Here, $N_{\rm BP}$ and $N_{\rm MVD}$ are the yield of the conversion pairs at the beam pipe and the converter. The $N_{\rm BP}$ also contains the contribution from Dalitz decays. Those are expressed as:

$$\begin{aligned} N_{\rm BP} &= \text{Dalitz} + \text{beampipe} + \text{MVD(excluding outershell)} && (4.41)\\ &\sim \text{Dalitz} + \text{beampipe} + \text{MVD}, && (4.42)\\ N_{\rm MVD} &= \text{MVD outershell} + \text{converter} && (4.43)\\ &\sim \text{converter}, && (4.44) \end{aligned}$$

where the contribution from the MVD outershell is small compared with the other contributions, then it is approximately neglected.

In the single electron analysis, R_γ is expressed as:

$$\begin{aligned} R_\gamma &= \frac{\text{Dalitz} + \text{beampipe} + \text{MVD} + \text{converter}}{\text{Dalitz} + \text{beampipe} + \text{MVD}}, && (4.45)\\ &= 1 + \frac{\text{converter}}{\text{Dalitz} + \text{beampipe} + \text{MVD}}, && (4.46)\\ &\sim 1 + \frac{N_{\rm BP}}{N_{\rm MVD}} = 1 + R_{\rm material}. && (4.47) \end{aligned}$$

Using this relation, the uncertainty of R_γ is determined as:

$$4.4\% \times \frac{R_\gamma - 1}{R_\gamma} = 2.0\%. \quad (4.48)$$

We assign 2.0% uncertainty for R_γ.

For the component B, the modification of R_γ due to the η/π^0 ratio is studied by changing the ratio within its error, $\eta/\pi^0 = 0.45 \pm 0.1$. The other mesons ($\eta'$, ω and ϕ) are

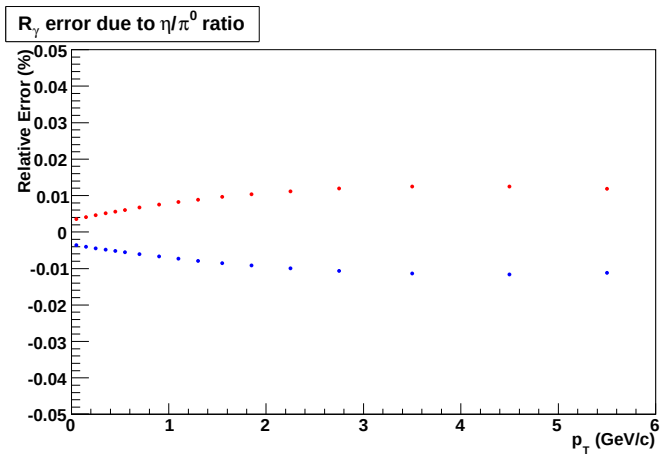

Figure 4.50: Relative error of R_γ calculated by changing the η/π^0 ratio.

also taken into account for the modification of R_γ. Figure 4.50 shows the relative error of R_γ calculated by changing the η/π^0 ratio. The error is roughly 1% at 0.5 GeV/c and increase slightly at high $p_{\rm T}$. To calculate the total uncertainty of R_γ, the uncertainties from the material budget and the η/π^0 ratio are added in quadrature. The obtained total uncertainty of R_γ is $\sqrt{(2.0\%)^2 + (1.0\%)^2} = 2.2\%$.

In the component C, the systematic uncertainty of $R_{\rm CN}$ is considered. If the acceptance between the converter run and the non-converter run is different, the electron yield in these two runs can not be directly compared. This difference should include as a systematic uncertainty. Figure 4.10, 4.11, 4.12 and 4.13 show the phi angle dependence of the electron yield for e^+ and e^- at the sorth and nouth side of the DC, respectively. These phi distributions represent the acceptances of electrons. By comparing the acceptances with and without the converter, we assign that the systematic uncertainty of $R_{\rm CN}$ is 2.5%.

Finally, we consider the error propagation of these four components to obtain the systematic uncertainty of the non-photonic electron yield. These four components differently contributes to the uncertainty of $N_e^{\rm non-\gamma}$ as shown in Eq. 4.31. Therefore, these contributions are estimated separately and added in quadrature. The component A and B affect R_γ. Thus, this can be expressed by changing R_γ to $R_\gamma(1 \pm \delta_{R_\gamma})$ in Eq. 4.31 as follows:

$$N_e^{\rm non-\gamma} = \frac{R_\gamma(1+\delta_{R_\gamma})N_e^{\rm Conv-out} - N_e^{\rm Conv-in}}{R_\gamma(1+\delta_{R_\gamma}) - 1 + \epsilon}, \tag{4.49}$$

where δ_{R_γ} denotes the error value. The combined uncertainty of A and B is 2.2% determined above.

The component C affects $R_{\rm CN}$. Since the uncertainty of $R_{\rm CN}$ is due to the difference of the acceptance with and without the converter, $N_e^{\rm Conv-in}$ is changed to $N_e^{\rm Conv-in}/(1+\delta_{R_{\rm CN}})$ to represent the changing of the electron yield in the converter run as follows:

$$N_e^{\rm non-\gamma} = \frac{R_\gamma(1+\delta_{R_{\rm CN}})N_e^{\rm Conv-out} - N_e^{\rm Conv-in}}{(1+\delta_{R_{\rm CN}})(R_\gamma - 1 + \epsilon)}, \tag{4.50}$$

where $\delta_{R_{\rm CN}} = \pm 0.025$ is used as described above.

The component D affects ϵ. As same as the other components, In order to evaluate the error of the blocking effect, ϵ is changed to $\epsilon + \delta_\epsilon$ as follows:

$$N_e^{\mathrm{non-}\gamma} = \frac{R_\gamma N_e^{\mathrm{Conv-out}} - N_e^{\mathrm{Conv-in}}}{R_\gamma - 1 + \epsilon + \delta_\epsilon}, \tag{4.51}$$

where $\delta_\epsilon = \pm 0.005$ is used which is 25% of 0.021. Then, the uncertainties calculated by these four components are added in quadrature.

Chapter 5

Results and Discussions

5.1 Invariant Yield of Heavy Flavor Electrons

The invariant differential yield of single electrons from semi-leptonic decays of heavy flavors has been measured in Au + Au collisions at $\sqrt{s_{\rm NN}} = 200$ GeV.

As described in previous sections, non-photonic electrons are extracted by the converter method from a large amount of photonic background electrons. The background electrons from K_{e3} and vector meson decays are subtracted. After these backgrounds are subtracted, the only remaining significant source of non-photonic electrons is electrons from semi-leptonic decays of heavy flavors. Therefore, we denote the remaining electrons as heavy flavor electrons. Here, we neglect the contributions from J/ψ and Drell-Yan processes due to their small contributions.

Figure 5.1 shows the invariant differential yield of heavy flavor electrons in minimum bias Au + Au collisions at $\sqrt{s_{\rm NN}} = 200$ GeV. The error bars and brackets represent the statistical and the systematic uncertainty, respectively. Figure 5.2, 5.3, 5.4, 5.5 and 5.6 show the heavy flavor electron spectra for 0-10%, 10-20%, 20-40%, 40-60% and 60-92% centralities, respectively. The data points of these spectra are summarized in Appendix C.

5.2 Comparison with $p + p$ result

The invariant differential yield of heavy flavor electrons in Au + Au collisions is compared with that in $p + p$ collisions at $\sqrt{s} = 200$ GeV. The heavy flavor electron spectrum in $p + p$ collisions was measured in PHENIX Run 2 [120]. Figure 5.7 shows the invariant yield of heavy flavor electrons for minimum bias collisions and for the five centrality classes. These spectra are scaled by several powers of ten for clarity. The curves in Fig. 5.7 show the best fit curve of the heavy flavor electron spectrum in $p + p$ collisions. The curves are scaled by T_{AA} for the corresponding Au + Au centrality. Here, T_{AA} is the nuclear overlap function calculated by the Glauber model described in section 4.2.3. The curves are also scaled by the same factor as the Au + Au data point for clarity. The Au + Au data points are in reasonable agreement with the T_{AA} scaled $p + p$ fit curve in all centrality classes within relatively large error at high $p_{\rm T}$.

Recently, the heavy flavor electron spectrum in $p + p$ collisions is extended to high $p_{\rm T}$

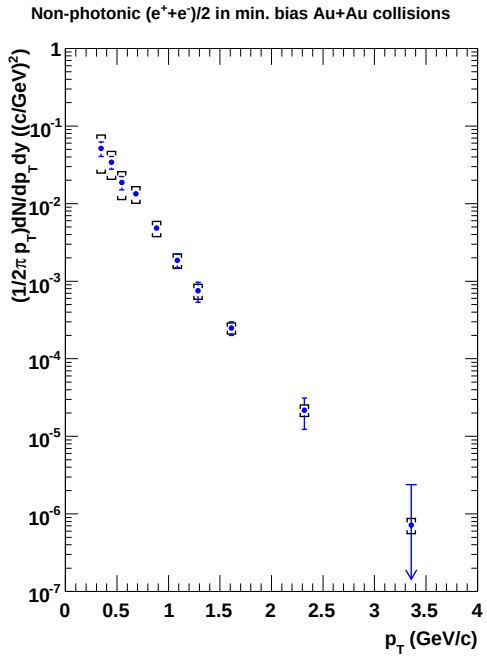

Figure 5.1: Invariant differential yield of heavy flavor electrons in minimum bias $\mathrm{Au}+\mathrm{Au}$ collisions at $\sqrt{s_{\mathrm{NN}}} = 200$ GeV.

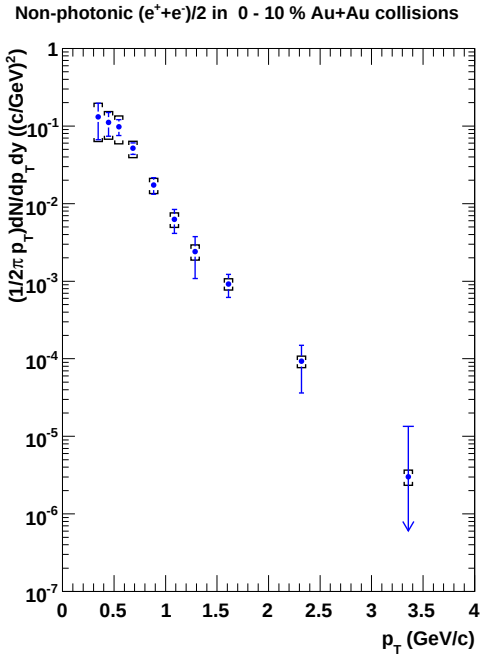

Figure 5.2: Invariant differential yield of heavy flavor electrons in 0-10% central $\mathrm{Au}+\mathrm{Au}$ collisions at $\sqrt{s_{\mathrm{NN}}} = 200$ GeV.

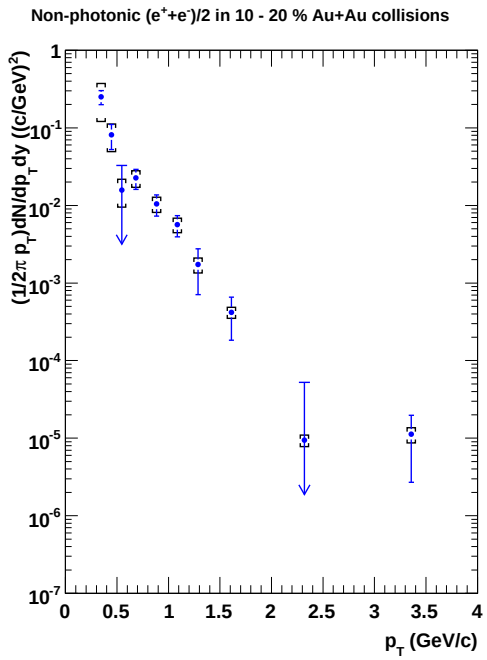

Figure 5.3: Invariant differential yield of heavy flavor electrons in 10-20% central $\mathrm{Au}+\mathrm{Au}$ collisions at $\sqrt{s_{\mathrm{NN}}} = 200$ GeV.

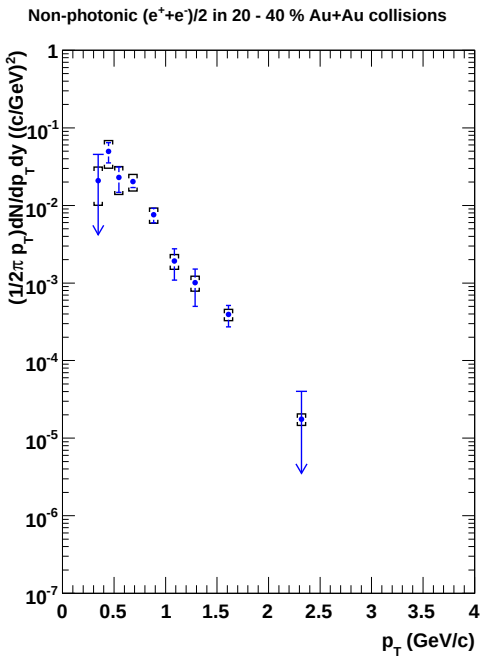

Figure 5.4: Invariant differential yield of heavy flavor electrons in 20-40% central $\mathrm{Au}+\mathrm{Au}$ collisions at $\sqrt{s_{\mathrm{NN}}} = 200$ GeV.

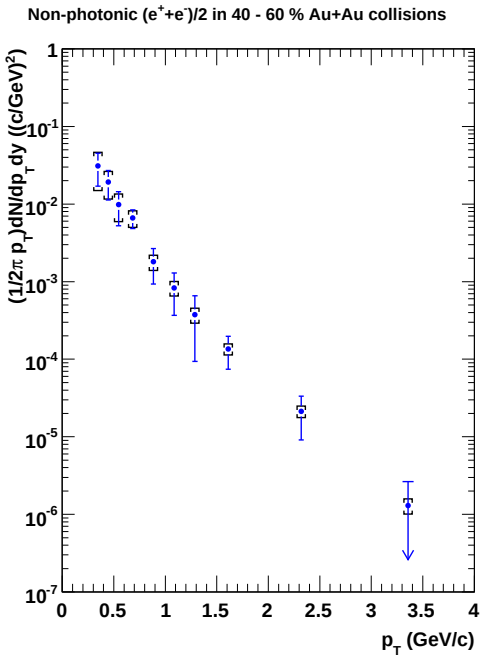

Figure 5.5: Invariant differential yield of heavy flavor electrons in 40-60% central Au + Au collisions at $\sqrt{s_{\rm NN}} = 200$ GeV.

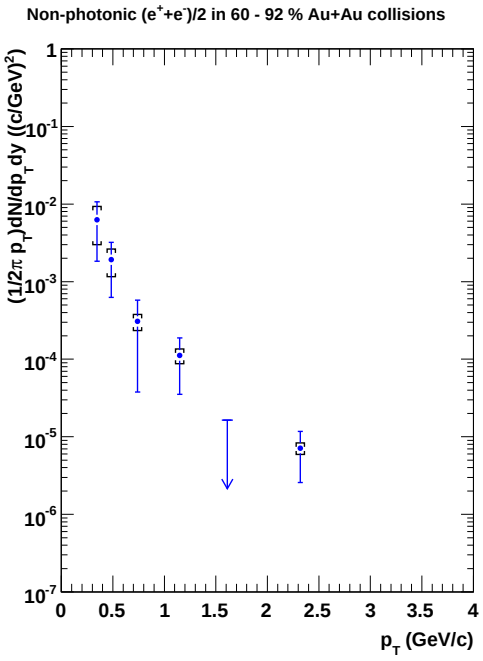

Figure 5.6: Invariant differential yield of heavy flavor electrons in 60-92% central Au + Au collisions at $\sqrt{s_{\rm NN}} = 200$ GeV.

with smaller statistical uncertainty in Run 5 [39]. The $p_{\rm T}$ spectrum in $p+p$ collisions in Run 2 is consistent with that in Run 5 within statistical and systematic uncertainty. The top panel in Fig. 5.9 shows the invariant differential cross sections of heavy flavor electrons in $p+p$ collisions at $\sqrt{s} = 200$ GeV. The red and black points are the electrons measured in Run 2 and Run 5 with statistical error bars. The brackets and the yellow bands represents the systematic uncertainties. These electron spectra in $p+p$ collisions are also compared with a Fixed-Order-Plus-Next-to-Leading-Log (FONLL) pQCD calculation [33] as described in section 2.2.1. The top curve in Fig. 5.9 shows the central value of the FONLL calculation. The contributions of charm and bottom are also shown. The contribution of bottom decays becomes larger than that from charm decays above $p_{\rm T} > 4$ GeV/c. The bottom panel in Fig. 5.9 shows the ratio of the data to the FONLL calculation. The ratio is nearly independent of $p_{\rm T}$ over the entire $p_{\rm T}$ range and is $1.71 \pm 0.02({\rm stat}) \pm 0.18({\rm sys})$ obtained by fitting. This indicates that the spectral shape of heavy flavor electrons in $p+p$ collisions is explained by the FONLL. From these comparisons of the spectral shape in Au + Au, $p+p$ and the FONLL, the spectral shape of heavy flavor electrons in Au + Au collisions is also explained by the FONLL within large error

In $p+p$ collisions, the ratio of electrons from bottom decays to heavy flavor electrons has been measured by the electron-hadron correlations [123]. The ratio is compared with the FONLL calculation. Figure 5.8 shows the ratio of $(b \to e)/[(b \to e) + (c \to e)]$ as a function of $p_{\rm T}$. The solid and dashed curves represent the FONLL calculation and its systematic uncertainties. The FONLL calculation agrees with the measured ratio. This result confirms that the main contribution is charms up to $p_{\rm T} < 4$ GeV/c for the spectra

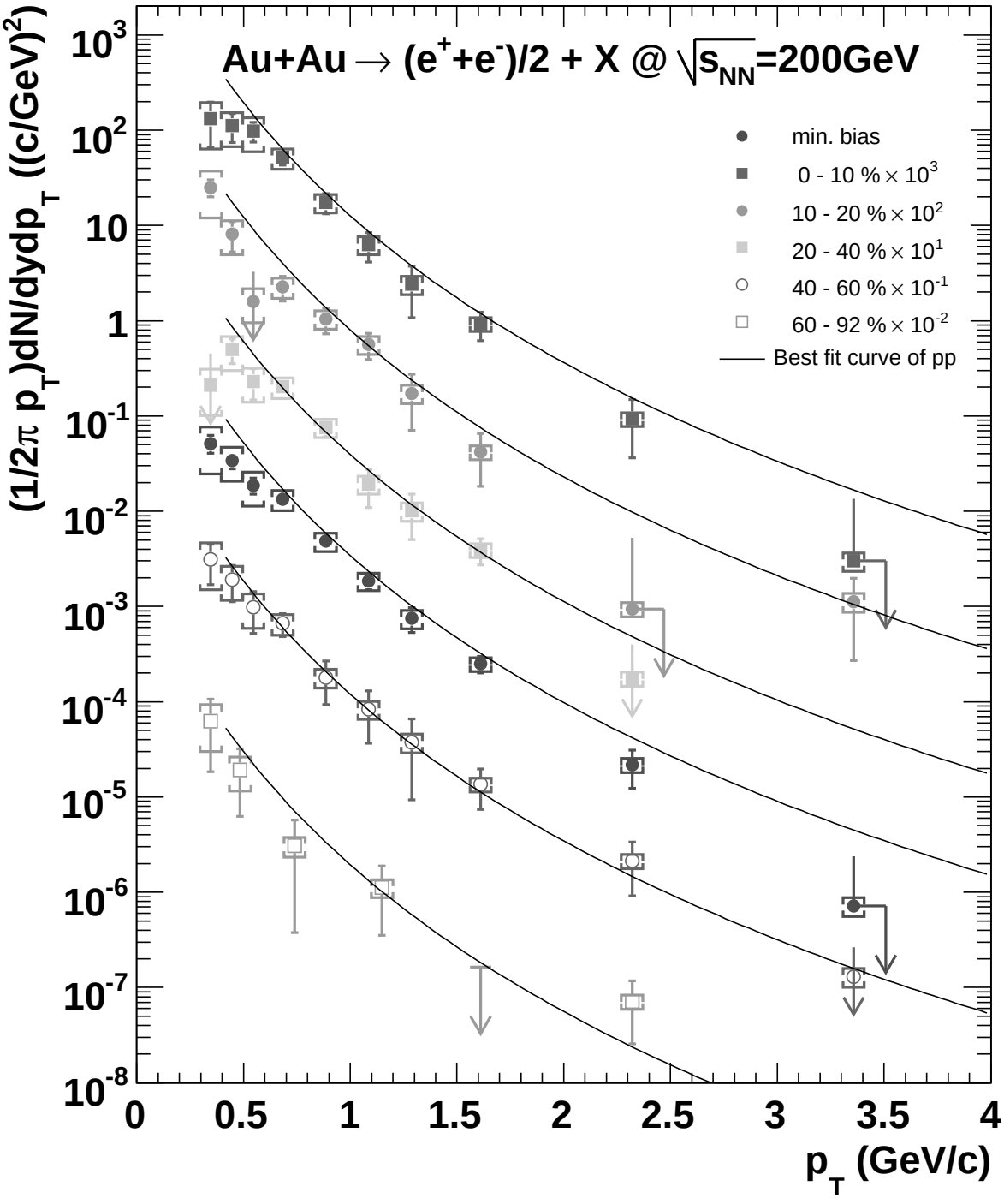

Figure 5.7: Invariant differential yields of heavy flavor electrons for different Au + Au centralities scaled by several powers of ten for clarity. Error bars and brackets correspond to the statistical and the systematic uncertainties, respectively. The curves are the best fit curves of electrons in $p + p$ collisions scaled by T_{AA} for the corresponding Au + Au centrality.

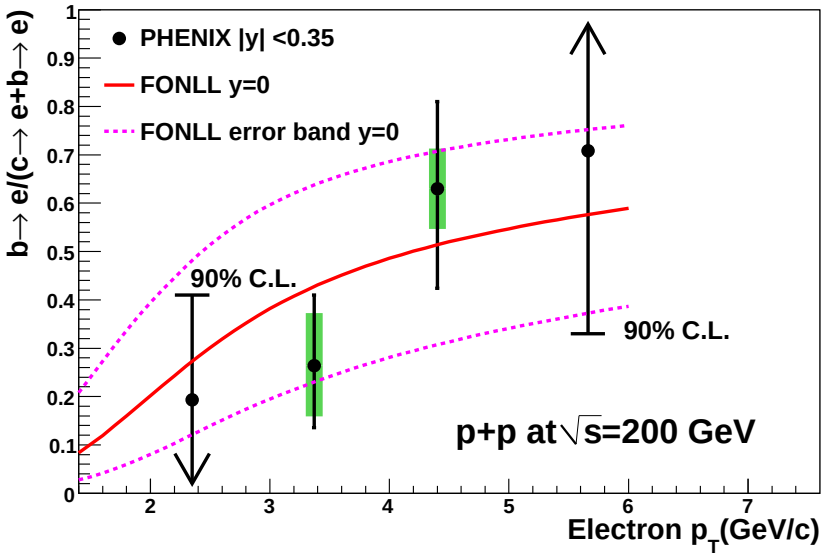

Figure 5.8: The ratio of bottom contribution to heavy flavor electrons as a function of p_{T} in $p+p$ collisions at $\sqrt{s} = 200$ GeV [123].

in Au + Au collisions.

5.3 Centrality Dependence of Charm Electron Yield

In order to quantify the centrality dependence of the charm production, the integrated yield (dN_e/dy) of heavy flavor electrons is calculated with $0.8 < p_{\mathrm{T}} < 4.0$ GeV/c for each centrality class. In this p_{T} range, the charm contribution is dominant as shown in Fig. 5.9. Therefore, we denote that heavy flavor electron within this p_{T} range is charm electron. Although the integration p_{T} range should be as wide as possible to study the total production of charm electrons, the high p_{T} is limited up to 4.0 GeV/c due to the increase of bottom contribution for higher p_{T}. By contrast, the low limit of the p_T range is chosen for $p_{\mathrm{T}} > 0.8$ GeV/c where the systematic uncertainty is comparable with the statistical error. Then, the calculated integrated yield is fit by an empirical function, $AN_{\mathrm{coll}}^{\alpha}$, where A is a normalization parameter and α is the parameter which describes the centrality dependence. If there is no initial and final state effects on the total charm production, we expect $\alpha = 1$. Figure 5.10 shows $dN_e/dy(0.8 < p_{\mathrm{T}} < 4.0)/N_{\mathrm{coll}}$ as a function of N_{coll} for minimum bias and the five centrality classes in Au + Au and $p+p$ collisions. The gray box and the black circles correspond to the minimum bias data and the five centrality classes. The cross symbol shows the $p+p$ data. The error bars and the brackets represent the statistical and systematic uncertainties. We find $\alpha = 0.938 \pm 0.075(\mathrm{stat}) \pm 0.018(\mathrm{sys})$. If $p+p$ data is included for the fitting, $\alpha = 0.958 \pm 0.035(\mathrm{stat})$. In this fitting, most of the systematic uncertainties will cancel. The systematic uncertainty of α is described in Appendix D.1. This shows that the total yield of charm electrons for all centralities is consistent with N_{coll} scaling.

This result is confirmed by the updated data with much higher statistics in measured

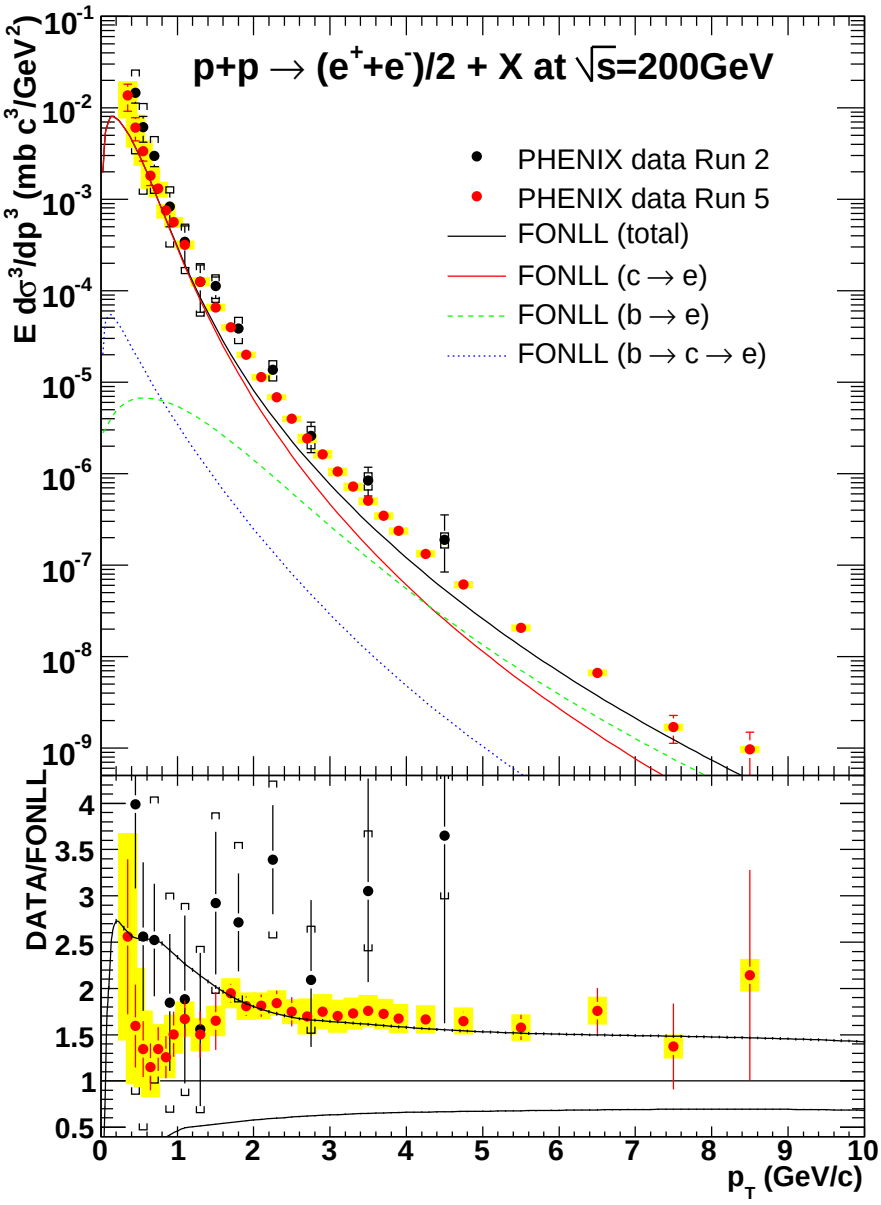

Figure 5.9: (top)Invariant differential cross sections of electrons from heavy flavor decays in $p+p$ collisions at $\sqrt{s} = 200$ GeV. The red and the black points correspond to the Run 2 data [120] and Run 5 data [39] with statistical errors, respectively. The brackets and the yellow bands are systematic uncertainty for Run 2 and Run 5, respectively. The curves are the FONLL calculation. (bottom) Ratio of the data and the FONLL calculations. The upper (lower) curves shows the theoretical upper (lower) limit of the FONLL calculation.

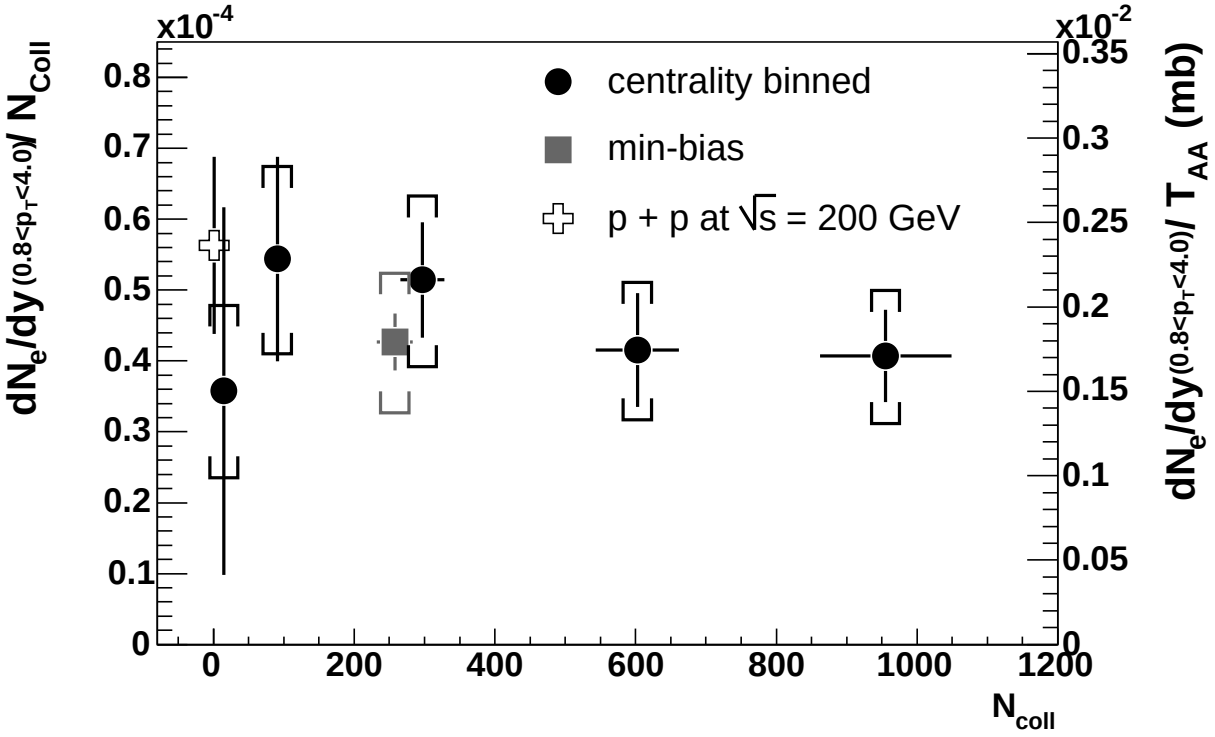

Figure 5.10: $dN_e/dy/N_{\rm coll}$ as a function of $N_{\rm coll}$ in Au + Au and $p+p$ collisions at $\sqrt{s_{\rm NN}} =$ 200 GeV. The gray box and the black circles correspond to the minimum bias data and five centrality data. The cross symbol shows the $p+p$ data. The error bars and the brackets represent the statistical and systematic uncertainties, respectively.

in PHENIX Run 4 [121]. Figure 5.11 shows the updated $dN_e/dy/T_{AA}$ as a function of $N_{\rm coll}$. The Au + Au and the $p+p$ data are measured in Run 4 and Run 5[39]. The integration range is slightly broadened for the updated data due to higher statistics. The updated α is $\alpha = 1.009 \pm 0.012({\rm stat}) \pm 0.051({\rm sys})$. If the $p+p$ data is included, $\alpha = 1.010 \pm 0.009({\rm stat}) \pm 0.040({\rm sys})$. All α values are consistent with unity within statistical and systematic uncertainty.

This is an important finding that the total charm production in Au + Au collisions is consistent with $N_{\rm coll}$ scaling of the production in $p+p$ collisions, as expected for point like pQCD processes. Therefore, the result rules out a large enhancement of total charm yield due to the secondary and/or the athermal charm production predicted in [18]. In addition, this result also gives the important baseline for charm suppression. It is found that the heavy flavor electrons are suppressed and its R_{AA} approaches the π^0 value at $p_{\rm T} > 4\,{\rm GeV}/c$ [121]. Therefore, it can be understood that most of charm quarks are produced in initial hard scatterings and they suffer the energy loss when they pass through the dense matter.

Even though the total charm production is consistent with the $N_{\rm coll}$ scaling, there might be small room for an possible secondary/thermal charm production.

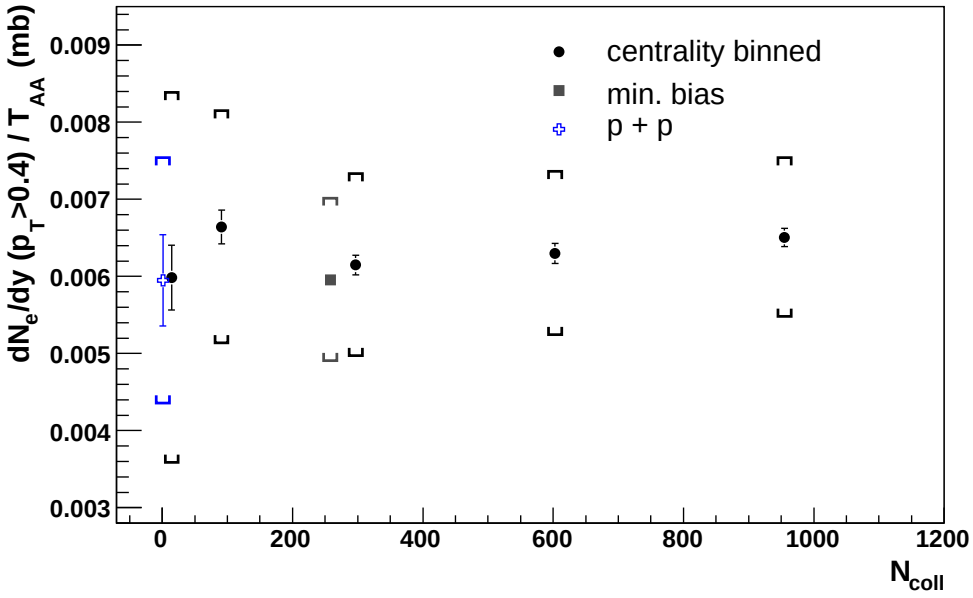

Figure 5.11: $dN_e/dy/T_{AA}$ as a function of $N_{\rm coll}$ in Au + Au and $p+p$ collisions measured in Run 4 [121] and Run 5 [39]. The gray box and the black circles correspond to the minimum bias data and the five centrality data. The cross symbol shows the $p+p$ data. The error bars and the brackets represent the statistical and systematic uncertainties, respectively.

Table 5.1: Summary of α values obtained by fitting.

Data for fitting	α
Au + Au	0.938 ± 0.075(stat) ± 0.018(sys)
Au + Au and $p+p$	0.958 ± 0.035(stat)
Updated Au + Au	1.009 ± 0.012(stat) ± 0.0506(sys)
Updated Au + Au and $p+p$	1.010 ± 0.009(stat) ± 0.0403(sys)

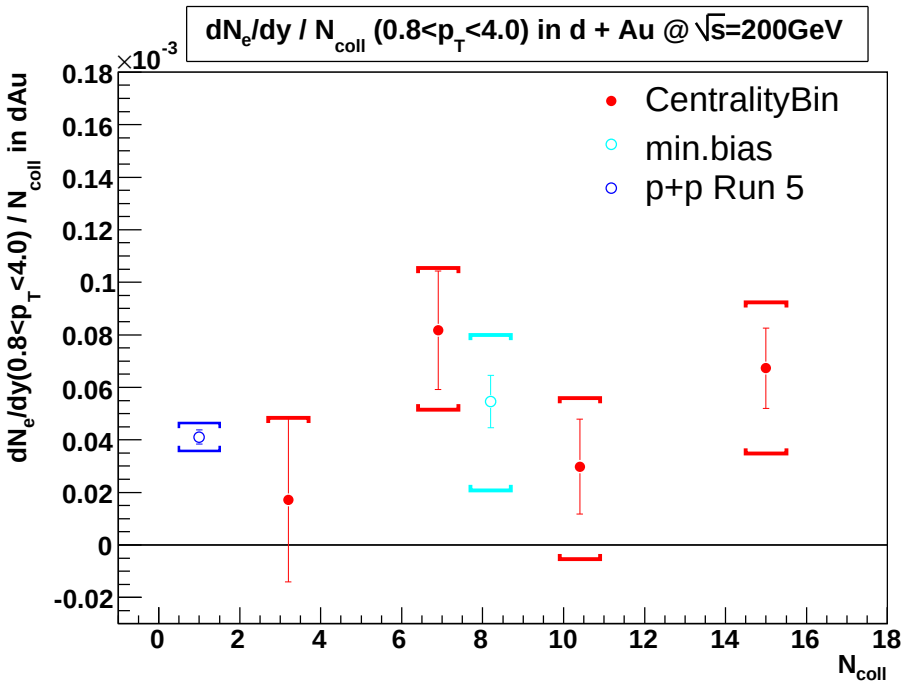

Figure 5.12: $dN_e/dy/N_{\rm coll}(0.8 < p_{\rm T} < 4.0$ GeV$/c)$ in d+Au collisions at $\sqrt{s_{\rm NN}} = 200$ GeV.

5.4 Comparison with $d+$Au collisions

Heavy flavor electrons in $d+$Au collisions at $\sqrt{s_{\rm NN}} = 200$ GeV are also measured by PHENIX [74]. The $N_{\rm coll}$ scaled yields of heavy flavor electrons ($dN_e/dy/N_{\rm coll}(0.8 < p_{\rm T} < 4.0$ GeV$/c)$) for minimum bias $d+$Au collisions and four centrality classes are calculated with $0.8 < p_{\rm T} < 4.0$ GeV$/c$ in the same way as the Au + Au data. The four centrality classes correspond to 0-20%, 20-40%, 40-60% and 60-88%, respectively. Figure 5.12 shows the $dN_e/dy/N_{\rm coll}(0.8 < p_{\rm T} < 4.0)$ as a function of $N_{\rm coll}$ in $d+$Au collisions. The error bars and the brackets represent the statistical and the systematic uncertainties, respectively. The $p+p$ data point is also shown in this figure. From the figure, the $dN_e/dy/N_{\rm coll}(0.8 < p_{\rm T} < 4.0)$ for all the centrality classes in $d+$Au collisions and for $p+p$ collisions are found to be consistent within their statistical and systematic uncertainties. Thus, this result indicates that the total production of charms in $d+$Au collisions is consistent with $N_{\rm coll}$ scaling. This implies that the modification of heavy flavor production due to the shadowing effect of the cold nuclear effect is small. However, the statistical and systematic error too large to make any strong constraints.

The FNAL-E866 experiment was reported the heavy flavor production in p+A collisions at $\sqrt{s} = 38.8$ GeV [124]. In order to compare the heavy flavor production in $d+$Au collisions with that in $p+p$ collisions, they define the following relation:

$$\sigma^{c\bar{c}}_{pA} = A^{\alpha} \cdot \sigma^{c\bar{c}}_{pp}, \tag{5.1}$$

where A is the mass number of the target nucleus and α is the parameter to study the cold nuclear effect. If there is no modification due to the cold nuclear effect, then, $\alpha = 1$.

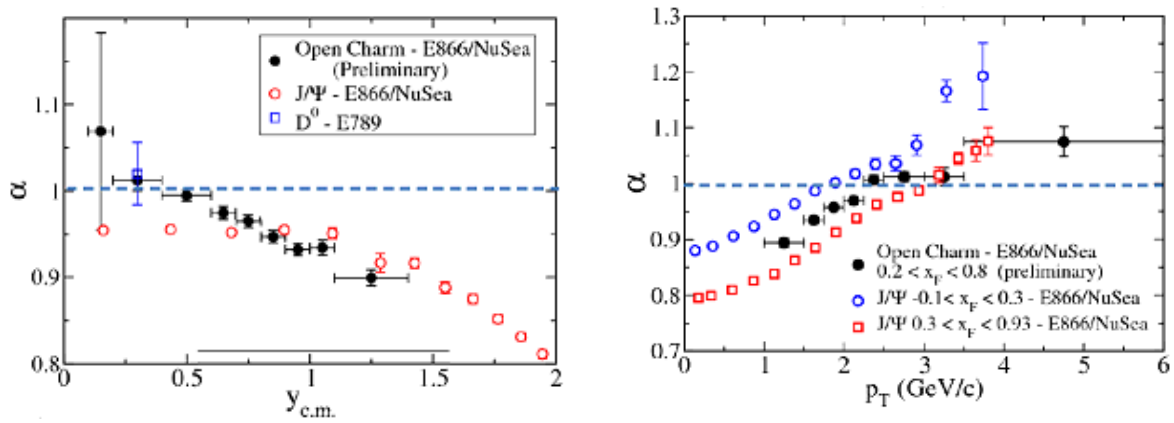

Figure 5.13: The parameter α of open charm and J/ψ as a function of rapidity (left) and p_{T} (right).

Figure 5.13 show α of open charm and J/ψ as a function of rapidity (left) and p_{T} (right). In the left panel of Fig. 5.13, α of open charm is unity near $y = 0$ and decreases gradually with increasing y. This result of $\alpha = 1$ at $y = 0$ could indicate that the shadowing effect is small. This is the same tendency with that in $d + \mathrm{Au}$ collisions at $\sqrt{s_{\mathrm{NN}}} = 200$ GeV, even though the small effect is expected since the related x region in the target nucleus is $x \sim 0.1$ where the shadowing effect is expected to be small compared with that of the RHIC energy ($x \sim 0.02$). For the forward rapidity region, α is smaller than unity. This might indicate that the modification of the charm production due to the shadowing. In a model [125], the intrinsic charm in a projectile is expected to contribute the charm production. Since the intrinsic charm in a nucleus is depend on $A^{2/3}$ in the model, the charm production in $p+A$ collisions is expected to be reduced compared with that in $p+p$ collisions. This is also a possible model to describe the experimental result at the forward rapidity. Therefore, it is difficult to discuss the modification of the charm production at the forward rapidity region.

5.5 Medium Modification of Heavy Quarks

PHENIX reported that the R_{AA} of heavy flavor electrons shows a strong suppression at high p_{T} as described in section 2.4.4. The R_{AA} value of heavy flavor electrons is about $R_{AA} = 0.35$ for $p_{\mathrm{T}} > 4$ GeV/c, which is similar with that of π^0. This clear suppression at high p_{T} is seen for 0-10%, 10-20%, 20-40% centrality and minimum bias events. This result indicates that not only light quarks, heavy quarks also lose their energy in the dense matter created in $\mathrm{Au} + \mathrm{Au}$ collisions.

The BDMPS and GLV models including gluon radiations failed to describe this strong suppression of heavy flavor electrons. These predictions show a larger R_{AA} compared with the data. The collisional energy loss is another possible model to describe the measured suppression of heavy flavor. The updated GLV model including both the radiative and the collisional energy loss can describe the substantial part of the energy loss. But there is still small difference between the model and the data.

Recently, the ratio of the bottom contribution to heavy flavor electrons was measured

in $p+p$ collisions at $\sqrt{s}$ = 200 GeV as shown in Fig. 5.8. The bottom contribution is about 40% relative to heavy flavor electrons and is increasing with $p_{\rm T}$. Using this result, we consider the energy loss of bottoms, although bottoms are expected to suffer smaller energy loss than that of charms due to their large mass. If the initial composition of charms and bottoms in Au + Au collisions were the same with that in $p+p$ collisions and bottoms suffer no energy loss in the dense matter, the expected R_{AA} is same or even a little larger than the measure R_{AA} within the statistical and the systematic uncertainty, even though in the case of all of charms are suppressed. This may interpret that bottoms also suffer an possible energy loss in the dense matter. But the current measurement can not set significant limits of the bottom energy loss.

5.6 Total Charm Cross Section

5.6.1 Calculation of Cross Section

In this section, we evaluate the total charm cross section per nucleon-nucleon collision. The procedure to obtain the total charm cross section is described step by step:

(1) We calculate the integrated invariant yield of charm electrons per nucleon-nucleon collision ($\frac{dN_e}{dy}(0.8 < p_{\rm T} < 4.0)/T_{AA}$) with the limited $p_{\rm T}$ range ($0.8 < p_{\rm T} < 4.0$ GeV/c). The $\frac{dN_e}{dy}(0.8 < p_{\rm T} < 4.0)/T_{AA}$ is equivalent to the integrated cross section of charm electrons per $N+N$ collisions ($\frac{d\sigma_e}{dy}$ $(0.8 < p_T < 4.0)$).

(2) Assuming the PYTHIA calculation can reproduce the spectral shapes of charm and bottom quarks, the $\frac{d\sigma_e}{dy}(0.8 < p_{\rm T} < 4.0)$ is extrapolated to the full $p_{\rm T}$ range. The conversion factor ($R_{p_{\rm T}} = \frac{d\sigma_e}{dy}(0.8 < p_{\rm T} < 4.0)/\frac{d\sigma_e}{dy}$) is 12.6%. The $R_{p_{\rm T}}$ is determined by the PYTHIA electron spectrum from charm and bottom decays.

$$\frac{d\sigma_e}{dy} = \frac{1}{R_{p_{\rm T}}}\frac{d\sigma_e}{dy}(0.8 < p_{\rm T} < 4.0) \tag{5.2}$$

(3) The electron cross section $\frac{d\sigma_e}{dy}$ is translated to the charm cross section $\frac{d\sigma_{c\bar{c}}}{dy}$ using a total branching ratio of charm decaying to electron. The total branching ratio of $BR(c \to e)$ is 9.5%. The bottom is neglected due to a small contribution for the integrated $\frac{d\sigma_e}{dy}$.

$$\frac{d\sigma_{c\bar{c}}}{dy} = \frac{1}{BR(c \to e)}\frac{d\sigma_e}{dy} \tag{5.3}$$

(4) The total charm cross section ($\sigma_{c\bar{c}}$) is finally obtained to extrapolate to the full rapidity range. It is assumed that the rapidity distribution of charm can be modeled by PYTHIA. The extrapolation factor (R_y) is 23.0%.

$$\sigma_{c\bar{c}} = \frac{1}{R_y}\frac{d\sigma_{c\bar{c}}}{dy} \tag{5.4}$$

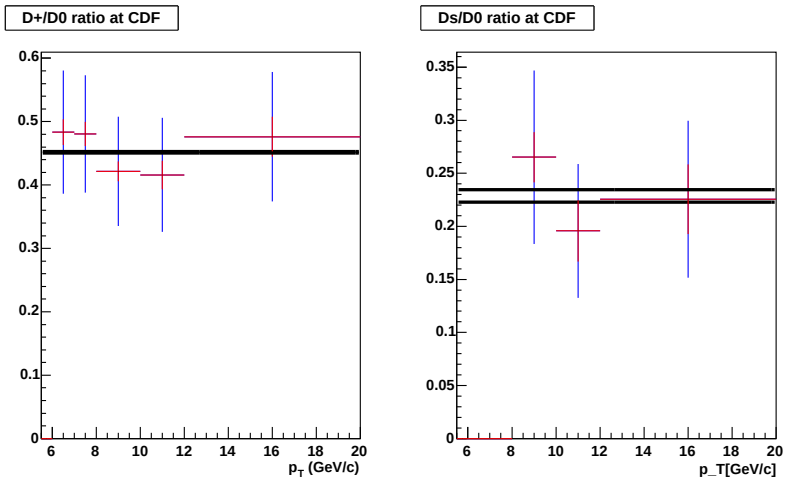

Figure 5.14: D^+/D^0 ratio (left) and D_s/D^0 ratio (right) measured at CDF [128].

Since the conversion and the extrapolation factors used in this analysis are determined by PYTHIA, we first describe a PYTHIA calculation with a modified set of parameters. We used PYTHIA 6.205 with $M_c = 1.25$ GeV/c^2, $M_b = 4.1$ GeV/c^2, $\langle k_{\rm T} \rangle = 1.5$ GeV/c, K factor = 3.5 and PDF = CTEQ5L for the input. Here, M_c and M_b are charm and bottom quark mass, $\langle k_{\rm T} \rangle$ is the width of intrinsic parton $k_{\rm T}$ smearing in a proton, and the K factor is a constant to take into account the higher order correction (e.g. NLO). These parameters are determined to reproduce the charm production data in lower energy experiments at SPS and FNAL [127, 126] and the charm electron production data at ISR experiments [22, 23, 24]. This set of the PYTHIA parameters were used for previous PHENIX electron analysis [114].

The total branching ratio of charm decaying to electron is obtained to combine the charmed hadron ratio and their electron branching ratios. The branching ratio is sensitive to the charmed hadron ratio, since the ratio of the charged D^+ meson is quit different from that of the neutral D^0 meson. The charmed hadron ratio in default PYTHIA does not agree with the experimental data. The CDF experiment reported the D^0 and D^+ cross section in $\sqrt{s} = 1.96$ TeV $p + \bar{p}$ collisions [128]. Figure 5.14 show the D^+/D^0 ratio (left) and D_s/D^0 ratio (right) measured at CDF. The STAR experiment also reported the D^+/D^0 ratio at $\sqrt{s_{\rm NN}} = 200$ GeV$d+$Au collisions [129]. In addition, the ratio in $e^+ + e^-$ experiments is summarized by the Particle Data Group [27].

From these experimental data, we assume in this analysis the these ratios to be 0.45, 0.25 and 0.1 for D^+/D^0, D_s/D^0 and Λ_c/D^0, respectively, as shown in Tab. 5.2. The total electron branching ratio ($BR(c \to e)$) is obtained by weighted averaging these electron branches with their charmed hadron ratios. This modification of the electron branch is applied to the PYTHIA calculation. This total branching ratio ($BR(c \to e)$) is also used when $\frac{d\sigma_e}{dy}$ is translated to $\frac{d\sigma_{c\bar{c}}}{dy}$ in step 3.

Figure 5.15 shows the differential cross section of electrons from charm and bottom decays calculated by PYTHIA. The green and blue points represent the charm and bottom contributions, and the red point is the combined contribution of charm and bottom,

Table 5.2: D^+/D^0, D_s/D^0, Λ_c/D^0 ratios in the experimental data and PYTHIA.

	CDF $(p+\bar{p})$	STAR $(d+\mathrm{Au})$	PDG $(e^+ + e^-$ at $\sqrt{s} = 91\mathrm{GeV})$	PYTHIA	This analysis
D^+/D^0	0.45	0.4		0.3	0.45 ± 0.1
D_s/D^0	0.23		0.29	0.2	0.25 ± 0.1
Λ_c/D^0			0.17	0.1	0.1 ± 0.05

Table 5.3: Electron branching ratio of charmed hadrons

Particles	Ratio to D^0	BR$(c \to e + X)$
D^0	1	$6.87 \pm 0.28\%$
D^+	0.45 ± 0.1	$17.2 \pm 1.9\%$
D_s	0.25 ± 0.1	$8 \pm 5\%$
Λ_c	0.1 ± 0.05	$4.5 \pm 1.7\%$
Total $BR(c \to e)$		$9.5 \pm 0.4\%$

Table 5.4: The parameters obtained by fitting the PYTHIA electron spectrum.

a $((c/\mathrm{GeV})^2)$	0.00101594
b $((\mathrm{GeV}/c))$	1.4598
c	4.11875
d $((c/\mathrm{GeV})^2)$	1.2852

respectively. Here, the PYTHIA electron spectrum is shown as the invariant yield using $T_{pp} = 1/\sigma_{pp} = 0.238$ mb^{-1} ($\sigma_{pp} = 42$ mb).

This PYTHIA electron spectrum is parameterized as follows:

$$f(p_{\mathrm{T}}) = a \cdot \left(\frac{1}{1 + p_{\mathrm{T}}/b + d \cdot p_{\mathrm{T}}^2} \right)^c , \tag{5.5}$$

where the parameters a, b, c and d are obtained by fitting. The magenta curve in Fig. 5.15 show the fit function. The obtained parameters are summarized in Tab. 5.4. Using the fit function, we obtained the conversion factor $R_{p_{\mathrm{T}}} = 12.6\%$.

Now all the extrapolation and the conversion factors are prepared. We can calculate the total charm cross section step by step. In step 1, In order to calculate the $d\sigma_e/dy(0.8 < p_{\mathrm{T}} < 4.0)$, the charm electron spectrum is scaled with T_{AA} and fit with the PYTHIA electron function within $0.8 < p_{\mathrm{T}} < 4.0$ GeV/c. In this fitting, the spectral shape is fixed and the normalization is only a free parameter. Figure 5.16 shows the scaled invariant yields of charm electrons ($\frac{1}{T_{AA}} \frac{1}{2\pi p_{\mathrm{T}}} \frac{dN_e}{dydp_{\mathrm{T}}}$) with the fit function. The panels from the top-left to the bottom-right correspond to minimum bias and the five centrality classes, respectively.

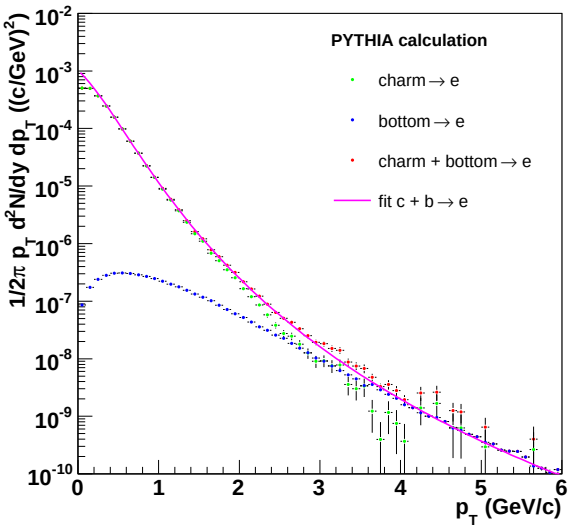

Figure 5.15: Invariant yield of electrons from charm and bottom decays calculated by PYTHIA. The green and the blue points represent the charm and the bottom contributions, and the red point is the combined contribution of charms and bottoms, respectively.

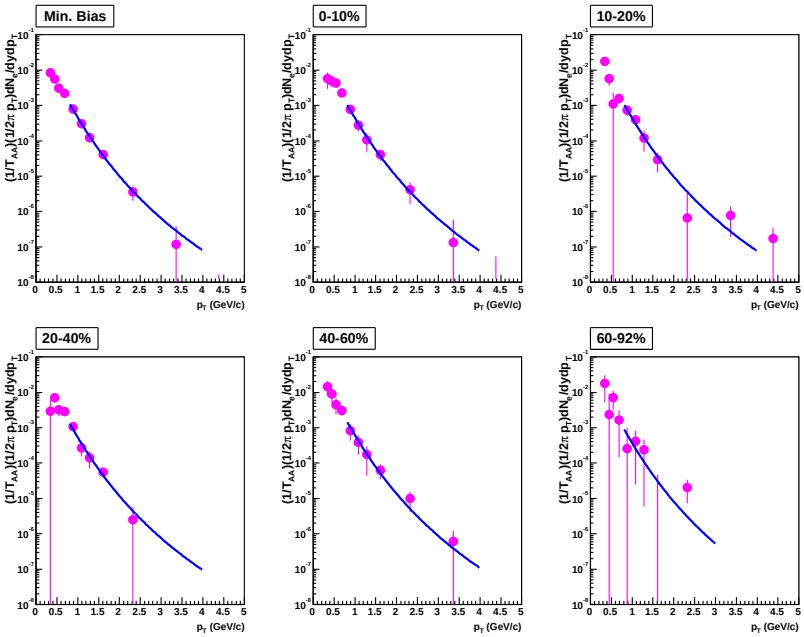

Figure 5.16: Scaled differential invariant yields $\frac{1}{T_{AA}}\frac{1}{2\pi p_{\mathrm{T}}}\frac{d\sigma_e}{dydp_{\mathrm{T}}}$ for minimum bias and the five centrality classes. The spectrum is fit by the PYTHIA electron function with $0.8 < p_{\mathrm{T}} < 4.0$ GeV/c (blue)

Using the fit function, the integrated yield $d\sigma_e/dy(0.8 < p_{\rm T} < 4.0)$ is calculated. The result is summarized in Tab. 5.5. Then, these integrated $d\sigma_e/dy(0.8 < p_{\rm T} < 4.0)$ are converted to the total charm cross section $\sigma_{c\bar{c}}$ per $N + N$ collision.

Table 5.5: $d\sigma_e/dy$ $(0.8 < p_{\rm T} < 4.0$ GeV/$c)$ for minimum bias and the five centrality classes. The systematic uncertainty represents the combined uncertainty of the spectrum and T_{AA}.

Centrality	$N_{\rm coll}$	dN_e/dy (μb) $(0.8 < p_{\rm T} < 4.0)$	stat.error	sys.error
Min. bias	257.8	1.707	$\pm$ 0.157	$\pm$ 0.373
0-10 %	955.4	1.638	$\pm$ 0.256	$\pm$ 0.357
10-20 %	602.6	1.634	$\pm$ 0.316	$\pm$ 0.349
20-40 %	296.8	2.006	$\pm$ 0.321	$\pm$ 0.446
40-60 %	90.65	2.308	$\pm$ 0.562	$\pm$ 0.559
60-92 %	14.83	1.382	$\pm$ 1.036	$\pm$ 0.486

To estimate the systematic uncertainty on the total charm cross section, we consider the following sources of the uncertainty:

(1) the uncertainty in $dN_e/dy(0.8 < p_{\rm T} < 4.0)$ obtained from the p_T distribution of heavy flavor electrons.

(2) the uncertainty in $N_{\rm coll}$.

(3) the uncertainty in the shape of the fit function.

(4) the uncertainty in the method to calculate the total charm cross section.

(5) the uncertainty in the $p_{\rm T}$ range of the fitting.

The uncertainty of $dN_e/dy(0.8 < p_{\rm T} < 4.0)$ of heavy flavor electrons (source (1)) is estimated (21%) by refitting the electron spectrum at the higher and lower error band. The uncertainties are summarized in Tab. 5.5. Here, the uncertainty in Tab. 5.5 represents the combined uncertainty of the source (1) and (2).

For the source (3), we tested the two other methods to calculate $dN_e/dy(0.8 < p_{\rm T} < 4.0)$. One is to count the bin entries in the $p_{\rm T}$ range and the other is to fit the spectrum with a power-law function. The uncertainty of the source (3) is summarized in Tab. 5.7.

For the source (4), we test the another conversion and the extrapolation factors , $R_{p_{\rm T}}$ in step (2), $BR(c \to e)$ in step (3) and R_y (4). Since the intrinsic $\langle k_{\rm T} \rangle$ can modify the shape of the $p_{\rm T}$ spectrum, we test the two other $\langle k_{\rm T} \rangle$ values, 1.0 and 2.0 instead of 1.5 GeV/c. Then, the $R_{p_{\rm T}} = 11.5\%$ and 14.1% is determined for $\langle k_{\rm T} \rangle = 1.0$ and 2.0 GeV/c, respectively. Thus, the $R_{p_{\rm T}}$ uncertainty is assigned as 10.1%. The $BR(c \to e)$ uncertainty is estimated using the errors of the charmed hadron ratios in Tab. 5.2 and assigned as 4.3%. The rapidity distribution of the PYTHIA charm calculation is studied. Since the rapidity distribution is sensitive to the initial state gluon distribution,

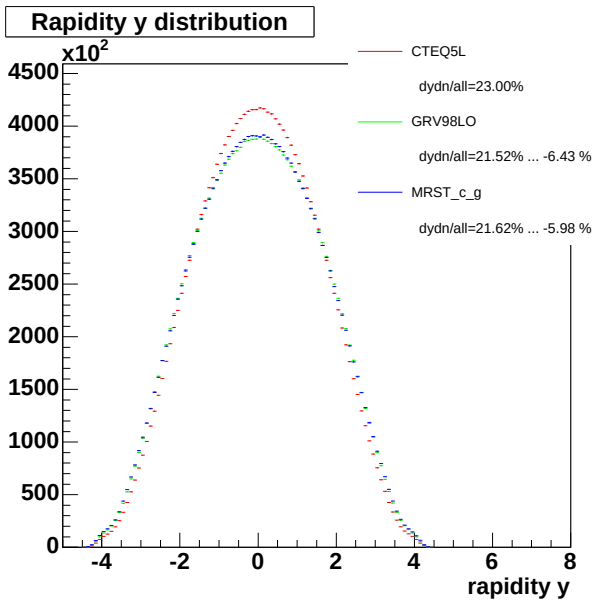

Figure 5.17: Rapidity distribution of charmed hadrons.

Table 5.6: The systematic uncertainty of the source (4).

	step	uncertainty
$R_{p_{\mathrm{T}}}$	step (2)	10.1%
$BR(c \to e)$	step (3)	4.3%
R_y	step (4)	6.2%
Total for $d\sigma_{c\bar{c}}/dy$	step (2) and (3)	11.0%
Total for $\sigma_{c\bar{c}}$	all 3 steps	12.6 %

we test the two other PDFs , GRV98LO and MRST(c-g) in stead of CTEQ5L. Fig. 5.17 shows the rapidity distributions of the charmed hadron. The red, the green and the blue histograms correspond to CTEQ5L, GRV98LO and MRST(c-g), respectively. From these distributions, The extrapolation factor $R_y = 23.0\%, 21.5\%$ and 21.6% are determined for CTEQ5L, GRV98LO and MRST(c-g), respectively. The relative difference of these values is 6.2% which is assigned as the R_y uncertainty. Total uncertainty of the source (4) is estimated by adding these uncertainties in quadrature. The systematic uncertainty of the source (4) is summarized in Tab. 5.6.

In order to estimate the uncertainty of the source (5), we test the p_{T} range of $0.6 - 4.0$ GeV/c to fit the charm electron spectrum, then calculate the integrated invariant yield using same p_{T} range $dN_e/dy(0.6 < p_{\mathrm{T}} < 4.0)$ and the total charm cross section. The conversion factor $R_{p_{\mathrm{T}}}$ for $dN_e/dy(0.6 < p_{\mathrm{T}} < 4.0)$ is 25.1% determined using the PYTHIA electron spectrum. Then, these total charm cross sections with the different p_{T} fit ranges are compared to estimate the uncertainty. The difference of these charm cross sections is assigned as the uncertainty of the source (5). Since all the systematic uncertainties

are independent each other, these uncertainties are added in quadrature to obtain the total systematic uncertainty. All the systematic uncertainties and total uncertainty are summarized in Tab. 5.7.

Finally, we calculated the differential ($d\sigma_{c\bar{c}}/dy$) and the total charm cross section ($\sigma_{c\bar{c}}$). The total charm cross section in minimum bias Au + Au collisions is $\sigma_{c\bar{c}} = 622 \pm 57 \pm 160$ μb. The result for minimum bias and the five centrality classes are summarized in Tab. 5.8.

Recently, the total charm cross section is updated using the new data with much higher statistics in Run 4 period. The updated total charm cross section in minimum bias Au + Au collisions at $\sqrt{s_{\rm NN}} = 200$ GeV is $\sigma_{c\bar{c}} = 568 \pm 8 \pm 150$ μb. The method and the result of the total charm cross section in Run4 are described in detail in Appendix E. Even though the statistical error is much reduced, the systematic uncertainty in Run 4 is similar compared to that in Run 2. The obtained cross section in Run 4 is consistent with that in Run 2 within the statistical and the systematic uncertainty. The comparison of the total charm cross section in $\sqrt{s} = 200$ GeV is described in next section.

Table 5.7: All the systematic uncertainties are summarized and the total uncertainty is obtained by adding these uncertainties in quadrature.

	Min.bias	0-10%	10-20%	20-40%	40-60%	60-92%
source (1)	20.6%	20.7%	20.4%	20.7%	21.0%	20.5%
source (2)	7.3%	6.9%	7.0%	8.2%	12.0%	28.6%
source (3)	3.8%	3.4%	4.6%	5.5%	0.3%	5.2%
source (4)	11.0% for $d\sigma_{c\bar{c}}/dy$ and 12.6% for $\sigma_{c\bar{c}}$					
source (5)	2.5%	5.9 %	8.0%	7.7%	4.2%	0.6%
Total for $d\sigma_{c\bar{c}}/dy$	24.8%	24.6%	24.5%	25.4%	26.6%	37.2%
Total for $\sigma_{c\bar{c}}$	25.5%	25.4%	25.2%	26.1%	27.3%	37.7%

Table 5.8: Centrality class, $N_{\rm coll}$, nuclear overlap function (T_{AA}), charm cross section ($d\sigma_{c\bar{c}}/dy$) and total charm cross section ($\sigma_{c\bar{c}}$) in Au + Au collisions at $\sqrt{s_{\rm NN}} = 200$ GeV.

Centrality	$N_{\rm coll}$	T_{AA} (mb$^-$1)	$d\sigma_{c\bar{c}}/dy$ (μb)	$\sigma_{c\bar{c}}$ (μb)
Min. bias	257.8±25.4	6.14±0.45	143±13±36	622± 57±160
0-10%	955.4±93.6	22.76±1.56	137±21±35	597± 93±156
10-20%	602.6±59.3	14.35±1.00	137±26±35	596±115±158
20-40%	296.8±31.1	7.07±0.58	168±27±45	731±117±199
40-60%	90.7±11.8	2.16±0.26	193±47±52	841±205±232
60-92%	14.5± 4.0	0.35±0.10	116±87±43	504±378±190

5.6.2 Comparison with Di-electron Measurement

There is an alternative measurement of the total charm cross section. This total charm cross section is measured by PHENIX using the mass spectrum of electron-positron pairs in $p+p$ collisions at $\sqrt{s} = 200$ GeV [132]. This result allows us to cross-check the charm cross section.

After the combinatorial and the correlated background are subtracted, the measured mass spectrum of e^+e^- pairs is compared with a cocktail calculation of e^+e^- pairs from light meson decays and vector meson decays. Then, the cocktail calculation can describe the measured mass spectrum of e^+e^- pairs in the mass region below $M_{e^+e^-} < 1.1$ GeV/c^2 within the systematic uncertainty. On the other hand, except for the vector meson peak, the e^+e^- pair yield in $M_{e^+e^-} > 1.1$ GeV/c^2 is dominated by semi-leptonic decays of charmed hadrons correlated through flavor conservation. Figure 5.18 shows the measured mass spectrum of e^+e^- pairs comparing the cocktail calculation. In addition to charm hadrons, the remaining contributions from bottom hadrons and Drell-Yan calculated by PYTHIA are also shown in Fig. 5.18. To determine the charm contribution, the pair yield is integrated within $1.1 < M_{e^+e^-} < 2.5$ GeV/c^2 after subtracting the cocktail of the light neutral mesons and the vector mesons. The integrated pair yield is extrapolated to zero e^+e^- mass using PYTHIA and translated to charm pair yield using the known branching ratio. Then, assuming the rapidity distribution from NLO pQCD, the charm cross section is obtained as $\sigma_{c\bar{c}} = 544 \pm 39(\text{stat}) \pm 142(\text{sys}) \pm 200(\text{model})\mu\text{b}$.

The result in the e^+e^- pair analysis is compared with the charm electron measurement in $p+p$ and Au + Au collisions at $\sqrt{s_{\text{NN}}} = 200$ GeV. Figure 5.19 shows the comparison of the total charm cross section measured by the single electron measurements and the e^+e^- pair measurement. All these charm cross sections measured by PHENIX are consistent each other within the statistical and systematic uncertainty. The STAR collaboration reported 2-3 times larger cross section in $d+$Au collisions [133]. The charm cross section by the FONLL calculation is smaller but compatible with these data within its uncertainty.

5.6.3 Collision Energy Dependence

The obtained total charm cross section in Au + Au collisions at $\sqrt{s_{\text{NN}}} = 200$ GeV is compared with those measured in the other experiments at several beam energies. The charm cross sections are measured in the fixed target experiments at SPS/FNAL [126, 135, 136, 137] and the collider experiments at S$\bar{\text{p}}$pS [134]. Figure 5.20 shows the total charm cross sections as a function of the collision energy $\sqrt{s}$. The theoretical curves of the charm cross section calculated by PYTHIA (solid) and NLO pQCD (dashed) are also shown. The shaded band in Fig. 5.20 represents the systematic uncertainty of the NLO pQCD calculation. The input parameters for PYTHIA is chosen to reproduce the charm data as described in section 5.6.1. For the NLO pQCD calculation, HVQMNR [130] is used to calculate the charm cross section with $M_c = 1.5$ GeV/c^2, $\mu_F = 2M_c$, $0.5\,M_c < \mu_R < 2\,M_c$ and CTEQ5M PDF as input.

The data obtained in this thesis are consistent with the energy dependences of the total charm cross section calculated by both PYTHIA and NLO pQCD within theoretical

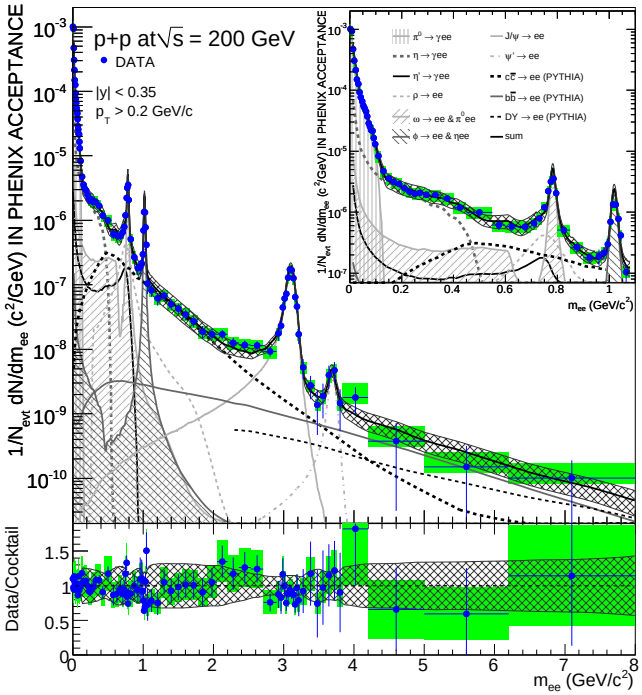

Figure 5.18: (top) The invariant mass spectrum of e^+e^- pairs in $p+p$ collisions [132]. The points show the measured data with the statistical(bar) and the systematic(shades) errors. The curves represent the cocktail calculation of the light neutral mesons and the vector mesons. The contributions from c and b quarks and Drell-Yan are also shown. (bottom) The ratio of the data to the cocktail.

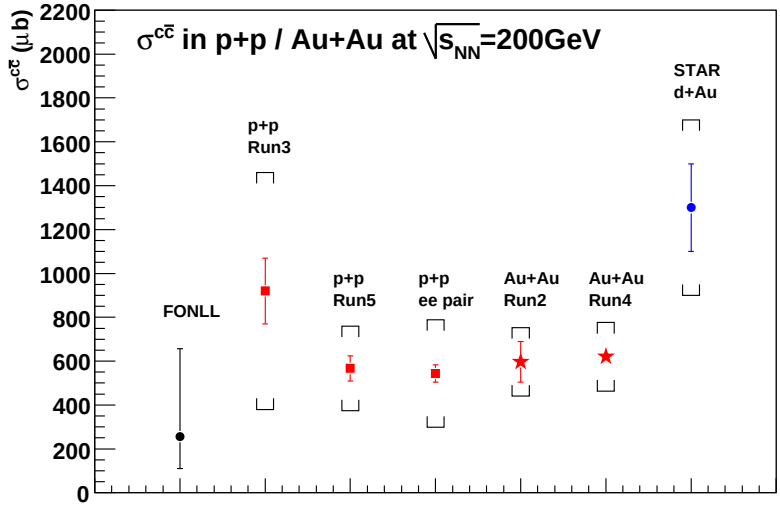

Figure 5.19: The comparison of the total charm cross sections from the single electrons measurements and the e^+e^- pair measurement.

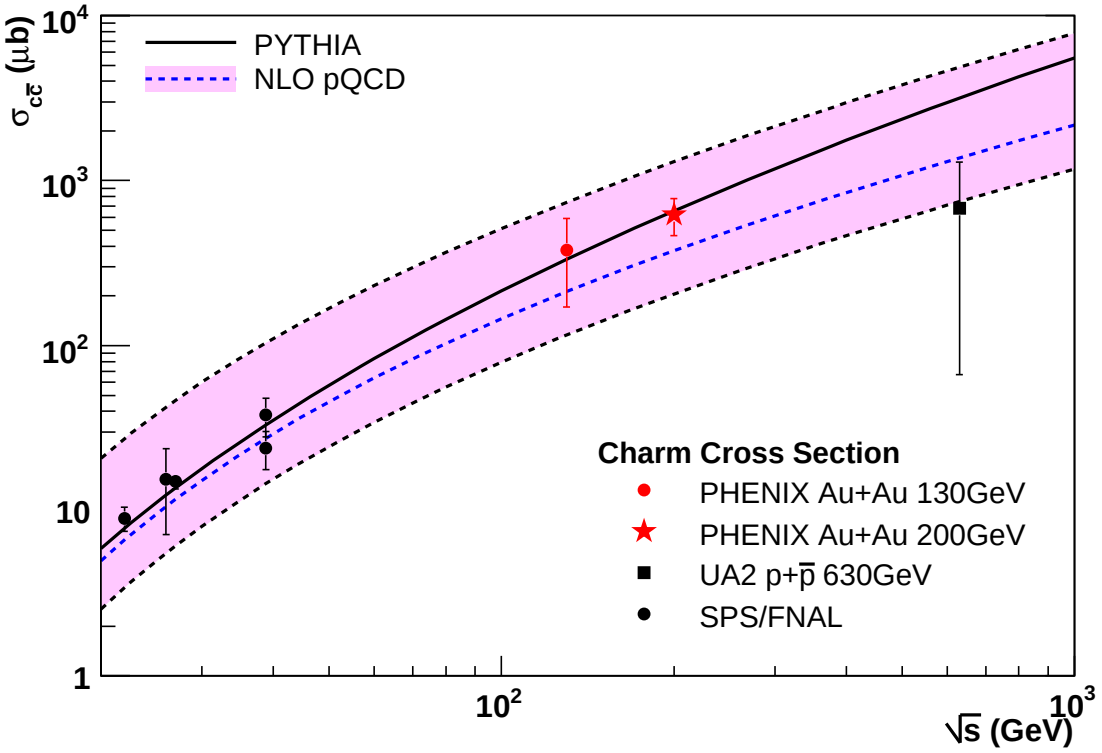

Figure 5.20: The total charm cross sections as a function of the collision energy. The theoretical curves by PYTHIA and NLO pQCD are also shown.

uncertainties. This indicates that the charm production is well reproduced by pQCD. Therefore, as expected, the most charm quarks are produced in the initial stage of the space time evolution in the heavy ion collisions.

Chapter 6

Summary and Conclusions

We have studied the centrality dependence of charm production in Au + Au collisions at $\sqrt{s_{\rm NN}}$ = 200 GeV. We have measured the single electrons from semi-leptonic decays of heavy flavors (charms and bottoms) in Au + Au collisions during Run 2 period.

In Run 2, RHIC first operated with the full energy in Au + Au collisions. PHENIX measured inclusive electrons in Au + Au collisions at $\sqrt{s_{\rm NN}}$ = 200 GeV. A photon converter was installed in a part of run period. By comparing the inclusive electron yield with and without the converter, signal electrons are extracted from large amount of photonic backgrounds which are electrons from Dalitz decays of light neutral mesons and photon conversions. After subtracting the backgrounds of K_{e3} and vector meson decays, only the significant source of non-photonic electrons is the semi-leptonic decays of heavy flavors, dominantly charm at low $p_{\rm T}$. Since the contributions from J/ψ decays and Drell-Yan process is small, they are neglected.

We have measured the invariant differential yields of heavy flavor electrons for minimum bias Au + Au collisions and the five centrality classes, 0-10%, 10-20%, 20-40%, 40-60% and 60-92% centralities, within the $p_{\rm T}$ range from 0.3 to 4.0 GeV/c. These yields are compared with that in $p+p$ collisions at $\sqrt{s}$ = 200 GeV scaled with the number of binary nucleon-nucleon collisions $N_{\rm coll}$, and are found to be consistent within relatively large error. Since the cross section of heavy flavor electrons in $p+p$ collisions agrees with a NLO pQCD theory (FONLL) with a normalization factor of $1.71 \pm 0.02 \pm 0.18$, the invariant yield scaled by $N_{\rm coll}$ in Au + Au collisions also agrees with the FONLL pQCD theory within the errors in the measured $p_{\rm T}$ region.

To quantify the centrality dependence of the charm production, the integrated yields of charm electrons $dN_e/dy/N_{\rm coll}(0.8 < p_{\rm T} < 4.0$ GeV/$c)$ are calculated for minimum bias and 0-10%, 10-20%, 20-40%, 40-60% and 60-92% centralities, and these yields are fitted with $AN_{\rm coll}^{\alpha}$ for the linearity test. We found $\alpha = 0.938 \pm 0.075({\rm stat}) \pm 0.018({\rm sys})$. This shows that the centrality dependence of the total charm production is consistent with $N_{\rm coll}$ scaling. This result is confirmed by the new data with higher statistic measured in Run 4. The updated result of the linearity test is $\alpha = 1.0097 \pm 0.0094({\rm stat}) \pm 0.0403({\rm sys})$. This result is consistent with the finding of energy loss of heavy quarks in the dense matter created in high energy heavy ion collisions. Since the final state effects such as the energy loss affect only the momentum distribution of charm, they have little or no effect on the total charm yield. Therefore, the result indicates that most charm quarks are produced

by point-like pQCD processes in the initial stage of space time evolution in high energy heavy ion collisions.

The total charm cross sections per nucleon-nucleon collision are calculated for minimum bias Au + Au collisions and the five centrality classes. The obtained charm cross section per $N + N$ collision is $\sigma_{c\bar{c}} = 622 \pm 57(\text{stat}) \pm 160(\text{sys})$ μb in minimum bias Au+Au collisions. In addition, the cross section is updated in Run 4 analysis as $\sigma_{c\bar{c}} = 568 \pm 8(\text{stat}) \pm 150(\text{sys})$ μb. These cross sections are confirmed by a complementary measurement of e^+e^- pairs. By comparing a NLO pQCD prediction, the obtained cross section is consistent with a NLO pQCD prediction within theoretical error.

The N_{coll} scaling of the total charm production provides an important information for the initial nuclear effect, e.g. Cronin effect and nuclear shadowing effect. From our results, no significant initial nuclear effect is observed. However, the present data can not exclude a small initial nuclear effect or possible cancellation of these effects. We need more systematic study of collision system, especially including data in d + Au collisions. This can help to understand the initial nuclear effects in Au + Au collisions.

High p_{T} suppression of heavy quarks has been observed in the R_{AA} measurement of heavy flavor electrons in central Au + Au collisions. It is a surprising discovery that the magnitude of heavy quark suppression is almost same with that of light quark at high p_{T}. This observation is not well explained by recent theoretical models for the heavy quark energy loss. In addition, the measurement of $(b \to e)/(b \to e + c \to e)$ in $p + p$ collisions by partial reconstruction of D meson shows the significant contribution of bottom quark above $p_{\text{T}} > 4$ GeV/c. Although theoretical models predict that heavy quarks suffer smaller energy loss than light quarks such as dead cone effect due to their large mass, this result indicates that not only charms, but bottoms could suffer energy losses.

In order to understand the initial gluon density, the systematic study of the heavy flavor production in $p + p$, d + Au and Au + Au collisions is necessary with a much large amount of statistics. The d + Au data in Run 7 with 20 times large statistics is now analyzed for the systematic study. In addition, to understand better the energy loss of heavy quarks in the dense matter, it is necessary to measure the R_{AA} of D and B mesons separately. The PHENIX experiment plans to install a silicon vertex detector (VTX) in order to directly measure D and B meson by reconstructing the secondary decay vertex of these mesons. Furthermore, high luminosity upgrade of RHIC facility is underway. Therefore, the upcoming experimental results with the new detector and much higher statistics will be shown in the near future.

Acknowledgments

First of all, I would like to appreciate all the people who advise and support my thesis work and school days. I would like to thank my supervisor Prof. T. Sugitate. He gave me the continues instruction and supported my student life at Hiroshima University. Once I gave up my thesis halfway and got a job. After the termination of my doctor course for a few years, I decided to restart my thesis work. At that time, he advised me to get a good start again. I would like to express my gratitude to Dr. Y. Akiba for his continues support. This thesis would never be finished without him. His valuable advises and discussions always encouraged me to get better understandings of both the analysis, the heavy quark productions and the phenomena of heavy ion collisions. I am grateful to Dr. K. Homma for his longstanding help. He taught me the way of thinking of experimental physics. I appreciate Prof. K. Shigaki for his arrangement of activity both at Hiroshima and BNL.

I wish to acknowledge all the PHENIX collaboration. I am obliged to the spokespersons of the PHENIX experiment, Prof. W. A. Zajc and Prof. B. V. Jacak for their arrangement of my research activity in PHENIX. I appreciate to the members of the paper preparation group and the internal review committee, Dr. V. Cianciolo, Prof. M. Rosati, Dr. S. Kelly, Prof. J.-C. Peng, Dr. A. Bazilevsky and Dr. A. Denisov for their combined effort of the publication. I would like to thank Dr. R. Averbeck and Dr. S. Butsyk for their advices and comments on my electron analysis.

I would like to express my thank to the PHENIX-J group. I acknowledge Prof. H. Hamagaki for his work as a leader of the PHENIX-J group and the financial support. I would like to thank Dr. K. Ozawa for his advices and comments on both research and life at BNL. I appreciate the chief scientist, Dr. H. En'yo for his various advices and financial support. He also gave me a chance to restart my thesis work. I wish to express my thank to Prof. Y. Miake for his help. He kindly gave me a working place in his laboratory.

I would like to thank Dr. H. Ohnishi, Dr. T. Nakamura, Dr. A. Enokizono and Dr. T. Kohama. We worked together for the maintenance and the operation of the BBC subsystem. With their help, I could handle my task as a BBC expert. I also appreciate Dr. C. Y. Chi, Dr. C. Mickey and Dr. S. Belikov for their cooperation of the BBC operation. I would like to express my deep thank to Dr. M. Kaneta, Dr. T. Chujo, Dr. A. Taketani, Prof. N. Saito, Dr. Y. Goto, Prof. K. Kurita, Dr. H. Torii, Dr. A. Kiyomichi, Dr. K. Okada, Dr. S. Sato, Prof. S. Esumi and Prof. M. Inaba for their instructive advices and discussions. In particular, Dr. M. Kaneta gave me a lot of supports for both my research and life at BNL. By discussed with Prof. S. Esumi and Dr. T. Chujo, I could know the latest understanding of QGP and the most interesting topics on heavy ion collisions. I wish to thank to the member of RIKEN-CCJ, Dr. T. Ichihara, Dr. Y. Watanabe and Dr. S. Yokkaichi for their maintenance works of CCJ. The main part of my analysis was

performed by CCJ.

I spent most part of my graduate school days at BNL. I would like to thank all the Japanese colleague who worked together at BNL, Mr. T. Matsumoto, Dr. S. Kametani, Dr. H. Masui, Dr. S. Sakai, Dr. T. Horaguchi, Dr. F. Kajihara, Dr. M. Konno, Dr. M. Shimomura, Dr. T. Gunji, Dr. T. Isobe, Dr. M. Togawa, Dr. Y. Fukao and Mr. Y. Nagata. I would also like to thank all the member of quark physics laboratory at Hiroshima University, Mr. T. Uzumaki, Mr. N. Sugita, Mr. Y. Tsuchimoto, Mr. R. Kohara, Dr. H. Harada, Mr. K. Haruna, Mr. Y. Nakamiya, Ms. M. Ouchida and Mr. D. Watanabe. I enjoyed my school days with their discussions and conversations. I wish to thank all the member of high energy nuclear physics group at University of Tsukuba, Mr. Y. Ikeda, Mr. K. Watanabe, Mr. M. Sano, Mr. D. Sakata, Ms. M. Kajigaya, Ms. M. Kimura, Mr. H. Yokoyama, Mr. E. Hamada, Mr. T. Todoroki, Mr. Y. Sekine, Mr. T. Takeuchi, Mr. S. Mizuno, Mr. Y. Watanabe, Mr. Y. Kondo, Mr. S. Kubota, Ms. H. Sakai and Mr. S. Kato. After I started my thesis work again, I had a very good time to discuss and talk with them. The journal club held in the Tsukuba laboratory was very useful for me to remember and understand the phenomena of heavy ion collisions.

I would like to express my greatest thanks to my parents, father Masao and mother Masami for their continues supports. With their helps, I could start again and finish my thesis work.

Appendix A

Simulation Condition

A.1 Comparison between Read Data and Simulation

The detector responses of the electron ID variables in the real data are compared with that in the simulation for several momentum classes. The momentum is subdivided for 11 classes which correspond to 0.2-0.3, 0.3-0.4, 0.4-0.5, 0.5-0.6, 0.6-0.8, 0.8-1.0, 1.0-1.5, 1.5-2.0, 2.0-3.0, 3.0-5.0 and 5.0-10.0 GeV/c, respectively. All the variables in the simulation are tuned and/or smeared to reproduce the real data whether the response is significantly different.

Figure A.1 and A.2 show the emcsdphi_e and emcsdz_e distributions measured by the PbSc EMCal. The black and red histograms correspond to the real data and the simulation. The left-top to the right-bottom panels correspond to the lower to the higher momentum classes. Although the statistics in the real data is too small for higher momentum class, the response in the simulation is in good agreement with the real data . The other comparisons are emcsdphi_e and emcsdz_e for the PbGl EMCal, n0, chi2/npe0 and disp for the RICH, dep for the PbSc and PbGl EMCal, and emcdt for the EMCal are shown in Fig. A.3, A.4, A.5, A.6 A.7, A.8, A.9 and A.10, respectively. These figures shows that the responses in the simulation are in good agreement with the real data.

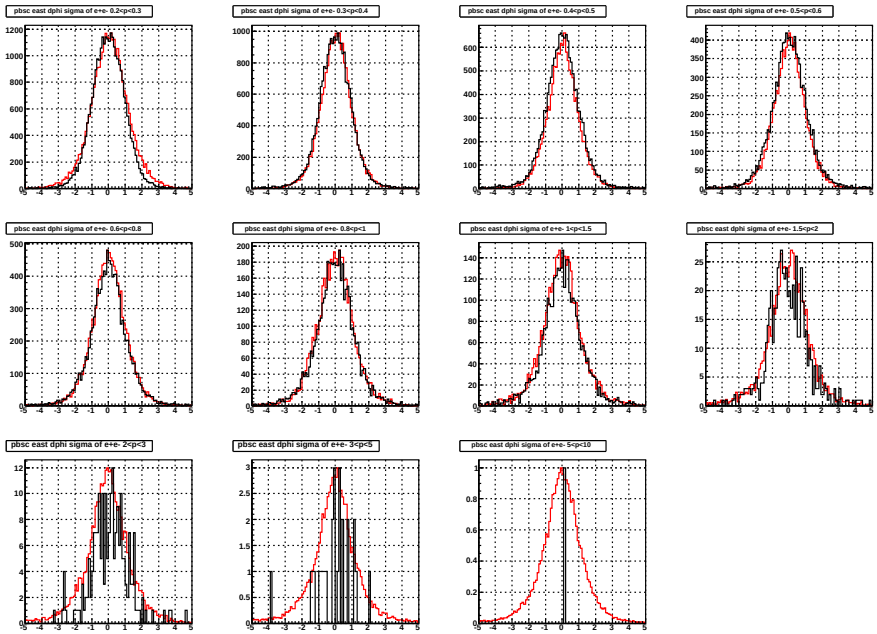

Figure A.1: Comparisons of emcsdphi_e measured at the PbSc EMCal for several momentum classes. The black and the red histograms correspond to the real data and the simulation, respectively.

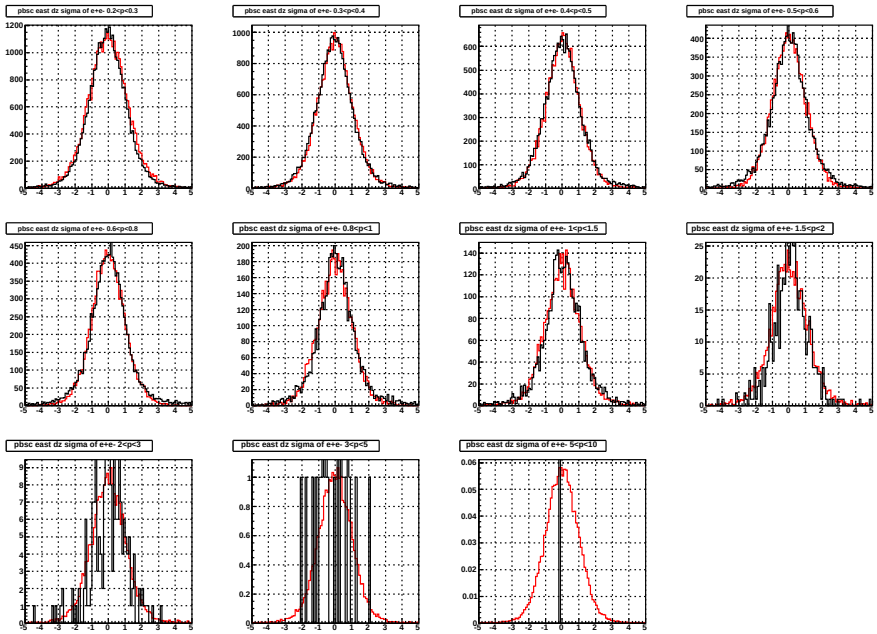

Figure A.2: Comparisons of emcsdz_e measured at the PbSc EMCal for several momentum classes. The black and the red histograms correspond to the real data and the simulation, respectively.

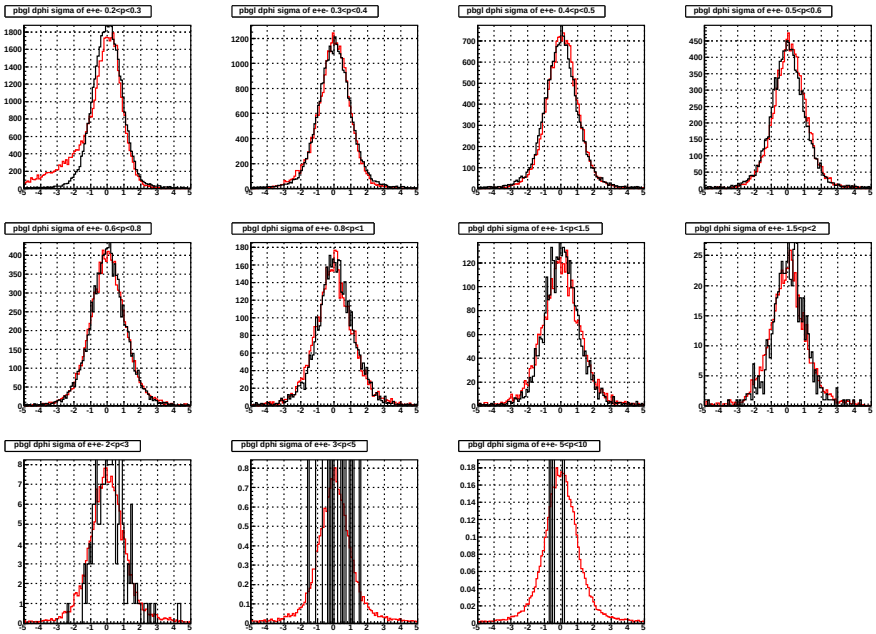

Figure A.3: Comparisons of emcsdphi_e measured at the PbGl EMCal for several momentum classes. The black and the red histograms correspond to the real data and the simulation, respectively.

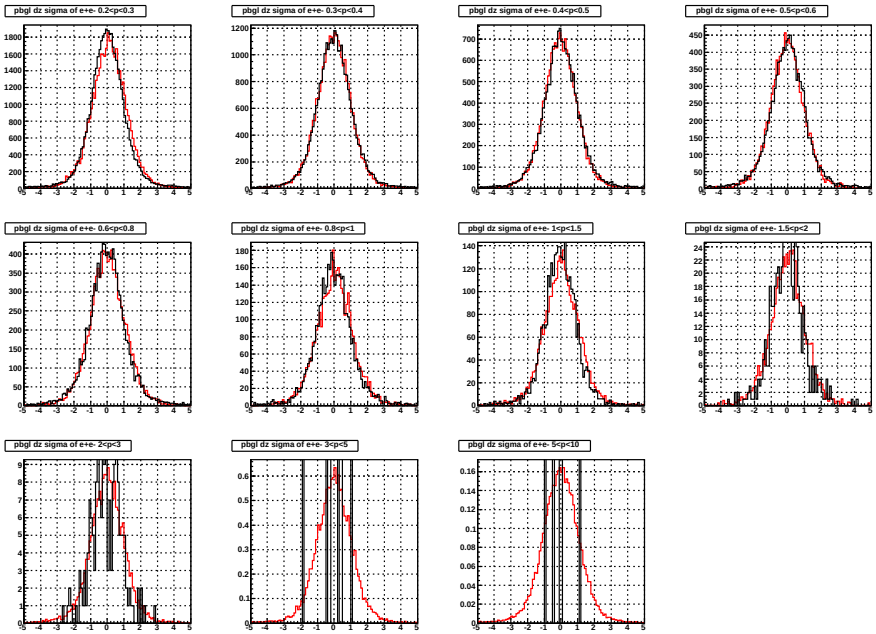

Figure A.4: Comparisons of emcsdz_e measured at the PbGl EMCal for several momentum classes. The black and the red histograms correspond to the real data and the simulation, respectively.

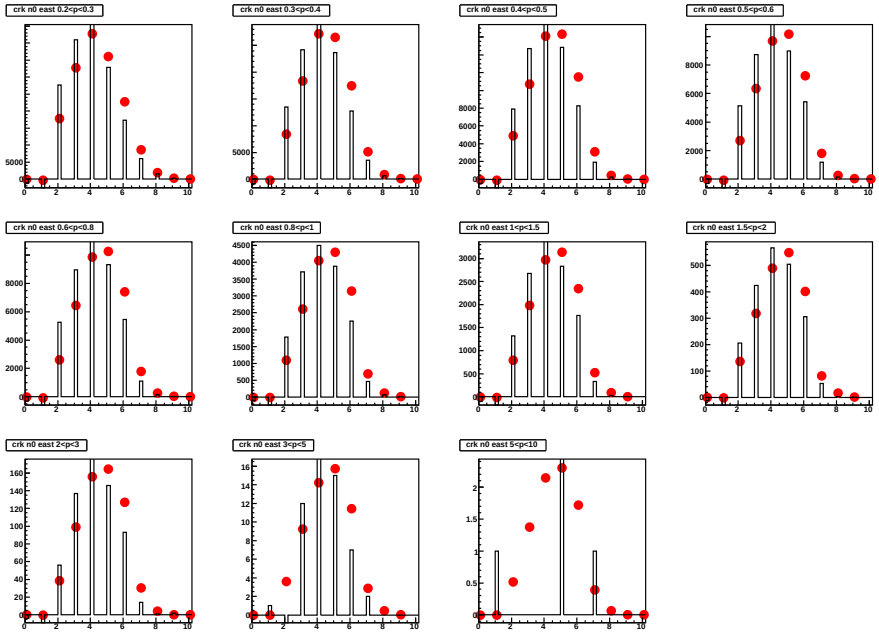

Figure A.5: Comparisons of n0 for several momentum classes. The black and the red histograms correspond to the real data and the simulation, respectively.

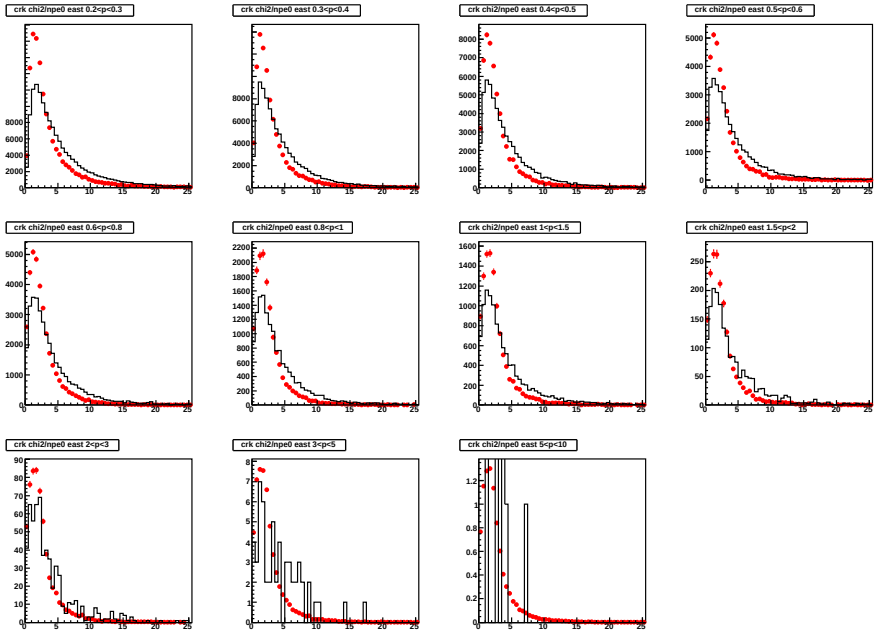

Figure A.6: Comparisons of chi2/npe0 for several momentum classes. The black and the red histograms correspond to the real data and the simulation, respectively.

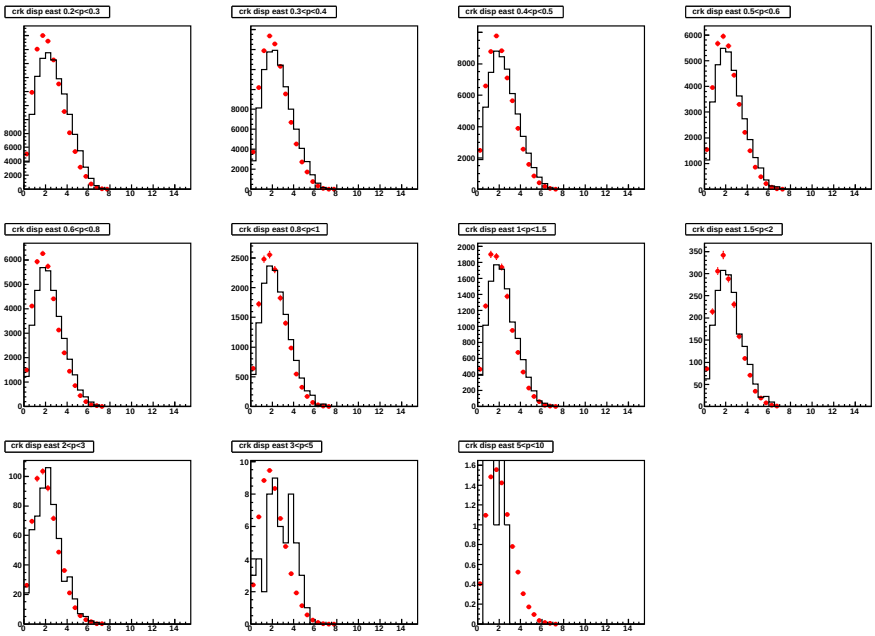

Figure A.7: Comparisons of disp for several momentum classes. The black and the red histograms correspond to the real data and the simulation, respectively.

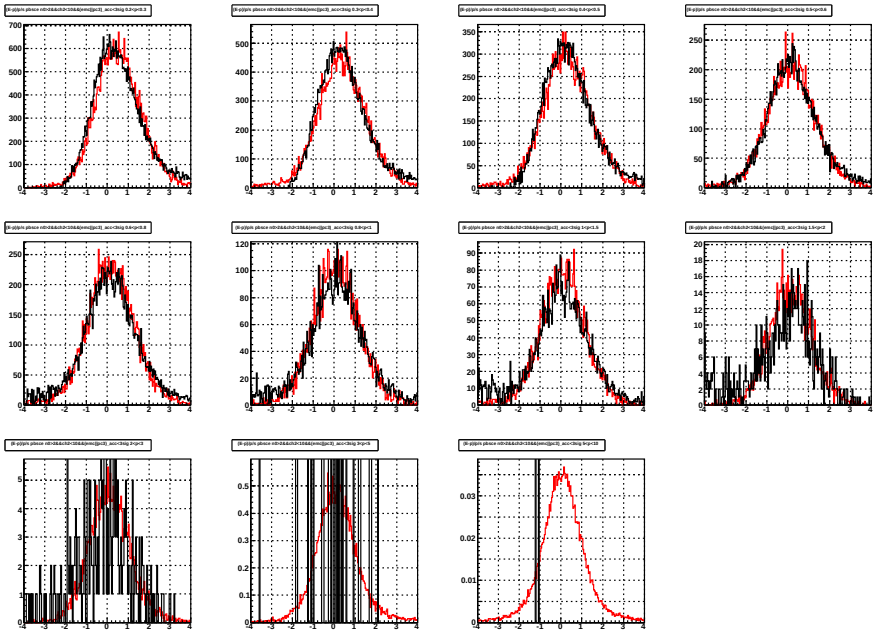

Figure A.8: Comparisons of dep measured at the PbSc EMCal for several momentum classes. The black and the red histograms correspond to the real data and the simulation, respectively.

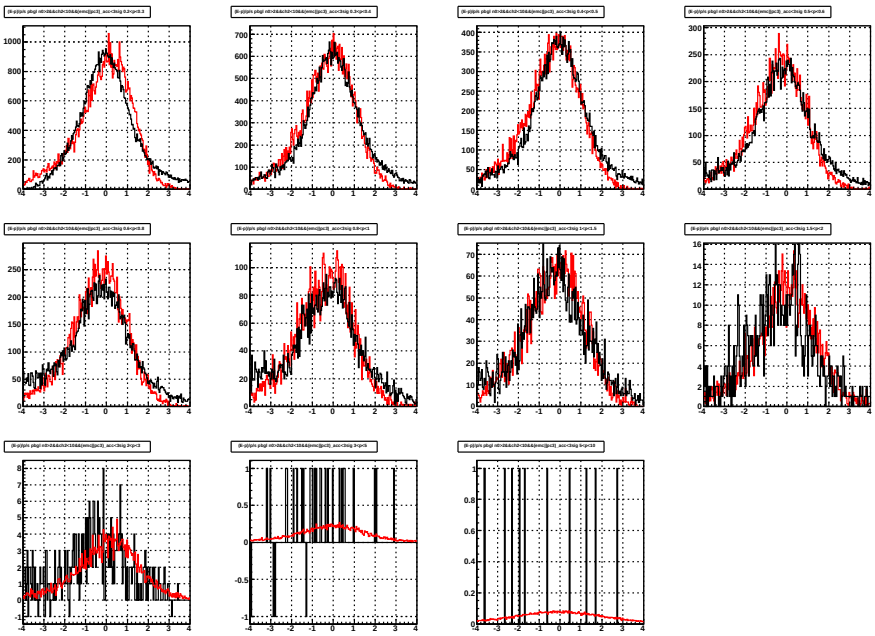

Figure A.9: Comparisons of dep measured at the PbGl EMCal for several momentum classes. The black and the red histograms correspond to the real data and the simulation, respectively.

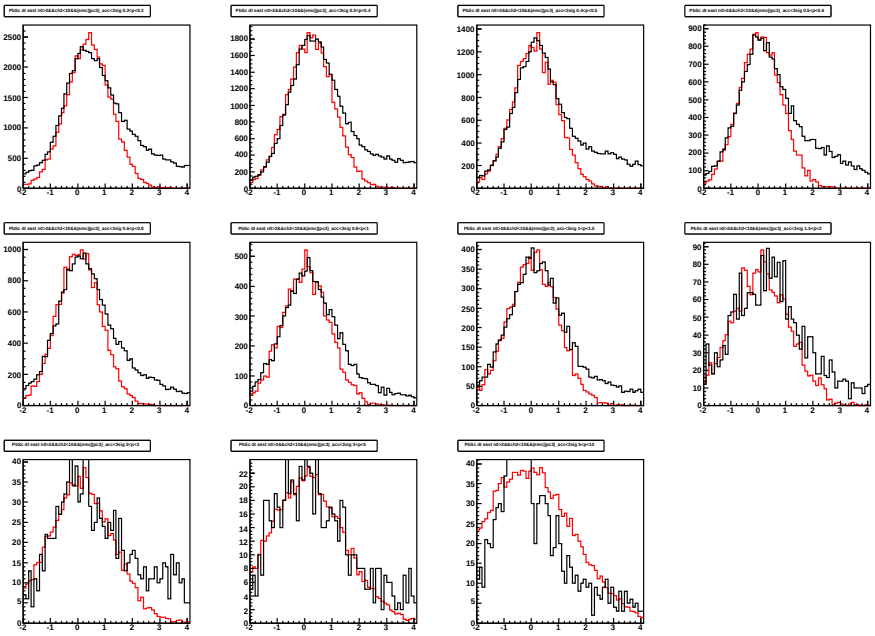

Figure A.10: Comparisons of emcdt for several momentum classes. The black and the red histograms correspond to the real data and the simulation, respectively.

A.2 Photon Converter in Simulation

The photon converter in the PISA simulation is implemented. The element composition of the converter material (brass) is Cu (70%), Zn (29.88%), Fe (0.05%) and Pb (0.07%). The mass density is 8.5 (g/cm^3). The tube shape with 29 cm radius, 60.96 cm height and 0.0254 cm thickness is placed at center of the PHENIX along with beam axis.

The density and the thickness of the converter was checked by measuring the area and the weight of a piece of the converter which was actually installed in the experiment. The measured area density is 0.215313 (g/cm^3). The converter is a 10 mil (= 0.0254 cm) thick brass sheet. The density of the converter is 8.4769 (g/cm^3). Therefore, the difference between the measured value and the simulation value is less than 0.3% (8.4769/8.5 = 0.9973).

In the real experiment, the converter is fixed around the MVD by a plastic tape with a overlap width at the bottom of the MVD. the radiation length of the plastic tape is negligible relative to the converter. Therefore, the tape is not implemented in the simulation. On the other hand, the overlap region with 6.985 cm overlap width at the bottom of the converter tube is also implemented.

Figure A.11 shows the photon converter wrapped the MVD in the simulation. The left and the right figure correspond to the beam view and the side view, respectively. The red tube around the MVD is the converter. The blue part at the bottom of the MVD is the overlap region of the converter.

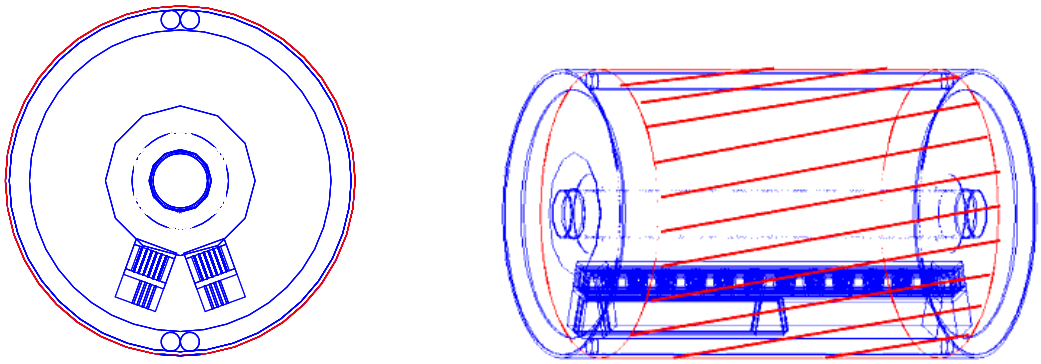

Figure A.11: The photon converter wrapped the MVD in simulation. The panels shows the beam view (left) and the side view (right), respectively. The blue part at the bottom of the MVD in the beam view (left) is the overlap width of the converter.

Appendix B

Cocktail Calculation for Centralities

The composition of photonic electrons in Au + Au collisions is modeled by the cocktail calculation. The method for the cocktail calculation is described in detail in section 4.10.2. For the inputs of the cocktail calculation, the spectral shapes of pion for each centrality classes are obtained by fitting the measured p_{T} spectra of charged and neutral pions simultaneously. The average of π^+ and π^- represents "charged pion". In this analysis, the fittings are performed for six centrality classes corresponding minimum bias, 0-10%, 10-20%, 20-40%, 40-60% and 60-92%, respectively. The fit functions are expressed as:

$$\frac{1}{2\pi p_{\mathrm{T}}}\frac{dN}{dydp_{\mathrm{T}}} = f(p_{\mathrm{T}}) \tag{B.1}$$

$$= p0\cdot(1+p_{\mathrm{T}}/p1)^{p2} + p3\cdot e^{-p_{\mathrm{T}}/p4} \quad (\text{for min. bias}), \tag{B.2}$$

$$= p0\cdot(1+p_{\mathrm{T}}/p1)^{p2}\cdot e^{-p_{\mathrm{T}}/p4} \quad (\text{for } 0-10\%), \tag{B.3}$$

$$= p0\cdot(1+p_{\mathrm{T}}/p1)^{p2}\cdot e^{p3+p4\cdot p_{\mathrm{T}}+p5\cdot p_{\mathrm{T}}^2} \quad (\text{for } 10-20\%), \tag{B.4}$$

$$= p0\cdot(1+p_{\mathrm{T}}/p1)^{p2} + p3\cdot e^{-p_{\mathrm{T}}/p4} \quad (\text{for } 20-40\%), \tag{B.5}$$

$$= p0\cdot(1+p_{\mathrm{T}}/p1)^{p2} + p3\cdot e^{-p_{\mathrm{T}}/p4} \quad (\text{for } 40-60\%), \tag{B.6}$$

$$= p0\cdot(1+p_{\mathrm{T}}/p1)^{p2} \quad (\text{for } 60-92\%), \tag{B.7}$$

where $p1-p6$ are the parameters.

Table B.1: The parameters obtained by fitting the pion spectra for each centrality.

Centrality	$p0$	$p1$ (GeV/c)	$p2$	$p3$	$p4$ (GeV/c)	$p5$ ($(c/\mathrm{GeV})^2$)
Min. bias	415.479	2.33895	-13.9435	6.71687×10^{-4}	1.2504	-
0-10%	1095.74	4.76572	-34.6169	-	0.554525	-
10-20%	716.026	2.5	-14.37	0.264	-0.231 (c/GeV)	0.04588
20-40%	530.297	2.03543	-12.5758	1.11136×10^{-4}	1.70697	-
40-60%	253.29	1.55091	-10.7785	1.64298	0.297068	-
60-92%	72.2085	1.29234	-9.99336	-	-	-

Figure B.1 shows the p_{T} spectra of charged and neutral pions for minimum bias and five centrality classes measured in PHENIX [105, 115]. The green, the blue points and the red curves correspond to the charged and the neutral pions, and their fit functions, respectively. The bottom plots in each panels are the ratio of the spectrum and the fit function. This indicates that the fit works reasonable. The obtained parameters are summarized in Tab. B.1.

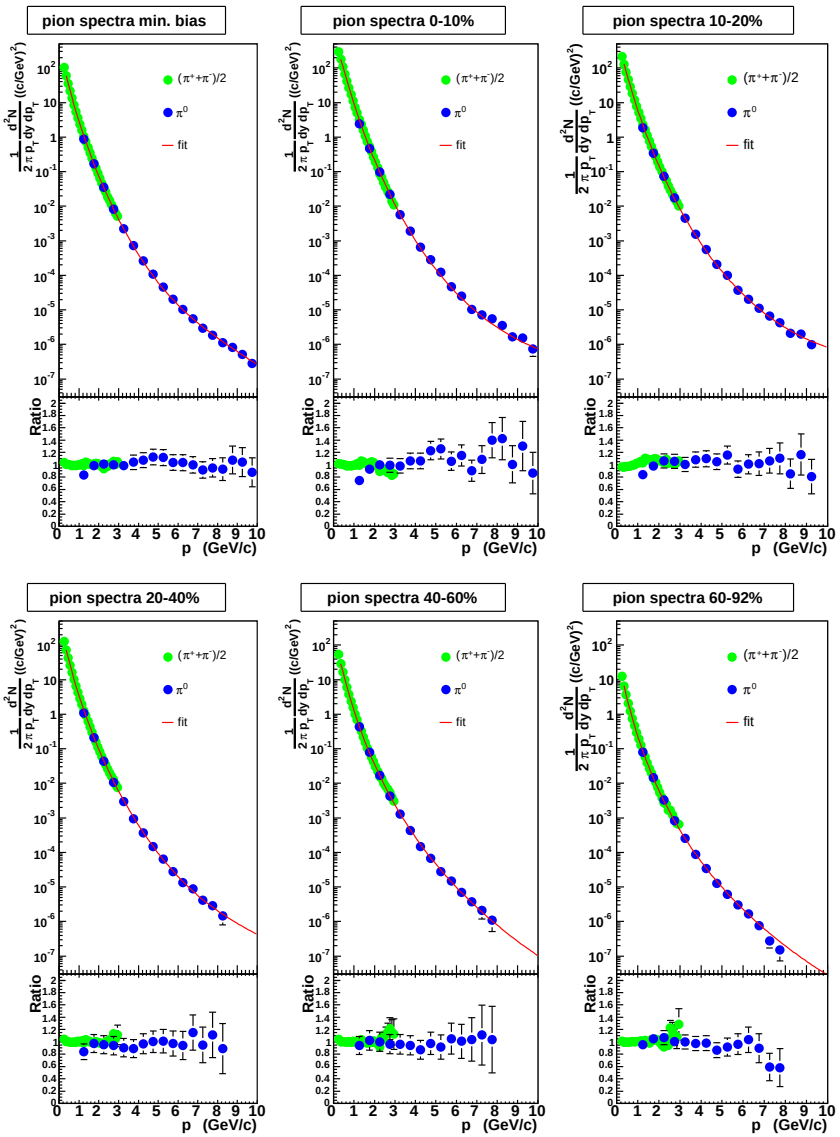

Figure B.1: The pion spectra for minimum bias and five centrality classes. The blue and the green points are the charged and the neutral pion, respectively. The spectral shape is obtained by fitting.

Based on the obtained spectral shape, photonic background electrons are determined by the cocktail calculation. The calculations are performed for centrality class by class independently. Figure B.2 shows the cocktails of photonic electrons for minimum bias and five centrality classes.

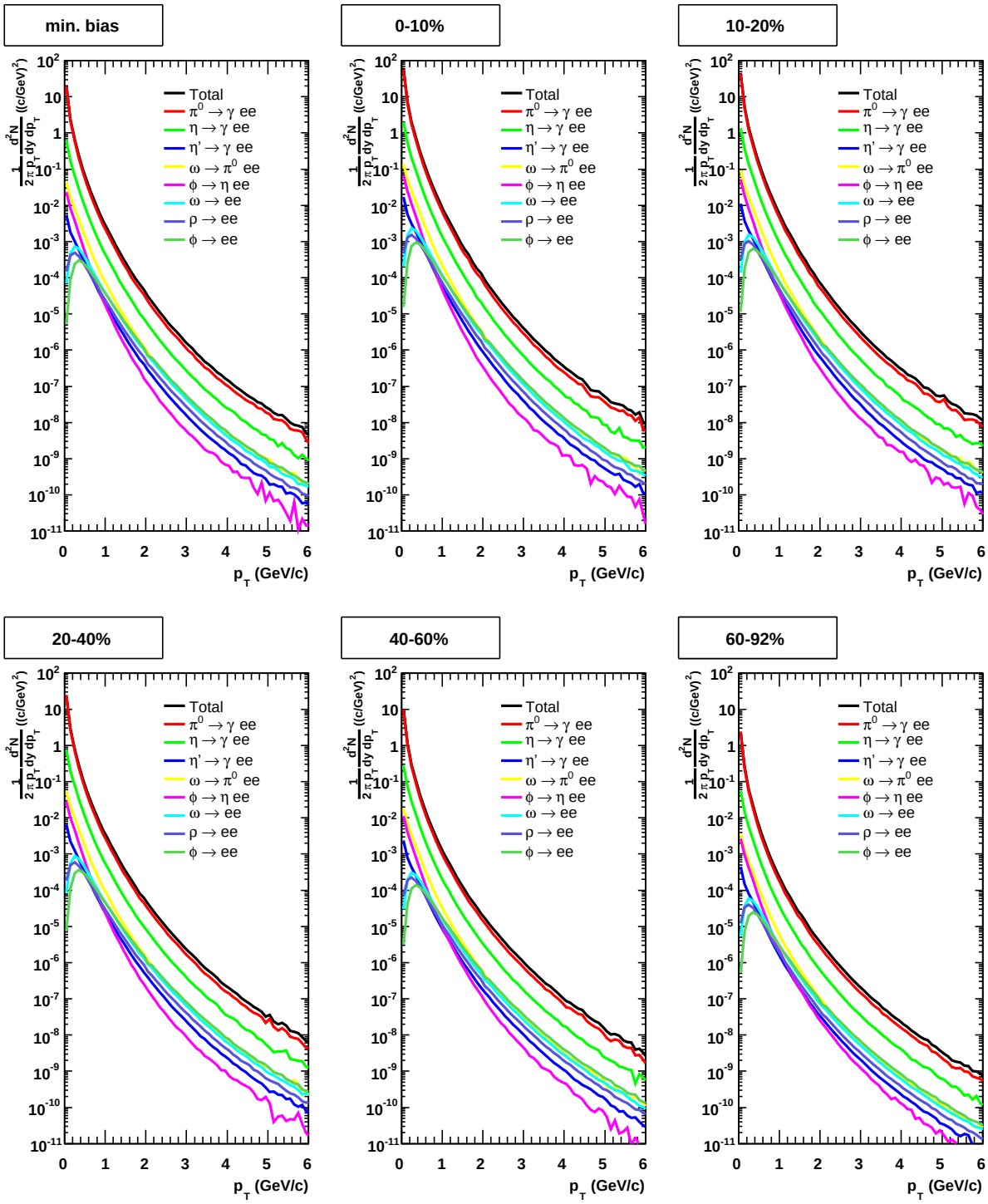

Figure B.2: The p_{T} spectra of photonic background electrons for minimum bias and five centrality classes. These contributions are determined by the cocktail calculation.

Appendix C

Data Table

C.1 Invariant Differential Yield of Heavy Flavor Electrons

The invariant differential yield of heavy flavor electrons has been measured in minimum bias Au + Au collisions at $\sqrt{s_{\rm NN}} = 200$ GeV and five centrality classes. These results are shown in Fig. 5.1, 5.2, 5.3, 5.4, 5.5 and 5.6. These are results in Run 2 analysis. The data points are summarized in the following tables.

Table C.1: The invariant differential yield of heavy flavor electrons in minimum bias Au + Au collisions in $\sqrt{s_{\rm NN}} = 200$ GeV.

$p_{\rm T}$ (GeV/c)	$\frac{1}{2\pi p_{\rm T}} \frac{dN_e}{dy dp_{\rm T}}$	stat. error	sys. error (+)	sys. error (−)	comment
0.347	5.1383e-02	1.0911e-02	2.5235e-02	2.6695e-02	
0.446	3.4119e-02	6.3093e-03	1.2778e-02	1.3485e-02	
0.546	1.8739e-02	3.6599e-03	7.0393e-03	7.4293e-03	
0.684	1.3407e-02	1.4443e-03	3.1393e-03	3.2799e-03	
0.885	4.8469e-03	6.9054e-04	1.0466e-03	1.0901e-03	
1.086	1.8593e-03	3.5921e-04	3.8546e-04	4.0074e-04	
1.288	7.5209e-04	2.1681e-04	1.6098e-04	1.6751e-04	
1.611	2.4963e-04	4.9966e-05	4.0639e-05	4.1719e-05	
2.320	2.1728e-05	9.3890e-06	3.6175e-06	3.7197e-06	
3.358	7.1900e-07	1.6719e-06	1.5439e-07	7.1900e-07	shown as "→"

Table C.2: The invariant differential yield of heavy flavor electrons in 0-10% central Au + Au collisions in $\sqrt{s_{\rm NN}} = 200$ GeV.

$p_{\rm T}$ (GeV/c)	$\frac{1}{2\pi p_{\rm T}}\frac{dN_e}{dydp_{\rm T}}$	stat. error	sys. error (+)	sys. error (−)	comment
0.347	1.3134e-01	6.4748e-02	6.4504e-02	6.8238e-02	
0.446	1.1149e-01	3.7788e-02	4.1752e-02	4.4062e-02	
0.546	9.7878e-02	2.2649e-02	3.6767e-02	3.8804e-02	
0.684	5.1656e-02	8.7366e-03	1.2095e-02	1.2637e-02	
0.885	1.7392e-02	4.1758e-03	3.7554e-03	3.9115e-03	
1.086	6.2817e-03	2.1480e-03	1.3023e-03	1.3539e-03	
1.288	2.4103e-03	1.3316e-03	5.1590e-04	5.3683e-04	
1.611	9.2125e-04	3.0212e-04	1.4998e-04	1.5396e-04	
2.320	9.2892e-05	5.6707e-05	1.5466e-05	1.5902e-05	
3.358	3.0122e-06	1.0429e-05	6.4678e-07	3.0122e-06	shown as "→"

Table C.3: The invariant differential yield of heavy flavor electrons in 10-20% central Au + Au collisions in $\sqrt{s_{\rm NN}} = 200$ GeV.

$p_{\rm T}$ (GeV/c)	$\frac{1}{2\pi p_{\rm T}}\frac{dN_e}{dydp_{\rm T}}$	stat. error	sys.error (+)	sys.error (−)	comment
0.347	2.5069e-01	5.1595e-02	1.2311e-01	1.3024e-01	
0.446	8.1438e-02	2.8830e-02	3.0498e-02	3.2186e-02	
0.546	1.5789e-02	1.6897e-02	5.9310e-03	1.5789e-02	shown as "→"
0.684	2.2646e-02	6.5243e-03	5.3026e-03	5.5401e-03	
0.885	1.0463e-02	3.1854e-03	2.2592e-03	2.3531e-03	
1.086	5.6593e-03	1.7259e-03	1.1732e-03	1.2197e-03	
1.288	1.7300e-03	1.0216e-03	3.7028e-04	3.8530e-04	
1.611	4.1933e-04	2.3646e-04	6.8267e-05	7.0080e-05	
2.320	9.4155e-06	4.3146e-05	1.5676e-06	9.4155e-06	shown as "→"
3.358	1.1223e-05	8.5209e-06	2.4099e-06	2.5168e-06	

Table C.4: The invariant differential yield of heavy flavor electrons in 20-40% central Au + Au collisions in $\sqrt{s_{\rm NN}} = 200$ GeV.

$p_{\rm T}$ (GeV/c)	$\frac{1}{2\pi p_{\rm T}}\frac{dN_e}{dydp_{\rm T}}$	stat. error	sys. error (+)	sys. error (−)	comment
0.347	2.0903e-02	2.4537e-02	1.0266e-02	2.0903e-02	shown as "→"
0.446	4.9819e-02	1.4409e-02	1.8657e-02	1.9690e-02	
0.546	2.2979e-02	8.2808e-03	8.6318e-03	9.1101e-03	
0.684	2.0266e-02	3.2620e-03	4.7454e-03	4.9579e-03	
0.885	7.5990e-03	1.6080e-03	1.6408e-03	1.7090e-03	
1.086	1.9210e-03	8.3206e-04	3.9825e-04	4.1403e-04	
1.288	1.0073e-03	5.0680e-04	2.1560e-04	2.2435e-04	
1.611	3.9285e-04	1.2126e-04	6.3957e-05	6.5655e-05	
2.320	1.7569e-05	2.2482e-05	2.9252e-06	1.7569e-05	shown as "→"

Table C.5: The invariant differential yield of heavy flavor electrons in 40-60% central Au + Au collisions in $\sqrt{s_{\rm NN}} = 200$ GeV.

$p_{\rm T}$ (GeV/c)	$\frac{1}{2\pi p_{\rm T}}\frac{dN_e}{dydp_{\rm T}}$	stat. error	sys. error (+)	sys. error (−)	comment
0.347	3.1060e-02	1.4112e-02	1.5254e-02	1.6137e-02	
0.446	1.9198e-02	7.9258e-03	7.1897e-03	7.5876e-03	
0.546	9.8178e-03	4.5819e-03	3.6879e-03	3.8923e-03	
0.684	6.6278e-03	1.7911e-03	1.5519e-03	1.6214e-03	
0.885	1.8013e-03	8.6796e-04	3.8894e-04	4.0511e-04	
1.086	8.3136e-04	4.6280e-04	1.7235e-04	1.7918e-04	
1.288	3.7519e-04	2.8169e-04	8.0305e-05	8.3563e-05	
1.611	1.3588e-04	6.1679e-05	2.2121e-05	2.2709e-05	
2.320	2.1301e-05	1.2180e-05	3.5465e-06	3.6466e-06	
3.358	1.3009e-06	1.3354e-06	2.7934e-07	1.3009e-06	shown as "→"

Table C.6: The invariant differential yield of heavy flavor electrons in 60-92% central Au + Au collisions in $\sqrt{s_{\rm NN}} = 200$ GeV.

$p_{\rm T}$ (GeV/c)	$\frac{1}{2\pi p_{\rm T}}\frac{dN_e}{dydp_{\rm T}}$	stat. error	sys. error (+)	sys. error(−)	comment
0.347	6.2483e-03	4.4116e-03	3.0686e-03	3.2462e-03	
0.484	1.9156e-03	1.2876e-03	7.1720e-04	7.5697e-04	
0.740	3.0672e-04	2.6902e-04	6.9811e-05	7.2860e-05	
1.149	1.1195e-04	7.6627e-05	2.3400e-05	2.4331e-05	
1.611	1.6400e-05				upper limit
2.320	7.1337e-06	4.5662e-06	1.1877e-06	1.2212e-06	

Table C.7: The $N_{\rm coll}$ scaled integrated yield of heavy flavor electrons $\frac{dN_e/dy}{N_{\rm coll}}(0.8 < p_{\rm T} < 4.0$ GeV/c).

Centrality	$N_{\rm coll}$	$\frac{dN_e/dy}{N_{\rm coll}}(0.8<p_{\rm T}<4.0)$	stat.error	sys.err(+)	sys.err(−)
0-10%	955.4 ± 93.6	4.072e-05	6.522e-06	9.222e-06	9.514e-06
10-20%	602.6 ± 59.3	4.155e-05	8.007e-06	9.533e-06	9.842e-06
20-40%	296.8 ± 31.1	5.143e-05	8.122e-06	1.185e-05	1.222e-05
40-60%	90.7 ± 11.8	5.437e-05	1.441e-05	1.304e-05	1.339e-05
60-92%	14.5 ± 4.0	3.576e-05	2.595e-05	1.207e-05	1.224e-05
minimum bias	257.8 ± 25.4	4.269e-05	4.000e-06	9.700e-06	1.001e-05
$p + p$	1.0	5.631e-05	1.247e-05		

Appendix D

Centrality Dependence of Charm Production

D.1 Systematic Uncertainty of α for Run 2 data

The systematic uncertainty of the parameter α is estimated for the linearity test of the charm production in Run 2. Since the α influences the curvature of the fit function $A \cdot N_{\rm coll}^{\alpha-1}$, we only consider the following sources:

(1) Multiplicity dependent efficiency loss (7%),

(2) Extraction of non-photonic electrons (uncertainty of R_γ and $R_{\rm CN}$).

These two sources change the shape of the distribution of $dN_e/dy(0.8 < p_{\rm T} < 4.0)/N_{\rm coll}$. In contrast, the other sources of the systematic uncertainties (e.g. the electron ID efficiency) do not affect the α, but contribute the overall normalization of dN_e/dy. Therefore, the other sources are neglected.

For the source (1), the systematic uncertainty is 7% as described in section 4.9.2. Applying the higher (lower) limit of the uncertainty instead of the center value, we re-calculate the $dN_e/dy(0.8 < p_{\rm T} < 4.0)/N_{\rm coll}$, and then fit it by the function, $A \cdot N_{\rm coll}^{\alpha-1}$. Figure D.1 (left) shows the three kinds of $dN_e/dy(0.8 < p_{\rm T} < 4.0)/N_{\rm coll}$ which correspond to the center (gray) value, the higher (blue point) and the lower (red point) limit of the multiplicity dependent efficiency applied, respectively. The curves represent the corresponding fit functions. The obtained α values are summarized in Tab. D.1. The difference of the α between the center and the higher (lower) is assigned as the higher (lower) systematic uncertainty.

Next, we study the systematic uncertainty of the source (2). We re-calculate the non-photonic electron spectrum by changing R_γ, $R_{\rm CN}$ and the blocking effect with their higher (lower) limit, and then re-calculate $dN_e/dy/N_{\rm coll}$. The combination of the higher (lower) R_γ, the lower (higher) $R_{\rm CN}$ and the lower (higher) blocking effect provides a larger (smaller) non-photonic electron yield. Then, α is obtained for the higher and lower $dN_e/dy/N_{\rm coll}$. Figure D.1 (right) shows the re-calculated $dN_e/dy(0.8 < p_{\rm T} < 4.0)/N_{\rm coll}$ using the uncertainty of the source (2). The gray, the blue and the red points correspond to the center

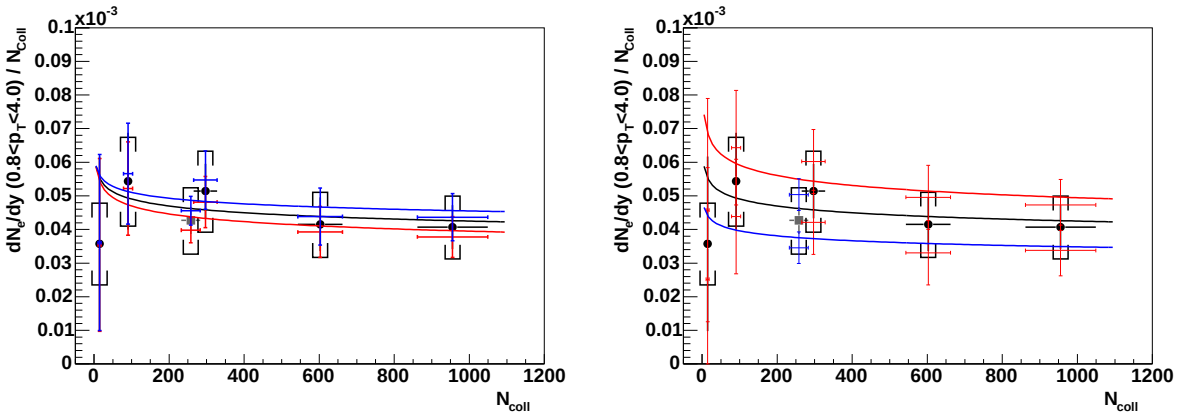

Figure D.1: The $dN_e/dy(0.8 < p_{\mathrm{T}} < 4.0)/N_{\mathrm{coll}}$ for the source (1) (left) and (2) (right). The gray, the blue and the red points correspond to the center value, the higher and the lower uncertainties, respectively. The curves represent the fit functions.

value, the higher and the lower uncertainties, respectively. The curves represent the fit functions. The obtained α is summarized in Tab. D.1.

In order to average the higher and the lower systematic uncertainties, we calculate a root mean square (RMS) of the higher and the lower errors for source (1) and (2), respectively. The total systematic uncertainty of α is calculated adding in quadrature these RMS errors of source (1) and (2). The total systematic error is also shown in Tab. D.1.

Table D.1: The systematic uncertainty of α for the source (1) and (2). The total systematic error is estimated adding these errors in quadrature.

Source of uncertainty	$\alpha - 1$	difference	RMS (high and low)
Center value	-0.0623	-	-
Source 1 for higher	-0.0496	0.0127	0.0130
Source 1 for lower	-0.0756	-0.0133	
Source 2 for higher	-0.0779	-0.0156	0.0120
Source 2 for lower	-0.0558	0.0065	
total sys. error	0.0177 (0.0130 $\oplus$ 0.0120)		

D.2 Systematic Uncertainty of α for Run 4 and Run 5 data

The systematic uncertainty of the linearity parameter α is estimated in Run 4 data analysis as same as Run 2. Since the most of the systematic errors (the electron ID and the acceptance) are independent of centrality. These errors do not affect the linearity (α). The sources of the systematic uncertainties are considered as following:

(1) Multiplicity dependent efficiency loss,

(2) R_γ which is used to separate non-photonic and photonic electrons,

(3) Number of nucleon-nucleon collisions, $N_{\rm coll}$.

First, the systematic uncertainty from the source (1) is considered. The systematic uncertainty of the multiplicity dependent efficiency loss ($\varepsilon_{\rm mult}$) is summarized in Tab. D.2 [122]. To estimate the systematic uncertainty of α from source (1), the data points are moved up (down) by the higher (lower) uncertainty of $\varepsilon_{\rm mult}$ for the corresponding centrality, and then the moved data are fit by the function, $A \cdot N_{\rm coll}^{\alpha-1}$. Figure D.2 shows the moved-up (down) $dN_e/dy(p_{\rm T} > 0.4)/T_{AA}$ as a function of $N_{\rm coll}$. The black, the magenta and the light-blue points correspond to the center, the moved data by the higher and the lower systematic uncertainties, respectively. The curves are the fit functions for the corresponding data. The fit are performed for Au + Au and for Au + Au and $p + p$ data. The fit results are shown in the left and the right panel of Fig. D.2.

Table D.2: Systematic uncertainty of the multiplicity dependent efficiency loss [122].

Centrality	Sys. error of $\varepsilon_{\rm mult}$
0-10%	4.43%
10-20%	3.47%
20-40%	2.50%
40-60%	1.72%
60-92%	1.26%
Min. bias	3.22%
$p + p$	0%

Second, the systematic uncertainty of α from source (2) is estimated. We, first, consider the error propagation of R_γ to the non-photonic electron yield based on Eq. D.1:

$$N_e^{\rm non-\gamma} = \frac{R_\gamma \cdot N_e^{\rm Conv-out} - N_e^{\rm Conv-in}}{R_\gamma - 1}, \tag{D.1}$$

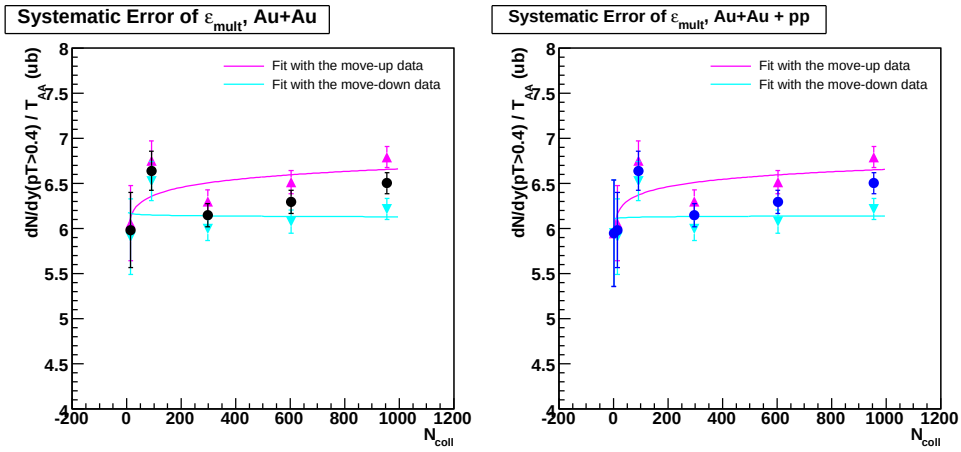

Figure D.2: $dN_e/dy(p_{\rm T} > 0.4)/T_{AA}$ as a function of $p_{\rm T}$. The data points are moved-up (down) by the systematic uncertainty of $\varepsilon_{\rm mult}$. The magenta and the light-blue points correspond to the higher and the lower systematic uncertainties. The curves are the fit functions for the corresponding data. The fit are performed for the Au + Au (left) and for the Au + Au and $p + p$ data (right) separately.

where the blocking effect is omitted for simplification. If R_γ has an error "e", R_γ is modified as $R_\gamma \to R'_\gamma = R_\gamma + e$. Then, Eq. D.1 is transformed as follows:

$$N_e^{\rm non-\gamma'} = \frac{R'_\gamma \cdot N_e^{\rm Conv-out} - N_e^{\rm Conv-in}}{R'_\gamma - 1} = \frac{(R_\gamma + e) \cdot N_e^{\rm Conv-out} - N_e^{\rm Conv-in}}{(R_\gamma + e) - 1} \quad \text{(D.2)}$$

$$= N_e^{\rm non-\gamma} \cdot \left(1 + \frac{e \cdot (k-1)}{R_\gamma + e - 1}\right), \quad \text{(D.3)}$$

where k is the ratio of inclusive to non-photonic electrons ($k = N_e^{\rm inc}/N_e^{\rm non-\gamma}$). Therefore, the relative error of non-photonic electrons ($\delta N_e^{\rm non-\gamma}/N_e^{\rm non-\gamma}$) is expressed as:

$$\frac{\delta N_e^{\rm non-\gamma}}{N_e^{\rm non-\gamma}} = \frac{N_e^{\rm non-\gamma'} - N_e^{\rm non-\gamma}}{N_e^{\rm non-\gamma}} = \frac{e \cdot (k-1)}{R_\gamma + e - 1}. \quad \text{(D.4)}$$

Based on Eq. D.4, we obtain the relative errors of non-photonic electrons from the systematic uncertainty of R_γ. Here, we use $R_\gamma = 2.333$ at $p_{\rm T} = 0.5$ GeV/c and $e = 0.064$ (2.74% of R_γ) described in [122]. Figure D.3 shows the ratio k of inclusive to non-photonic electrons as a function of centrality classes. The ratio k and the obtained relative errors are summarized in Tab. D.4.

Using these relative errors, the data points are moved to the higher and the lower limit of systematic uncertainty for $dN_e/dy/T_{AA}$. Then, they are fit to obtain the limit of α. Figure D.4 shows the higher and the lower limit of $dN_e/dy/T_{AA}$ and the center value. The curves represent the fit functions. The left and right panels correspond to the data in Au + Au and in Au + Au and $p + p$ collisions, respectively. The systematic uncertainty of α is obtained by averaging in the same way. The obtained uncertainty are summarized in Tab. D.5.

Table D.3: The systematic uncertainty of α for the source (1). The parameter α are obtained for the Au + Au data and for the Au + Au and $p + p$ data separately.

	Au + Au data		
	α	difference	RMS of difference
center	1.00922	-	-
higher	1.01944	0.01022	0.01042
lower	0.99860	-0.01062	
	Au + Au and $p + p$ data		
center	1.00971	-	-
higher	1.01826	0.00855	0.00864
lower	1.00097	-0.00874	

Table D.4: Summary of the ratio k and the relative error of non-photonic electrons in Run 4 analysis.

Centrality	k	Relative Error
0-10%	3.47	11.30%
10-10%	3.86	13.08%
20-10%	4.45	15.78%
40-10%	4.95	18.07%
60-10%	6.08	23.23%
Min.bias	4.09	14.13%
$p + p$	6.942	27.18%

Third, the systematic uncertainty from the source (3) is estimated. The systematic uncertainty of $N_{\rm coll}$ consists of two components. There is the correlated and the un-correlated term with respect to centrality. The un-correlated error only contributes to the α. The estimation of the un-correlated term of $N_{\rm coll}$ is described in detail in Appendix D.3.

Using the higher and the lower limits of $N_{\rm coll}$ systematic uncertainty, the higher and the lower limit of $dN_e/dy/N_{\rm coll}$ is calculated, and then they are fit to obtain the uncertainty of α. The $N_{\rm coll}$ value used in this analysis is summarized in Tab. D.6. The $N_{\rm coll}$ value in $p + p$ collisions is by definition 1.0 with no error. However, the relative value between $p + p$ data point and all five Au + Au data points are moved up/down due to the common systematic error of $N_{\rm coll}$. Therefore, we assign 7.3% to the $p + p$ point as this common error of $N_{\rm coll}$ which is equivalent to the systematic uncertainty of T_{AA} in minimum bias collisions.

Figure D.5 shows the higher and the lower limit of $dN_e/dy/T_{AA}$ and the center value. These three curves represent the fit functions for these data points. The left and the right panels correspond to the data in Au + Au and in Au + Au and $p + p$ collisions, respectively. The systematic uncertainty of α is obtained by averaging in the same way.

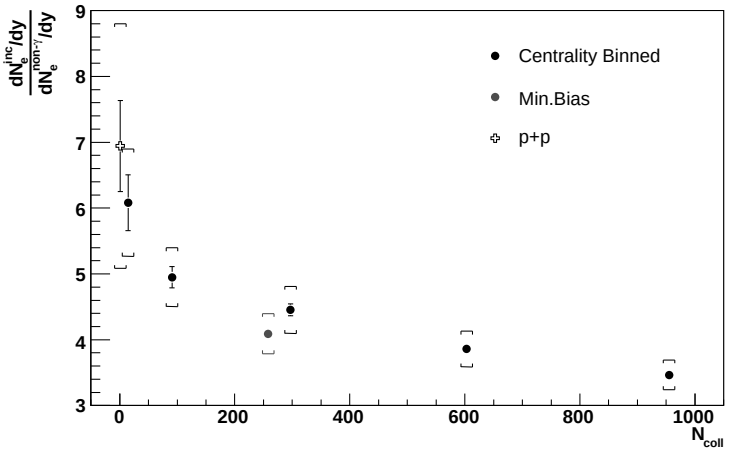

Figure D.3: Ratio k of inclusive to non-photonic electrons. Electrons are measured in Run 4 Au + Au [121] and Run 5 $p+p$ collisions [39].

Table D.5: The systematic uncertainty of α for the source (2). The parameter α are obtained for Au + Au and for Au + Au and $p+p$ separately.

	Au + Au data		
	α	difference	RMS of difference
center	1.00922	-	-
higher	0.98326	-0.02596	0.03169
lower	1.04576	0.03654	
	Au + Au and $p+p$ data		
center	1.00971	-	-
higher	0.98690	-0.02281	0.02881
lower	1.04348	0.03377	

The uncertainty is summarized in Tab. D.7.

Finally, these three uncertainties are added in quadrature to obtain the total uncertainty. Table D.8 shows these three and the total uncertainties. As the result, we obtain $\alpha = 1.0092 \pm 0.0120(\text{stat}) \pm 0.0506(\text{sys})$ in Au + Au collisions. If the $p+p$ point is included, $\alpha = 1.0097 \pm 0.0094(\text{stat}) \pm 0.0403(\text{sys})$.

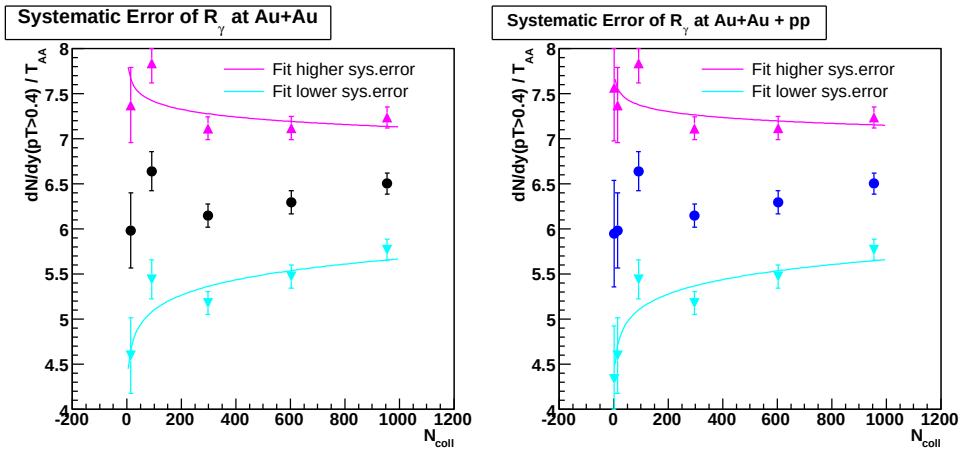

Figure D.4: $dN_e/dy(p_{\rm T} > 0.4)/T_{AA}$ as a function of $p_{\rm T}$. The data points are moved-up (down) by the systematic uncertainty of R_γ. The magenta and the light-blue points correspond to the higher and the lower systematic uncertainties. The curves are the fit functions for corresponding data. The fit are performed for Au + Au (left) and for Au + Au + $p+p$ data (right) separately.

Table D.6: Uncorrelated systematic uncertainty of $N_{\rm coll}$ described in Appendix D.3.

Centrality	$N_{\rm coll}$	Sys. error (Uncorrelated term only)	Comment
0-10%	955.4	9.7	
10-20%	602.6	3.3	
20-40%	296.8	7.8	
40-60%	90.7	5.3	
60-92%	14.5	3.6	
$p+p$	1	18.9	7.3%. systematic error of T_{AA} in minimum bias

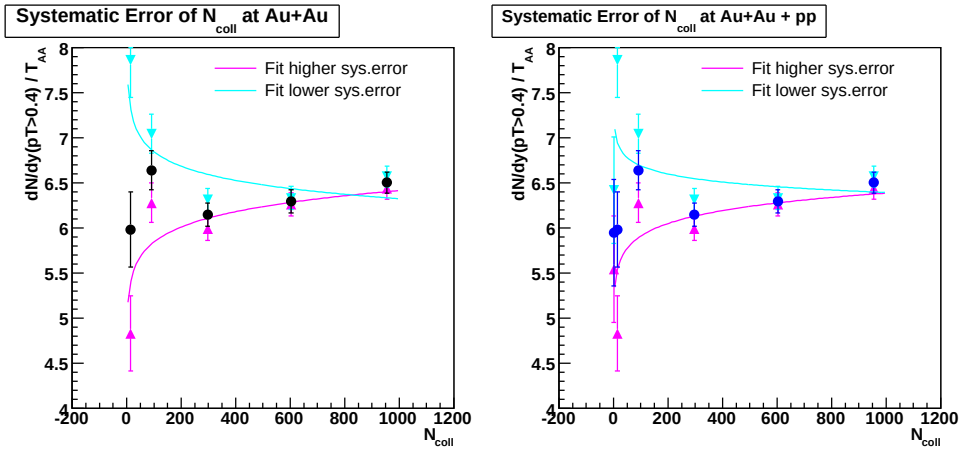

Figure D.5: $dN_e/dy(p_{\rm T} > 0.4)/T_{AA}$ as a function of $p_{\rm T}$. The data points are moved-up (down) by the systematic uncertainty of $N_{\rm coll}$. The magenta and the light-blue points correspond to the higher and the lower systematic uncertainties. The curves represent the fit functions for the corresponding data. The fit are performed for Au + Au (left) and for Au + Au + $p + p$ data (right).

Table D.7: The systematic uncertainty of α for the source (3). The parameter α are obtained for Au + Au and for Au + Au and $p + p$ separately.

	Au + Au data		
	α	difference	RMS of difference
center	1.00922	-	-
higher	1.04051	0.03131	0.03800
lower	0.96553	-0.04369	
	Au + Au and $p + p$ data		
center	1.00971	-	-
higher	1.03369	0.02398	0.02683
lower	0.98031	-0.02940	

Table D.8: Summary of the α systematic uncertainty from all three sources

	Au + Au	Au + Au and $p + p$
Source (1)	0.01042	0.00864
Source (2)	0.03169	0.02881
Source (3)	0.03800	0.02683
Total	0.05057	0.04031

D.3 Uncorrelated Systematic Uncertainty of $N_{\rm coll}$

We studied the systematic uncertainty of $N_{\rm coll}$. The uncertainty of $N_{\rm coll}$ is subdivided to the correlated and the uncorrelated term with respect to centrality. The uncertainty is made from 14 components [106] listed below:

1. $\sigma_{pp} = 39$ mb, instead of $\sigma_{NN} = 42$ mb,
2. $\sigma_{pp} = 45$ mb, instead of $\sigma_{NN} = 42$ mb,
3. Different Woods-Saxon parameters ($R = 6.65$ fm, $a = 0.55$ fm),
4. Different Woods-Saxon parameters ($R = 6.25$ fm, $a = 0.53$ fm),
5. Different radius of hard-core. ($R_{\rm core} = 0.4$),
6. Different neutron loss in the ZDC,
7. Different BBC fluctuation,
8. Gray disk nucleon overlap function,
9. Gaussian nucleon overlap function,
10. Different origin of angles for the centrality selection,
11. Higher BBC trigger efficiency (92.2 + 2.5%),
12. Lower BBC trigger efficiency (92.2 - 3.0%),
13. Additional uncertainty of the centrality determination (more central),
14. Additional uncertainty of the centrality determination (less central).

The uncertainties calculated by these modified parameters are compared to that of the default parameters. The some components are the pair of the higher and the lower limit. Thus, the differences from the following pairs are averaged.

(i) σ_{NN} (average of 1 and 2)

(ii) Wood-Saxon parameter (average of 3 and 4)

(iii) Different radius of hard-core (5)

(iv) Different neutron loss in the ZDC (6)

(v) Different BBC fluctuation (7)

(vi) Overlap function (average of 8 and 9)

(vii) Different origin of angles (10)

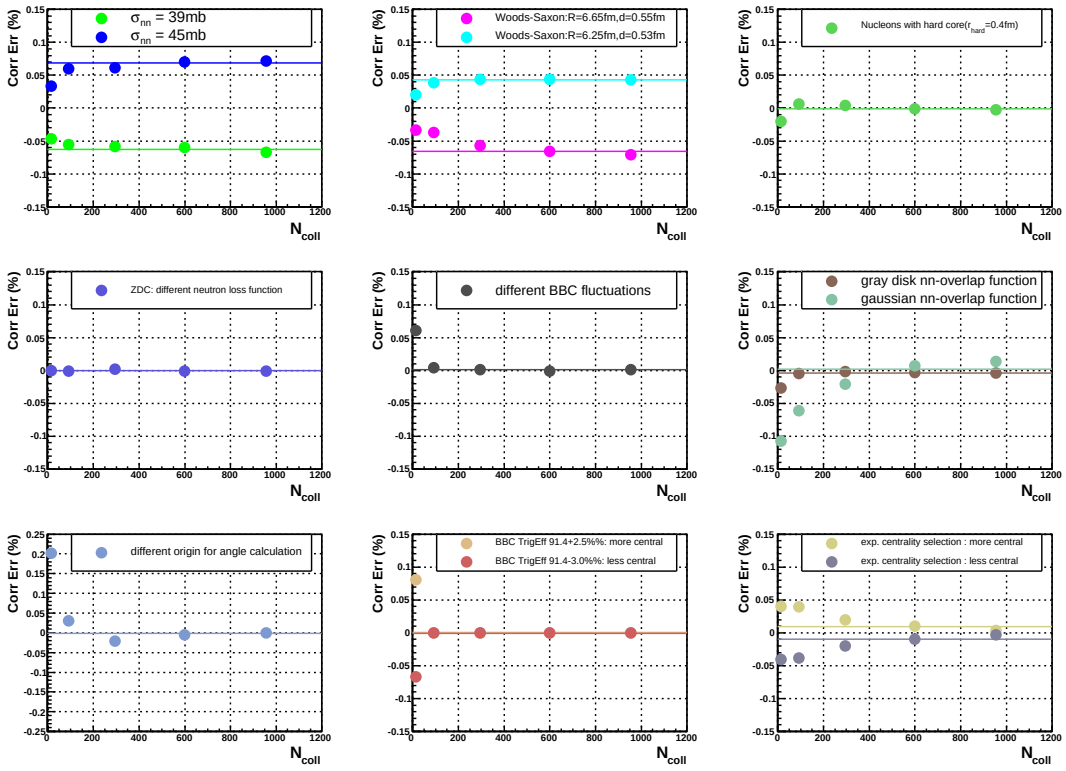

Figure D.6: The correlated terms of the uncertainty as a function of centrality. These panels from the top-left to the bottom-right correspond to the errors from components (i) to (ix), respectively. The line in each panel shows the weighted average.

(viii) BBC trigger efficiency (11 and 12)

(ix) Additional uncertainty (13 and 14)

The total error is calculated adding these averaged errors in quadrature (from i to ix). Each component contains both the correlated and uncorrelated terms. To separate these terms, we define that the correlated term is the weighted average of these errors at the five centrality bins and the uncorrelated term is the difference from the weighted average. Here, the N_{coll} value in each centrality class is used as the weight factor. Figure D.6 shows the errors from these components. These panels from the top-left to the bottom-right correspond to the errors from the components (i) to (ix), respectively. The line in each panel shows the weighted average which is the correlated term for each component.

Figure D.7 shows the uncorrelated errors as a function of N_{coll} for these components. In each panel, the error pairs (closed circles) listed above and the averages of these pairs (open circles) are shown. The averages of these pairs represent the uncorrelated errors. The obtained uncorrelated errors from these components (i to ix) are summarized in Tab. D.9.

Figure D.8 shows the systematic error of N_{coll} as a function of N_{coll}. The yellow and the gray band represent the total and the uncorrelated errors, respectively. The uncorrelated

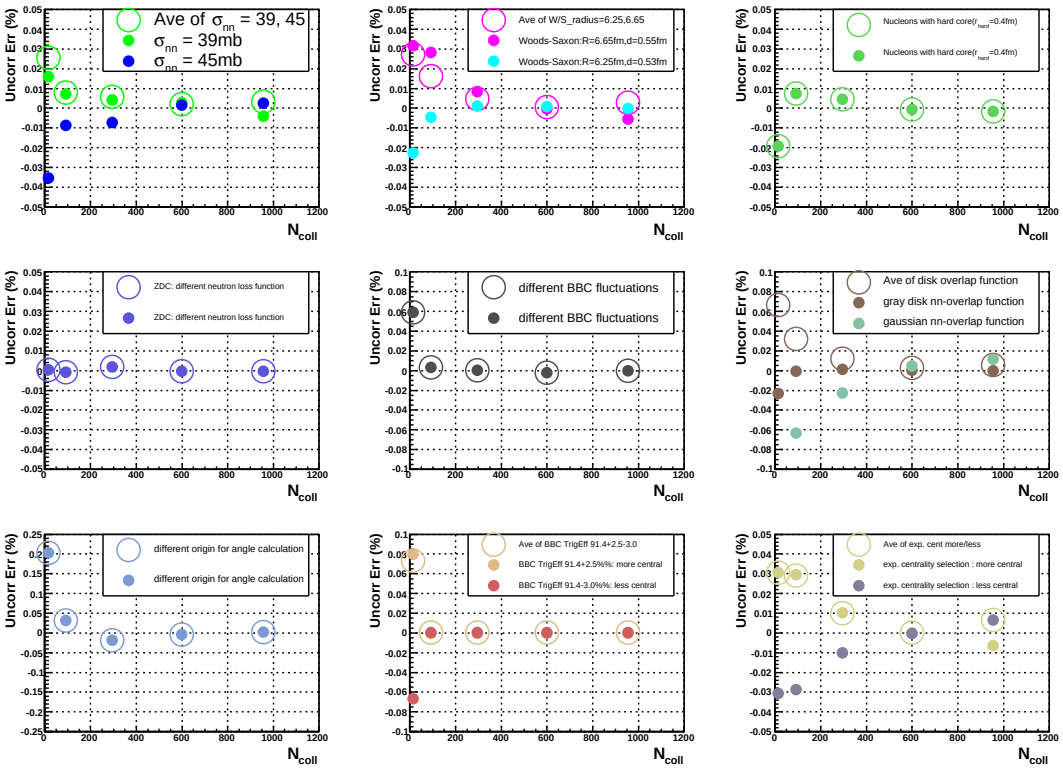

Figure D.7: The uncorrelated terms of the uncertainty as a function of centrality. In each panel, the closed circles are the errors from these components and the open circles are the averages of these error pairs.

Table D.9: Summary of the uncorrelated $N_{\rm coll}$ uncertainty for the five centrality classes.

Centrality	0-10%	10-20%	20-40%	40-60%	60-92%
Component	Uncorrelated error (average of pair)				
i	0.33%	0.21%	0.58%	0.80%	2.56%
ii	0.28%	0.07%	0.48%	1.64%	2.73%
iii	-0.15%	-0.05%	0.45%	0.74%	-1.93%
iv	-0.03%	-0.04%	0.20%	-0.08%	0.03%
v	0.01%	-0.22%	0.03%	-0.33%	5.93%
vi	0.60%	0.25%	1.21%	3.20%	6.63%
vii	0.19%	-0.37%	-1.90%	3.22%	20.30%
viii	0.06%	0.06%	0.06%	0.06%	7.33%
ix	0.65%	0.02%	1.01%	2.91%	3.05%
Total	1.02%	0.55%	2.63%	5.75%	23.92%

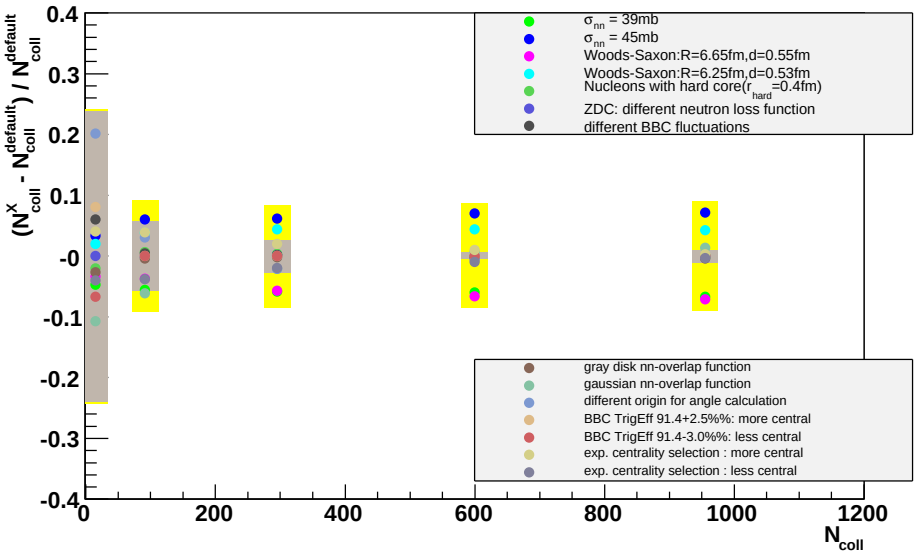

Figure D.8: Systematic uncertainty of N_{coll} as a function of centrality. The points represent the difference of the calculated N_{coll} compared to the default value. The yellow and gray bands correspond to the total and the uncorrelated error of N_{coll}.

errors are summarized in Tab. D.10.

Table D.10: Summary of the total and the uncorrelated systematic uncertainties for the five centrality classes.

Centrality	N_{coll}	Total error	Uncorrelated error
0-10%	955	86.0	9.7
10-20%	599.8	51.7	3.3
20-40%	295.4	24.9	7.8
40-60%	91.5	8.4	5.3
60-92%	14.9	3.6	3.6

Appendix E

Charm Cross Section in Run 4

The total charm cross section in Au + Au collisions at $\sqrt{s_{\rm NN}} = 200$ GeV is calculated using the heavy flavor electron spectra with high statistics measured in Run 4 [121]. The method to calculate the cross section is slightly modified from that described in section 5.6.1. This modified method is initially used to calculate the charm cross section in $p + p$ collisions [39, 131]. The procedure is described as follow:

(1) The invariant integrated yield per nucleon-nucleon collision ($\frac{dN_e}{dy}/T_{AA}$ ($p_{\rm T} > p_{\rm Tlow}$)) above $p_{\rm T} > p_{\rm Tlow}$ is calculated. We denote $\frac{dN_e}{dy}/T_{AA}$ ($p_{\rm T} > p_{\rm Tlow}$) = $d\sigma_e/dy$ ($p_{\rm T} > p_{\rm Tlow}$). The $p_{\rm Tlow} = 0.4$ GeV/c is chosen, since the available $p_{\rm T}$ range is extended to lower $p_{\rm T}$ due to the higher statistics.

(2) The obtained integrated yield ($d\sigma_e/dy$ ($p_{\rm T} > p_{\rm Tlow}$) is extrapolated to the entire $p_{\rm T}$ range ($d\sigma_e/dy$). The extrapolation factor $R_{p_{\rm T}} = 0.54$ is obtained from the FONLL calculation instead of the PYTHIA calculation.

(3) The contributions from bottom decays ($b \to e$) and bottom cascade decays ($b \to c \to e$) are subtracted. These contributions ($b \to e, b \to c \to e$) is determined based on a FONLL calculation. These contributions are $\sigma_{b\to e} = 0.061$ μb and $\sigma_{b\to c\to e} = 0.053$ μb, respectively.

(4) The integrated yield ($d\sigma_e/dy$) of electrons is converted to the charm yield ($d\sigma_{c\bar{c}}/dy$) using a total branching ratio $BR(c \to e) = 9.5 \pm 1.0\%$.

$$\frac{d\sigma_{c\bar{c}}}{dy} = \frac{1}{BR(c \to e)} \frac{1}{C_{e/D}} \frac{d\sigma_e}{dy} \tag{E.1}$$

Here, $C_{e/D} = 0.935$ is a correction factor to account for the difference of the rapidity distribution between D mesons and their decayed electrons.

(5) $d\sigma_{c\bar{c}}/dy$ is extrapolated to the entire rapidity range to obtain the total cross section.

$$\sigma_{c\bar{c}} = \frac{1}{R_y} \frac{1}{C_{c/D}} \frac{d\sigma_{c\bar{c}}}{dy} \tag{E.2}$$

The extrapolation factor $R_y = 0.225$ is determined using a HVQMNR calculation [130] instead of the PYTHIA calculation. Here, the factor $C_{c/D} = 0.96$ accounts for the difference of rapidity distribution between D mesons and charm quarks.

For the step 1, we calculate $d\sigma_e/dy(p_{\rm T} > p_{\rm Tlow})$ by adding the bin entries of heavy flavor electron spectra with $p_{\rm T} > p_{\rm Tlow}$, instead of fitting by a PYTHIA electron function described in section 5.6.1. The bin counting method is more reliable, because the fitting uncertainty is not involved to the systematic uncertainty. The obtained integrated yield ($d\sigma_e/dy(p_{\rm T} > p_{\rm Tlow})$) is summarized in Tab. E.1. The systematic uncertainty is calculated from the heavy flavor electron spectrum and T_{AA}.

Table E.1: The summary of $d\sigma_e/dy(p_{\rm T} > 0.4)$ calculated in the step 1.

Centrality	$T_{AA}(\mathrm{mb}^{-1})$	$dN_e/dy(p_{\rm T} > 0.4)(\times 10^{-3})$	$d\sigma_e/dy(p_{\rm T} > 0.4)(\mu\mathrm{b})$
0-10%	22.8	$148.0 \pm 2.7 \pm 21.1$	$6.50 \pm 0.12 \pm 0.92$
10-20%	14.4	$90.7 \pm 1.9 \pm 13.9$	$6.30 \pm 0.13 \pm 0.96$
20-40%	7.07	$43.5 \pm 0.9 \pm 7.6$	$6.15 \pm 0.13 \pm 1.07$
40-60%	2.16	$14.3 \pm 0.5 \pm 2.8$	$6.64 \pm 0.22 \pm 1.28$
60-92%	0.35	$2.10 \pm 0.15 \pm 0.59$	$5.98 \pm 0.42 \pm 1.68$
Min.bias	6.14	$36.6 \pm 0.5 \pm 5.9$	$5.96 \pm 0.08 \pm 0.96$
$p+p$ [131]			$5.95 \pm 0.59 \pm 1.59$

For the step 2 to 5, the extrapolation factor $R_{p_{\rm T}}$ and R_y are determined based on the FONLL and the HVQMNR calculation, respectively, instead of the PYTHIA calculation. Although PYTHIA contains only lowest order (LO) pQCD, FONLL and HVQMNR is NLO and beyond. Thus, FONLL and HVQMNR can provide a trustworthy calculation. In addition, the FONLL calculation agrees well with the data within the statistical and the systematic uncertainty [39]. As a result, the factor $R_{p_{\rm T}} = 0.54 \pm 0.05(10\%)$ and $R_y = 0.225 \pm 0.034(15\%)$ are obtained. The errors of these factors are assigned as the systematic uncertainty.

HVQMNR calculates the rapidity distribution of bare charm quarks, but not charmed hadrons and/or charm electrons. We need to take into account the difference of rapidity distribution between charm quarks, D mesons and charmed electrons. The factor $C_{e/D}$ is used to correct the rapidity distribution of charm electrons to D mesons, and $C_{c/D}$ also corrects the rapidity spread of charm quarks to D mesons. These factors $C_{e/D} = 0.935$ and $C_{c/D} = 0.96$ are determined by PYTHIA.

The results in step 2 and 3 are summarized in Tab. E.2. In these steps, the invariant integrated yield $d\sigma_e/dy$ is calculated and then bottom contributions calculated by FONLL are subtracted.

After the subtraction of the b contribution, the charm contribution only remains in heavy flavor electrons. Therefore, we denote the electrons as charm electrons. In step 4 and 5, the integrated yield of charm electrons is translated to the charms yield ($d\sigma_{c\bar{c}}/dy$) using $BR(c \to e) = 9.5 \pm 1.0\%$. Then, that is extrapolated to the total charm cross

Table E.2: Summary of $d\sigma_e/dy$ and then b contribution is subtracted.

Centrality	$d\sigma_e/dy$ (μb)	$d\sigma_e/dy$ after b subtraction (μb)
0-10%	12.04±0.22±2.04	11.93±0.22±2.04
10-20%	11.66±0.24±2.09	11.55±0.24±2.09
20-40%	11.38±0.23±2.24	11.27±0.23±2.24
40-60%	12.30±0.40±2.62	12.18±0.40±2.62
60-92%	11.08±0.77±2.38	10.97±0.77±2.38
Min.bias	11.03±0.15±2.05	10.92±0.15±2.05
$p+p$ [131]	11.02±1.10±3.12	10.90±1.10±3.12

section ($\sigma_{c\bar{c}}$). The obtained $d\sigma_{c\bar{c}}/dy$ and $\sigma_{c\bar{c}}$ are summarized in Tab. E.3. The systematic uncertainties are determined by adding the errors in these steps in quadrature.

Table E.3: Summary of $d\sigma_{c\bar{c}}/dy$ and $\sigma_{c\bar{c}}$ in minimum bias Au+Au collisions and five centrality classes. The charm cross section in $p+p$ collisions is also shown [39].

Centrality	T_{AA} (mb^{-1})	$d\sigma_{c\bar{c}}/dy$ (μb)	$\sigma_{c\bar{c}}$ (μb)
0-10%	22.8	134.3±2.4±27.0	620±11±156
10-20%	14.4	130.0±2.7±27.3	600±12±155
20-40%	7.07	126.8±2.6±28.6	586±12±159
40-60%	2.16	137.1±4.6±32.9	633±21±180
60-92%	0.35	123.4±8.7±39.2	570±40±201
Min.bias	6.14	122.9±1.6±26.5	568± 8±150
$p+p$ [131]		122.8±12.3±37.5	567±57±193

Bibliography

[1] F. Halzen and A. D. Martin, John Wiley & Sons (1984) [Quarks and Leptons].

[2] K. Yagi, T. Hatsuda and Y. Miake, Camb. Monogr. Part. Phys. Nucl. Phys. Cosmol. **23**, 1 (2005) [Quark-Gluon Plasma].

[3] E. V. Shuryak, Phys. Rep. **61**, 71 1980.

[4] F. Karsch, Lect. Notes Phys. **583**, 209 2002.

[5] K. Rajagopal, Nucl. Phys. **A 661**, 150 1999.

[6] K. Adcox *et al.*, Nucl. Phys. **A 757**, 184 (2005) [PHENIX Collaboration].

[7] X. N. Wang, M. Gyalassy, Phys. Rev. Lett. **68**, 1480 2002.

[8] X M. Gyalassy *et al.*, nucl-th/0302077.

[9] S. S. Adler *et al.*, Phys. Rev. Lett. **91**, 072301 (2003) [PHENIX Collaboration].

[10] S. S. Adler *et al.*, Phys. Rev. Lett. **91**, 072303 (2003) [PHENIX Collaboration].

[11] U. Heinz, nucl-th/0407067 (2004)

[12] K. H. Ackermann *et al.*, Phys. Rev. Lett. **86**, 402 (2001) [STAR Collaboration].

[13] S. S. Adler *et al.*, Phys. Rev. Lett. **91**, 182301 (2003) [PHENIX Collaboration].

[14] J. Adams *et al.*, Phys. Rev. **C 72**, 014904 (2005) [STAR Collaboration].

[15] P. Huovinen *et al.*, Phys. Lett. **B503**, 58 (2001).

[16] D. Molnar and S. Voloshin, Phys. Rev. Lett. **91**, 092301 (2003).

[17] J. A. Appel, Annu. Rev. Nucl. Part. Sci. **42**, 367 (1992).

[18] B. Müller and X. N. Wang, Phys. Rev. Lett. **68**, 2437 (1992).

[19] Y. L. Dokshitzer and D. E. Kharzeev, Phys. Lett. **B 519**, 199 (2001).

[20] R. Vogt, Heavy Ion Phys. **17**, 75 (2003).

[21] F. W. Busser *et al.*, Phys. Lett. **B 53**, 212 (1974).

[22] F. W. Busser *et al.*, Nucl. Phys. **B 113**, 189 (1976).

[23] P. Perez *et al.*, Phys. Lett. **B 112**, 260 (1982).

[24] M. Basile *et al.*, Nuovo Cimento **A 65**, 421 (1981).

[25] I. Hinchliffe and C. H. Llewellyn Smith, Phys. Lett. **B 61**, 472 (1976).

[26] E. Norrbin and T. Sjostrand, Eur. Phys. J. **C 17**, 137 (2000).

[27] C. Amsler *et al.*, Phys. Lett. **B 667**, 1 (2008). [Particle Data Group] (URL: http://pdg.lbl.gov)

[28] T. Sjostrand, Comput. Phys. Commun. 82, 74 (1994).

[29] H. L. Lai *et al.* Eur. Phys. J. **C 12**, 375 (2000).

[30] A. D. Martin *et al.* Eur. Phys. J. **C 35**, 325 (2004).

[31] M. Gluck *et al.* Eur. Phys. J. **C 53**, 355 (2008).

[32] M. Cacciari *et al.* JHEP **9805**, 007 (1998).

[33] M. Cacciari *et al.* Phys. Rev. Lett. **95**, 122001 (2005).

[34] M. Cacciari *et al.* Phys. Rev. Lett. **89** , 122003 (2002).

[35] M. Cacciari *et al.* JHEP **0407**, 033 (2004).

[36] M. Cacciari, http://www-rnc.lbl.gov/ esichter/HeavyQuark-2007/talks/Fri/cacciari.pdf

[37] A. Abulencia *et al.* Phys. Rev. **D 75** , 012010 (2007) [CDF Collaboration].

[38] D. Acosta *et al.* Phys. Rev. **D 71** , 032001 (2005) [CDF Collaboration].

[39] A. Adare *et al.* Phys. Rev. Lett. **97** , 252002 (2006) [PHENIX Collaboration].

[40] J. D. Bjorken, Phys. Rev. **D 17**, 171 (1978).

[41] C. Peterson *et al.*, Phys. Rev. **D 27**, 105 (1983).

[42] V. G. Kartvelishvili *et al.*, Phys. Lett. **B 78**, 615 (1978).

[43] P. Collins and T. Spiller, J. Phys. **G 11**, 1289 (1985).

[44] G. Colangelo and P. Nason, Phys. Lett. **B 285**, 167 (1992).

[45] M. G. Bowler, Z. Phys. **C 11**, 169 (1981).

[46] E. Braaten *et al.*, Phys. Rev. **D 51**, 4819 (1995).

[47] P. Nason and C. Oleari, Nucl. Phys. **B 565**, 245 (2000).

[48] M. Cacciari and P. Nason, Phys. Rev. Lett. **89**, 12 (2002).

[49] M. Artuso *et al.*, Phys. Rev. **D 70**, 112001 (2004) [CLEO Collaboration].

[50] R. Seuster *et al.*, Phys. Rev. **D 73**, 032002 (2006) [BELLE Collaboration].

[51] A. Heister *et al.*, Phys. Lett. **B 512**, 30 (2001) [ALEPH Collaboration].

[52] G. Abbiendi *et al.*, Eur. Phys. J. **C 29**, 463 (2003) [OPAL Collaboration].

[53] K. Abe *et al.*, Phys. Rev. **D 65**, 092006 (2002) [SLD Collaboration].

[54] R. K. Ellis, W. J. Stirling and B. R. Webber, Camb. Monogr. Part. Phys. Nucl. Phys. Cosmol. **8**, 1 (1996) [QCD and Collider Physics].

[55] R. K. llis, 2004 CTEQ Summer School Document (2004).

[56] J. D. Bjorken, Phys. Rev. **D 27**, 140 (1983).

[57] P. F. Kolb, Heavy Ion Phys. **21**, 234 (2004).

[58] L. Ahle *et al.*, Phys. Lett. **B 332**, 258 (1994).

[59] T. Alber *et al.*, Phys. Rev. Lett. **75**, 3814 (1995).

[60] K. Adkox *et al.*, Phys. Rev. Lett. **87**, 052301 (2001).

[61] S. S. Adler *et al.*, Phys. Rev. **C 71**, 034908 (2005).

[62] S. S. Adler *et al.*, Phys. Rev. **C 71**, 049901 (2005).

[63] R. J. Glauber and G. Matthiae, Nucl. Phys. **B 21**, 135 (1970).

[64] M. J. Tannenbaum, PHENIX Analysis Note 294 (2004).

[65] P. Levai *et al.*, Phys. Rev. **C 51**, 3326 (1995).

[66] J. W. Cronin *et al.*, Phys. Rev. **D 11**, 3105 (1975).

[67] M. Lev and B. Petersson, Z. Phys. **C 21**, 155 (1983).

[68] S. S. Adler *et al.*, Phys. Rev. **C 74**, 024904 (2006) [PHENIX Collaboration].

[69] C. N. Brown *et al.*, Phys. Rev. **C 54**, 3195 (1996) [E789 Collaboration].

[70] J. J. Aubert *et al.*, Phys. Lett. **B 123**, 275 (1985) [EMC Collaboration].

[71] M. Arneodo *et al.*, Nucl. Phys. **B 441**, 12 (1995) [NMC Collaboration].

[72] H. Wohri and C. Lourenco, J. Phys. G **30**, S315 (2004).

[73] K. K. Eskola *et al.*, Eur. Phys. J. **C 9**, 61 (1999).

[74] S. Kelly, J. Phys. G. **30**, S1189 (2004).

[75] R. Baier *et al.*, Nucl. Phys. **B 483**, 291 (1997) .

[76] M. Gyulassy *et al.*, Nucl. Phys. **A 661**, 637c (1999) .

[77] M. Gyulassy *et al.*, Phys. Rev. Lett. **85**, 5535 (2000) .

[78] M. Gyulassy *et al.*, Nucl. Phys. **B 571**, 197 (2000) .

[79] M. Gyulassy *et al.*, Phys. Rev. Lett. **86**, 2537 (2001) .

[80] M. G. Mustafa, Phys. Rev. **C 72**, 014905 (2005) .

[81] S. Wicks *et al.*, Nucl. Phys. **A 784**, 426 (2007) .

[82] M. Djordjevic, Phys. Rev. **C 74**, 064907 (2006) .

[83] A. Adare *et al.*, Phys. Rev. **C 77**, 064907 (2008) [PHENIX Collaboration].

[84] To be published. [PHENIX Collaboration].

[85] H. Hahn *et al.*, Nucl. Inst. and Meth. A **499**, 245 (2003) .

[86] K. Adcox *et al.*, Nucl. Inst. and Meth. A **499**, 469 (2003) .

[87] M. Allen *et al.*, Nucl. Inst. and Meth. A **499**, 549 (2003) .

[88] T. Hachiya *et al.*, PHENIX Technical Note 393 (2002) .

[89] C. Adler *et al.*, Nucl. Inst. and Meth. A **499**, 433 (2003) .

[90] C. Adler *et al.*, Nucl. Inst. and Meth. A **470**, 488 (2001) .

[91] M. Chiu *et al.*, Phys. Rev. Lett. **89**, 012302 (2002) .

[92] S. H. Aronson *et al.*, Nucl. Inst. and Meth. A **499**, 480 (2003) .

[93] K. Adcox *et al.*, Nucl. Inst. and Meth. A **499**, 489 (2003) .

[94] M. Aizawa *et al.*, Nucl. Inst. and Meth. A **499**, 508 (2003) .

[95] M. Aizawa *et al.*, Nucl. Inst. and Meth. A **433**, 143 (1999) .

[96] L. Aphecetche *et al.*, Nucl. Inst. and Meth. A **499**, 521 (2003) .

[97] M. M. Aggarwal *et al.*, Phys. Rev. Lett. **81**, 4087 (1998) [WA98 collaboration].

[98] S. S. Adler *et al.*, Nucl. Inst. and Meth. A **499**, 560 (2003)

[99] GEANT 3.2.1, CERN program library.

[100] X. N. Wang and M. Gyulassy, Phys. Rev. **D 44** 3501 (1991).

[101] T. Hachiya *et al.*, PHENIX Analysis Note 107 (2002).

[102] J. Nagle *et al.*, PHENIX Analysis Note 113 (2002).

[103] H. Appelshauser *et al.*, Eur. Phys. J. **A 2**, 383 (1998) [NA49 collaboration].

[104] S. Kelly *et al.*, PHENIX Analysis Note 33 (2000)

[105] S. S. Adler *et al.*, Phys. Rev. **C 69**, 034909 (2004)

[106] K. Reygers, PHENIX Analysis Note 169 (2003)

[107] J. T. Mitchell *et al.*, Nucl. Inst. and Meth. A **482**, 491 (2002)

[108] J. Burward-Hoy *et al.*, PHENIX Analysis Note 172 (2003)

[109] T. Chujo *et al.*, PHENIX Analysis Note 187 (2003)

[110] S. S. Adler *et al.*, Phys. Rev. **C 69**, 034910 (2004)

[111] R. Averbeck for the PHENIX collaboration, Nucl. Phys. **A 715**, 695c (2003)

[112] A. Lebedev *et al.*, PHENIX Analysis Note 137

[113] Y. Akiba *et al.*, PHENIX Analysis Note 124

[114] K. Adcox *et al.*, Phys. Rev. Lett. **88**, 192303 (2002)

[115] D. d'Enterria for the PHENIX collaboration, Nucl. Phys. **A 715**, 749c (2003)

[116] M. Kaufman and D. d'Enterria, PHENIX Analysis Note 337 (2004)

[117] T. Hachiya and Y. Akiba, PHENIX Analysis Note 340 (2004)

[118] R. Averbeck *et al.*, PHENIX Analysis Note 89 (2001)

[119] R. Seto for the PHENIX collaboration, J. Phys. G **30**, S1017 (2004)

[120] S. S. Adler *et al.*, Phys. Rev. Lett. **96**, 032001 (2006)

[121] A. Adare *et al.*, Phys. Rev. Lett. **98**, 172301 (2007)

[122] Y. Akiba *et al.*, PHENIX Analysis Note 557 (2007)

[123] A. Adare *et al.*, Phys. Rev. Lett. **103**, 082002 (2009)

[124] M. Leitch,
http://www.int.washington.edu/talks/WorkShops
/int_09_42W/People/Leitch_M/Leitch.pdf

[125] S. Brodsky,
http://indico.cern.ch/getFile.py/access?contribId=6&
resId=1&materialId=slides&confId=72423

[126] G. A. Alves *et al.*, Phys. Rev. Lett. **77**, 2388 (1996) [E769 Collaboration].

[127] M. Adamovich *et al.*, Nucl. Phys. **B 495**, 3 (1997) [WA92 Collaboration].

[128] D. Acosta *et al.*, Phys. Rev. Lett. **91**, 241804 (2003) [CDF Collaboration].

[129] A. Tai for the STAR Collaboration, J. Phys. G **30**, S809 (2004)

[130] M. Mangano *et al.*, Nucl. Phys. **B 405**, 507 (1993)

[131] Y. Akiba *et al.*, PHENIX Analysis Note 509.

[132] A. Adare *et al.*, Phys. Lett. **B 670**, 313 (2009) [PHENIX Collaboration]

[133] J. Adams *et al.*, Phys. Rev. Lett. **94**, 062301 (2005) [STAR Collaboration]

[134] O. Botner *et al.*, Phys. Lett. **B236**, 488 (1990) [UA2 Collaboration]

[135] M. Aguilar-Benitez *et al.*, Z. Phys. **C 40**, 321 (1988) [NA27 Collaboration]

[136] K. Kodama *et al.*, Phys. Lett. **B 263**, 573 (1991) [E653 Collaboration]

[137] R. Ammar *et al.*, Phys. Rev. Lett. **61**, 2185 (1988) [E653 Collaboration]

公表論文

(1) Centrality Dependence of Charm Production from a Measurement of Single Electrons in Au+Au Collisions at $\sqrt{s_{NN}}$ = 200 GeV

S. S. Adler *et al.*, (別紙、共著者リスト①参照)

Physical Review Letters 94, 082301 (2005).

Letter of Acceptance

We approve that Mr. Takashi Hachiya preferentially applies following article as the main part of his doctoral dissertation at Hiroshima University.

Article: Physical Review Letters 94, 082301 (2005)
Title: Centrality Dependence of Charm Production from a Measurement of Single Electrons in Au + Au Collisions at $\sqrt{s_{NN}}$ = 200 GeV

Spokesperson of the PHENIX Collaboration:
Barbara V. Jacak
Professor of Physics and Astronomy at SUNY Stony Brook University

Date: Jan. 22, 2010

Signature: Barbara V. Jacak

Letter of Acceptance

We approve that Mr. Takashi Hachiya preferentially applies following article as the main part of his doctoral dissertation at Hiroshima University.

Article: Physical Review Letters 94, 082301 (2005)
Title: Centrality Dependence of Charm Production from a Measurement of Single Electrons in Au + Au Collisions at $\sqrt{s_{NN}}$ = 200 GeV

Spokesperson of the PHENIX Collaboration:
Barbara V. Jacak
Professor of Physics and Astronomy at SUNY Stony Brook University

Date: Jan. 22, 2010

Signature: Barbara V. Jacak

参考論文

(1) Measurement of Single Electrons and Implications for Charm Production in Au+Au Collisions at $\sqrt{s_{NN}}$ = 130 GeV
K. Adcox *et al.,* (別紙、共著者リスト②参照)
Physical Review Letters 88, 192303 (2002).

(2) Measurement of Bottom Versus Charm as a Function of Transverse Momentum with Electron-Hadron Correlations in p + p Collisions at $\sqrt{s}$ = 200 GeV
A. Adare *et al.,* (別紙、共著者リスト③参照)
Physical Review Letters 103, 082002 (2009).

(3) PHENIX inner detectors
M. Allen et al., (別紙，共著者リスト④参照)
Nuclear Instruments and Methods in Physics Research A 499, 549 (2003).